# Dual-AAV mediated transfer of full-length otoferlin cDNA into auditory inner hair cells and the effects of different mutations in the *OTOF* gene on the protein levels and cellular distribution of otoferlin in auditory inner hair cells

**Dissertation**

for the award of the degree

"Doctor of Philosophy"
Division of Mathematics and Natural Sciences

of the Georg-August-Universität Göttingen

within the doctoral program "Sensory Motor Neuroscience (SMN)"

of the Georg-August University School of Science (GAUSS)

submitted by
**Hanan Al-Moyed**

born in Sana'a, Yemen

Göttingen, January 2019

**Members of the Thesis Committee**

**PD Dr. Ellen Reisinger**

Department of Otorhinolaryngology and InnerEarLab, University Medical Center Göttingen

**Prof. Dr. Nils Brose**

Department of Molecular Neurobiology, Max-Planck-Institute of Experimental Medicine

**Dr. Sebastian Kügler**

Department of Neurology, University Medical Center Göttingen

**Additional Members of the Examination Board**

**Prof. Dr. Silvio Rizzoli**

Department of Neuro- and Sensory Physiology, University Medical Center Göttingen

**Prof. Dr. Thomas Dresbach**

Department of Anatomy and Embryology, University Medical Center Göttingen

**PD Dr. Sven Thoms**

Department of Neuropaediatrics, University Medical Center Göttingen

Date of oral examination: February 28th, 2019

I hereby declare that this Ph.D. thesis entitled "Dual-AAV mediated transfer of full-length otoferlin cDNA into auditory inner hair cells and the effects of different mutations in the *OTOF* gene on the protein levels and cellular distribution of otoferlin in auditory inner hair cells" was written independently and with no other sources and aids than quoted.

Hanan Al-Moyed

Göttingen, January 17th,2019

# Abstract

Otoferlin is a large multi-$C_2$ domain protein indispensable for hearing and synaptic transmission in auditory inner hair cells (IHCs). Mutations within the *OTOF* gene, coding for otoferlin, cause non-syndromic recessive hearing loss DFNB9. The severity of the hearing impairment can range from profound deafness to moderate hearing loss depending on the pathogenic *OTOF* variant the patient is carrying. Three different otoferlin mutant mouse models have been studied during the course of this thesis to understand the effects of these mutations on the expression levels, cellular distribution, ultrastructural subcellular localization, and stability of otoferlin in IHCs and how these factors relate to the impaired IHC physiology and auditory function deficits observed in these mice. Otoferlin knock-out (*Otof*$^{-/-}$) mice are deaf and have almost completely abolished IHC exocytosis as a result of absent otoferlin protein. *Pachanga* (*Otof*$^{Pga/Pga}$) otoferlin mutant mice, carrying the p.Asp1767Gly missense mutation, show no auditory brain stem responses (ABRs) and have a reduced sustained IHC exocytosis. *Otof*$^{I515T/I515T}$ otoferlin knock-in mice, carrying the human p.Ile515Thr missense mutation, suffer from a moderate hearing impairment and their sustained IHC exocytosis levels are between the levels of wild-type and *Otof*$^{Pga/Pga}$ IHCs. My analysis revealed that the amount of plasma membrane-bound otoferlin in these IHCs seems to correlate with the sustained exocytosis levels and hearing phenotypes found in all three genotypes. Temperature elevation reduces membrane-bound otoferlin even further in *Otof*$^{I515T/I515T}$ mutants, thus providing a potential explanation for the temperature-sensitive hearing loss found in individuals carrying this mutation. Additionally, both the p.Asp1767Gly and the p.Ile515Thr mutation appear to interfere with the membrane targeting of otoferlin and its functions in membrane retrieval and synaptic vesicle reformation from endosomal IHC compartments.

DFNB9 patients would benefit significantly from gene replacement therapies due to the limitations of cochlear implants, which are the only current available treatment for these individuals. Gene transfer mediated by recombinant adeno-associated viruses (AAVs) is seen as a promising tool to treat inherited deafness forms because of the high safety profile

and IHC targeting efficiency of this virus. However, the limited cargo capacity of AAVs (~4.7 kb) hinders the transport of the 6 kb-long full-length otoferlin coding sequence into IHCs. With the goal of overcoming this obstacle, I have designed dual-AAV half vectors, each carrying one half of the full-length otoferlin cDNA. $Otof^{-/-}$ mice co-injected with these dual-AAV half vectors showed full-length otoferlin expression in auditory hair cells and partially recovered sustained IHC exocytosis and auditory function. Broadband click sound-evoked ABR thresholds could be restored to near wild-type thresholds of 40-60 dB SPL. However, trans-splicing and hybrid dual-AAV half vectors were not able to rescue the 40% synaptic ribbon loss in these mice when injected into the cochlea at postnatal day (P) 5-7. Further analysis revealed that the development and maturation of IHC ribbon synapses during the first two postnatal weeks was altered in $Otof^{-/-}$ mice. All of these findings point towards a yet unknown role of otoferlin in IHC ribbon synapse maturation. My data additionally showed that using a different AAV serotype does not improve full-length otoferlin IHC transduction rates or protein levels in transduced $Otof^{-/-}$ IHCs. Optimization of the dual-AAV large transgene reassembly, transcription, and translation is thus crucial to obtain higher protein levels and IHC targeting rates and to subsequently increase ABR wave amplitudes in otoferlin dual-AAV treated animals. Nevertheless, this work shows the first successful gene therapy application using dual-AAV vectors to transfer large genes into the mammalian inner ear in a mouse model for human deafness.

# Table of contents

# Table of figures

# 1  Introduction

## *1.1    Hearing*

Sound waves travel through the outer and middle ear to the inner ear generating pressure waves within the cochlear fluids that cause the basilar membrane of the organ of Corti to vibrate. These vibrations are detected by the mechanosensory epithelial cells, known as the auditory hair cells (HCs), which are embedded into the organ of Corti and sitting on top of the basilar membrane (Figure 1.1). There are two types of auditory HCs in the mammalian cochlea: i) outer hair cells (OHCs) and ii) inner hair cells (IHCs). The OHCs are responsible for mechanically amplifying the sound-evoked basilar membrane deflections to boost the sound stimulus. Distortion-product otoacoustic emissions (DPOAEs) are used to diagnose hearing deficits in infants by measuring the mechanoelectrical activity of OHCs and their sound amplification function. The IHCs, on the other hand, convert the sound-induced pressure waves into an equivalent electrical signal and transmit this signal to the afferent boutons of the spiral ganglion neurons (SGNs) of the auditory nerve. The auditory signal is, then, forwarded along the central auditory pathway to the cortex and further processed in the different auditory centers of the brain (Figure 1.2) (Kiang, 2011; Fettiplace, 2017). Auditory brain stem responses (ABRs) are used to measure the electrical activity of the primary auditory neurons and the central auditory pathway in response to sound stimuli played with different frequencies and sound pressure levels (Figure 1.2) An abnormal or absent ABR wave I, in particular, points towards a dysfunction in IHC synaptic transmission and/or lesions in the auditory nerve fibers (Starr *et al.*, 1996; Shearer and Smith, 2015).
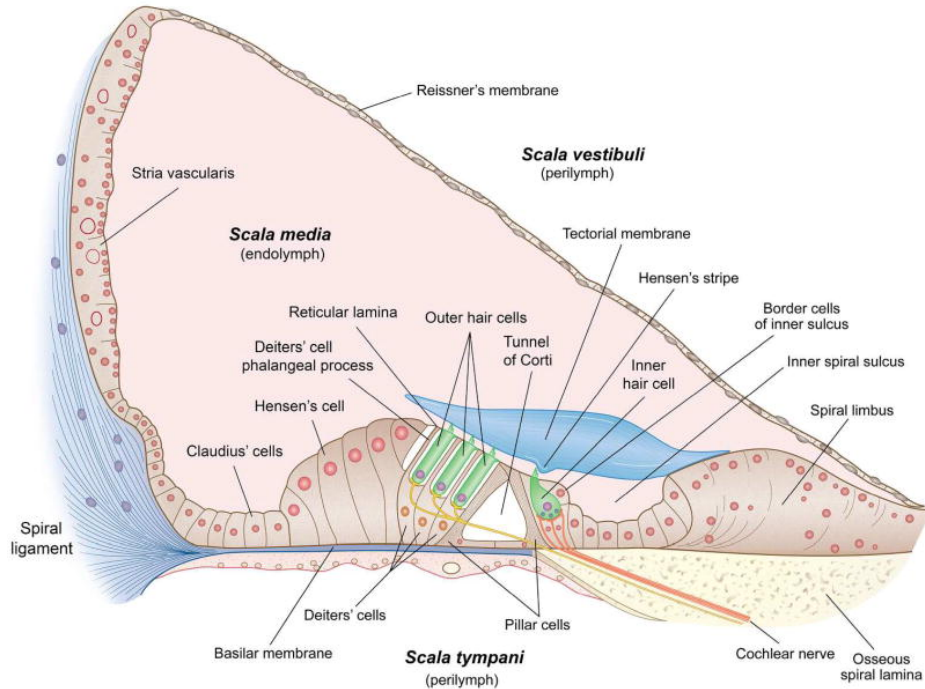
**Figure 1.1**

**Schematic representation of the organ of Corti in the inner ear.**

A cross section through the cochlea showing the organ of Corti and the three fluid-filled cochlear chambers. The auditory outer hair cells (OHCs) and inner hair cells (IHCs) are the mechanosensory epithelial cells of the inner ear and are embedded into the organ of Corti. The three cochlear chambers consist of the scala tympani, the scala media, and the scala vestibuli (Fettiplace, 2017).

The cochlea is organized in a tonotopic manner with each sound frequency generating a traveling wave that propagates along the cochlear turn from the base to the apex of the cochlea. This wave reaches its highest magnitude at the basilar membrane region specific for that frequency and activates the HCs in that region. The HCs located at the apical cochlear turn are tuned to lower frequencies and the ones located at the base are tuned to higher frequencies. Thus, sound stimuli consisting of different frequencies activate several subsets of IHCs along the cochlea and generate spike discharges in the auditory nerve fibers selective for those specific frequencies (Narayan, 1998; Fettiplace, 2017).
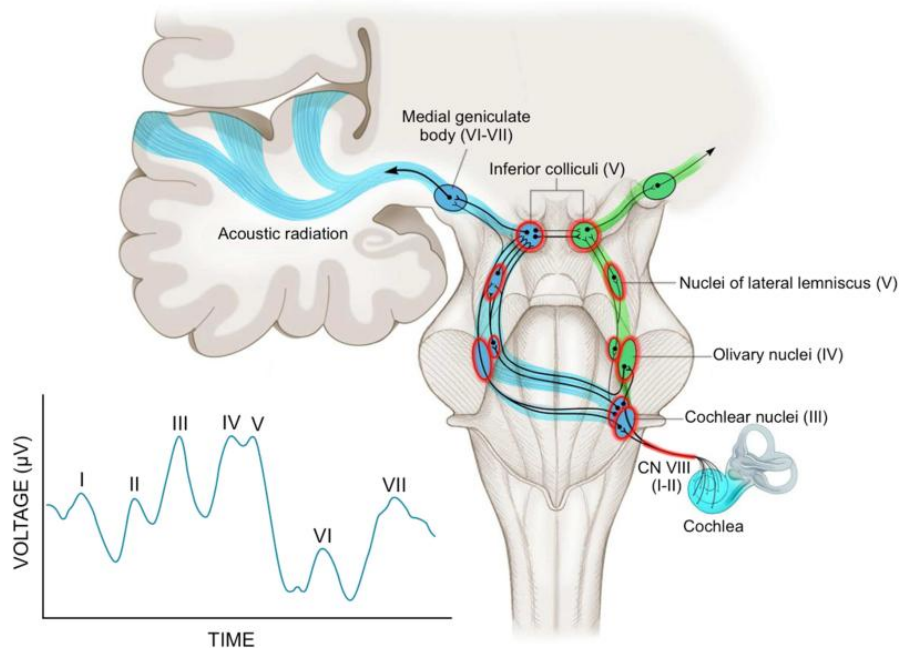
**Figure 1.2:**

**Auditory brain stem responses (ABRs) to sound stimuli and the corresponding neuronal activity along the auditory pathway.**

A representation of the different ipsilateral (green) and contralateral (blue) auditory pathway centers in the brain stem and Thalamus (Olds and Oghalai, 2015) . Each auditory pathway structure is believed to generate a specific ABR wave (waves I-VII) indicated as roman numerals. ABR wave I reflects the compound action potential of the auditory nerve in the distal part of cranial nerve (CN) VIII. ABR wave II arises from the electrical activity of the proximal portion of the CN VIII entering into the brain stem. ABR wave III is generated by the second-order neurons of cochlear nucleus in the brain stem. ABR wave IV reflects the activity of the third-order neurons mainly located in superior olivary complex, but also in the nucleus of the lateral lemniscus and the cochlear nucleus. ABR wave V is thought to be generated by the neurons of multiple auditory structures mostly the inferior colliculus and second-order neurons from lower auditory brainstem regions traveling though the lateral lemniscus. ABR waves VI and VII are believed to arise from the medial geniculate body in the thalamus, but the exact structures contributing to these waves are unknown (Hall, 2007).

## 1.2    Auditory IHC synapses

The process of temporally precise sound encoding and indefatigable neurotransmission requires the presence of a highly specialized molecular synaptic machinery in IHCs. IHC synapses are, therefore, equipped with structures termed "synaptic ribbons" located at presynaptic release sites at the basolateral IHC plasma membrane. These synaptic ribbons tether a halo of synaptic vesicles (SVs) and consist mainly of the two proteins ribeye and piccolo. The large scaffolding protein bassoon anchors the ribbon to the presynaptic density (Figure 1.3) (Frank *et al.*, 2010). Local sound-evoked basilar membrane vibrations lead to the synchronous deflection of HC bundles at the apical tip of the IHCs, generating a depolarizing IHC receptor potential that scales with the sound intensity (Glowatzki and Fuchs, 2002) and subsequently activates voltage-sensitive $Ca_v1.3$ L-type $Ca^{2+}$ channels (Brandt, Striessnig and Moser, 2003). $Ca_v1.3$ $Ca^{2+}$ channels are clustered at the presynaptic release sites, also known as active zones (AZs), beneath the ribbon and opposite to the post-synaptic membrane of the afferent SGN boutons (Figure 1.3). Both ribeye (Frank *et al.*, 2010; Jean *et al.*, 2018) and bassoon (Khimich *et al.*, 2005; Frank *et al.*, 2010; Jing *et al.*, 2013) are essential for this $Ca^{2+}$ channel clustering. IHCs have on average between 5-20 presynaptic AZs depending on the position of the IHC along the tonotopic axis of the cochlea (Meyer *et al.*, 2009) with each AZ being in close proximity to an afferent SGN bouton in mammals (Fettiplace, 2017).

SVs in IHC synapses have been classified morphologically via electron microscopy into three pools based on their relative distance to the synaptic ribbon and AZ plasma membrane: i) the membrane-proximal SV pool  with a distance of up to 40 nm from the AZ membrane (Figure 1.3Figure 1.4); ii) the ribbon-associated SV pool not facing the AZ membrane and having a distance of up to 80 nm from the ribbon (Figure 1.3; Figure 1.4); iii) the outlying SV pool  not facing the AZ membrane and found between 80-350 nm away from the ribbon (Figure 1.4) (Kantardzhieva, Liberman and Sewell, 2013; Chakrabarti, Michanski and Wichmann, 2018).

Other studies have classified SVs via electrophysiological capacitance measurements into four functionally distinct SV pools based on their dynamics and release kinetics. The
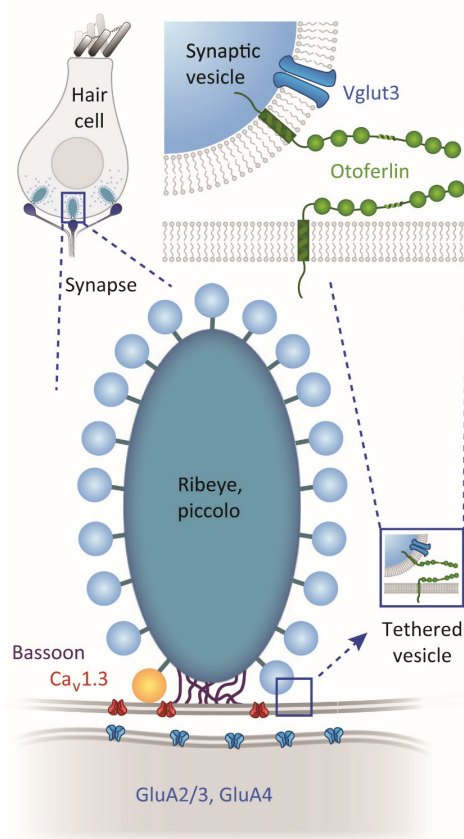
**Figure 1.3:**

**The synaptic ribbon and the different components of the IHC synapse.**

Auditory IHC synapses are equipped with synaptic ribbons and $Ca_v1.3$ $Ca^{2+}$ channels at their presynaptic active zone (AZ) plasma membranes. The postsynaptic site contains the AMPA-receptor subunits GluR2/3 and GluR4. The ribbon tethers a large number of synaptic vesicles (SVs) and mainly consists of ribeye and piccolo. The protein bassoon anchors the ribbon to the AZ membrane. SVs are equipped with Vglut3 and can be classified into the readily release SV pool (RRP, yellow SVs) and the ribbon-associated SV pool (blue). The protein otoferlin is distributed along the cytoplasm and plasma membrane of IHCs and is involved in SV priming and fusion (adapted from Pangršič, Reisinger and Moser, 2012).

readily releasable SV pool (RRP) is the nearest SV population to the AZ membrane and represents all SVs that can be released immediately upon IHC depolarization and $Ca^{2+}$ influx is tought to reflect the fast component of IHC exocytosis upon short IHC depolarization (up to 20 ms). The recycling SV pool is more distant from the AZ membrane and refills the RRP. The larger reserve SV pool constantly refills the recycling and RRP pools in a $Ca^{2+}$ dependent manner and is belived to represent the sustained component of exocytosis upon longer IHC depolarization (20-100 ms). The distant SV pool is proposed to act as a SV reservoir to fill up the other SV pools. The SVs in these pools are dynamic and move from one pool to the next until they reach the RRP (Moser and Beutner, 2000; Beutner and Moser, 2001; Nouvian *et al.*, 2006; Pangrsic *et al.*, 2010; Schnee *et al.*, 2011; Michalski *et al.*, 2017).

The opening of the $Ca^{2+}$ channels upon IHC depolarization leads to the influx of $Ca^{2+}$ ions into

the cell. These ions, in turn, facilitate SV priming at the AZ release sites at the IHC ribbon synapse. The interaction between the IHC $Ca^{2+}$ sensor and the $Ca^{2+}$ ions subsequently triggers the fusion of the RRP vesicles and the release of the neurotransmitter glutamate into the synaptic cleft (Figure 1.3; Figure 1.4). Glutamate consequently activates AMPA (α-amino-3-hydroxy-5-methyl-4-isoxazolepropionic acid) receptors located at the afferent dendrites of the SGNs (Figure 1.3) (Glowatzki and Fuchs, 2002; Schnee *et al.*, 2011; reviewed in: Fettiplace, 2017).
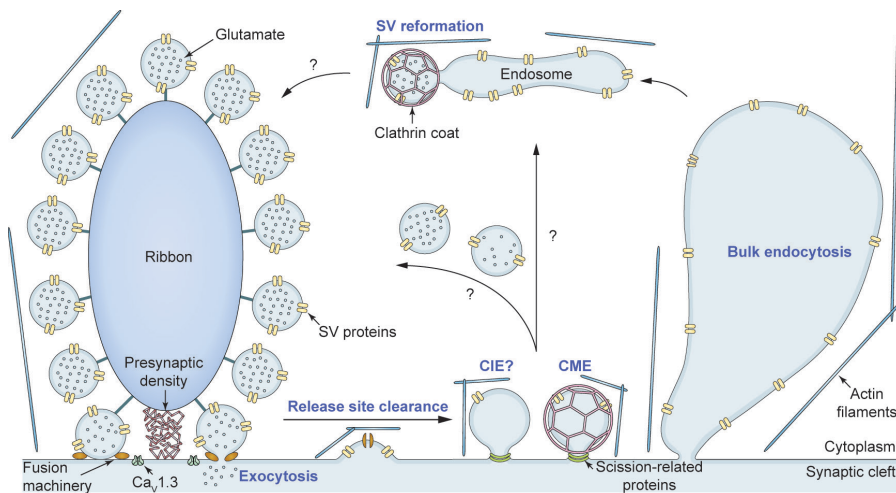


**Figure 1.4:**

**The IHC ribbon synapse and the synaptic vesicle cycle.**

A large number of synaptic vesicles (SVs) are tethered around the synaptic ribbon and transported upon IHC depolarization and $Ca^{2+}$ influx towards the release sites at the IHC active zone (AZ) plasma membrane. These SVs fuse at the release sites and release the neurotransmitter glutamate into the synaptic cleft. The accumulated SV membrane content and exocytic machinery is subsequently recycled from the release sites at the AZ membrane to generate new docking spots for arriving SVs. This AZ membrane clearance is mediated by clathrin-mediated endocytosis (CME), bulk endocytosis, and possibly clathrin-independent endocytosis (CIE). The retrieved endocytosed membranes likely fuse with larger endosomal vesicular structures close to the synaptic ribbon. New SVs are reformed from these endosomal compartments via a clathrin-dependent and/or a clathrin-independent pathway. Parts of the molecular machinery involved in IHC exocytosis and endocytosis are still unknown to date. $Ca_v1.3$: L-type $Ca_v1.3$ $Ca^{2+}$ channels (adapted from Pangrsic and Vogl, 2018).

Sustained neurotransmitter release in IHCs requires efficient SV recruitment to the synaptic ribbons, SV replenishment of the RRP, and AZ release site clearance. Synaptic ribbons are believed to recruit and mediate the transport of SVs from the ribbon-associated and cytosolic SV pools to the presynaptic AZ release sites to refill the membrane-proximal SV pool (Figure 1.4). This process is thought to reflect the sustained component of IHC exocytosis (Schnee *et al.*, 2011; Chakrabarti, Michanski and Wichmann, 2018; Pangrsic and Vogl, 2018). Two hypotheses have been proposed that might explain SV trafficking along the ribbon in response to IHC depolarization and $Ca^{2+}$ influx. In the "crowd surfing" or "conveyor belt" model, which is the most likely scenario, SVs get transported towards the AZ membrane through passive diffusion (Graydon *et al.*, 2014; Chakrabarti, Michanski and Wichmann, 2018). In contrast, the "active SV transport" model states that molecular motors and cytoskeleton proteins (Muresan, Lyass and Schnapp, 1999; Tom Dieck *et al.*, 2005) like actin and tubulin, which can directly interact with the ribbon though ribeye (Uthaiah and Hudspeth, 2010; Kantardzhieva *et al.*, 2012), coordinate this process. SV transport additionally seems to involve the filaments known as tethers, that interconnect the ribbon-associated SVs to each other and attach them to the ribbon itself (Figure 1.3; Figure 1.4) (Chakrabarti, Michanski and Wichmann, 2018). The SVs transported to the release sites are presumably linked to the presynaptic density first via a single tether followed by multiple tethers that precede the docking and fusion steps of exocytosis (Chakrabarti, Michanski and Wichmann, 2018).

The molecular components of the exocytic machinery in IHCs are partly unknown. Several studies have pointed out that the major proteins crucial for exocytosis in neuronal synapses are unnecessary for exocytosis in mature IHCs like the SNARE (soluble N-ethylmaleimide-sensitive factor attachment protein receptor) complex proteins snap-25, syntaxin-1, and the synaptobrevins (Nouvian *et al.*, 2011). Other proteins that are important for the late steps of exocytosis in neurons like synaptophysins, synapsins, complexins (Safieddine and Wenthold, 1999; Strenzke *et al.*, 2009), and the priming proteins CAPS and Munc13 (Vogl *et al.*, 2015) seem to be missing in IHCs. Synaptotagmins 1 and 2 (Syt1 and Syt2), which regulate $Ca^{2+}$ triggered rapid synchronous SV fusion in neurons, are not essential for exocytosis in mature IHCs either (Safieddine and Wenthold,

1999; Beurg *et al.*, 2010; Reisinger *et al.*, 2011). The multi-functional protein otoferlin seems to take over some of these functions and likely acts as the $Ca^{2+}$ sensor in IHCs instead (Roux *et al.*, 2006; Vincent *et al.*, 2014; Michalski *et al.*, 2017).

The IHC AZ membrane is cleared after neurotransmitter release by recycling the SV membrane contents and exocytic machinery via endocytosis. This constant SV turnover is important to generate new available docking spots for the arriving RRP vesicles transported from the ribbon to the release sites (Figure 1.4). IHC endocytosis has to take place in a fast and efficient manner to keep up with the high rates of continuous SV release. Increasing evidence suggests that this process is regulated by slow clathrin-mediated endocytosis and/or invagination of large plasma membrane pieces (bulk endocytosis) (Figure 1.4) (Neef *et al.*, 2014; Jung *et al.*, 2015; Michalski *et al.*, 2017). Reports showed that SVs are not directly formed from clathrin-coated vesicles as these vesicles are larger in size (diameter: 50-60 nm) than the average size of a SV (diameter: 30-45 nm) (Neef *et al.*, 2007, 2014; Chakrabarti, Michanski and Wichmann, 2018). It rather seems that SVs are formed by pinching off from cisterns found at the AZ membrane, from membrane invaginations, and from larger endocytic compartments like endosomes in close proximity to the synaptic ribbon (Figure 1.4) (Neef et al., 2014; Jung et al., 2015; Pangrsic and Vogl, 2018). Bulk endocytosis, in particular, seems to contribute to the formation of larger vesicles (diameter: 50-70 nm) and endosome like vacuoles (diameter: >70 nm) in IHCs (Chakrabarti, Michanski and Wichmann, 2018). Properly sized fusion-competent SVs are formed from these larger structures (Figure 1.4) (Strenzke *et al.*, 2016), refilled with glutamate via the vesicular glutamate transporter 3 (Vglut3) (Figure 1.3) (Ruel *et al.*, 2008; Seal *et al.*, 2008), and transported to the synaptic ribbon (Figure 1.4) (Safieddine, El-Amraoui and Petit, 2012; Wichmann and Moser, 2015; Pangrsic and Vogl, 2018). Several proteins like the scaffold protein clathrin, the scission-related protein dynamin, the dynamin recruiter amphiphysin (Neef *et al.*, 2014), and endophilin (Kroll *et al.*, 2019) are involved in clathrin-mediated endocytosis in IHCs. The heterotetrameric clathrin-adaptor-protein complex 2 (AP-2) is thought to play a role in clathrin-dependent SV reformation and AZ release site clearance as well (Duncker *et al.*, 2013; Jung *et al.*, 2015). The presynaptic $Ca^{2+}$ signal not only seems to trigger exocytosis, but also regulates the compensatory endocytosis (Pangrsic and Vogl,

2018) with higher $Ca^{2+}$ concentrations leading to faster endocytosis rates (Beutner *et al.*, 2001). The coupling of endo- and exocytosis does not only require $Ca^{2+}$, but most likely involves other yet to be identified recycling proteins and membrane lipids like phosphatidylinositol 4,5-bisphosphate [$PI(4,5)P_2$] (Maritzen and Haucke, 2017; Pangrsic and Vogl, 2018). How this coupling occurs in IHC synapses and which proteins are involved in this process is mostly unclear and needs to be studied further (Pangrsic and Vogl, 2018).

## *1.3    Otoferlin*

Otoferlin, a member of the ferlin protein family, is a large tail-anchored multi-$C_2$ domain protein encoded by the 48 exons of the *OTOF* gene (Yasunaga *et al.*, 1999, 2000; Roux *et al.*, 2006; Lek *et al.*, 2012; Pangršič, Reisinger and Moser, 2012). Yasunaga *et al.*, 2000 reported the presence of long (~7 kb-long) otoferlin transcripts in human and mouse brain and inner ear tissue. The same research group also detected short (~5 kb-long) otoferlin transcripts in human heart, placenta, liver, pancreas, skeletal muscle, kidney, inner ear, and brain tissue, but not in mouse tissue (Yasunaga *et al.*, 1999, 2000). The long otoferlin isoform (1997 amino acids long) consists of six $C_2$ domains ($C_2$A-$C_2$F) connected via long linker regions, a FerA domain, a FerB domain, and a single C-terminal transmembrane domain. A seventh $C_2$ domain ($C_2$de) was additionally predicted between the $C_2$D and $C_2$E domain of otoferlin (Figure 1.5) (Yasunaga *et al.*, 1999, 2000; Roux *et al.*, 2006; Lek *et al.*, 2012; Pangršič, Reisinger and Moser, 2012; Harsini *et al.*, 2018). The short isoform (1230 amino acids long), on the contrary, only contains the last three $C_2$ domains and the transmembrane domain (Yasunaga *et al.*, 1999, 2000). Nevertheless, the exact structure of otoferlin, except for the FerA domain and $C_2$A domain (Helfmann *et al.*, 2011; Harsini *et al.*, 2018), is still unknown (Pangršič, Reisinger and Moser, 2012; Johnson, 2017).

The expression of otoferlin in auditory HCs first starts at the embryonic stage E16 for IHCs and E18 for OHCs and reaches its peak at approximately postnatal day (P) 6 for both HC types. After P6 its expression starts to change during development and decreases in OHCs until it almost disappears after maturation. In contrast, IHCs continue to express otoferlin throughout their cytosol and plasma membrane even after maturation (Roux *et al.*, 2006; Beurg *et al.*, 2008; Pangrsic *et al.*, 2010; Strenzke *et al.*, 2016).
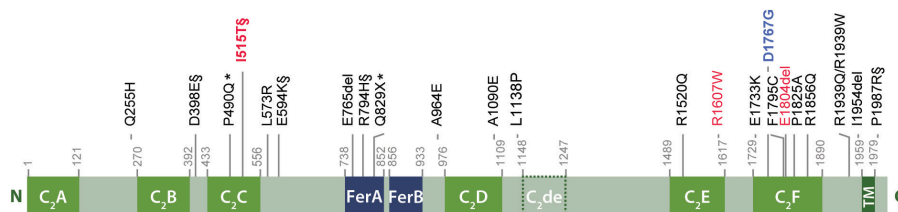
**Figure 1.5 :**

**Schematic representation of the otoferlin protein and the pathogenic mutations associated with autosomal recessive hearing impairment DFNB9.**

The long otoferlin isoform present in auditory IHCs and necessary for hearing consists of six $C_2$ domains: $C_2A$ (aa 1-121), $C_2B$ (aa 270-392), $C_2C$ (aa 433-556), $C_2D$ (aa 976-1109), $C_2E$ (aa 1489-1617), and $C_2F$ (aa 1729-1890). A possible seventh $C_2$ domain ($C_2$de, aa 1148-1247) has been predicted between the $C_2D$ and $C_2E$ domain. The protein also possesses a ferlin-specific FerA domain (aa 738-852), a FerB domain (aa 856-933), and a transmembrane domain (TM, aa 1959-1979) at the C-terminus. Different pathogenic otoferlin missense mutations or in-frame deletions associated with *OTOF*-related hearing loss are presented on the top. Missense mutations linked to temperature sensitive hearing impairment like the p.Ile515Thr (I515T) mutation are displayed in magenta. The p.Asp1767Gly (D1767G) missense mutation is depicted in blue (adapted from Pangršič, Reisinger and Moser, 2012).

Pathogenic mutations in the *OTOF* gene have been linked to autosomal recessive non-syndromic hearing loss (DFNB9) in humans (Yasunaga *et al.*, 1999, 2000; Roux *et al.*, 2006; Longo-Guess *et al.*, 2007; Rodríguez-Ballesteros *et al.*, 2008; Marlin *et al.*, 2010). Otoferlin knock-out (*Otof$^{-/-}$*) mice lack otoferlin expression and show no characteristic ABR waves when subjected to sound stimuli, but still have a normal OHC function (Roux *et al.*, 2006; Reisinger *et al.*, 2011). *Pachanga* (*Otof$^{Pga/Pga}$*) mice, carrying an N-ethyl-N-nitrosourea–mediated p.Asp1767Gly (D1767G) missense mutation that affects the $C_2F$ domain of otoferlin (Schwander *et al.*, 2007; Figure 1.5; Pangrsic *et al.*, 2010), are also profoundly deaf despite having some scarce SGN spiking at high stimulus intensities (>100 dB SPL for less than 10 stimuli/s) and some residual otoferlin expression in their IHCs (Pangrsic *et al.*, 2010). Other otoferlin mutant mouse models like the *Otof$^{C2C/C2C}$* mice, carrying two missense mutations that are predicted to alter the $Ca^{2+}$ binding affinity of the $C_2C$ domain (Johnson and Chapman, 2010; Michalski *et al.*, 2017), have normal otoferlin protein levels, but a moderate hearing loss phenotype. Furthermore, the knock-down of otoferlin seems

to cause hearing and balance defects in zebrafish (Chatterjee *et al.*, 2015). It was, therefore, suggested that the long otoferlin isoform is essential for normal synaptic transmission in auditory IHCs (Roux *et al.*, 2006; Pangrsic *et al.*, 2010) and plays a role in vestibular HC synaptic transmission as well (Dulon et al., 2009).

Otoferlin is not required for IHC survival and development since $Otof^{-/-}$ IHCs were morphologically indistinguishable from wild-type IHCs (Roux *et al.*, 2006). This protein additionally seems not to be required for IHC ribbon synapse formation as $Otof^{-/-}$ mice have normal ribbon synapse numbers at P6 (Roux *et al.*, 2006). However, $Otof^{-/-}$ (~40%) and $Otof^{Pga/Pga}$ mice (~19%) have fewer ribbon synapses after the onset of hearing than wild-type animals. These observations indicate that otoferlin is important for IHC ribbon synapse maintenance after the onset of hearing (Roux *et al.*, 2006; Pangrsic *et al.*, 2010).

Research has shown that otoferlin is a major key player in several IHC exocytosis steps (Pangršič, Reisinger and Moser, 2012; Pangrsic and Vogl, 2018). This protein is crucial for the late steps of RRP exocytosis like SV priming and fusion since $Otof^{-/-}$ IHCs have almost completely abolished exocytosis despite normal $Ca^{2+}$ currents (Roux *et al.*, 2006; Pangrsic *et al.*, 2010; Reisinger *et al.*, 2011) and SV numbers (Roux *et al.*, 2006; Vogl *et al.*, 2015). It was proposed, in this regard, that otoferlin either takes over the function of the neuronal docking and priming factors CAPS and Munc13, which are not required for IHC exocytosis (Vogl *et al.*, 2015), or interacts with yet unidentified proteins involved in these steps (Johnson, 2017; Pangrsic and Vogl, 2018). This protein additionally seems to plays a role in SV tethering as the length of tethers connecting the SVs to the AZ membrane is altered in $Otof^{-/-}$ IHCs (Vogl *et al.*, 2015). Otoferlin is not only necessary for the late steps of exocytosis, but also for RRP replenishment (Roux *et al.*, 2006; Pangrsic *et al.*, 2010; Jung *et al.*, 2015; Strenzke *et al.*, 2016; Michalski *et al.*, 2017; Chakrabarti, Michanski and Wichmann, 2018). $Otof^{Pga/Pga}$ IHCs, unlike $Otof^{-/-}$ mutants, have normal RRP exocytosis upon short IHC depolarizations up to 10 ms and an unchanged RRP size (Pangrsic *et al.*, 2010). SV tethering and docking are also unaltered in these mutants (Chakrabarti, Michanski and Wichmann, 2018). The RRP replenishment rates and sustained IHC exocytosis levels upon longer IHC depolarizations are, however, strongly reduced in $Otof^{Pga/Pga}$ IHCs (Pangrsic *et al.*, 2010). In addition, multiple-tethered and docked SVs seem to accumulate at the AZ

membrane of these mutants, which was attributed to a defect in active zone clearance (Chakrabarti, Michanski and Wichmann, 2018).

Otoferlin is hypothesized to function as a $Ca^{2+}$ sensor that modulates RRP fusion rates and $Ca^{2+}$ dependent RRP replenishment (Roux *et al.*, 2006; Johnson and Chapman, 2010; Vincent *et al.*, 2014; Meese *et al.*, 2017; Michalski *et al.*, 2017) since both Syt1 and Syt2, which regulate these processes in neurons, are not required for IHC exocytosis (Safieddine and Wenthold, 1999; Beurg *et al.*, 2010; Reisinger *et al.*, 2011). It was further demonstrated that the $Ca^{2+}$ sensor Syt1 and otoferlin cannot substitute each other. Virus-mediated Syt1 expression could not rescue exocytosis in otoferlin deficient IHCs and otoferlin expression could not restore exocytosis in Syt1 knock-out neurons in this regard (Reisinger et al., 2011). *In vitro* assays further demonstrated that the $C_2D$-$C_2F$ domains of otoferlin, but not the $C_2A$ domain, can bind $Ca^{2+}$ (Johnson and Chapman, 2010; Meese *et al.*, 2017). The *Otof$^{C2C/C2C}$* otoferlin mutant mouse, carrying two missense mutations that are predicted to change the $Ca^{2+}$ binding affinity of the $C_2C$ domain (Johnson and Chapman, 2010; Michalski *et al.*, 2017), had a delayed fast and sustained IHC exocytosis and an increased ribbon-associated SV pool distance to the ribbon (Michalski *et al.*, 2017). Meese *et al.*, 2017 further reported that the $C_2C$ domain of otoferlin can only bind $Ca^{2+}$ when phosphorylated *in vitro*. In addition, $Ca^{2+}$/calmodulin-dependent serine/threonine kinase II delta (CaMKIIδ) and potentially other kinases seem to regulate the functions of otoferlin by enhancing or decreasing the $Ca^{2+}$ binding affinity of the $C_2$ domains through phosphorylation (Meese *et al.*, 2017). The $Ca_v1.3$ $Ca^{2+}$ channels also co-localize with otoferlin in IHCs *in vivo* (Vincent *et al.*, 2014, 2017). It seems as if this interaction allows IHCs to better synchronize the exocytosis to the transient $Ca^{2+}$ concentration changes by keeping the $Ca^{2+}$ sensor close the $Ca^{2+}$ ion entry sites at the AZ membrane (Johnson, 2017). The ratio of the fast and slow inactivating $Ca_v1.3$ splice isoforms is also changed by the presence or absence of otoferlin, indicating that otoferlin can influence $Ca^{2+}$ entry dynamics in IHCs (Vincent *et al.*, 2014). Nevertheless, it cannot be ruled out that other yet unidentified $Ca^{2+}$-sensing proteins in IHCs might assist otoferlin in its functions (Michalski *et al.*, 2017).

In contrast to many other synapses, IHCs appear to utilize the same $Ca^{2+}$ sensor, otoferlin, in different steps of the SV cycle (Figure 1.4) (Pangršič, Reisinger and Moser, 2012;

Strenzke *et al.*, 2016; Michalski *et al.*, 2017; Pangrsic and Vogl, 2018). A further role for otoferlin in SV recycling and coupling IHC exocytosis and endocytosis was proposed because of its interaction with proteins involved in these processes. Several *in vitro* and *in vivo* studies have reported that otoferlin can interact with the endocytic protein AP-2, the SNAREs, the N-ethylmaleimide sensitive fusion (NSF) protein, the $Ca_v1.3$ $Ca^{2+}$ channels, the small GTPase Rab protein 8b (Rab8b), and myosin VI (MyoVI) (Heidrych *et al.*, 2008, 2009; Ramakrishnan, Drescher and Drescher, 2009; Johnson and Chapman, 2010; Duncker *et al.*, 2013; Ramakrishnan *et al.*, 2014; Vincent *et al.*, 2014; Jung *et al.*, 2015; Hams *et al.*, 2017). It was even implicated, at this point, that otoferlin might bind to several proteins at the same time with the number and type of interaction partners depending on the amount of $Ca^{2+}$ influx into IHCs (Johnson, 2017). Whether the *in vitro* interaction of several otoferlin $C_2$ domains with neuronal t-SNARE proteins (Ramakrishnan, Drescher and Drescher, 2009; Johnson and Chapman, 2010; Hams *et al.*, 2017) is relevant for IHC exocytosis under physiological conditions *in vivo* is unclear as the presence of neuronal SNARE proteins in IHCs is questionable (see introduction "chapter 1.2") (Nouvian *et al.*, 2011). The interaction of otoferlin with AP-2 complexes, the phospholipid [PI(4,5)P$_2$], clathrin, and other yet unidentified proteins, in particular, is believed to trigger SVs to pinch off from endosomal vacuoles and plasma membrane invaginations (Kononenko *et al.*, 2014; Pangrsic and Vogl, 2018). Since the AP-2 complex is involved in both AZ clearance and SV reformation it was further suggested that it might function as a sorting factor for otoferlin by inducing the clearance of "used" otoferlin from AZ release sites after SV fusion (Jung *et al.*, 2015). Another study found that otoferlin immunofluorescence staining correlates with the majority of newly endocytosed organelles in IHCs with the highest correlation found at the basal IHC region and the lowest at the nucleus (Revelo *et al.*, 2014).

It is still unclear whether and to which degree otoferlin can regulate other cellular processes like cargo transport within IHCs, enzymatic activity, and post-translational modifications (Wu *et al.*, 2015; Johnson, 2017). $C_2$ domain proteins are believed to regulate the $Ca^{2+}$-dependent assembly of membrane-trafficking complexes and cellular trafficking events (Lek *et al.*, 2012; Johnson, 2017). In fact, it was shown that ferlins can regulate $Ca^{2+}$-induced membrane fission and fusion events (Lek *et al.*, 2012; Johnson, 2017). An *in vitro*

study showed that both the $C_2C$ and the $C_2F$ domains of otoferlin are able to interact with the phospholipid [PI(4,5)P$_2$] facing the cytoplasmic side of cell membranes (Padmanarayana *et al.*, 2014). This finding led to the assumption that these two domains mediate the targeting of otoferlin towards the plasma membrane and induce fusion events (Johnson and Chapman, 2010; Marty et al., 2014; Padmanarayana et al., 2014). Unlike the synaptotagmins, which only possess two $C_2$ domains (Johnson, 2017), otoferlin can interact with membrane-trafficking proteins like MyoVI (Heidrych *et al.*, 2009; Roux *et al.*, 2009). Otoferlin's interaction partners MyoVI and Rab8 are both involved in cargo sorting and endosomal trans-Golgi networking (Heidrych *et al.*, 2008, 2009; Roux *et al.*, 2009; Pangrsic and Vogl, 2018). These interactions further strengthen the theory that otoferlin is involved in trafficking events in IHCs.

A truncated mini-dysferlin protein variant, generated by cleaving some dysferlin splice variants via $Ca^{2+}$-dependent calpain proteolytic cleavage, contributes to the process of membrane repair in striated muscles. Similar to synaptotagmins, the short dysferlin variant only contains the last two C-terminal $C_2$ domains of the protein and its transmembrane domain (Lek *et al.*, 2013). It is unknown whether such a truncated mini-otoferlin variant exists in IHCs and if it mediates similar functions as the truncated mini-dysferlin version. Several truncated otoferlin forms were supposedly able to rescue hearing and balance in otoferlin knock-down zebrafish (Chatterjee et al., 2015), but were not able to rescue auditory function in otoferlin knock-out mice (Tertrais *et al.*, 2019). These results imply that full-length otoferlin is needed for proper IHC synaptic transmission in mice and probably humans.

In conclusion, otoferlin is a multi-functional protein involved in many cellular processes in auditory IHCs and all six $C_2$ domains of this protein seems to be necessary for proper IHC synaptic transmission. Yet, there are still many open questions regarding the exact role of this protein and how different *OTOF* mutations interfere with its different functions.

## 1.4    Otoferlin related hearing impairment (DFNB9)

Hearing loss is the most common sensory deficiency among humans and can be divided into conductive and sensorineural deafness. While conductive hearing loss is caused by a sound conduction defect in the outer and/or middle ear, the sensorineural deafness results from an impairment in the inner ear or auditory nerve. Sensorineural hearing impairment can be congenital or acquired through exposure to different risk factors like infections (Varga, 2003; Matsunaga *et al.*, 2012; Shearer and Smith, 2015; Nishio and Usami, 2017). At least 50-60% of childhood deafness cases in developed countries can be attributed to genetic causes and can appear as syndromic or non-syndromic hearing loss (Morton and Nance, 2006). Whereas syndromic hearing loss is accompanied by symptoms in other body parts like blindness, non-syndromic hearing loss only affects the auditory function. Non-syndromic hearing impairment can be classified further into autosomal dominant (DFNA), autosomal recessive (DFNB), and X-linked (DFNX) deafness (Petit, 1996). Around seventy genes have been linked to autosomal recessive non-syndromic hearing loss (DFNB) (Hereditary Hearing Loss Homepage: http://hereditaryhearingloss.org/).

One of these deafness genes is the *OTOF* gene coding for the protein otoferlin and located in chromosome 2 at position p23.1 (Yasunaga *et al.*, 1999; Varga *et al.*, 2006; Shearer and Smith, 2015). Mutations in this gene cause congenital prelingual recessive hearing loss DFNB9 (Yasunaga *et al.*, 1999; Shearer and Smith, 2015). Over one thousand pathogenic *OTOF* sequence variants have been identified so far (Ensembl Database: http://www.ensembl.org/). Many of these pathogenic mutations are found within the $C_2$ domains of otoferlin (Rodríguez-Ballesteros *et al.*, 2008). The exact number of individuals diagnosed with congenital non-syndromic hearing loss or auditory neuropathy, carrying a pathogenic variant of this gene, is unknown and hard to asses. The prevalence of DFNB9 also varies between different ethnic populations (Varga, 2003; Varga *et al.*, 2006; Rodríguez-Ballesteros *et al.*, 2008; Matsunaga *et al.*, 2012; Shearer and Smith, 2015). For instance, approximately 2.3% of prelingual-onset or congenital recessive severe-to-profound deafness cases among the Pakistani population are estimated to be caused by pathogenic *OTOF* related variants (Choi *et al.*, 2009). The most frequent genetic mutation identified among the Spanish population is the p.Gln829* (Q829X) *OTOF* nonsense

mutation (Figure 1.5) found in 3-5% of patients diagnosed with severe-to-profound pre-lingual recessive autosomal hearing loss (Migliosi, 2002; Rodríguez-Ballesteros *et al.*, 2008). Profound deafness, in this context, is defined as hearing impairment with a hearing threshold higher than 90 dB and severe deafness is characterized by thresholds between 71-90 dB (Santarelli *et al.*, 2015; Shearer and Smith, 2015; Kaga, 2016).

There appears to be a genotype-phenotype correlation between the pathogenic *OTOF* variants and the phenotype seen in affected patients. Many of these deafness-causing *OTOF* variants are inactivating variants with a premature stop codon that likely lead to the production of abnormal otoferlin or no otoferlin at all as a result of nonsense-mediated mRNA decay. Individuals carrying two inactivating variants mostly suffer from severe-to-profound congenital hearing loss and their IHCs are predicted to completely lack otoferlin or have severely abnormal protein. In contrast, individuals carrying one inactivating and one missense variant (compound heterozygous genotype) or two missense variants suffer from less severe hearing loss and their IHCs are believed to express functionally defective otoferlin (Matsunaga *et al.*, 2012; Yildirim-Baylan *et al.*, 2014; Shearer and Smith, 2015; Wang *et al.*, 2018). Some *OTOF* missense variants have also been linked to mild age-progressive hearing loss like the p.Pro1987Arg, the p.Glu1700Gln, and the p.Ile1573Thr mutations (Varga, 2003; Chiu *et al.*, 2010; Yildirim-Baylan *et al.*, 2014).

In many cases, *OTOF*-related deafness appears as an auditory neuropathy in the first two years of life. Auditory neuropathy is characterized by present DPOAEs and absent or abnormal ABRs (Figure 1.2). In many of these cases the DPOAEs disappear later on in life, indicating a cochlear defect or a delayed OHC damage (Starr *et al.*, 1996; Varga, 2003; Varga *et al.*, 2006; Marlin *et al.*, 2010; Matsunaga *et al.*, 2012; Shearer and Smith, 2015; Hosoya *et al.*, 2018). Since mutations in the *OTOF* gene cause a disruption in synaptic transmission between IHCs and the SGNs of the auditory nerve, DFNB9 also considered to be an auditory synaptopathy (Moser, Predoehl and Starr, 2013; Moser and Starr, 2016).

The only available treatment for patients suffering from *OTOF*-related hearing loss is a combination of cochlear implants and educational programs for hearing impaired individuals (Shearer and Smith, 2015). Cochlear implants, in particular, have been

successful in treating individuals affected by cochlear defects like DFNB9 (Eppsteiner *et al.*, 2012). Identifying the presence or absence of pathogenic *OTOF* variants in newborn siblings of DFNB9 patients through molecular genetic testing can also be very useful to provide the appropriate support and care for the affected young child (Shearer and Smith, 2015; Nishio and Usami, 2017).

## 1.5 The temperature sensitive Ile515Thr otoferlin missense mutation

Some pathogenic *OTOF* variants cause temperature sensitive auditory neuropathy. Individuals affected by this DFNB9 form usually display normal-to-mild hearing impairment at normal core body temperature, but suffer from severe-to-profound deafness once the body temperature increases due to physical activity or fever (Starr *et al.*, 1996; Shearer and Smith, 2015). Once the fever is resolved and the body temperature decreases, the hearing goes back to the normal baseline hearing state. In addition, affected individuals usually show no inner ear anomalies and often report difficulties in speech perception and speech discrimination that gets worse during fever or body temperature elevating activities (Starr *et al.*, 1996; Varga *et al.*, 2006; Wynne *et al.*, 2013; Shearer and Smith, 2015). Continuous pure tone stimulation performed during psychoacoustic measurements further showed that some of these patients have severe abnormalities in loudness adaptation, also referred to as "auditory fatigue" (Wynne *et al.*, 2013). Preventive measures to avoid an increase in body temperature in addition to cochlear implants can be beneficial for individuals suffering from this DFNB9 form.

Several *OTOF* mutations have been identified in patients diagnosed with temperature-sensitive auditory synaptopathy/neuropathy including the p.Glu1804del in-frame deletion mutation (Marlin *et al.*, 2010), the compound heterozygous missense mutations p.Arg1080Pro and p.Gly614Glu (Romanos *et al.*, 2009; Marlin *et al.*, 2010), and the heterozygous missense mutations p.Gly541Ser (Matsunaga *et al.*, 2012), p.Arg1607Trp (Wang *et al.*, 2010; Matsunaga *et al.*, 2012), and p.Ile515Thr (Mirghomizadeh *et al.*, 2002; Varga *et al.*, 2006).

The p.Ile515Thr (I515T, c.1544T>C) missense mutation (Figure 1.5), in particular, was identified in one *OTOF* allele in two siblings diagnosed with temperature sensitive auditory neuropathy as well as in one *OTOF* allele in the unaffected father. Like other temperature sensitive auditory synaptopathy/neuropathy cases, the two siblings suffer from temporary severe-to-profound deafness when their core body temperature reaches 38.1 °C or higher. Once the body temperature drops back to normal levels hearing returns to the baseline state. The two siblings further experience moderate hearing loss for low-frequency sounds and speech comprehension difficulties (under the 10th percentile) during quiet and noise when afebrile (Varga *et al.*, 2006). Later analysis revealed that the pathogenic variant in their second *OTOF* allele is an inactivating p.Arg1116* nonsense mutation (Strenzke *et al.*, 2016). The phenotype observed in both patients is probably due to a combined effect of the p.Ile515Thr missense and the p.Arg1116* nonsense mutations that lead to the production of a dysfunctional protein (Varga *et al.*, 2006).

The *Otof$^{I515T/I515T}$* otoferlin knock-in mouse model, studied during the course of this thesis, is homozygous for this temperature-sensitive mutation and shows a moderate hearing impairment that is similar to the phenotype seen in these patients at normal body temperature (Strenzke *et al.*, 2016). These mutant mice are, however, less sensitive to heat in comparison to *OTOF$^{I515T/R1116*}$* individuals (Strenzke *et al.*, 2016). Electrophysiological membrane-capacitance measurements further revealed that *Otof$^{I515T/I515T}$* IHCs have normal RRP exocytosis upon IHC depolarization up to 20 ms and a defective RRP replenishment that is less severe than in *Otof$^{Pga/Pga}$* mutants (Pangrsic *et al.*, 2010; Strenzke *et al.*, 2016). Nevertheless, it is unclear whether the p.Ile515Thr mutation leads to lower otoferlin protein levels in these mutants as the p.Asp1767Gly mutation in *Otof$^{Pga/Pga}$* mice, which might influence the exocytosis in *Otof$^{I515T/I515T}$* mutants.

## 1.6    *Inner ear gene therapy*

In contrast to conductive hearing loss, sensorineural hearing loss is often caused by damage in auditory HCs and/or afferent auditory nerve fibers (Lee and Park, 2018). This damage can result from different factors like acoustic overexposure, ototoxic agents, or mutations in genes involved in hearing and aging (Lee and Park, 2018; Lee *et al.*, 2018). In

most cases such damage is irreversible and leads to permanent hearing impairment (Lee and Park, 2018; Lee *et al.*, 2018). As previously mentioned, the most common treatment option to rehabilitate hearing in deaf patients are hearing aids like externally worn amplification devices and cochlear implants (Lee and Park, 2018; Lee *et al.*, 2018). Although cochlear implants have proven over the years to be very effective in improving auditory function in hearing impaired patients, they still do not completely reproduce hearing with the sound quality of a naïve unaffected cochlea. Despite ongoing technical development, musical sound perception and speech comprehension during noise are still two major drawbacks of these devices (Bruns, Mürbe and Hahne, 2016; Huang *et al.*, 2017; Lee and Park, 2018). Two alternative approaches to protect and restore hearing are being extensively investigated. These approaches are stem cell therapy to regenerate auditory HCs and gene therapy to regulate the expression of genes involved in hearing (Lee and Park, 2018; Lee *et al.*, 2018).

The anatomical structure and complex function of the inner ear, however, hamper the delivery of genes to treat hearing loss via gene therapy (Lee and Park, 2018; Lee *et al.*, 2018). The cochlear tissue is very sensitive to changes in the composition and amount of inner ear fluids that fill the closed cochlear chambers. This makes it challenging to apply therapeutic agents into the cochlea without disturbing the cochlear fluid homeostasis (Lee and Park, 2018; Lee *et al.*, 2018). Several drug administration routes into the cochlea have been tested for the last years to minimize inner ear tissue damage. The most common route is the application through the round window membrane (RWM), covering the perilymph filled scala tympani chamber (Figure 1.6) (Lee and Park, 2018; Lee *et al.*, 2018; Plontke and Salt, 2018). Another application route to access other inner ear structures is to create an opening in one of the inner ear cavities like the scala vestibuli, the scala media, or the semicircular canals of the vestibular organ. In this context, opening the cochlear chambers is called cochleostomy and opening the vestibular semicircular canals is termed canalostomy (Lee and Park, 2018; Lee *et al.*, 2018; Plontke and Salt, 2018).
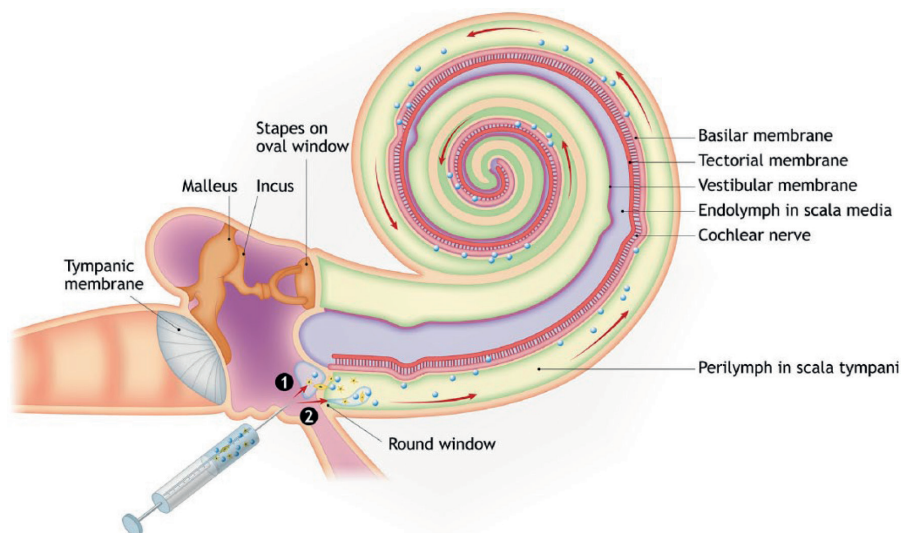
**Figure 1.6:**

**Round window membrane (RWM) drug delivery route in the cochlea**

Therapeutic agents used to treat inner ear disorders like AAVs can be delivered into the perilymph filled scala tympani by injecting these materials around (1) or through (2) the RWM. The arrows reflect the drug distribution along the cochlear turn after RWM injection (Lee *et al.*, 2018).

Recombinant adenoviruses and adeno-associated viruses (AAVs) are the most common viral vectors used for gene therapy applications into the cochlea (Lee and Park, 2018). AAVs, in particular, are well characterized and have, so far, been widely used to treat or improve the disease phenotype observed in animal models for several genetic disorders (Ahmed, Shubina-Oleinik and Holt, 2017; McClements and Maclaren, 2017). Further research has shown that AAVs have a high transduction efficiency and lead to long-term protein expression in terminally differentiated cells such as photoreceptors and auditory HCs (Anson, 2004; Géléoc and Holt, 2014; Ahmed, Shubina-Oleinik and Holt, 2017; McClements and Maclaren, 2017). One important advantage of AAVs over other viral vectors is the low probability of its genome to integrate itself into the host genome. The AAV genome rather persists as circular episomes in the nucleus of the infected cell, which consequently reduces potential harmful side effects like mutagenesis or oncogene

activation. AAVs also cause a lower immune response than other virus types in the infected tissue, making it a safer approach than many other viral vectors in general.

AAVs have become especially popular for the delivery of genes into IHCs and OHCs because of their high safety profile and good transduction efficacy (Shu *et al.*, 2016; Ahmed, Shubina-Oleinik and Holt, 2017; Suzuki *et al.*, 2017; Lee and Park, 2018). Other viral vectors like adenoviruses, lentiviruses, and retroviruses also used for gene therapy applications in other tissues have a much lower inner ear transduction efficacy and/or safety profile (Ahmed, Shubina-Oleinik and Holt, 2017; Lee and Park, 2018; Lee *et al.*, 2018). It was reported that AAVs with capsid proteins form serotypes AAV1, AAV2, AAV6, AAV8, AAV9, and AAVAnc80L65 have a good transduction efficiency in the cochlea (Akil *et al.*, 2012; Askew *et al.*, 2015; Chien *et al.*, 2016; Shu *et al.*, 2016; Geng *et al.*, 2017; Landegger *et al.*, 2017; Pan *et al.*, 2017; Suzuki *et al.*, 2017; Yoshimura *et al.*, 2018). Each AAV serotype even seems to have a specific cell type tropism in the cochlea (Shu *et al.*, 2016; Lee and Park, 2018). Several studies have demonstrated successful hearing restoration or improvement in mouse models for deafness-related proteins like Vglut3 (Akil *et al.*, 2012), clarin-1 (Geng *et al.*, 2017), Tmc1 (Askew *et al.*, 2015), and harmonin (Pan *et al.*, 2017) via AAV-mediated gene transfer. Nevertheless, the safety and potential side effects of AAVs like oncogene activation, tumorigenesis, and integration into the host genome need to be studied in depth and minimized before any human inner ear gene therapy application is possible (Anson, 2004; Lee and Park, 2018; Lee *et al.*, 2018).

## *1.7    AAV-mediated large gene transfer*

Recombinant AAVs are non-enveloped viruses that consist of a capsid carrying the gene of interest, also termed transgene, as a single-stranded DNA (ssDNA) flanked by palindromic inverted terminal repeat (ITRs) sequences (Figure 1.7). The transgene expression cassette not only includes the coding sequence (CDS) of the gene of interest, but also genetic control elements like a promoter, a polyadenylation site, and other post-transcriptional regulatory elements. During AAV production, the plus or minus strand version of the double-stranded (dsDNA) template transgene is packaged into the assembled AAV capsids. The resulting AAV population contains the plus and the minus

strands of the transgene in a 50:50 ratio (McClements and Maclaren, 2017). After AAV infection and transduction, the ssDNA needs to be transformed into dsDNA in the nucleus of the host cell before transgene expression. For this purpose, the ssDNA strand either anneals to a complementary plus or minus strand transferred to the same cell, or native nuclear mechanisms of the cell start the synthesis of a second-strand from the ssDNA strand (McClements and Maclaren, 2017).
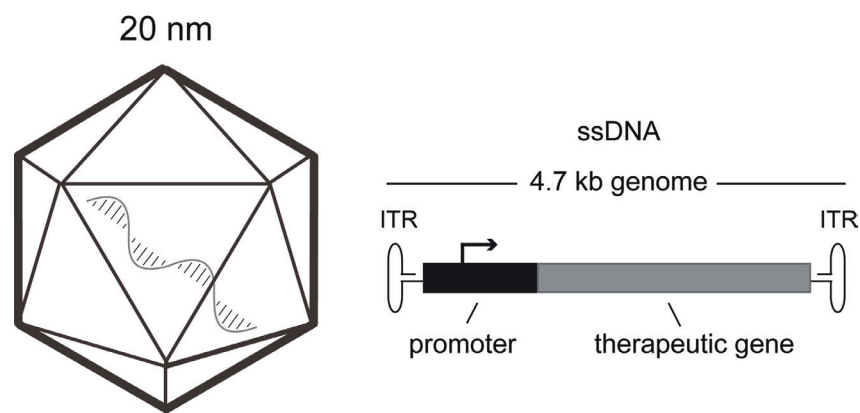
**Figure 1.7:**

**Schematic representation of an AAV vector.**

The AAV vector consists of an icosahedral capsid carrying a single-stranded DNA (ssDNA) genome. The AAV genome is approximately 4.7 kb long and flanked by palindromic inverted terminal repeat (ITRs) sequences (adapted from Tretiakova et al., 2018).

One of the major disadvantages of AAVs are their limited packaging capacity as their wild-type AAV genome size is only 4.7 kb-long (Figure 1.7) (Grieger and Samulski, 2005; McClements and Maclaren, 2017). The transgene packaging efficiency of AAVs during AAV production even appears to decrease with increasing transgene length (Dong, Nakai and Xiao, 2010; Lai, Yue and Duan, 2010; McClements and Maclaren, 2017; Lee and Park, 2018). Since the transgene expression cassette also contains other genetic control elements apart from the gene of interest and the ITRs, the CDS of the gene cannot be longer than approximately 3.5 kb (Dong, Nakai and Xiao, 2010; Lai, Yue and Duan, 2010; McClements and Maclaren, 2017). This presents an obstacle for the transfer of large genes associated

with some hereditary disorders such as the *OTOF* gene, which has a CDS of about 6 kb. As mentioned in the previous chapter, other vectors with a larger packaging capacity, like adenoviruses or lentiviruses, do not have the same transduction efficiency and safety profile as AAVs. This makes developing a gene therapy approach for diseases caused by mutations in large genes challenging (Anson, 2004; McClements and Maclaren, 2017; Lee and Park, 2018; Lee *et al.*, 2018).

One possibility to circumvent this limitation is to try to package the entire large transgene into a single AAV using an "oversize/overload" (OZ) strategy (Figure 1.8, oversize) (Chamberlain, Riyad and Weber, 2016; McClements and Maclaren, 2017). Some studies have reported successful AAV-mediated large transgene expression using this technique. Later investigation revealed that the resulting AAV vector population did not carry the full-length transgene, but rather different truncated fragments of the plus and minus strands of the large transgene. The reassembly of the large transgene in this approach is thought to be facilitated by homologous recombination of the complementary overlapping
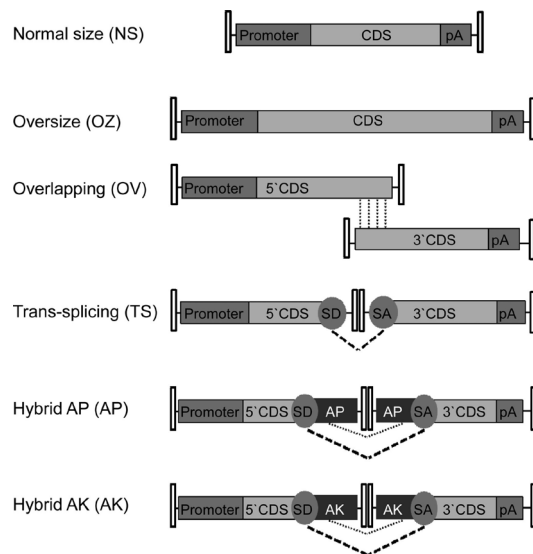


**Figure 1.8:**

**Different AAV vector strategies used for large transgene delivery.**

Fragmented or oversize (OZ) AAV vectors and split-AAV vectors have been developed to transfer large transgenes into various tissues. There are three split-AAV vector strategies: the overlap (OV), the trans-splicing (TS), and the hybrid (AP and AK) split-AAV approach. The process of homologous recombination (broken thin lines) and trans-splicing (broken thick lines) are depicted. NS: AVVs with a genome that does not exceed 4.7-5kb; CDS: coding sequence; pA: polyadenylation site, SD: splice donor site, SA: splice acceptor site, AP: recombinogenic region from the alkaline phosphate gene, AK: recombinogenic region from the F1 phage sequence (Trapani *et al.*, 2014).

regions present in the truncated ssDNA strands (Dong, Nakai and Xiao, 2010; Lai, Yue and Duan, 2010; Wu, Yang and Colosi, 2010). To further improve the reassembly of the full-length transgene, the AAV preparations were enriched with AAV fractions containing larger transgene fragments through a fractionation proc edure (Pryadkina *et al.*, 2015; McClements and Maclaren, 2017). Despite all these attempts, the enriched AAV fractions still carried a heterogeneous mixture of truncated transgene fragments. Thus, it cannot be ruled out that these transgene fragments can reassemble to form hybrid transgenes that express a mutated or truncated protein, which makes this approach less suitable for human gene therapy applications (McClements *et al.*, 2016).

Another more applicable approach to overcome the packaging capacity of AAVs in regard to human gene therapy are split-AAV systems. In the spilt-AAV approach, the large transgene expression cassette is split into two or three fragments and each fragment is packaged into a separate AAV vector (Figure 1.8) (Ghosh *et al.*, 2008; Koo *et al.*, 2014; Trapani *et al.*, 2014; Chamberlain, Riyad and Weber, 2016; McClements and Maclaren, 2017). In the dual-AAV delivery system, the 5'-AAV half vector contains the promotor and the first half of the large gene CDS (5'CDS). The 3'-AAV half vector consists of the second half of the large gene CDS (3'CDS) at its 5'-end followed by a polyadenylation sequence (polyA). The transgene expression cassette of each AAV half vector is additionally flanked by ITR sequences. Many studies have reported that co-infection of target cells with a mixture of these split-AAV vectors results in the production a mature full-length mRNA and a full size protein (Chamberlain, Riyad and Weber, 2016; McClements and Maclaren, 2017).

There are three different spilt-AAV strategies that can facilitate the reconstitution of the large transgene expression cassette. In the "overlap" (OV) strategy, both the 5'CDS and 3'CDS fragments contain an overlapping homologous transgene cDNA region (Figure 1.8, overlapping). The reassembly of the large transgene in this technique is mediated by the homologous recombination of these overlapping CDS sequences (Trapani *et al.*, 2014; Pryadkina *et al.*, 2015; Sondergaard *et al.*, 2015; Chamberlain, Riyad and Weber, 2016; McClements and Maclaren, 2017; McClements *et al.*, 2018). Further studies showed that the recombinogenic properties of these overlapping sequences are critical for the success of this approach (Lostal *et al.*, 2014; McClements and Maclaren, 2017). The "trans-splicing"

(TS) split-AAV strategy, in contrast, relies on the tendency of AAVs to link several transgene copies to each other through non-homologous end-joining of their ITRs after second-strand synthesis to form stable circular head-to-tail episomal structures in the host cell nucleus (Figure 1.8, trans-splicing). This process is called concatemerization and these episomes are termed "concatemers" (Duan *et al.*, 1998; Chamberlain, Riyad and Weber, 2016; McClements and Maclaren, 2017). The ITRs can subsequently be removed from these episomes upon transcription by incorporating a splice donor (SD) site at the 3'-end of the 5'-AAV half vector and a splice acceptor (SA) site at the 5'-end of the 3'-AAV half vector (Lai *et al.*, 2005; Colella *et al.*, 2014; Trapani *et al.*, 2014; Chamberlain, Riyad and Weber, 2016; McClements and Maclaren, 2017). The third strategy is the "hybrid" (Hyb) strategy, where the transgenes of each AAV half vector contain an overlapping sequence as well as a SD-site or a SA-site (Figure 1.8, hybrid). This technique is a combination of both the split-AAV overlapping and trans-splicing strategy. The overlapping sequences used in this technique are highly recombinogenic sequences derived from foreign genes like regions from the alkaline phosphatase (AP; Figure 1.8, hybrid AP) or the F1 phage (AK; Figure 1.8, hybrid AK) sequences. These sequences are placed downstream the SD-site in the 5'-AAV half vector and upstream the SA-site in the 3'-AAV half vector. The reassembly of the large transgene in this case can occur via concatemerization as in the TS-split-AAV strategy and/or homologous recombination as in the split-AAV overlapping approach (Ghosh *et al.*, 2008; Chamberlain, Riyad and Weber, 2016; McClements and Maclaren, 2017).

All three split-AAV strategies have been successfully used to deliver large transgenes into various tissues like the retina and muscles *in vitro* and *in vivo* (Lai *et al.*, 2005; Ghosh *et al.*, 2009; Zhang *et al.*, 2013; Colella *et al.*, 2014; Trapani *et al.*, 2014; Pryadkina *et al.*, 2015). However, no conclusions can be drawn on which one of them results in better full-length large transgene reconstitution and which leads to more efficient transgene expression in the specific target tissue. Several research groups have reported contradicting findings in this regard (Lai *et al.*, 2005; Ghosh *et al.*, 2009; Zhang *et al.*, 2013; Colella *et al.*, 2014; Trapani *et al.*, 2014; Pryadkina *et al.*, 2015; McClements and Maclaren, 2017). Split-AAV mediated large gene transfer further resulted in the significant improvement of the disease phenotype seen in animal models for some inherited retinal

and muscular dystrophy disorders (Lai *et al.*, 2005; Ghosh *et al.*, 2009; Zhang and Duan, 2012; Zhang *et al.*, 2013; Colella *et al.*, 2014; Trapani *et al.*, 2014; Pryadkina *et al.*, 2015). These findings led researchers to believe that split-AAV vectors, once optimized, can be a suitable tool to treat genetic disorders caused by mutations in large genes in humans (Trapani *et al.*, 2014; Chamberlain, Riyad and Weber, 2016; McClements and Maclaren, 2017).

## *1.8    Scope of the project*

The large multi-$C_2$ domain protein otoferlin is essential for auditory function and IHC exocytosis (Roux *et al.*, 2006; Pangršič, Reisinger and Moser, 2012). Different pathogenic mutant variants of the *OTOF* gene, coding for otoferlin, have been identified in individuals suffering from severe-to-profound congenital non-syndromic hearing loss or temperature sensitive non-syndromic auditory neuropathy (Yasunaga *et al.*, 1999, 2000; Varga, 2003; Varga *et al.*, 2006; Shearer and Smith, 2015). The hearing impairment seen in these patients is believed to be a consequence of absent protein or reduced protein levels and/or abnormal otoferlin function caused by these mutations (Roux *et al.*, 2006; Pangrsic *et al.*, 2010; Pangršič, Reisinger and Moser, 2012).

One of these mutations is the p.Ile515Thr missense mutation associated with auditory fatigue, speech comprehension difficulties, and temperature sensitive hearing loss (see introduction "chapter 1.5") (Mirghomizadeh *et al.*, 2002; Varga *et al.*, 2006). The $Otof^{I515T/I515T}$ otoferlin knock-in mouse model (Strenzke *et al.*, 2016) was generated to investigate the effects of this missense mutation on hearing and IHC exocytosis and to determine whether it is responsible for the temperature-sensitive hearing loss phenotype seen in patients carrying this mutation (Mirghomizadeh *et al.*, 2002; Varga *et al.*, 2006). One of the goals of this project was to understand the underlying disease mechanisms by studying the impact of this mutation on otoferlin distribution, subcellular localization, protein expression levels, and stability in IHCs. Investigating this topic was an ongoing work that spanned over the course of my bachelor, master, and Ph.D. thesis. The obtained results were later published during this thesis in "Strenzke *et al.*, 2016".

Cochlear implants are currently the only available treatment option for individuals diagnosed with *OTOF*-related hearing impairment (DFNB9) (Eppsteiner *et al.*, 2012; Shearer and Smith, 2015; Nishio and Usami, 2017). These patients would, therefore, benefit significantly from gene replacement therapies as an alternative to cochlear implants that still do not entirely reproduce hearing with the sound quality of a cochlea in an individual without hearing impairment (Bruns, Mürbe and Hahne, 2016; Huang *et al.*, 2017; Lee and Park, 2018). AAV-mediated gene transfer is considered to be a promising approach to treat inherited deafness forms due to its high safety profile and high IHC transduction efficiency (Akil *et al.*, 2012; Askew *et al.*, 2015; Pan *et al.*, 2017; Lee and Park, 2018; Lee *et al.*, 2018). However, the AAVs limited cargo capacity to deliver genes larger than 4.7 kb (Grieger and Samulski, 2005; McClements and Maclaren, 2017) presents an obstacle for the transfer of the 6 kb-long full-length otoferlin CDS into auditory IHCs. Dual- and triple-AAV vectors have successfully been used to delivery large transgenes into photoreceptors (Colella *et al.*, 2014; Trapani *et al.*, 2014) and other cell types (Zhang *et al.*, 2013; Kodippili *et al.*, 2017), but have not been established for IHCs yet (Ahmed, Shubina-Oleinik and Holt, 2017; Lee *et al.*, 2018). Thus, the major aim of this Ph.D. thesis was to determine whether a dual-AAV approach would be suitable to transfer the large full-length otoferlin cDNA into auditory IHCs of deaf otoferlin knock-out mice (Roux *et al.*, 2006; Reisinger *et al.*, 2011) and to restore IHC exocytosis and auditory function in these animals. The cloning of the two otoferlin dual-AAV half vector expression cassettes, used for the experiments performed during the scope of this Ph.D. thesis and later published in "Al-Moyed *et al.*, 2019" was started during my master thesis and later finished during this thesis.

# 2 Results

## 2.1 Otoferlin protein levels and cellular distribution in auditory IHCs from different otoferlin mutant mouse models

### 2.1.1 Synopsis

Different mutations in the *OTOF* gene can lead to different degrees of IHC function and hearing impairment (Roux *et al.*, 2006; Pangršič, Reisinger and Moser, 2012; Strenzke *et al.*, 2016; Michalski *et al.*, 2017; Pangrsic and Vogl, 2018). *Otof*^Pga/Pga^ otoferlin mutant mice, carrying the p.Asp1767Gly missense mutation, are profoundly deaf and have decreased cellular otoferlin protein levels and severely impaired sustained IHC exocytosis (Pangrsic *et al.*, 2010). In contrast, *Otof*^I515T/I515T^ otoferlin knock-in mice, homozygous for the human p.Ile515Thr missense mutation, display a moderate hearing loss phenotype and a less severe defect in sustained IHC exocytosis compared to *Otof*^Pga/Pga^ mutants (Strenzke *et al.*, 2016).

In this study, I have investigated the connection between the hearing loss phenotype seen these mutant mouse models and the cellular distribution and protein levels of otoferlin in their auditory IHCs via immunohistochemistry. Measuring the overall otoferlin levels in *Otof*^I515T/I515T^ and *Otof*^Pga/Pga^ IHCs revealed that both mutants had similar reduced protein levels of around 31-35% compared to wild-type levels (Strenzke *et al.*, 2016: Fig. 1A-C, Fig. 1G, Appendix Fig. S1A-D). Since both mutants had comparable protein levels, but different sustained IHC exocytosis levels and hearing loss phenotypes, I additionally quantified the amount of plasma membrane-bound otoferlin in these IHCs. Interestingly, *Otof*^Pga/Pga^ IHCs showed an extreme reduction of ~97% in the amount of plasma membrane-bound otoferlin compared to *Otof*^I515T/I515T^ IHCs with a reduction of ~66% (Strenzke *et al.*, 2016: Fig. 1 D-F, Fig. 1J). The decrease in overall and plasma membrane-bound otoferlin expression in *Otof*^I515T/I515T^ IHCs was further confirmed via pre-embedding immunogold electron microscopy by counting the number of otoferlin-immunolabeled

gold particles in these cells (Strenzke *et al.*, 2016: Fig. 7A-C, Fig. 7L-M). Given that older *Otof$^{I515T/I515T}$* mutant mice (8-25 weeks) show an even further deterioration of ABR wave amplitudes and hearing thresholds (Strenzke *et al.*, 2016), I have measured the overall otoferlin protein levels in P99 (14-15 weeks) old animals and compared them to the levels in P19 (2-3 weeks) old mice. A further reduction in overall otoferlin protein levels from ~30% of wild-type levels at P19 to ~15% at P99 was observed in these mutant IHCs (Strenzke *et al.*, 2016: Fig. EV1D). To examine whether the p.Ile515Thr mutation leads to a faster degradation of otoferlin, I have added 50 μg/ml of cycloheximide (CHX) for 8 hours to explanted *Otof$^{I515T/I515T}$* organs of Corti (P7-8) to inhibit protein biosynthesis in these mutant IHCs. CHX treated *Otof$^{I515T/I515T}$* IHCs (+CHX, 22% of wild-type levels) showed significantly lower overall otoferlin levels than non-treated *Otof$^{I515T/I515T}$* IHCs (-CHX, 30% of wild-type levels). In comparison, CHX treated and non-treated wild-type IHCs did not have significantly different otoferlin protein levels (Strenzke *et al.*, 2016: Appendix Fig. S1E).

The human p.Ile515Thr missense mutation was detected in patients suffering from temperature-sensitive hearing impairment once their core body temperature rises up to 38.1°C and higher (Varga *et al.*, 2006). Since the sustained IHC exocytosis in *Otof$^{I515T/I515T}$* IHCs declines even more at higher temperatures (38.5-40°C) (Strenzke *et al.*, 2016), I have studied the effects of temperature elevation on the protein levels and cellular distribution of otoferlin in these IHCs via immunohistochemistry. Incubating explanted organs of Corti from *Otof$^{I515T/I515T}$* mice (P7-8) at 38.5°C for 24 hours caused a reduction in overall otoferlin IHC levels from ~29% at 37°C to ~21% at 38.5°C (Strenzke *et al.*, 2016: Fig. 6H-K). In addition, the levels of plasma membrane-bound otoferlin decreased from 26% at 37°C to 12% at 38.5°C in these IHCs (Strenzke *et al.*, 2016: Fig. 6N). Higher temperatures (38.5°C) further led to a more apical otoferlin and Vglut3 localization within *Otof$^{I515T/I515T}$* IHCs (Strenzke *et al.*, 2016 Fig.6 L). The lower amount of plasma membrane-bound otoferlin and the more apical cellular distribution of both otoferlin and Vglut3 at 38.5°C in *Otof$^{I515T/I515T}$* mutants resembles the membrane-bound levels and distribution of otoferlin in *Otof$^{Pga/Pga}$* IHCs under normal experimental conditions (Strenzke *et al.*, 2016: Fig. 1H-J).

Otoferlin was reported to be located at the IHC plasma membrane, the SVs surrounding the synaptic ribbon, and intracellular membranes (Roux *et al.*, 2006; Pangrsic *et al.*, 2010;

Revelo *et al.*, 2014). I have, therefore, examined the effects of the p.Ile515Thr mutation on otoferlin's subcellular localization via pre-embedding immunogold electron microscopy. Ultrastructural analysis revealed a prominent otoferlin immunogold labeling at the plasma membrane and endosomal structures, but not at SVs surrounding the ribbon in both wild-type and *Otof^I515T/I515T^* IHCs (Strenzke *et al.*, 2016: Fig. 7A-B, Fig. 7D-G, Appendix Fig. S5B-C). However, these endosomal vacuoles were on average larger in *Otof^I515T/I515T^* mutants (average: 210 ± 13 nm, range: 51-625 nm) than in wild-type IHCs (average: 151 ± 8nm, range: 52-423nm) (Strenzke *et al.*, 2016: Fig. 7I-K).

In conclusion, the p.Asp1767Gly and the p.Ile515Thr *OTOF* missense mutation have an impact on the cellular distribution, and expression levels of otoferlin in IHCs of *Otof^Pga/Pga^* and *Otof^I515T/I515T^* mutant mice. Both mutants exhibit similar reduced overall otoferlin protein levels, but have very different amounts of plasma membrane bound otoferlin in their IHCs. This difference might explain the different sustained IHC exocytosis levels and hearing phenotypes seen in these two otoferlin mutant mice. The overall and plasma membrane bound otoferlin levels decreased even more in *Otof^I515T/I515T^* IHCs when subjected to higher temperatures and altered the cellular localization of otoferlin similarly to *Otof^Pga/Pga^* IHCs. These changes could potentially explain the temperature-sensitive hearing loss found in individuals carrying the p.Ile515Thr *OTOF* mutation. The immunogold electron microscopy data further showed that otoferlin was not located at SVs surrounding the ribbon in wild-type and *Otof^I515T/I515T^* IHCs as previously reported by Roux *et al.*, 2006. In addition, the otoferlin labeled endosomal structures were larger in *Otof^I515T/I515T^* IHCs and together with the presence of enlarged SVs in these mutants (Strenzke *et al.*, 2016) point towards a role of otoferlin in membrane retrieval and the formation of correctly sized fusion-competent SVs from endosome-like vacuoles.

## 2.1.2  Own contribution

This project was an ongoing work that spanned over the course of my bachelor, master, and Ph.D. thesis as stated earlier in "chapter 1.8" I have performed experiments and analyzed data for the following figures in "Strenzke *et al.*, 2016":

- Figure 1: immunohistochemistry, confocal microscopy, data analysis, statistics, figure preparation.

- Figure 6H-N: organotypic cultures, temperature temperatures, immunohistochemistry, confocal microscopy, data analysis, statistics, figure preparation.

- Figure 7A-M: pre-embedding immunogold labeling, electron microscopy, data analysis, statistics, figure preparation.

- Figure EV1D-F: immunohistochemistry, confocal microscopy, data analysis, statistics, figure preparation.

- Appendix Figure S1: organotypic cultures, protein biosynthesis inhibition via CHX, immunohistochemistry, confocal microscopy, data analysis, statistics, figure preparation.

- Appendix Figure S5: pre-embedding immunogold labeling, electron microscopy, figure preparation.

The data sets depicted in Fig. 1, Fig. 6H-N, Fig. EV1E-F, and Appendix Fig. S1E were collected, imaged, and analyzed during my bachelor, master, and Ph.D. thesis. The samples displayed in Fig. 7A-B, Fig. 7D-J, and Appendix Fig. S5 were collected and imaged during my master thesis and a lab rotation during my master. The data sets shown in Fig. 7K-M were collected and imaged during my master thesis and analyzed during the scope of this Ph.D. thesis. The data sets and samples indicated in Fig. 7C, Fig. EV1D, and Appendix Fig. S1A-D were collected, imaged, and analyzed during my Ph.D. thesis. All experiments and the subsequent data analysis was performed as described in the materials and methods section in "Strenzke *et al.*, 2016". The statistical analysis for all experiments was performed during my Ph.D. thesis as mentioned in "Strenzke *et al.*, 2016". Gerhard Hoch (Institute for Auditory Neuroscience and InnerEarLab, University Medical Center Göttingen) developed the custom-written *Matlab* (MathWorks) routine integrated into *Imaris 7.6.5* (Bitplane Scientific Software) for the otoferlin protein level quantifications in this thesis see "materials and methods" section in "Strenzke *et al.*, 2016". In this context, I have helped Gerhard Hoch in improving this analysis routine further during my Ph.D. thesis. All figures mentioned above were prepared as described in "Strenzke *et al.*, 2016" during the course

of this thesis. The manuscript for this publication was written, edited, and revised together with the other authors of the publication during the scope of this Ph.D. thesis and published in 2016 see the "authors contributions" section in "Strenzke *et al.*, 2016".

## 2.1.3 Publication

The results of this project were published by the "EMBO Journal" in "Strenzke *et al.*, 2016" (see attached publication in "chapter 2.1.3").

# Hair cell synaptic dysfunction, auditory fatigue and thermal sensitivity in otoferlin Ile515Thr mutants

Nicola Strenzke[1,2,*,†], Rituparna Chakrabarti[2,3,4,†], Hanan Al-Moyed[4,5,†], Alexandra Müller[2,4,5], Gerhard Hoch[6], Tina Pangrsic[2,7], Gulnara Yamanbaeva[1,2,4], Christof Lenz[8,9], Kuan-Ting Pan[8], Elisabeth Auge[1], Ruth Geiss-Friedlander[10], Henning Urlaub[2,8,9], Nils Brose[2,11], Carolin Wichmann[2,3,**] & Ellen Reisinger[2,5,11,***]

## Abstract

The multi-$C_2$ domain protein otoferlin is required for hearing and mutated in human deafness. Some *OTOF* mutations cause a mild elevation of auditory thresholds but strong impairment of speech perception. At elevated body temperature, hearing is lost. Mice homozygous for one of these mutations, *Otof*[I515T/I515T], exhibit a moderate hearing impairment involving enhanced adaptation to continuous or repetitive sound stimulation. In *Otof*[I515T/I515T] inner hair cells (IHCs), otoferlin levels are diminished by 65%, and synaptic vesicles are enlarged. Exocytosis during prolonged stimulation is strongly reduced. This indicates that otoferlin is critical for the reformation of properly sized and fusion-competent synaptic vesicles. Moreover, we found sustained exocytosis and sound encoding to scale with the amount of otoferlin at the plasma membrane. We identified a 20 amino acid motif including an RXR motif, presumably present in human but not in mouse otoferlin, which reduces the plasma membrane abundance of Ile515Thr-otoferlin. Together, this likely explains the auditory synaptopathy at normal temperature and the temperature-sensitive deafness in humans carrying the Ile515Thr mutation.

## Introduction

Mutations in *OTOF*, the gene coding for the multi-$C_2$ domain protein otoferlin, cause human prelingual deafness DFNB9 (Yasunaga *et al*, 1999). Otoferlin is required for a late step in exocytosis in mouse inner hair cells (IHCs), as its absence nearly abolishes depolarization-induced exocytosis despite the presence of synaptic vesicles at the ribbon-type active zones (Roux *et al*, 2006). It was proposed that this phenotype reflects a role of otoferlin as a $Ca^{2+}$ sensor of exocytosis (Roux *et al*, 2006; Johnson & Chapman, 2010), but this idea requires further experimental testing. Indeed, in the profoundly hearing impaired *pachanga* mouse model (*Otof*[Pga/Pga]), which carries a point mutation in otoferlin (Schwander *et al*, 2007), only sustained exocytosis is impaired, while fast exocytosis, reporting the fusion of the readily releasable pool (RRP), is not (Pangrsic *et al*, 2010). The finding of impaired vesicle replenishment led to the hypothesis that otoferlin also functions in vesicle priming, which was subsequently supported by a recent study showing a reduction in short tethers connecting synaptic vesicles with the active zone membrane in otoferlin knockout (*Otof*^{−/−}) mice (Vogl *et al*, 2015). In addition to these putative roles in priming and fusion, otoferlin may be involved in exocytosis–endocytosis coupling via an

---

interaction with the clathrin adapter protein AP-2 (Duncker *et al*, 2013; Jung *et al*, 2015).

While most mutations in human *OTOF* lead to profound deafness, a defined set of missense mutations cause a striking nonsyndromic recessive temperature-sensitive auditory synaptopathy (reviewed in Pangršič *et al*, 2012) that is exceptional in several aspects. First, at normal body temperature, patients have near-normal pure tone hearing thresholds but impaired speech recognition, especially in background noise (Starr *et al*, 1998). Second, psychoacoustic testing of some patients revealed severe abnormalities of loudness adaptation to continuous pure tone stimulation, also called "auditory fatigue" (Wynne *et al*, 2013). Third, elevation of body temperature to $\geq 38.1°C$ due to physical activity or fever causes severe to profound deafness. In the five independent familial cases described so far, different missense mutations (Ile515Thr, Gly541Ser, Arg1607Trp and compound heterozygosity for Gly614Glu and Arg1080Pro) and an in-frame deletion (Glu1804del) were discovered (Varga *et al*, 2006; Romanos *et al*, 2009; Marlin *et al*, 2010; Wang *et al*, 2010; Matsunaga *et al*, 2012). Furthermore, three more missense mutations in otoferlin (Pro1987Arg, Glu1700Gln and Ile1573Thr) were described to cause moderate age-progressive hearing loss without evident temperature sensitivity (Varga *et al*, 2003; Chiu *et al*, 2010; Yildirim-Baylan *et al*, 2014). Unfortunately, speech perception, auditory temporal processing, auditory fatigue and temperature sensitivity have not been tested on these patients so far.

The severity of the hearing impairment of otoferlin mutant mouse lines studied to date (Roux *et al*, 2006; Longo-Guess *et al*, 2007; Pangrsic *et al*, 2010; Reisinger *et al*, 2011) has precluded further functional studies at the cellular, systems and behavioural level. To address this problem, we set out to generate a novel *Otof* mutant mouse model with an intermediate hearing defect, which would allow us to tackle current open questions regarding the function of otoferlin in synaptic sound encoding. We generated a knock-in mouse carrying the p.Ile515Thr point mutation (in NP_001274418), which was identified in one *OTOF* allele in siblings suffering from severe to profound hearing loss when their body temperature rises to $\geq 38.1°C$ (Varga *et al*, 2006). At normal body temperature, patients had mild low-frequency hearing loss, speech comprehension below the 10th percentile both in quiet and noise and lacked ABRs. Later analysis revealed a premature STOP codon (Arg1116*) in the second *OTOF* allele (A. Starr, personal communication). The hearing disorder in *Otof*$^{I515T/I515T}$ mice largely recapitulates the phenotype described in human patients, except for the temperature sensitivity. Comprehensive analyses of synaptic sound encoding in *Otof*$^{I515T/I515T}$ mice from the molecular to the systems level indicate that otoferlin is critical for reformation of synaptic vesicles from endosome-like intermediates and for the replenishment of the RRP. Finally, we provide a candidate molecular mechanism for temperature-induced deafness in humans.

## Results

### The Ile515Thr mutation lowers otoferlin protein levels

We introduced the Ile515Thr substitution in mouse *Otof* via targeted knock-in (Appendix Supplementary Methods). First, we investigated the abundance and localization of otoferlin by using immunohistochemistry and confocal fluorescence microscopy in organs of Corti of 14- to 15-day-old (P14-15) mice (Fig 1). Quantifying immunofluorescence per cell, we found a 65% reduction in otoferlin levels in *Otof*$^{I515T/I515T}$ IHCs compared to wild-type (*Otof*$^{+/+}$) controls (Fig 1A, B and G). In a parallel analysis of *Otof*$^{Pga/Pga}$ IHCs, a 69% reduction of protein levels was detected (Fig 1C and G), close to previous results (73%, Pangrsic *et al*, 2010). The reduction of otoferlin in the mutant genotypes was confirmed using another anti-otoferlin antibody (Appendix Fig S1A–D). The lower protein levels in *Otof*$^{I515T/I515T}$ IHCs are likely due to a faster degradation of mutated otoferlin (Appendix Fig S1E). In *Otof*$^{I515T/I515T}$ IHCs, the remaining otoferlin localized more towards the synaptic area below the midline of the nucleus of IHCs compared to *Otof*$^{+/+}$, while it was found more apically in *Otof*$^{Pga/Pga}$ IHCs (Fig 1H). In the IHCs of all genotypes, otoferlin immunoreactivity was found in the cytoplasm and at the plasma membrane. In *Otof*$^{I515T/I515T}$ IHCs, the otoferlin immunofluorescence at the plasma membrane relative to total cellular protein levels was unaltered as compared to *Otof*$^{+/+}$ IHCs. In contrast, *Otof*$^{Pga/Pga}$ IHCs showed an 85% lower relative membrane staining (Fig 1D–F and I). Taken together, the calculated absolute level of membrane-bound otoferlin was reduced by 66% in *Otof*$^{I515T/I515}$ and by 97% in *Otof*$^{Pga/Pga}$ IHCs (Fig 1J).

We conclude that the Ile515Thr mutation lowers the absolute otoferlin levels, but preserves the relative distribution between plasma membrane and cytoplasm.

### Auditory brainstem responses (ABRs) indicate a progressive hearing impairment in *Otof*$^{I515T/I515T}$ mice

Hearing was first assessed by ABR recordings. ABR thresholds were elevated by 20 dB for pure tones and 10 dB for click stimuli in young *Otof*$^{I515T/I515T}$ mice (Fig 2A). The amplitude of the spiral ganglion neuron (SGN) compound action potential, approximated as the amplitude of ABR wave I in response to clicks, was reduced to one-third of the *Otof*$^{+/+}$ littermate values, while subsequent waves were better preserved (Figs 2B and C, and EV1A and B). Together, population responses indicate a mild impairment of synchronous auditory signalling already in juvenile mice. We then cross-bred *Otof*$^{I515T/I515T}$ mice with deaf *Otof*$^{-/-}$ mice in order to model the human *OTOF*$^{I515T/R1116*}$ subjects (Varga *et al*, 2006) even more closely. We found an additional elevation of ABR thresholds by 15 dB and a further reduction of ABR amplitudes in *Otof*$^{-/I515T}$ mice, indicating a gene dosage-dependent effect (Figs 2A–C and EV1A). Consistent with a primary defect of the IHC synapse, distortion product otoacoustic emissions (DPOAE) were present, which report active cochlear amplification and require intact mechanoelectrical transduction (Fig EV1C).

Like in some patients with age-progressive hearing loss due to *OTOF* mutations (Varga *et al*, 2003; Chiu *et al*, 2010; Yildirim-Baylan *et al*, 2014), the hearing impairment, reflected by altered ABR thresholds and amplitudes, progressed rapidly during adolescence (Fig 2D–F), which correlated with a further reduction in otoferlin protein levels (Fig EV1D).

### Intact synaptic vesicle fusion but impaired vesicle replenishment in *Otof*$^{I515T/I515T}$ IHCs

Perturbations of otoferlin function have been shown to interfere with presynaptic function in IHCs (Roux *et al*, 2006; Pangrsic *et al*,
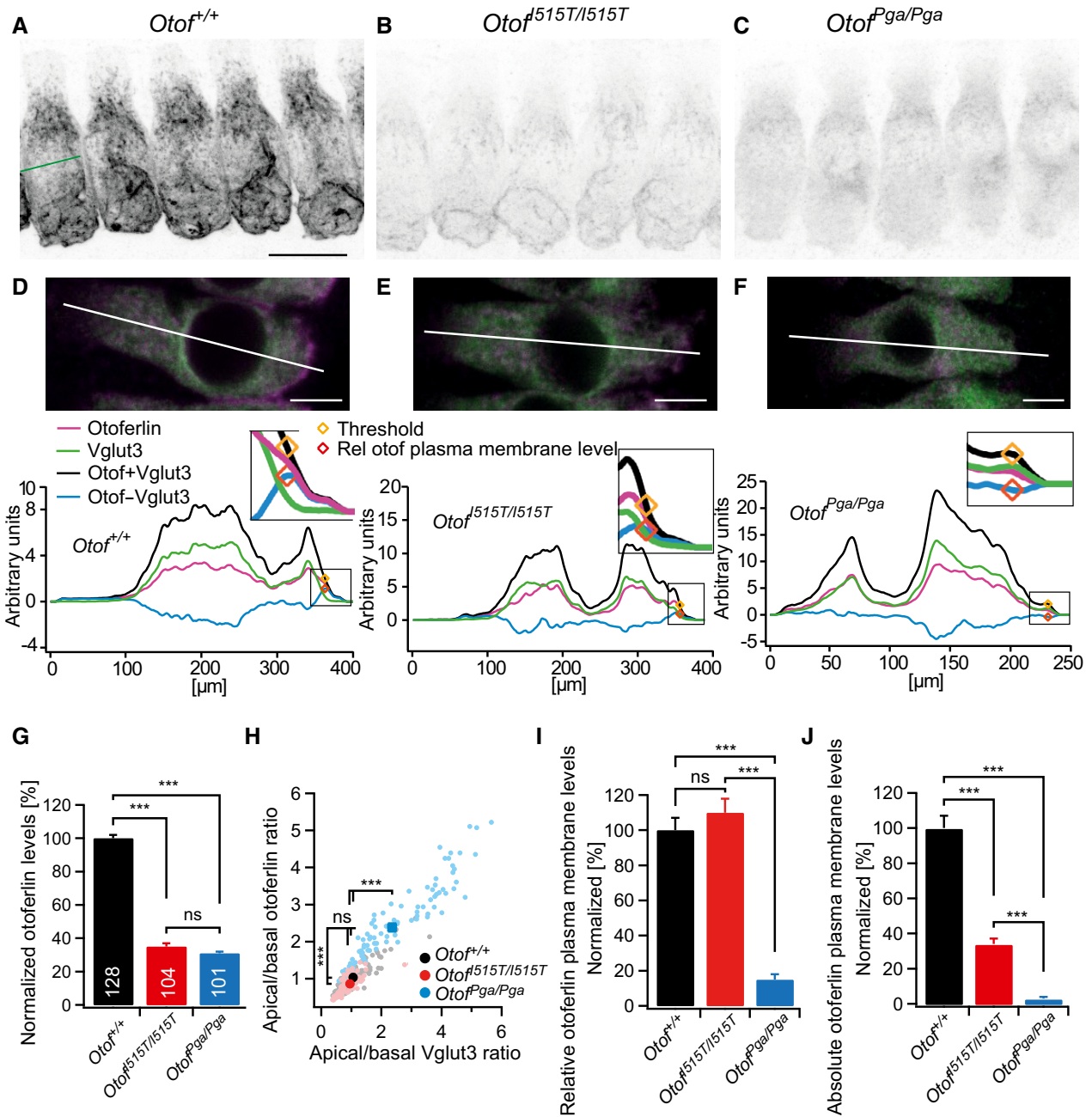
**Figure 1. Otoferlin levels and cellular distribution are differentially affected in *Otof^{I515T/I515T}* and *Otof^{PgaPpga}* IHCs.**

A–C  Immunofluorescence images (inverted intensity) of P14-P15 IHCs from indicated genotypes, revealing differences in otoferlin fluorescence intensity and distribution. Maximum projection of confocal stacks; scale bar, 10 μm.

D–F  Upper panels, examples for IHCs, co-labelled for otoferlin (magenta) and Vglut3 (green) and position of the line for line scans; maximum projection of few optical sections; scale bars, 5 μm. Lower panels, for quantification of membrane staining, the fluorescence was normalized to the cellular fluorescence for each fluorophore, and then the average of five parallel line scans through the middle of the cells for the sum of both fluorescence values (black line) was used to determine the position of the basal membrane. At the most basal cellular point along this line which exceeds the threshold value of 2 (yellow diamond), the otoferlin-Vglut3 fluorescence difference (blue line) gave the value for relative otoferlin plasma membrane levels (orange diamond). Insets: enlargements of basal regions.

G  Otoferlin protein levels were reduced in *Otof^{I515T/I515T}* IHCs (indicated numbers represent numbers of cells) and *Otof^{Pga/Pga}* IHCs compared to wild-type (*Otof^{+/+}*) controls (mean ± SEM).

H  Ratio of apical/basal protein levels (above/below nuclear midline depicted as green line in (A) indicates an apical shift of otoferlin in *Otof^{Pga/Pga}* IHCs.

I  Relative levels of membrane-bound otoferlin at the basal pole of IHCs (mean ± SEM).

J  Absolute amount of otoferlin at the basal IHC plasma membrane, gained by multiplication of relative plasma membrane levels (I) × total cellular otoferlin protein levels (G) (mean ± SEM).

Data information: Cell numbers in (G) apply also to (H–J); Kruskal–Wallis test; ***P < 0.001.
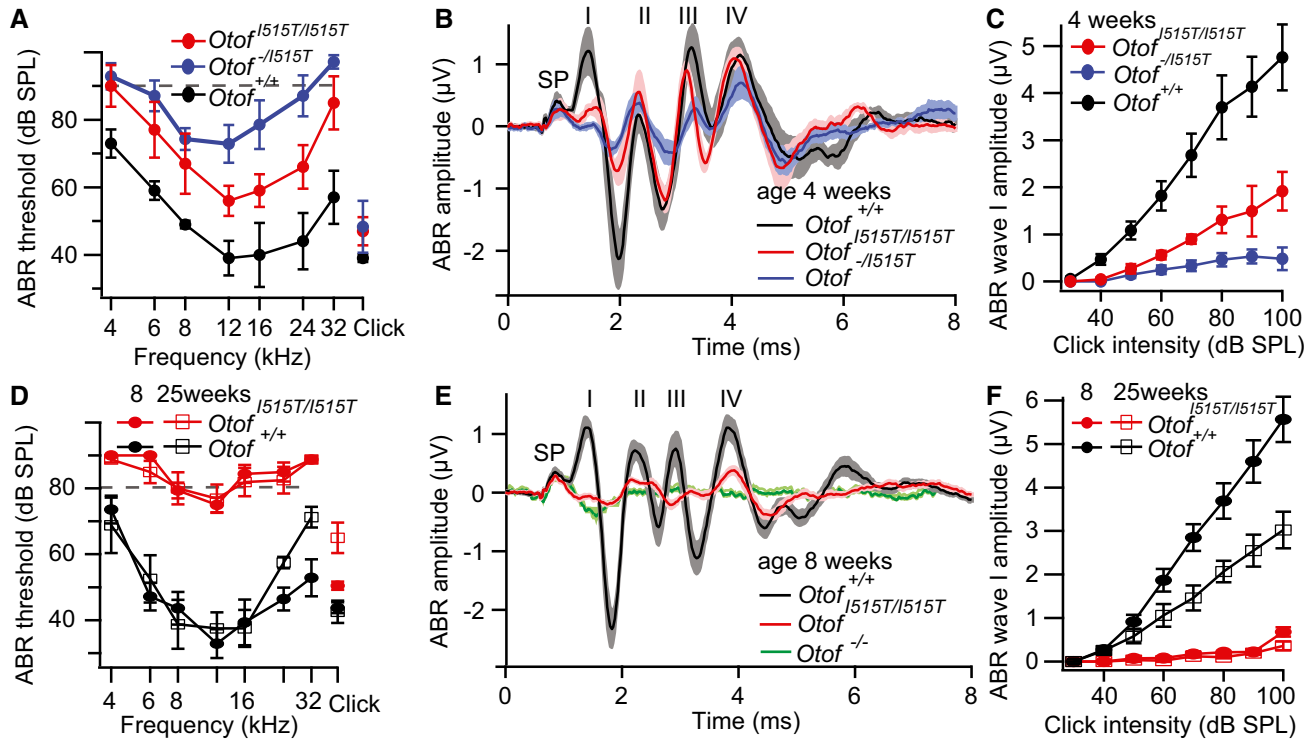
**Figure 2. Hearing, assessed by ABR, is impaired due to the Ile515Thr mutation in otoferlin.**

A   ABR thresholds in $Otof^{I515T/I515T}$ (red, $n = 5$) and $Otof^{-/I515T}$ (blue, $n = 7$) mice were elevated compared to $Otof^{+/+}$ mice (black, $n = 5$) at an age of 3–4 weeks. The grey dotted line indicates the maximum loudspeaker output of 90 dB; thresholds exceeding this value were set to 100 dB for calculation of the mean ± SEM. At 12 kHz, only the threshold increase for $Otof^{-/I515T}$ versus $Otof^{+/+}$ is significant (Kruskal–Wallis test with Dunn's multiple comparisons test between all three groups).

B   Grand averages of ABR waveforms ± SEM in response to 80 dB click stimulation of the mice analysed in (A): The small wave preceding ABR wave I probably represents the summating potential (SP, hair cell receptor potential), which is intact in $Otof$ mutants. ABR wave I is reduced in amplitude while subsequent peaks are better preserved in $Otof^{I515T/I515T}$ mice (Fig EV1).

C   Mean ABR wave I amplitude ± SEM for different stimulus intensities (all differences between genotypes are significant; two-way ANOVA with Tukey's multiple comparison test).

D   At 8 weeks (circles) and 25 weeks (open squares), $Otof^{I515T/I515T}$ mice showed highly elevated ABR thresholds compared to $Otof^{+/+}$ mice ($n = 7$–8 each; $P < 0.001$ at 12 kHz, Mann–Whitney $U$-test). Grey dotted line as in (A).

E   Grand averages of ABR waveforms ± SEM in response to 80 dB click stimulation in mice aged 8 weeks. $Otof^{I515T/I515T}$ ($n = 8$) have drastically reduced ABR amplitudes compared to $Otof^{+/+}$ mice ($n = 7$). $Otof^{-/-}$ mice have no ABR (green, $n = 9$).

F   Mean ABR wave I amplitude ± SEM for different stimulus intensities for 8-week-old and 25-week-old $Otof^{I515T/I515T}$ and $Otof^{+/+}$ mice ($P < 0.001$, two-way ANOVA).

2010). To test the effect of the Ile515Thr mutation, we performed perforated-patch recordings from IHCs in P14-P17 mice at room temperature (RT). The current–voltage relationship revealed a normal voltage dependence of activation and amplitude of $Ca^{2+}$ currents in $Otof^{I515T/I515T}$ IHCs (Fig 3A and B). We then measured exocytosis as increments of plasma membrane capacitance ($\Delta C_m$) in response to step depolarizations to the voltage where maximal $Ca^{2+}$ currents are elicited (typically $-14$ mV). Depolarizations were followed by recovery periods of 30 to 60 s at $-84$ mV, which precludes exocytosis triggered by voltage-gated $Ca^{2+}$ influx. Comparable $\Delta C_m$ in response to short depolarizations (2–20 ms) indicated intact fusion of a normally sized RRP under these experimental conditions (Fig 3C and D). Consistently, the number of ribbon synapses was normal in mutant IHCs (Fig EV1E and F). However, when $Otof^{I515T/I515T}$ IHCs were depolarized for 50 ms or longer, exocytosis was significantly smaller than in controls (Fig 3C and D). Such sustained exocytosis is thought to reflect replenishment of synaptic vesicles to the RRP and their subsequent fusion, and/or active zone clearance (Pangršič *et al*, 2012). The rate of sustained

exocytosis was reduced to ~340 vesicles/s/active zone, compared to ~700 vesicles/s/active zone in $Otof^{+/+}$ IHCs (see Appendix Supplementary Methods), but was still considerably faster than in $Otof^{Pga/Pga}$ IHCs (~200 vesicles/s/active zone, Pangrsic *et al*, 2010).

In order to test the fusion kinetics of RRP vesicles in $Otof^{I515T/I515T}$ IHCs, we recorded $\Delta C_m$ in response to fast $Ca^{2+}$ uncaging by UV laser. Here, exocytosis was comparable in kinetics between $Otof^{I515T/I515T}$ and $Otof^{+/+}$. The amplitude was significantly reduced in $Otof^{I515T/I515T}$ IHCs (Fig 3E and F; fast and slow components reduced to 40 and 63%, respectively). This indicates that the Ile515Thr mutation does not impair the $Ca^{2+}$-triggered fusion of vesicles to the plasma membrane itself, but instead impairs vesicle replenishment, potentially affecting priming, active zone clearance or yet another mechanism.

### *In vivo* postsynaptic recordings reveal a use-dependent depression of sound encoding at $Otof^{I515T/I515T}$ synapses

In order to directly assess sound encoding at $Otof^{I515T/I515T}$ synapses *in vivo,* we performed extracellular recordings from individual SGNs,
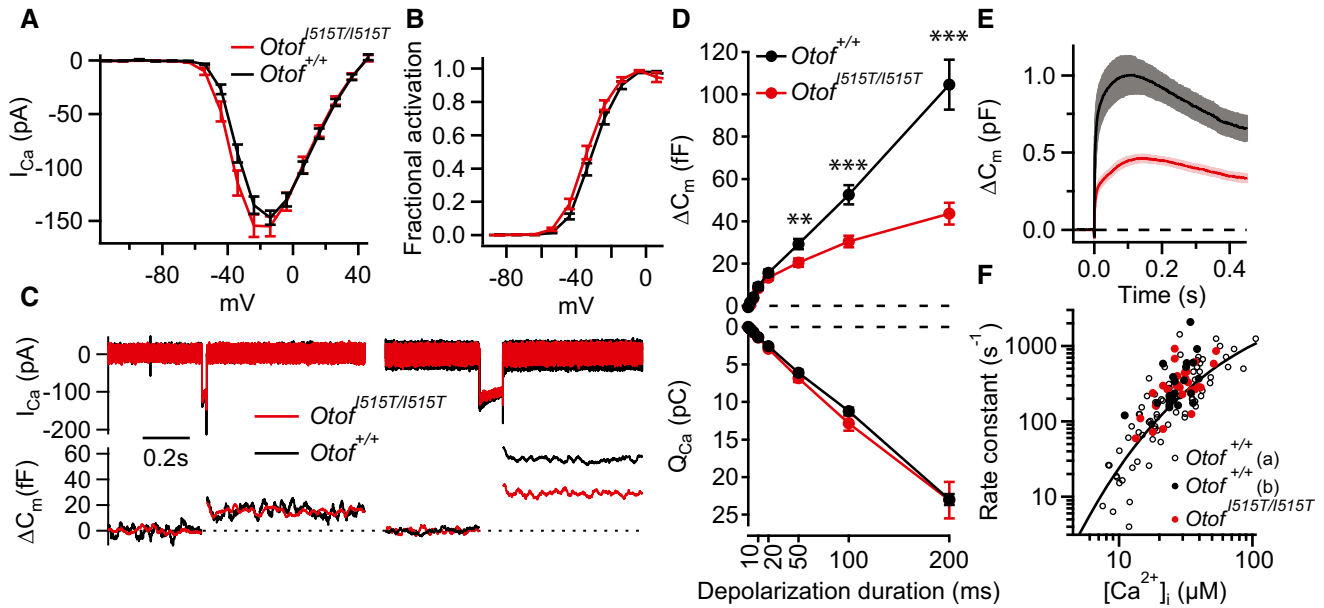
**Figure 3. Sustained exocytosis is impaired in *Otof^{I515T/I515T}* hair cells.**

A, B   No difference in voltage-dependent Ca$^{2+}$ currents (A) and fractional activation of I$_{Ca}$ channels (B) between *Otof^{I515T/I515T}* IHCs (*n* = 16) and IHCs of *Otof^{+/+}* littermates (*n* = 13; mean ± SEM).

C   Exocytosis was recorded by measures of changes in membrane capacitance (ΔCm, lower panel) in response to depolarization (left, 20 ms; right, 100 ms) to the voltage where maximum Ca$^{2+}$ currents were elicited (upper panel), typically −14 mV. Representative examples.

D   Upper panel, while for stimuli up to 20 ms exocytosis from *Otof^{I515T/I515T}* (*n* = 13) and *Otof^{+/+}* (*n* = 11) IHCs was similar, sustained exocytosis, representing most likely the release of replenished vesicles, was significantly reduced in *Otof^{I515T/I515T}* IHCs (mean ± SEM; *t*-test; **P < 0.01; ***P < 0.001). Lower panel, Ca$^{2+}$ current integrals were of similar size (mean ± SEM).

E   Flash photolysis of caged Ca$^{2+}$ elicited a smaller exocytic response in *Otof^{I515T/I515T}* IHCs (mean ± SEM).

F   The kinetics of the fast component from (E) was comparable between *Otof^{I515T/I515T}* IHCs and *Otof^{+/+}* littermates (black circles). Open circles represent previously published data on IHCs of hearing wild-type mice (Beutner *et al*, 2001; Pangrsic *et al*, 2010).

each driven by a single IHC active zone (Fig 4). We found spontaneous spiking (Fig 4A), sound thresholds and frequency tuning (Fig EV2A and B) of individual SGNs to be normal which corroborates our notion of intact cochlear amplification in *Otof^{I515T/I515T}* mice. Upon stimulation with tone bursts at a stimulus rate of 2 Hz, *Otof^{I515T/I515T}* SGNs showed a near-normal onset response with a high rate of instantaneous spiking, but then underwent stronger spike rate adaptation, not reaching a steady state within the 50 ms of stimulation (Fig 4B and E; ratio of onset/adapted rates 5.2 ± 1.8 in *Otof^{I515T/I515T}* SGNs versus 3.5 ± 0.2 in *Otof^{+/+}* SGNs, *P* = 0.03, *t*-test). Compared to SGNs from *Otof^{+/+}* littermates, the time course of adaptation was slower (Tau 10.9 ± 3.0 ms versus 6.1 ± 1.7 ms, single exponential fit, *P* < 0.001, *t*-test).

At higher stimulus rates of 5 or 10 Hz, both onset and adapted spike rates decreased dramatically (Fig 4C–E). Consistent with the reduced spiking at sound onset, the first spikes then also showed a highly significant increase in latency (Fig EV2C) and jitter (Fig 4F). As evoked spike rates were low and the dynamic range unchanged, rate-intensity functions of individual SGNs were shallower than normal (Figs 4G and EV2D and E). The spike rates and precision of spike timing were even further decreased when continuous amplitude-modulated sound stimuli were applied (Figs 4G and H, and EV2F). The enhanced adaptation and slowed recovery from adaptation were also obvious from responses to paired stimuli (Fig 4I) where the half-time of recovery from forward masking was fivefold increased from 28.7 ± 5.6 ms in 9

*Otof^{+/+}* to 157.5 ± 40.5 ms in 13 *Otof^{I515T/I515T}* SGNs (*P* < 0.001, Mann–Whitney *U*-test). In summary, *Otof^{I515T/I515T}* SGNs show an unusual sound encoding deficit that is dominated by a use-dependent reduction of sound-evoked spiking, likely resulting from impaired replenishment of the RRP and/or impaired active zone clearance.

### Impaired synaptic sound encoding in *Otof^{I515T/I515T}* mice affects the perception of silent gaps in noise

Using prepulse inhibition of the acoustic startle response, we found an impairment of gap detection performance in *Otof^{I515T/I515T}* mutants compared to *Otof^{+/+}* littermates (Fig EV3A–C). We propose that this is consistent with the delayed recovery from adaptation (Fig 4I) and reflects the impaired vesicle replenishment during the gap. For a more sensitive method that approaches the physiological limit of gap detection abilities, we then employed operant conditioning using the Audiobox system (de Hoz & Nelken, 2014). We conditioned mice to attempt to drink water only when continuous broadband noise was present. When the noise was interrupted by 90 ms silent gaps, access to the water bottles was denied and drink attempts were punished by air puffs. After reaching > 30% discrimination performance, we introduced shorter gaps in a total of 8% of the trials. The two *Otof^{+/+}* mice avoided drinking when gaps lasted 3 ms or more. This agrees well with descriptions of gap thresholds near 2 ms in CBA/J mice (Radziwon *et al*, 2009).
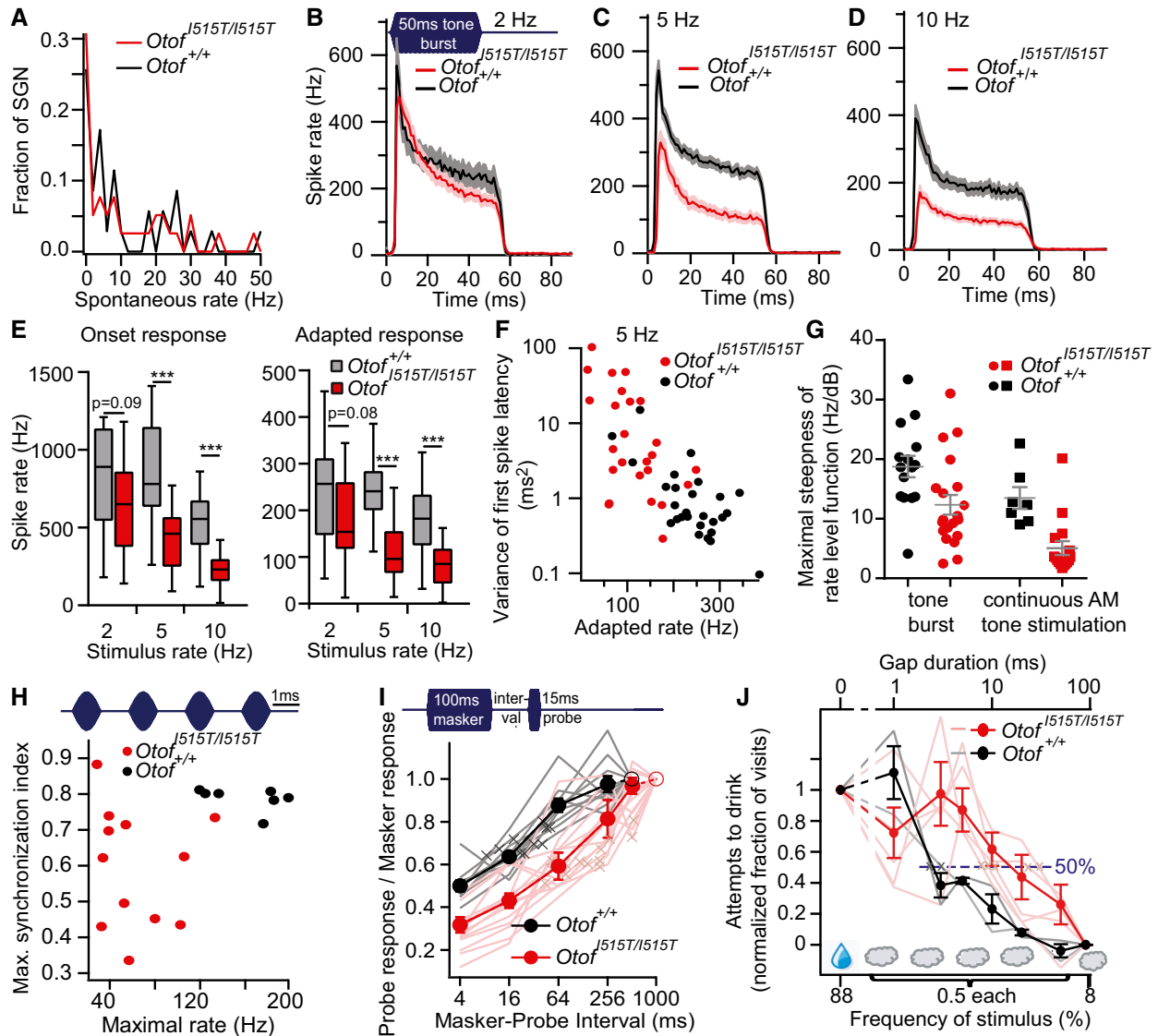
**Figure 4. Enhanced adaptation and slowed recovery of SGN spiking in *Otof^{I515T/I515T}*.**

A   Spontaneous rates of SGNs from *Otof^{I515T/I515T}* (red, n = 35) and *Otof^{+/+}* littermates (black, n = 39) were not significantly different (P = 0.83, Kolmogorov–Smirnov test).

B–D   Averaged poststimulus time histograms ± SEM from *Otof^{I515T/I515T}* mice (n = 25–32) and *Otof^{+/+}* littermate SGNs (n = 13–27) to stimulation with 50 ms tone bursts at the characteristic frequency (CF) of each fibre, 30 dB above threshold at indicated stimulus rates.

E   Quantification of onset (largest 0.5 ms bin, Mann–Whitney U-test) and adapted responses (averaged 35–45 ms from response onset, ***P < 0.001, t-test, Tukey quartile box plot) from data in (B–D).

F   The jitter of the first sound-evoked spike was significantly increased (P < 0.001, Mann–Whitney U-test) but retained its inverse correlation with spike rates.

G   Spike rate increases with rising stimulus intensity were significantly shallower in *Otof^{I515T/I515T}* SGNs, both for repetitive stimulation with 50 ms tone bursts (left, P = 0.014, t-test) and for continuous stimulation with amplitude-modulated tones (right, P < 0.001, Mann–Whitney U-test). Lines represent mean ± SEM.

H   Phase locking to amplitude-modulated tones (assessed as the maximal synchronization index) was typically less precise in *Otof^{I515T/I515T}* SGNs than in *Otof^{+/+}* SGNs (P = 0.09, Mann–Whitney U-test).

I   100 ms masker tone and 15 ms probe tones (both at CF, 30 dB above threshold) were separated by silent intervals of variable duration. Inter-masker intervals were 500 ms for *Otof^{+/+}* and 1,000 ms for *Otof^{I515T/I515T}*. The ratio of probe and masker onset responses revealed enhanced RRP depletion after stimulation in *Otof^{I515T/I515T}* (pink; mean ± SEM red) compared to *Otof^{+/+}* (grey; mean ± SEM black; for 4 ms interval: P = 0.001, t-test) and a slowed time course of recovery (x: half-time of recovery, interpolated from normalized recovery functions; P < 0.001, Mann–Whitney U-test).

J   Mice learned to drink water when continuous noise was present but avoided drinking when the noise was interrupted by silent gaps. 5 *Otof^{I515T/I515T}* mice (pink, mean ± SEM red) avoided drinking less efficiently than 2 *Otof^{+/+}* mice (grey, mean ± SEM black) for shorter gap durations. See also Fig EV3.

In contrast, *Otof^{I515T/I515T}* often attempted to drink in trials with short gaps (Figs 4J and EV3F). The interpolated 50% value of the normalized discrimination function was 2.7 ± 0.4 ms in *Otof^{+/+}* mice and 17.2 ± 4.9 ms in *Otof^{I515T/I515T}*.

In a second task, we conditioned mice to avoid drinking when they heard 12 kHz tone bursts. The responses to varying tone intensities indicate comparable hearing thresholds in two *Otof^{I515T/I515T}* mice and one *Otof^{+/+}* mouse (Fig EV3D and E).

Together, the impaired gap detection performance and normal sound sensitivity in $Otof^{I515T/I515T}$ mice are consistent with the results of *in vivo* recordings from SGNs that show normal sound sensitivity but impaired recovery from adaptation. Like in other mice with synaptic transmission deficits (e.g. Buran *et al*, 2010; Jung *et al*, 2015) and patients with auditory synaptopathy/neuropathy, the deficit appears overly pronounced in ABR recordings which represent a combination of the sensitivity, the rate and the synchronicity of SGN firing.

## ABR amplitudes gradually decline at elevated temperature

Our data show that $Otof^{I515T/I515T}$ mice reflect the auditory phenotype of human patients at normal body temperature very well. Thus, we assume that the synaptic disease mechanisms found in mice at or below physiological temperature likely describe the situation in human patients. We next assayed whether mice, like the human patients, experience an exacerbation of their hearing loss when their body temperature exceeds 38°C (Varga *et al*, 2006). We monitored the amplitude of ABR wave I in response to click stimulation while locally applying heat to the inner ear (Fig 5A–C and Appendix Fig S2). Here, we found a reversible linear decrease in ABR wave I amplitude in both $Otof^{I515T/I515T}$ and $Otof^{+/+}$ littermate mice, with comparable average regression slopes of 0.084 μV/°C and 0.081 μV/°C, respectively. The effect varied considerably between animals, presumably due to variable experimental conditions. In some animals (3/6 $Otof^{I515T/I515T}$ and 2/6 $Otof^{+/+}$), ABR amplitudes did not recover after extensive heating (Appendix Fig S2B and C), presumably indicating permanent heat damage. Nonetheless, since ABRs in the mouse model never disappeared completely, we conclude that the elevated cochlear temperature did not fully abolish sound encoding in $Otof^{I515T/I515T}$ mouse mutants, as it seems to be the case in human $Otof^{I515T/R1116*}$ patients. Thus, as the heat-induced phenotype seems to be weaker in mice compared to human patients, the cell physiological or ultrastructural effect of fever found in our mouse model might also be weaker than in human patients.

## A 20 amino acid stretch present in human otoferlin reduces plasma membrane localization of Ile515Thr-otoferlin

Looking at differences in the protein sequence of human and mouse otoferlin which might contribute to the less pronounced heat sensitivity in mice, we found an arginine-rich insertion including an RXR motif at position 1244–1263 in the long human reference sequences (e.g. variant e; NP_001274418). While there is currently no experimental evidence which splice isoform regarding this motif is expressed in human IHCs, PCRs on mouse organ of Corti cDNA revealed that the isoform lacking this RXR motif is predominant in mouse IHCs (Fig EV4). A similar motif was described to cause a temperature-dependent decrease in surface expression of an alpha-adrenergic receptor (Filipeanu *et al*, 2011, 2015). We subcloned the human RXR stretch into mouse otoferlin cDNA and performed biolistic transfection into $Otof^{-/-}$ IHCs (Fig 5E–I). RXR-otoferlin showed a strong plasma membrane immunostaining (relative to total cellular otoferlin levels), which was comparable to the values from explanted $Otof^{+/+}$ cells

(Fig 5D and J). Otoferlin with both the Ile515Thr mutation and the RXR motif, however, displayed almost complete absence from the plasma membrane already at 37°C (Fig 5H–J), which is in stark contrast to mouse Ile515Thr-otoferlin (Fig 1). Since the abundance of otoferlin at the plasma membrane seems to be most relevant for sound encoding *in vivo*, this might explain the more pronounced heat sensitivity in human patients. When comparing to the hearing phenotype of our mouse models, hearing at normal and elevated temperature in human Ile515Thr patients would best be explained by a mixture of the splice variant with RXR and the splice variant without being expressed in human IHCs.

## Heat reduces exocytosis and otoferlin membrane levels

We next tested for a synaptic dysfunction elicited by fever by performing patch clamp recordings of IHCs (Fig 6). We recorded $\Delta C_m$ in IHCs induced by 5–100 ms depolarization steps, first at room temperature (RT), then at near physiological temperature (PT, 35–36.5°C), followed by high temperature (38.5–40°C). Consistent with a previous study (Nouvian, 2007), we found $Ca^{2+}$ currents and exocytosis from $Otof^{+/+}$ IHCs to increase when temperature was raised from RT to PT (Fig 6A and B). While $Ca^{2+}$ current integrals increased only by 27 and 15% in $Otof^{+/+}$ ($n = 4$) and $Otof^{I515T/I515T}$ ($n = 5$), respectively, exocytosis was more strongly enhanced by warming (Fig 6B) and increased 2.7- to threefold in both genotypes.

We next heated the bath to 38.5–40°C expecting a strong reduction of exocytosis for $Otof^{I515T/I515T}$ IHCs given the human fever-induced deafness. Recordings were started as soon as the temperature recorded in the bath close to the tissue was stable. Surprisingly, we found a strong decline in $\Delta C_m$ for $Otof^{+/+}$ IHCs compared to PT, especially for sustained exocytosis which was halved (Fig 6C and F). This fever-induced reduction was weaker in $Otof^{I515T/I515T}$ (13% less than at PT; Fig 6G). As a result, $\Delta C_m$ did not differ between $Otof^{I515T/I515T}$ and $Otof^{+/+}$ IHCs at high temperature for all depolarization durations tested (Fig 6C). However, we cannot exclude that a longer heating period might have unravelled a stronger synaptic dysfunction in $Otof^{I515T/I515T}$ IHCs. In fact, sustained exocytosis between the genotypes appeared slightly stronger in recordings after heating. At 2 min of recovery at < 29°C, exocytosis in $Otof^{+/+}$ IHCs was reduced to 52% relative to RT before heating for depolarization stimuli of $\geq 10$ ms ($n = 4$), while in $Otof^{I515T/I515T}$ IHCs, it was reduced to 40% of initial RT values ($n = 3$; Fig 6D, F and G). $Ca^{2+}$ currents were of similar size as before heating and comparable between $Otof^{+/+}$ and $Otof^{I515T/I515T}$ IHCs. In few of these IHCs, exocytosis was tested also after a longer recovery period of 5–20 min, and we recorded additional cells only after heating (Fig 6E). Considering IHCs of both conditions, we found $\Delta C_m$ levels for 100 ms depolarization in $Otof^{+/+}$ IHCs to be restored to 61% compared to observations at RT before heating ($n = 7$ from 4 cells). In contrast, in $Otof^{I515T/I515T}$ IHCs, sustained exocytosis remained reduced (37% of initial values for 100 ms depolarization, $n = 8$ from 4 cells).

Based on the loss of exocytic capacity in wild-type and mutant IHCs between PT and $\geq 38.5$°C, we propose that part of the synaptic machinery is thermally unstable. The poorer recovery from heat in $Otof^{I515T/I515T}$ IHCs and the temperature-sensitive phenotype of patients with different *OTOF* mutations suggest that otoferlin itself
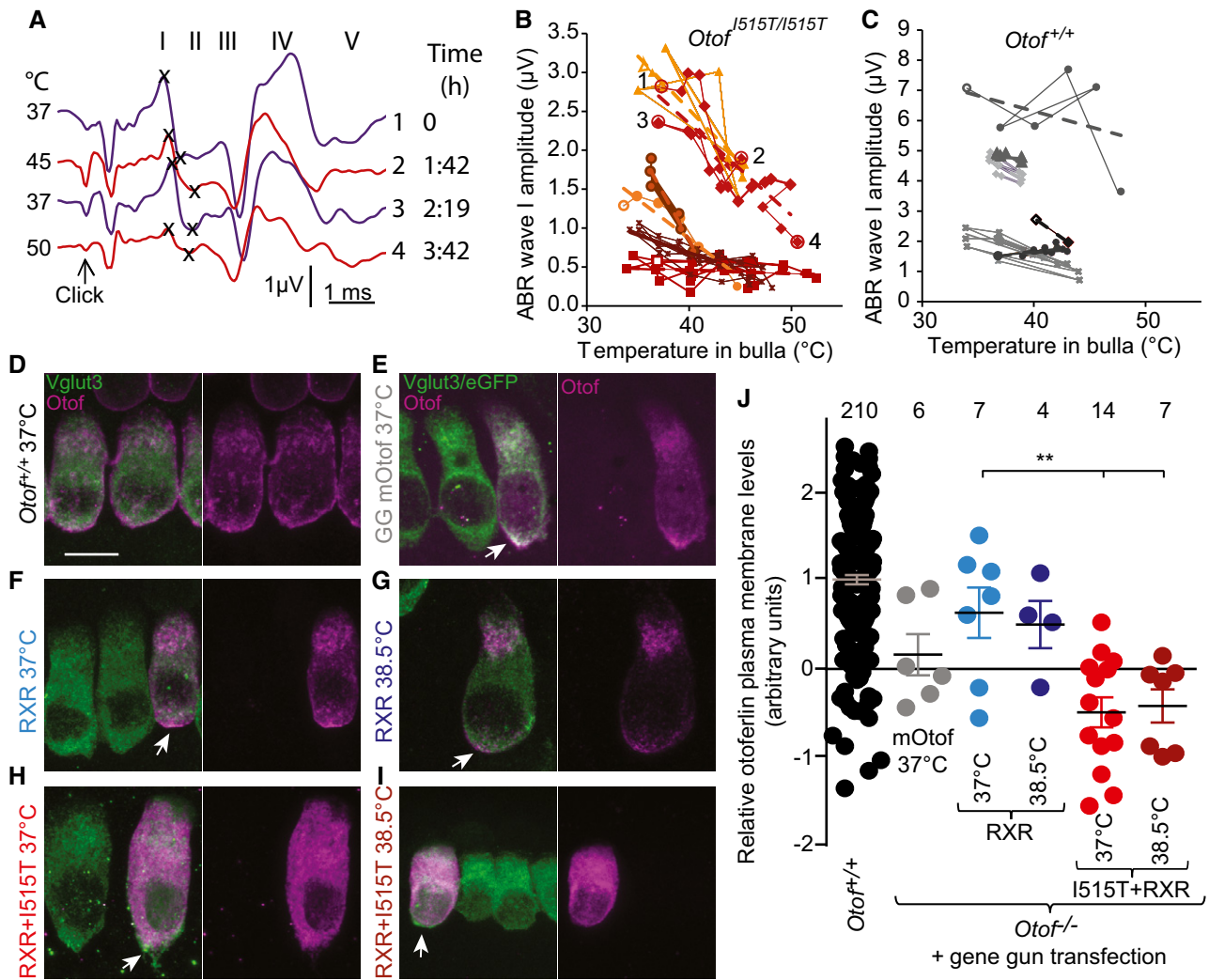
**Figure 5.** **Apparently lower thermal sensitivity of hearing in mice than in humans, likely due to a human RXR motif reducing plasma membrane localization of Ile515Thr-otoferlin.**

A    Exemplary ABR traces (click 100 dB) from one *Otof*$^{I515T/I515T}$ mouse recorded at indicated bulla temperatures during local heating. Note that ABRs never disappeared completely, but wave I amplitude changed reversibly with temperature.

B, C   ABR wave I amplitudes in *Otof*$^{I515T/I515T}$ (B, click 100 dB) and *Otof*$^{+/+}$ mice (C, click 80 dB) decreased with increasing temperature in the bulla. Each colour represents a different experiment, and dashed lines are line fits. Open symbols indicate the beginning of the experiments; subsequent recordings are connected by lines. The four indicated data points in (B) correspond to ABRs in (A).

D    Explanted organ of Corti from an *Otof*$^{+/+}$ mouse at P4 after 2 days *in vitro* (DIV2) at 37°C immunostained against otoferlin (magenta) and Vglut3 (green). Note the intense immunostaining of otoferlin at the plasma membrane. Scale bar, 10 μm.

E–I   Explanted organs of Corti from *Otof*$^{-/-}$ mice at P4 were transfected by GeneGun with otoferlin cDNA and eGFP and immunostained at DIV2. (E) Example cell transfected with wild-type mouse otoferlin. (F, G) Representative cells transfected with mouse otoferlin including the 20 amino acids of the RXR motif (see Fig EV4). Cells in (G) were incubated at 38.5°C for 30 min prior to fixation. The RXR-otoferlin transfected cells (F, G) show a membrane localization of otoferlin surrounding the Vglut3 immunofluorescence/eGFP fluorescence at the basal pole of the cells (arrows), similar as in controls (D, E). (H, I) Both the human RXR motif and the Ile515Thr mutation were introduced in mouse cDNA, and cells were incubated at 37°C (H) or for 30 min at 38.5°C (I) before fixation. Here, green fluorescence surrounds the otoferlin immunofluorescence (arrows), suggesting loss of otoferlin from the plasma membrane.

J    Quantification of the relative plasma membrane levels of otoferlin (as in Fig 1) revealed normal plasma membrane abundance when the human RXR motif was present, but a strong reduction for otoferlin with RXR and Ile515Thr (individual cells; mean ± SEM; *t*-test; \*\**P* < 0.01).

is the heat-sensitive protein and that heat instability of otoferlin is enhanced by certain mutations like Ile515Thr.

Indeed, 3D structure predictions show that the isoleucine 515 points towards the hydrophobic core of the C$_2$C domain (Appendix Fig S3), suggesting that an exchange into the more hydrophilic threonine potentially decreases the stability of the protein. Since we also did not find a change in otoferlin mRNA

levels in *Otof*$^{I515T/I515T}$ organs of Corti, ruling out lower transcription levels or destabilized mRNA as a cause (Appendix Fig S4A), we hypothesized that mutations in otoferlin lead to faster protein degradation at elevated temperature. Testing the degradation rate of a series of otoferlin mutants related to human heat-induced deafness after heterologous expression in HEK293T cells, we found hardly any degradation within 2 or 24 h even at elevated temperature,
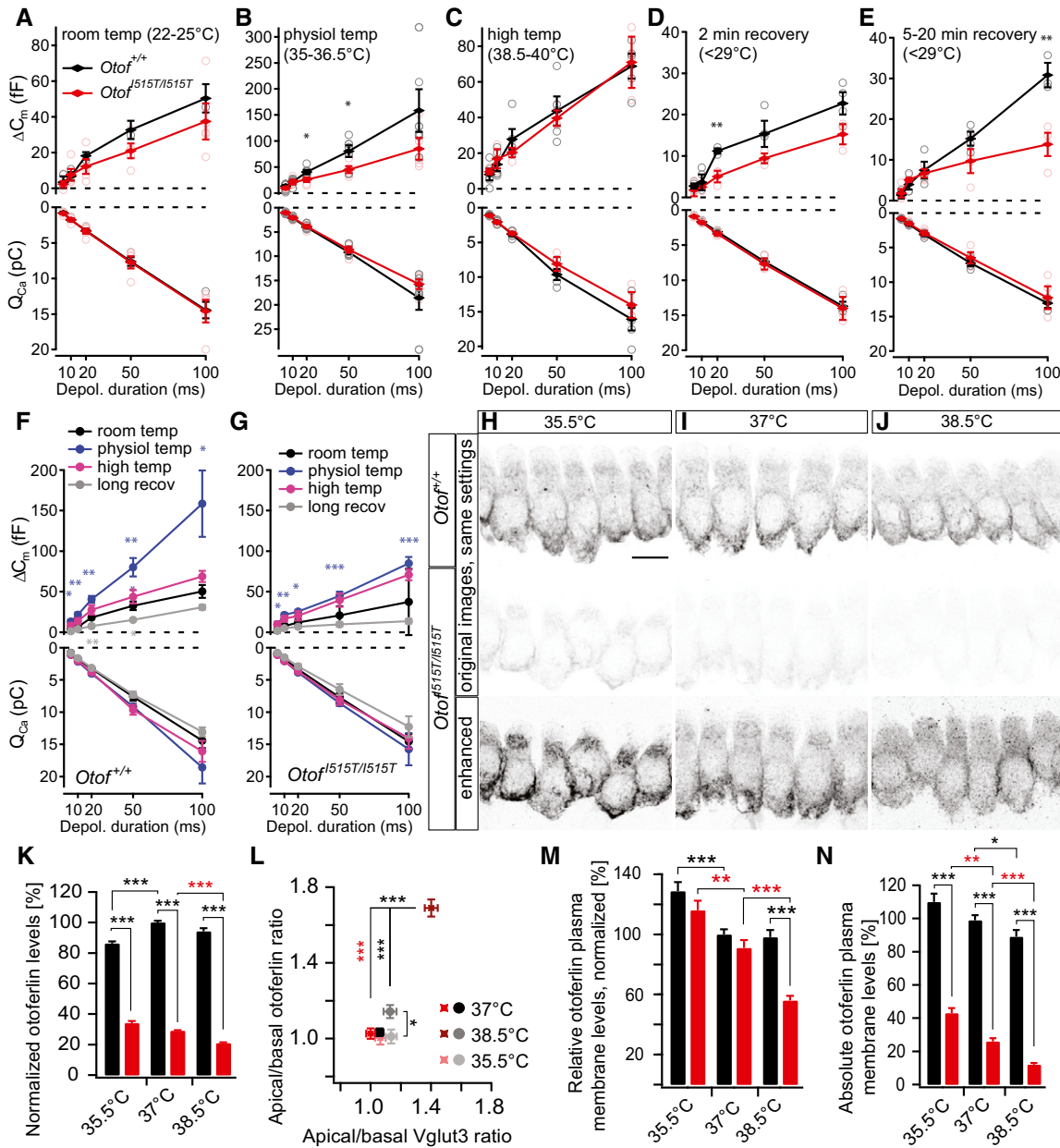
**Figure 6.  Temperature alters exocytosis, otoferlin protein levels and plasma membrane abundance.**

A–E   Capacitance increments recorded from *Otof*^{+/+} (black) and *Otof*[I515T/I515T] (red) IHCs. Individual cells recorded at indicated temperatures (light circles), mean ± SEM (filled circles) for perforated-patch clamp experiments.

F, G   Summary of the capacitance changes and $Ca^{2+}$ current integrals for *Otof*^{+/+} (F) and *Otof*[I515T/I515T] IHCs (G) at the different temperatures illustrates the drastic increase in exocytosis for physiological temperature. Significant differences compared to RT measurements are indicated with colours of the respective temperature, and between PT and high temperature in violet.

H–J   Otoferlin immunofluorescence in *Otof*^{+/+} IHCs (upper panel) and *Otof*[I515T/I515T] IHCs (middle and lower panels) of explanted organs of Corti at P7-P8 after incubation at indicated temperatures for 24 h; maximum projections of z-stacks, inverted images; scale bar, 10 µm. The same imaging settings have been applied in all experiments, and the same lookup table was applied for the upper and middle panels. Images of lower panels are enhanced compared to middle panels (lookup table covering full data range of only this genotype) to visualize otoferlin distribution.

K   Quantification of otoferlin immunofluorescence in *Otof*^{+/+} IHCs (black bars) and *Otof*[I515T/I515T] IHCs (red bars) indicates reduced protein levels with increasing temperature.

L   Apical/basal otoferlin protein distribution, revealing a significant apical shift of otoferlin and Vglut3 for *Otof*[I515T/I515T] IHCs (red symbols) at 38.5°C compared to *Otof*^{+/+} (grey/black symbols).

M   Relative levels of membrane-bound otoferlin were lowered with increasing temperature.

N   Absolute otoferlin membrane immunostaining strongly decreased with temperature.

Data information: All data presented are mean ± SEM. $n$ = 98–137 *Otof*^{+/+} cells and $n$ = 90–97 *Otof*[I515T/I515T] cells in (K–N), 4–5 experiments. $t$-test (A–G) or Kruskal–Wallis test (K–N); \*$P < 0.05$; \*\*$P < 0.01$; \*\*\*$P < 0.001$.

similar as for wild-type otoferlin (Appendix Fig S4B and C). Although the lifetime of mutated otoferlin might be shorter in IHCs (see Appendix Fig S1E), the degradation seems too slow to explain hearing loss due to elevation of the body temperature. We hypothesize that loss of otoferlin from the plasma membrane in addition to protein unfolding might explain acute IHC presynaptic dysfunction at fever.

Next, we tested steady-state levels and subcellular distribution of otoferlin after prolonged incubation at elevated temperature (Fig 6H–J). In cultures of P7-8 organs of Corti incubated for 24 h at 37°C, the physiological temperature of mice (http://www.informatics. jax.org), otoferlin protein levels in $Otof^{I515T/I515T}$ IHCs were reduced to 29% of $Otof^{+/+}$ controls at 37°C (Fig 6K). After 24-h incubation at 38.5°C, otoferlin protein levels were even further reduced to 21%, and, remarkably, both otoferlin and Vglut3 localized more apically in $Otof^{I515T/I515T}$ IHCs (Fig 6L), resembling the distribution found in $Otof^{Pga/Pga}$ IHCs (Fig 1H). The relative levels of plasma membrane-bound otoferlin were strongly reduced at febrile temperature (56% of controls, Fig 6M), resulting in a strong temperature-dependent reduction of the absolute amount of plasma membrane-bound otoferlin in $Otof^{I515T/I515T}$ IHCs (12% of controls, Fig 6N).

In summary, otoferlin is sensitive to heat, which is exacerbated by mutations like Ile515Thr. We found indications for faster degradation and loss from the plasma membrane of Ile515Thr-otoferlin at febrile temperature.

### Otoferlin is localized at the plasma membrane and at endosomal vesicles, and synaptic vesicles are enlarged in $Otof^{I515T/I515T}$ IHCs

Next, we analysed the subcellular distribution of otoferlin at the ultrastructural level by performing pre-embedding immunogold labelling and electron microscopy (EM) of P15-P16 IHCs (Fig 7 and Appendix Fig S5). The near absence of gold clusters in $Otof^{-/-}$ tissue confirmed specificity of immunogold labelling (Fig 7C). In both $Otof^{+/+}$ and $Otof^{I515T/I515T}$ IHCs, otoferlin immunogold signal was present at the plasma membrane including the active zone membrane (Fig 7A, B and D–G, and Appendix Fig S5), and at vesicular structures, some of which exhibited clathrin-coated vesicle budding (Fig 7I and J) indicating endosomal nature. The diameter of labelled intracellular membranous structures was, on average, larger in $Otof^{I515T/I515T}$ ($210 \pm 13$ nm; smallest diameter: 51 nm; $n = 86$) than in $Otof^{+/+}$ IHCs ($151 \pm 8$ nm, smallest 52 nm; $n = 82$, $P < 0.001$; Fig 7K) and thus clearly exceeded the typical synaptic vesicle diameter in IHCs (Chapochnikov *et al*, 2014). Hardly any otoferlin labelling was visible in < 100 nm distance to the ribbons where a halo of synaptic vesicles resides, neither in $Otof^{+/+}$ nor in $Otof^{I515T/I515T}$ IHCs, using two different pre-embedding protocols (Fig 7D–G). This discrepancy to earlier immunogold studies reporting a synaptic vesicle localization of otoferlin (Roux *et al*, 2006) might be due to pre- versus postembedding protocols used and/or different primary antibodies and a potential masking of our antibody epitope specifically at synaptic vesicles. In contrast, immunogold labelling for the vesicular glutamate transporter Vglut3 resulted in a strong signal around the ribbon (Fig 7H and Appendix Fig S5). Quantification of the gold particles revealed an overall reduction of otoferlin labelling in the cytoplasm and a strong trend towards lower levels at the membrane in $Otof^{I515T/I515T}$ hair cells (Fig 7L and M), consistent with our immunofluorescence results. We conclude that the Ile515Thr mutation does not alter the subcellular distribution of otoferlin.

The larger average diameter of otoferlin-labelled structures in $Otof^{I515T/I515T}$ IHCs might point towards impaired membrane turnover. We thus assessed the effects of the Ile515Thr mutation on synaptic ultrastructure and vesicle pool dynamics at 36 and 39°C by performing transmission EM of IHC ribbon synapses following inhibition or stimulation of exocytosis and subsequent chemical fixation. To inhibit IHC exocytosis, isolated organs of Corti were incubated in $Ca^{2+}$-free saline, while stimulation employed extracellular saline with 1.3 mM $Ca^{2+}$ and 40 mM $K^+$ (according to the Nernst equation depolarizing IHCs to ~−30 mV). We found the number of membrane-proximal and ribbon-associated vesicles quantified in random ultrathin sections to be similar in all four conditions (stimulatory and inhibitory at 36/39°C) and both

**Figure 7.** **The Ile515Thr mutation does not affect the subcellular localization of otoferlin but alters the size of endosomal and synaptic vesicles.**

A–C   Pre-embedding immunogold labelling for EM visualizes otoferlin localization in random ultrathin sections through the basal part of IHCs in $Otof^{+/+}$ (A) and $Otof^{I515T/I515T}$ (B) but not in $Otof^{-/-}$ (C) mice. IHCs are highlighted in beige. Scale bar, 200 nm.

D–G   Magnified synaptic ribbons (R) and postsynaptic afferent boutons of SGNs (Aff), displaying otoferlin immunogold labelling at active zone membranes (pink arrowheads) but not around the synaptic ribbon, using saponin permeabilization (D–F), or Triton X-100 treatment (G). Scale bar, 100 nm.

H   Vglut3 immunogold labelling adjacent to the ribbon as expected for a synaptic vesicle protein. Scale bar, 100 nm.

I, J   Some otoferlin-labelled structures bear clathrin coats (red arrowheads), suggesting that they originate from bulk endocytosis. Scale bar, 100 nm.

K   Otoferlin-labelled vesicles were on average larger in $Otof^{I515T/I515T}$ IHCs (mean $\pm$ SEM; $Otof^{I515T/I515T}$, $n = 86$ vesicles, 18 images; $Otof^{+/+}$, $n = 82$ vesicles, 6 images; Wilcoxon rank-sum test; ***$P < 0.001$).

L   Quantification of immunogold clusters at the plasma membrane revealed a strong trend towards reduced levels of otoferlin in $Otof^{I515T/I515T}$ (six images each) (mean $\pm$ SEM; Wilcoxon rank-sum test).

M   Distal from the plasma membrane, immunogold labels were reduced in $Otof^{I515T/I515T}$ IHCs (mean $\pm$ SEM; Kruskal-Wallis test; *$P < 0.05$; **$P < 0.01$).

N   Representative electron micrographs of IHC ribbon synapses in $Otof^{I515T/I515T}$ and $Otof^{+/+}$ (conventional embedding without immunogold) after pre-incubation for 10 min at the indicated temperature followed by high $K^+$ stimulation or 0 $Ca^{2+}$ inhibition for 1 min 45 s. Scale bars, 100 nm.

O   Illustration depicting criteria for random section analysis (not drawn to scale). Ribbon-associated synaptic vesicles (SVs, green) in the first row $\leq 80$ nm from ribbon (R) and membrane-proximal vesicles (yellow) in $\leq 25$ nm membrane-to-membrane distance from the plasma membrane (blue) and $\leq 80$ nm from each side of the presynaptic density.

P, Q   Synaptic vesicles with > 45 nm diameter appeared at 39°C in random sections; fraction of large membrane-proximal (P; Kruskal–Wallis test followed by non-parametric multiple comparison test; *$P < 0.05$) and ribbon-associated (Q; one-way ANOVA followed by Tukey's test; *$P < 0.05$; **$P < 0.01$) synaptic vesicles (mean $\pm$ SEM; $Otof^{+/+}$ inhibitory, $n = 24$ synaptic ribbons, $Otof^{+/+}$ stimulatory, $n = 27$ synaptic ribbons, $Otof^{I515T/I515T}$ inhibitory, $n = 36$ synaptic ribbons, $Otof^{I515T/I515T}$ stimulatory, $n = 21$ synaptic ribbons; see also Appendix Table S1).
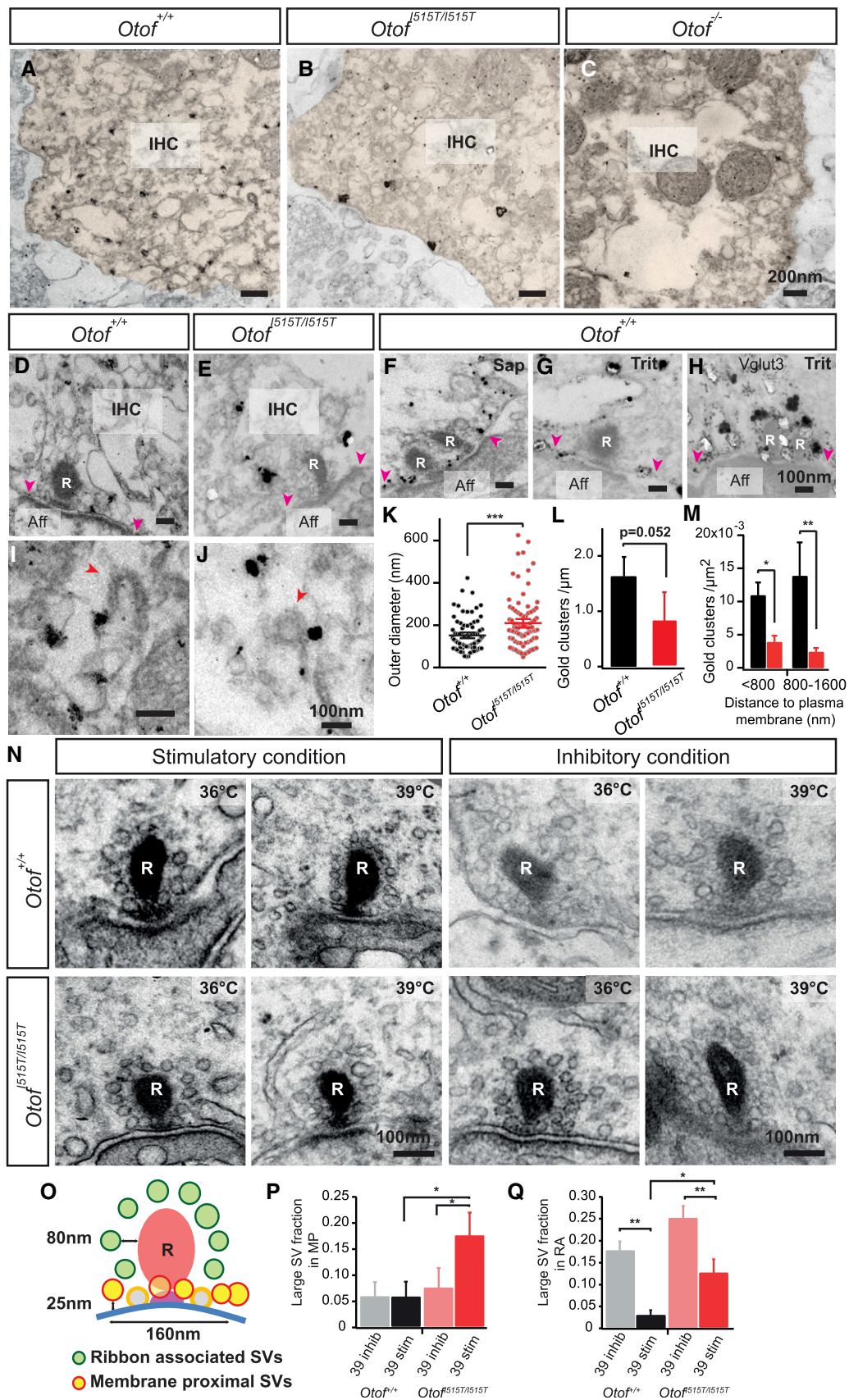
**Figure 7.**

genotypes ($N$ = 2 mice/condition and genotype; Fig 7N and O, and Appendix Fig S6 and Appendix Table S1). The only significant effect was an increase in the number of membrane-proximal vesicles in $Otof^{I515T/I515T}$ as compared to $Otof^{+/+}$ IHCs after stimulation at either temperature (Appendix Table S1).

We next determined the vesicle diameter in all four conditions for both ribbon-associated and membrane-proximal vesicles. We found the majority of vesicle diameters to be in a 35–45 nm range, consistent with previous reports from IHC ribbon synapses (Neef *et al*, 2007; Appendix Fig S6). Remarkably, in the membrane-proximal pool at $Otof^{I515T/I515T}$ synapses after stimulation at 39°C, vesicles with diameter > 45 nm were observed, that were less frequent after inhibition, and rarely observed in $Otof^{+/+}$ (Fig 7P, Appendix Fig S6A and Appendix Table S1). In contrast, for the ribbon-associated pool, we found more large vesicles for inhibitory than for stimulatory condition at $Otof^{+/+}$ (39°C) and, remarkably, even more for both conditions at $Otof^{I515T/I515T}$ synapses (Fig 7Q, Appendix Fig S6B and Appendix Table S1).

We further analysed number and size of synaptic vesicles by performing electron tomography after stimulation at 36 and 39°C (Fig 8, $n$ = 4 tomograms/genotype and condition; Table EV1). While the number of synaptic vesicles was unaltered in tomograms, we found the vesicles to be larger in $Otof^{I515T/I515T}$ IHCs, both the membrane-proximal (Fig 8N and O) and the ribbon-associated ones (Fig 8P and Q). In all conditions tested, we also found some flattened vesicles (Table EV1), but their longest axis was not significantly different (Fig 8O and Q).

Together, the enlarged otoferlin-labelled endosomal vesicles and the enlarged synaptic vesicles point towards a deficit in vesicle reformation in $Otof^{I515T/I515T}$ IHCs, which is more pronounced at febrile temperature.

## Discussion

Here, we present a mouse model for auditory fatigue and otoferlin-related hearing impairment, allowing us to study the disease mechanism from molecular to systems level. Our analysis reveals that the remarkable IHC capability of indefatigable sustained exocytosis requires otoferlin. This likely involves roles of otoferlin in reformation of synaptic vesicles from endocytosed membrane as demonstrated here, in addition to tethering synaptic vesicles to the plasma membrane (Vogl *et al*, 2015), and priming and/or active zone clearance (Pangrsic *et al*, 2010; Jung *et al*, 2015). Presynaptic function of IHCs and sound encoding correlate with the abundance of otoferlin at the plasma membrane. We postulate that upon an elevation of the body temperature in human patients with temperature-sensitive *OTOF* mutations, properly folded otoferlin at the plasma membrane drops below a level critical for promoting synaptic sound encoding.

### Hearing impairment correlates with the amount of otoferlin at the IHC plasma membrane

Most human *OTOF* mutations lead to profound deafness, but some patients have residual hearing. While two mouse missense mutants, $Otof^{I515T/I515T}$ and $Otof^{Pga/Pga}$, show a similar overall reduction of otoferlin protein levels, $Otof^{Pga/Pga}$ IHCs, in addition,

display a perturbed plasma membrane localization of otoferlin. This results in a reduction of absolute otoferlin membrane levels to only 3% of wild-type in $Otof^{Pga/Pga}$ (Pangrsic *et al*, 2010 and this study), while $Otof^{I515T/I515T}$ IHCs retain 34%. The comparison of the hearing phenotypes of $Otof^{I515T/I515T}$, $Otof^{I515T/-}$, $Otof^{Pga/Pga}$ and $Otof^{-/-}$ mice indicates that synaptic function and sound encoding scale with the amount of plasma membrane-bound otoferlin, which might generalize to human missense mutations. A further heat-induced reduction of the plasma membrane abundance of mouse Ile515Thr-otoferlin appeared rather slowly and the temperature-dependent hearing loss was relatively mild in $Otof^{I515T/I515T}$ mice.

Direct comparison of mouse ABRs at febrile temperature with psychoacoustic testing of human patients is challenging. However, it seems that our mice are less susceptible to heat than human $OTOF^{I515T/R1116*}$ subjects who exhibit a threshold elevation by $\geq 60$ dB and loss of speech perception at 38.1°C body temperature. Our data indicate that this may be due to the RXR motif sequence presumably present in human otoferlin which reduces the plasma membrane abundance of Ile515Thr-otoferlin beyond what we found in $Otof^{I515T/I515T}$ mice. The expression of this RXR motif depends on whether the first or the second splice acceptor site in exon 30 is used, which is currently unknown. Together, the lower cellular otoferlin protein levels due to the Ile515Thr mutation, the presumed presence of the RXR splice isoform, which causes a weaker potency of the Ile515Thr-otoferlin for plasma membrane localization, and a likely heat-induced protein unfolding provide a candidate mechanism for temperature-sensitive hearing loss in humans.

### High rates of synaptic vesicle exocytosis at physiological temperature challenge current models for release mechanisms at ribbon synapses

Reconciling IHC physiological and morphological data with *in vivo* responses has remained difficult because of the clearly distinct experimental conditions (Buran *et al*, 2010; Pangrsic *et al*, 2010). Here, we set out to remove one important variable by combining data sets obtained near PT. Similar to a previous report (Nouvian, 2007), membrane capacitance estimates showed a ~threefold increase of exocytosis at PT compared to RT. Considering the *in vitro* patch clamp experiments at PT and assuming all exocytosis to occur at active zones, the calculated rate of sustained exocytosis amounts to ~2,300 vesicles/s/presynaptic active zone. This number appears very high when compared to EM counts of membrane- and ribbon-associated vesicles (on the order of 50/ribbon and with no obvious temperature dependence; Fig 8, Table EV1) and the average sustained SGN firing rate of 240 Hz in wild-type mice (Fig 4). Possible explanations for this discrepancy include more extrasynaptic exocytosis than described (Fuchs *et al*, 2003), a higher failure rate than assumed from *in vitro* and modelling studies (Siegel & Dallos, 1986; Rutherford *et al*, 2012) and/or synchronized multivesicular release. The mechanism of release at the hair cell synapse is a topic of active research and both synchronized multivesicular release (e.g. Glowatzki & Fuchs, 2002; Graydon *et al*, 2011) and univesicular release through a dynamic fusion pore (Chapochnikov *et al*, 2014) have been put forward to explain the heterogenous size and shape of EPSCs. Based on modelling Graydon *et al* (2011) proposed synchronization of readily releasable vesicles by a common $Ca^{2+}$

**Figure 8.  EM tomography reveals enlargement of synaptic vesicles under continuous exocytosis in *Otof^{I515T/I515T}* IHCs.**

A–D   Exemplary virtual sections through EM tomograms for stimulatory condition at 36 and 39°C. Scale bar, 100 nm.

E   Illustration depicting the tomogram analysis (not drawn to scale). Ribbon-associated synaptic vesicles (SVs, green) in the first row ≤ 80 nm from ribbon (R) and membrane-proximal vesicles (yellow) in ≤ 50 nm membrane-to-membrane distance from the plasma membrane (blue) and ≤ 100 nm from each side of the presynaptic density.

F–M   3D reconstruction of the membrane-proximal pool (top view) (F–I) and the ribbon-associated pool of vesicles (front view) (J–M). Active zone membrane is depicted in blue, presynaptic density in pink and ribbons in red; scale bars, 100 nm.

N–Q   Cumulative probability distribution of the diameter of round vesicles as well as the longest axis of flattened vesicles in the membrane-proximal pool (N, O) and ribbon-associated pool (P, Q). (N–P), one-way ANOVA followed by Tukey's test; (Q), Kruskal–Wallis test followed by non-parametric multiple comparison test. Round vesicles tested in both pools appeared larger in *Otof^{I515T/I515T}* IHC synapses but the long axis of flattened vesicles was comparable for both genotypes (see also Table EV1).

nanodomain at frog hair cell active zones, which, however, seemed insufficient to explain large and fast EPSCs in a model of the rat IHC active zone (Chapochnikov *et al*, 2014). The comparable vesicle diameters in EM at RT and PT for $Otof^{+/+}$ mice seemingly argue against homotypic fusion of synaptic vesicles, although a rapid exocytosis of such enlarged vesicles might have prevented their detection so far.

**Otoferlin plays a key role for vesicle reformation**

Using immunogold labelling, we found otoferlin at the plasma membrane (also reported in Roux *et al*, 2006) and, specifically, at the membrane of the active zones, which is consistent with a recent immunofluorescence analysis (Vogl *et al*, 2015). We found otoferlin labelling also at endosomal structures partially exhibiting budding of clathrin-coated vesicles, which is in agreement with STED fluorescence imaging data (Revelo *et al*, 2014), but not on synaptic vesicles of < 50 nm diameter. Remarkably, in $Otof^{I515T/I515T}$ IHCs, we found enlarged otoferlin-labelled vesicular structures, potentially of endosomal origin, and on average larger synaptic vesicles after incubation both at 36 and 39°C. In contrast, deficiency of the otoferlin interacting molecule AP-2μ, adapter protein for clathrin-mediated endocytosis, caused ablation of ribbon-associated vesicles distal from the active zone membrane, and a reduction of clathrin-coated structures close to ribbon synapses (Jung *et al*, 2015), indicating that otoferlin and AP-2μ act on different steps of the vesicle reformation process.

In summary, we propose a new role for otoferlin in reformation of proper sized synaptic vesicles. The extent of the hearing loss in $Otof^{I515T/I515T}$ might be explained by such a synaptic vesicle reformation defect, given that the high vesicle turnover rates at the IHC ribbon synapse require an ultrafast vesicle reformation mechanism. However, the impaired sustained exocytosis in $Otof^{I515T/I515T}$ at RT points towards an additional deficit in priming (Pangrsic *et al*, 2010) and/or active zone clearance (Duncker *et al*, 2013; Jung *et al*, 2015).

**Studying auditory fatigue at the level of single synapses in $Otof^{I515T/I515T}$ mice**

The normal size of the RRP observed in $Otof^{I515T/I515T}$ IHCs *in vitro* seems in contrast to the SGN spike rate reduction *in vivo*. This discrepancy can be reconciled when considering that in the voltage clamp experiment, hyperpolarization allows for RRP recovery in the absence of $Ca^{2+}$ influx-driven exocytosis, while *in vivo* spontaneous release diminishes the occupancy of the release sites that compose the RRP, reducing the "standing" RRP. Moreover, the lower time resolution of the capacitance recordings obscures the finding of a combined reduction of rate and synchronicity of sound onset firing which is observed in single unit recordings and highlighted by the ABR amplitude reduction.

At physiological temperature, the phenotype of $Otof^{I515T/I515T}$ mice reproduces the clinical picture very well and single SGN response recordings in $Otof^{I515T/I515T}$ mice provide an explanation for the apparent discrepancy between the normal sound sensitivity and the poor speech perception and ABRs in human patients: while few spikes from individual SGNs with normal thresholds may suffice for tone detection, the combination of reduced spike rates and higher jitter of action potential firing at sound onset can cause a dramatic reduction in ABR wave I amplitude, as also observed in other mutants with impaired synaptic sound encoding (Buran *et al*, 2010). In response to constant or repetitive stimuli, $Otof^{I515T/I515T}$ SGNs display markedly enhanced adaptation and slowed recovery from adaptation. This is consistent with the finding that patients with otoferlin deficiency show auditory fatigue when challenged with continuous sounds (Wynne *et al*, 2013). In contrast, none of the patient reports mention tinnitus as an additional symptom. We thus consider it unlikely that impairment of the perception of silent gaps in noise in our mice is due to tinnitus (Turner *et al*, 2006). Instead, it is likely explained by the combination of the reduction of adapted spike rates and the delayed recovery of the sound onset response. The resulting deficit in the encoding of fast fluctuations in sound envelope structure seems well consistent with the speech comprehension difficulties experienced by human patients which obviously cannot be restored by sound amplification using traditional hearing aids. Our data suggests that a more promising approach would be to devise a new speech processing strategy that aims to compensate for the increased adaptation. Clinicians should expect ABR latencies to be close to normal (Fig EV1B) and late ABR waves to be better preserved than wave I, suggesting partial compensation in the auditory brainstem. Finally, we suggest that tests for sound adaptation and temporal coding (e.g. gap detection) should be more generally applied in clinical settings to detect deficits that are independent of sound sensitivity.

# Materials and Methods

## Mouse genetics

$Otof^{I515T/I515T}$ mice were generated by targeted mutagenesis of a genomic vector and homologous recombination in mouse embryonic stem cells (see Appendix Supplementary Methods for details).

## Immunohistochemistry and quantification of fluorescence

Immunostaining and confocal fluorescence microscopy was performed essentially as described (Khimich *et al*, 2005) and detailed in Appendix Supplementary Methods.

For quantification of otoferlin and Vglut3 immunofluorescence, same experimental settings were used for each series. Using a *Matlab* routine implemented in *Imaris*, the cells were aligned in the xy- and yz-plane and the outer border of each cell was labelled manually in a 3D projection. Summed fluorescence intensities in voxels above or below the mid-nuclear plane were used for calculating the ratio of apical/basal fluorescence. Quantification of relative otoferlin membrane staining was performed after normalization of total cellular fluorescence levels and is illustrated in Fig 1D–F and was normalized to $Otof^{+/+}$ values (at 37°C if applicable).

## Pre-embedding immunogold labelling

Anti-otoferlin (Abcam, 1:300) and anti-Vglut3 (Synaptic Systems, 1:300) antibodies were applied after fixation and permeabilization with either saponin (Fig 7A–F, I and J) or Triton X-100 (Fig 7G and H). Silver enhancement was used prior to sample embedding, as described in Appendix Supplementary Methods.

**Patch clamp recordings**

IHCs from the apical coils of freshly dissected organs of Corti were patch-clamped in the perforated-patch configuration as described (Moser & Beutner, 2000). Experiments at elevated temperature and flash photolysis were performed as described (Beutner *et al*, 2001; Nouvian, 2007; respectively). For details, see Appendix Supplementary Methods.

**Systems physiology and behaviour**

ABRs, DPOAE and recordings from individual SGNs were performed as described (Jing *et al*, 2013), except for offline action potential detection which was based on spike waveform and amplitude using a custom-written *Matlab* routine (see Appendix Supplementary Methods for details). For ABR recordings with local temperature changes, ABRs in response to click stimuli at 60, 80 and 100 dB were measured using a custom-written *Matlab* routine controlling TDT system III (Tucker Davis Technologies) and a JBL 2402 speaker. A custom-designed heat probe (Appendix Fig S2A) was placed on the bony wall of the mouse bulla. The local temperature of the heat probe was constantly monitored, same for two miniaturized thermo-probes (H*MT, Newport Omega, Deckenpfronn) placed on the promontory wall within the bulla and in the mouth or in the cerebellum (accessed through a small hole in the occipital bone). Operant conditioning in the "Audiobox" was carried out essentially as described (de Hoz & Nelken, 2014), and startle responses were recorded and quantified as detailed in Appendix Supplementary Methods.

**Electron microscopy and electron tomography**

Organs of Corti (P14) were explanted in HEPES-Hanks solution and incubated for 1 min 45 s in pre-warmed $Ca^{2+}$ free saline (5 mM $K^+$, 0 $Ca^{2+}$ and 5 mM EGTA; inhibitory condition) or in a solution containing 40 mM $K^+$ and 1.3 mM $Ca^{2+}$ (stimulatory condition). Samples were fixed and prepared as described (Wong *et al*, 2014) and detailed in Appendix Supplementary Methods. For random section analysis, electron micrographs were acquired with transmission electron microscope (JEM-1011, 80 kV). For the 3D analysis, the semi-thin sections (250 nm) were imaged with JEM-2100 transmission electron microscope at 200 kV. Tomograms were reconstructed and analysed using *IMOD* package (bio3d.colorado.edu/imod/) and *ImageJ*. For details, see Appendix Supplementary Methods.

**Molecular biology**

Quantitative PCR, subcloning of full-length otoferlin cDNA from mouse organs of Corti and mutagenesis thereafter are described in Appendix Supplementary Methods, as transfection of IHCs or HEK cells and mass spectrometric quantification of otoferlin protein levels.

**Statistics**

The data were analysed using *Matlab* (Mathworks), *Microsoft Access* and *Excel*, the *Igor Pro 6* software package (WaveMetrics), *Origin 6.0*

(Microcal Software) and *GraphPad Prism*. Averaged data are expressed as mean ± SEM unless otherwise specified. Normality was assessed using Jarque–Bera test for sample size of $n \geq 7$ and by Kolmogorov—Smirnov test for $n < 7$. For normally distributed samples, significance was tested using the unpaired, two-tailed Student's *t*-test, others with Mann–Whitney *U*-test, unless stated otherwise. Statistical significance of fluorescence immunohistochemistry and EM analysis was calculated by one-way ANOVA followed by Tukey–Newman–Keuls test for parametric and Kruskal–Wallis test followed by non-parametric multiple comparisons (NPMC).

**Study approval**

Animal handling and experiments complied with national animal care guidelines and were approved by the University of Goettingen Board for animal welfare and the animal welfare office of the state of Lower Saxony.

**Expanded View** for this article is available online.

## Author contributions

ER, NS and CW designed research; GH developed hard- and software; NS, RC, HA-M, ER, AM, TP, KTP and CL analysed data; NS, ER, RC, HA-M, AM, GY, CL, EA, TP and CW performed experiments; ER, NS, CW, RC, CL, AM, HA-M, TP and NB wrote and edited the manuscript; NS, ER, HA-M and RC prepared figures; ER, CW, NS, HU, NB and RG-F supervised research; ER and NS managed and coordinated the study; and NS, ER, CW, HU, RG-F and NB acquired funding.

## Conflict of interest

The authors declare that they have no conflict of interest.

# References

Beutner D, Voets T, Neher E, Moser T (2001) Calcium dependence of exocytosis and endocytosis at the cochlear inner hair cell afferent synapse. *Neuron* 29: 681–690

Buran BN, Strenzke N, Neef A, Gundelfinger ED, Moser T, Liberman MC (2010) Onset coding is degraded in auditory nerve fibers from mutant mice lacking synaptic ribbons. *J Neurosci Off J Soc Neurosci* 30: 7587–7597

Chapochnikov NM, Takago H, Huang C-H, Pangršič T, Khimich D, Neef J, Auge E, Göttfert F, Hell SW, Wichmann C, Wolf F, Moser T (2014) Uniquantal

release through a dynamic fusion pore is a candidate mechanism of hair cell exocytosis. *Neuron* 17: 1389–1403

Chiu Y-H, Wu C-C, Lu Y-C, Chen P-J, Lee W-Y, Liu AY-Z, Hsu C-J (2010) Mutations in the OTOF gene in Taiwanese patients with auditory neuropathy. *Audiol Neurootol* 15: 364–374

Duncker SV, Franz C, Kuhn S, Schulte U, Campanelli D, Brandt N, Hirt B, Fakler B, Blin N, Ruth P, Engel J, Marcotti W, Zimmermann U, Knipper M (2013) Otoferlin couples to clathrin-mediated endocytosis in mature cochlear inner hair cells. *J Neurosci* 33: 9508–9519

Filipeanu CM, de Vries R, Danser AHJ, Kapusta DR (2011) Modulation of α2C adrenergic receptor temperature-sensitive trafficking by HSP90. *Biochim Biophys Acta* 1813: 346–357

Filipeanu CM, Pullikuth AK, Guidry JJ (2015) Molecular determinants of the human α2C-adrenergic receptor temperature-sensitive intracellular traffic. *Mol Pharmacol* 87: 792–802

Fuchs PA, Glowatzki E, Moser T (2003) The afferent synapse of cochlear hair cells. *Curr Opin Neurobiol* 13: 452–458

Glowatzki E, Fuchs PA (2002) Transmitter release at the hair cell ribbon synapse. *Nat Neurosci* 5: 147–154

Graydon CW, Cho S, Li G-L, Kachar B, von Gersdorff H (2011) Sharp Ca$^{2+}$ nanodomains beneath the ribbon promote highly synchronous multivesicular release at hair cell synapses. *J Neurosci* 31: 16637–16650

de Hoz L, Nelken I (2014) Frequency tuning in the behaving mouse: different bandwidths for discrimination and generalization. *PLoS ONE* 9: e91676

Jing Z, Rutherford MA, Takago H, Frank T, Fejtova A, Khimich D, Moser T, Strenzke N (2013) Disruption of the presynaptic cytomatrix protein bassoon degrades ribbon anchorage, multiquantal release, and sound encoding at the hair cell afferent synapse. *J Neurosci* 33: 4456–4467

Johnson CP, Chapman ER (2010) Otoferlin is a calcium sensor that directly regulates SNARE-mediated membrane fusion. *J Cell Biol* 191: 187–197

Jung S, Maritzen T, Wichmann C, Jing Z, Neef A, Revelo NH, Al-Moyed H, Meese S, Wojcik SM, Panou I, Bulut H, Schu P, Ficner R, Reisinger E, Rizzoli SO, Neef J, Strenzke N, Haucke V, Moser T (2015) Disruption of adaptor protein 2μ (AP-2μ) in cochlear hair cells impairs vesicle reloading of synaptic release sites and hearing. *EMBO J* 34: 2686–2702

Khimich D, Nouvian R, Pujol R, tom Dieck S, Egner A, Gundelfinger ED, Moser T (2005) Hair cell synaptic ribbons are essential for synchronous auditory signalling. *Nature* 434: 889–894

Longo-Guess C, Gagnon LH, Bergstrom DE, Johnson KR (2007) A missense mutation in the conserved C2B domain of otoferlin causes deafness in a new mouse model of DFNB9. *Hear Res* 234: 21–28

Marlin S, Feldmann D, Nguyen Y, Rouillon I, Loundon N, Jonard L, Bonnet C, Couderc R, Garabedian EN, Petit C, Denoyelle F (2010) Temperature-sensitive auditory neuropathy associated with an otoferlin mutation: deafening fever!. *Biochem Biophys Res Commun* 394: 737–742

Matsunaga T, Mutai H, Kunishima S, Namba K, Morimoto N, Shinjo Y, Arimoto Y, Kataoka Y, Shintani T, Morita N, Sugiuchi T, Masuda S, Nakano A, Taiji H, Kaga K (2012) A prevalent founder mutation and genotype–phenotype correlations of OTOF in Japanese patients with auditory neuropathy. *Clin Genet* 82: 425–432

Moser T, Beutner D (2000) Kinetics of exocytosis and endocytosis at the cochlear inner hair cell afferent synapse of the mouse. *Proc Natl Acad Sci USA* 97: 883–888

Neef A, Khimich D, Pirih P, Riedel D, Wolf F, Moser T (2007) Probing the mechanism of exocytosis at the hair cell ribbon synapse. *J Neurosci* 27: 12933–12944

Nouvian R (2007) Temperature enhances exocytosis efficiency at the mouse inner hair cell ribbon synapse. *J Physiol* 584: 535–542

Pangrsic T, Lasarow L, Reuter K, Takago H, Schwander M, Riedel D, Frank T, Tarantino LM, Bailey JS, Strenzke N, Brose N, Müller U, Reisinger E, Moser T (2010) Hearing requires otoferlin-dependent efficient replenishment of synaptic vesicles in hair cells. *Nat Neurosci* 13: 869–876

Pangršič T, Reisinger E, Moser T (2012) Otoferlin: a multi-C2 domain protein essential for hearing. *Trends Neurosci* 35: 671–680

Radziwon KE, June KM, Stolzberg DJ, Xu-Friedman MA, Salvi RJ, Dent ML (2009) Behaviorally measured audiograms and gap detection thresholds in CBA/CaJ mice. *J Comp Physiol A Neuroethol Sens Neural Behav Physiol* 195: 961–969

Reisinger E, Bresee C, Neef J, Nair R, Reuter K, Bulankina A, Nouvian R, Koch M, Bückers J, Kastrup L, Roux I, Petit C, Hell SW, Brose N, Rhee J-S, Kügler S, Brigande JV, Moser T (2011) Probing the functional equivalence of otoferlin and synaptotagmin 1 in exocytosis. *J Neurosci Off J Soc Neurosci* 31: 4886–4895

Revelo NH, Kamin D, Truckenbrodt S, Wong AB, Reuter-Jessen K, Reisinger E, Moser T, Rizzoli SO (2014) A new probe for super-resolution imaging of membranes elucidates trafficking pathways. *J Cell Biol* 205: 591–606

Romanos J, Kimura L, Fávero ML, Izarra FAR, de Mello Auricchio MTB, Batissoco AC, Lezirovitz K, Abreu-Silva RS, Mingroni-Netto RC (2009) Novel OTOF mutations in Brazilian patients with auditory neuropathy. *J Hum Genet* 54: 382–385

Roux I, Safieddine S, Nouvian R, Grati M, Simmler M-C, Bahloul A, Perfettini I, Le Gall M, Rostaing P, Hamard G, Triller A, Avan P, Moser T, Petit C (2006) Otoferlin, defective in a human deafness form, is essential for exocytosis at the auditory ribbon synapse. *Cell* 127: 277–289

Rutherford MA, Chapochnikov NM, Moser T (2012) Spike encoding of neurotransmitter release timing by spiral ganglion neurons of the cochlea. *J Neurosci* 32: 4773–4789

Schwander M, Sczaniecka A, Grillet N, Bailey JS, Avenarius M, Najmabadi H, Steffy BM, Federe GC, Lagler EA, Banan R, Hice R, Grabowski-Boase L, Keithley EM, Ryan AF, Housley GD, Wiltshire T, Smith RJH, Tarantino LM, Müller U (2007) A forward genetics screen in mice identifies recessive deafness traits and reveals that pejvakin is essential for outer hair cell function. *J Neurosci* 27: 2163–2175

Siegel JH, Dallos P (1986) Spike activity recorded from the organ of Corti. *Hear Res* 22: 245–248

Starr A, Sininger Y, Winter M, Derebery MJ, Oba S, Michalewski HJ (1998) Transient deafness due to temperature-sensitive auditory neuropathy. *Ear Hear* 19: 169–179

Turner JG, Brozoski TJ, Bauer CA, Parrish JL, Myers K, Hughes LF, Caspary DM (2006) Gap detection deficits in rats with tinnitus: a potential novel screening tool. *Behav Neurosci* 120: 188–195

Varga R, Kelley PM, Keats BJ, Starr A, Leal SM, Cohn E, Kimberling WJ (2003) Non-syndromic recessive auditory neuropathy is the result of mutations in the otoferlin (OTOF) gene. *J Med Genet* 40: 45–50

Varga R, Avenarius MR, Kelley PM, Keats BJ, Berlin CI, Hood LJ, Morlet TG, Brashears SM, Starr A, Cohn ES, Smith RJH, Kimberling WJ (2006) OTOF mutations revealed by genetic analysis of hearing loss families including a potential temperature sensitive auditory neuropathy allele. *J Med Genet* 43: 576–581

Vogl C, Cooper BH, Neef J, Wojcik SM, Reim K, Reisinger E, Brose N, Rhee J-S, Moser T, Wichmann C (2015) Unconventional molecular regulation of synaptic vesicle replenishment in cochlear inner hair cells. *J Cell Sci* 128: 638–644

Wang D-Y, Wang Y-C, Weil D, Zhao Y-L, Rao S-Q, Zong L, Ji Y-B, Liu Q, Li J-Q, Yang H-M, Shen Y, Benedict-Alderfer C, Zheng Q-Y, Petit C, Wang Q-J (2010) Screening mutations of OTOF gene in Chinese patients with auditory neuropathy, including a familial case of temperature-sensitive auditory neuropathy. *BMC Med Genet* 11: 79

Wong AB, Rutherford MA, Gabrielaitis M, Pangršič T, Göttfert F, Frank T, Michanski S, Hell S, Wolf F, Wichmann C, Moser T (2014) Developmental refinement of hair cell synapses tightens the coupling of Ca$^{2+}$ influx to exocytosis. *EMBO J* 33: 247−264

Wynne DP, Zeng F-G, Bhatt S, Michalewski HJ, Dimitrijevic A, Starr A (2013) Loudness adaptation accompanying ribbon synapse and auditory nerve disorders. *Brain J Neurol* 136: 1626−1638

Yasunaga S, Grati M, Cohen-Salmon M, El-Amraoui A, Mustapha M, Salem N, El-Zir E, Loiselet J, Petit C (1999) A mutation in OTOF, encoding otoferlin, a FER-1-like protein, causes DFNB9, a nonsyndromic form of deafness. *Nat Genet* 21: 363−369

Yildirim-Baylan M, Bademci G, Duman D, Ozturkmen-Akay H, Tokgoz-Yilmaz S, Tekin M (2014) Evidence for genotype-phenotype correlation for OTOF mutations. *Int J Pediatr Otorhinolaryngol* 78: 950−953

# Expanded View Figures
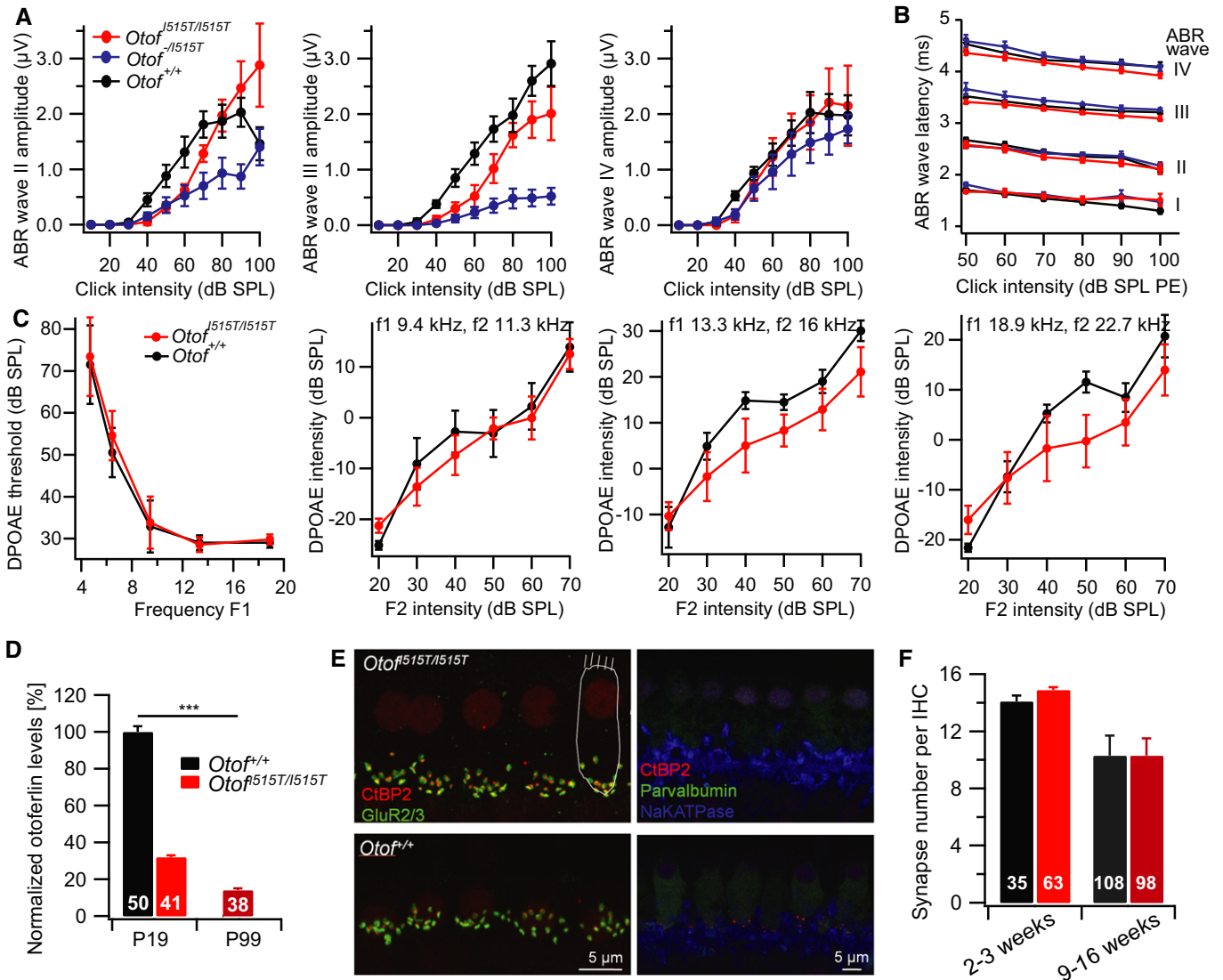


**Figure EV1. Partial central compensation of ABR wave I amplitude reduction, otoferlin protein levels during ageing and intact cochlear amplification.**

A   Amplitude growth of ABR waves II–IV with rising stimulus intensity to click stimulation in $Otof^{I515T/I515T}$ (red, $n = 5$), $Otof^{-/I515T}$ (blue, $n = 6$) and $Otof^{+/+}$ (black, $n = 5$) animals tested at an age of 3–4 weeks, indicating a severe deficit of synchronous spiral ganglion neuron activation in $Otof$ mutants but partial compensation in the auditory brainstem (mean ± SEM).

B   Latencies of ABR waves I–IV from the same data set.

C   Left: Interpolated DPOAE thresholds determined as the F1 intensity at which DPOAE intensity reached −10 dB SPL are comparable between $Otof^{I515T/I515T}$ (red) and $Otof^{+/+}$ (black) mice. Right: Amplitude growth of DPOAE in response to pairs of sine waves (frequencies indicated above each panel) at rising intensities. F1 intensity was always 10 dB above F2 intensity.

D   Otoferlin protein levels were even further reduced during ageing in $Otof^{I515T/I515T}$ IHCs, explaining the age-dependent decrease in ABR amplitudes. Numbers indicate number of IHCs analysed (Tukey–Newman–Keuls test for parametric multiple comparisons; ***$P < 0.001$).

E   Representative images used for synapse counting in $Otof^{I515T/I515T}$ (top) and $Otof^{+/+}$ (bottom) IHCs. For 2- to 3-week-old mice (left), z-projections of confocal stacks stained for ribbons (CtBP2, red) and postsynaptic glutamate receptors (GluR2/3, green) are shown. For 9- to 16-week-old mice (right), single sections of IHCs imaged in z-stacks, stained for ribbons (CtBP2, red), the cytoplasmatic calcium buffer parvalbumin (green) and SGNs stained for Na/K-ATPase (blue) are shown.

F   Quantification of synapses; numbers indicate the number of IHCs analysed; mean ± SEM.
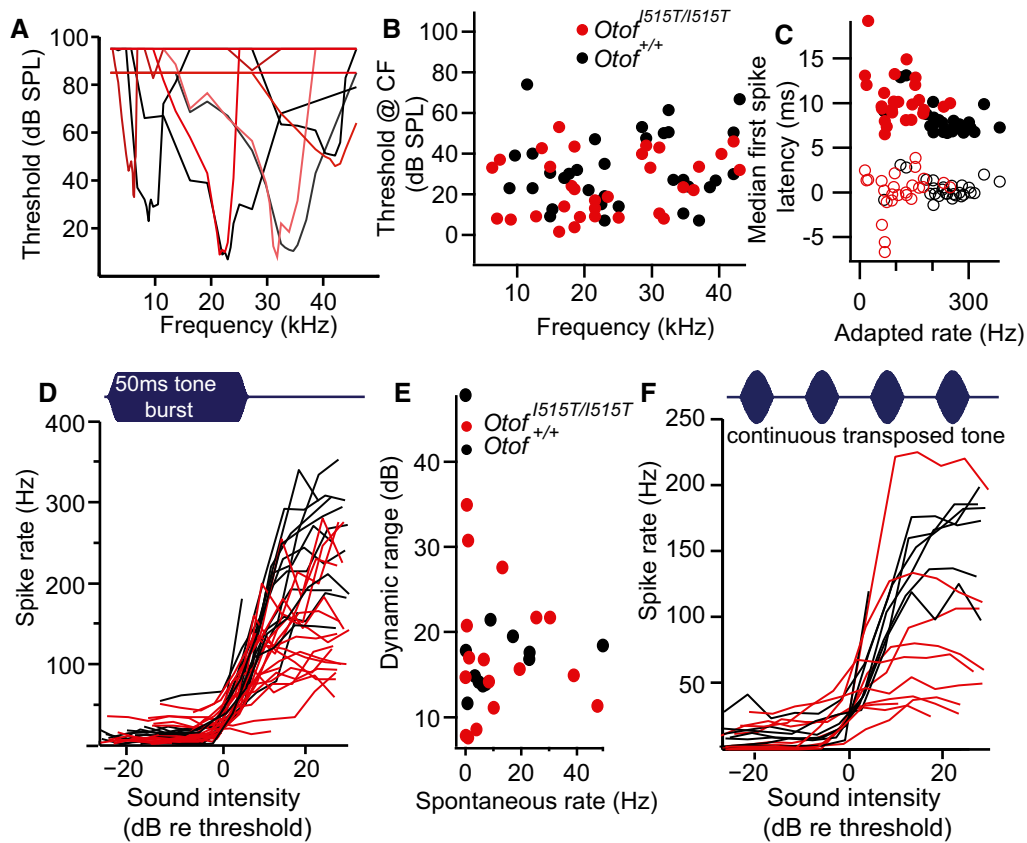
**Figure EV2.  Single SGN responses show normal frequency tuning and thresholds, but abnormalities of latencies and spike rates.**

A    Representative examples of SGN tuning curves from *Otof*$^{I515T/I515T}$ (pink/red) and *Otof*$^{+/+}$ (grey/black) mice.

B    Thresholds at CF were comparable in *Otof*$^{I515T/I515T}$ (red) and *Otof*$^{+/+}$ (black) SGNs.

C    The median first spike latency (FSL) in response to 200 repetitions of tone bursts at CF, 30 dB above threshold at a stimulus rate of 5 Hz was significantly prolonged in *Otof*$^{I515T/I515T}$ (red closed circles) and *Otof*$^{+/+}$ (black closed circles) (*P* = 0.0003, *t*-test). However, when the expected median FSL for the respective onset spike rate was subtracted (open symbols), FSLs were normal. The expected median FSL was calculated by the following formula which was derived from a large population of wild-type SGNs: $-2.5 \times \log(\text{onset rate}) + 20.23$. All FSL estimates were first corrected for the system delay (3.6 ms), for the time of the 4 ms tone burst ramp to reach fibre threshold and for the travelling wave delay (up to 0.8 ms according to our wild-type data set).

D    Spike rate increases in individual *Otof*$^{I515T/I515T}$ (red) SGNs in response to tone burst stimulation at CF and varying intensities were shallower than in *Otof*$^{+/+}$ (black) SGNs. The sound intensity refers to the threshold of each SGN, defined by a spike rate increase of 20 Hz over spontaneous rate.

E    Their dynamic range (the range of intensities over which the spike rate increased from 10% to 90% of the evoked rate) was normal.

F    Spike rate increases in individual *Otof*$^{I515T/I515T}$ (red) SGNs in response to continuous presentation of amplitude-modulated sounds (CF, varying intensities, referenced to threshold like in D, modulation frequency 500 Hz) were much shallower than in *Otof*$^{+/+}$ (black) SGNs.
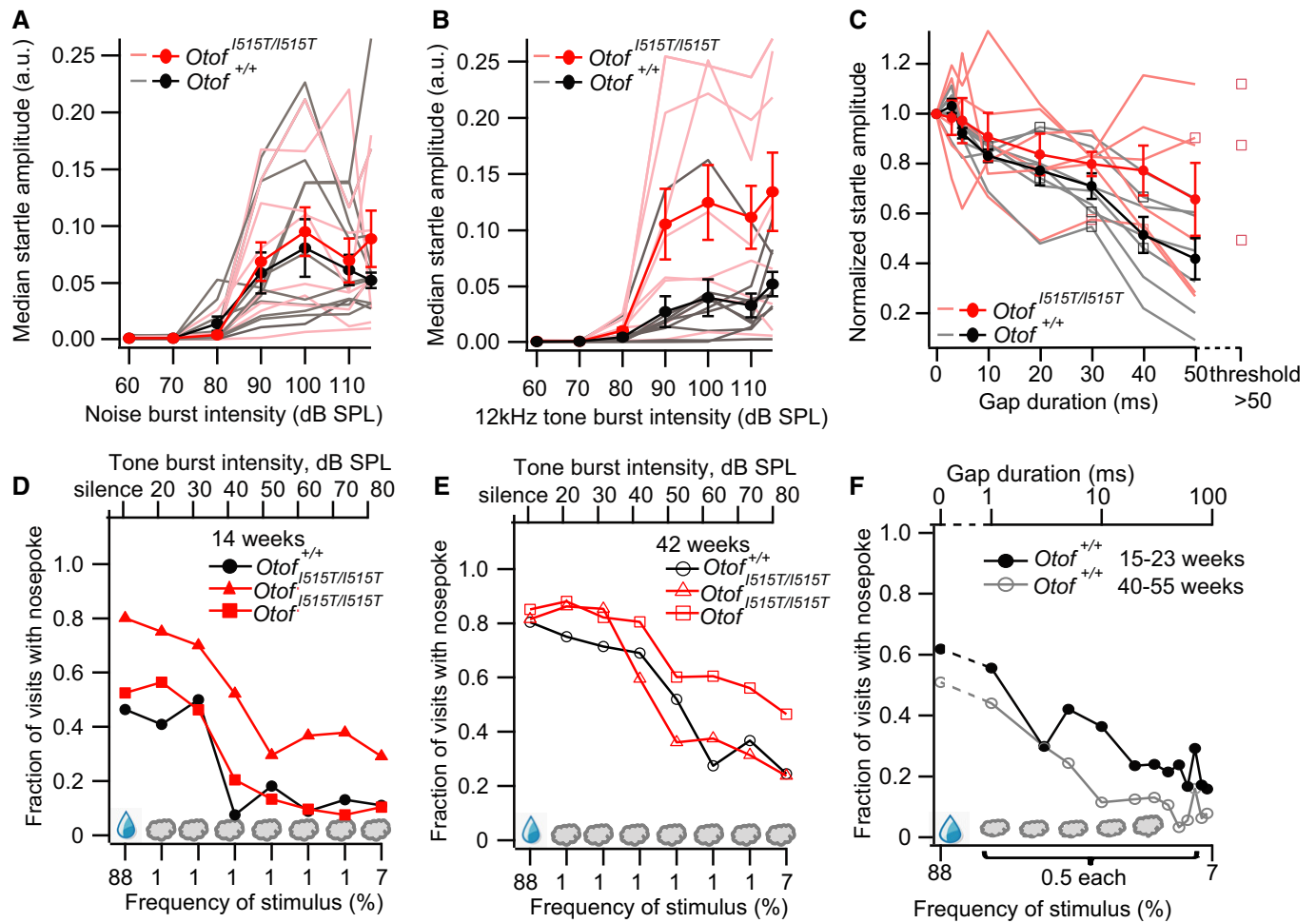
**Figure EV3. Hearing impairment was assessed by startle responses and operant conditioning of mice.**

A, B Acoustic startle responses to stimulation with 10 ms noise (A) or 12 kHz tone (B) bursts in *Otof*$^{I515T/I515T}$ (10 individuals pink, mean ± SEM red) and *Otof*$^{+/+}$ (9 individuals grey, mean ± SEM black) animals backcrossed to a CBA/J strain background.

C   Prepulse inhibition of the startle response induced by silent gaps of varying duration was stronger in wild-type (eight individuals grey, mean ± SEM black) than in *Otof*$^{I515T/I515T}$ mice (eight individuals pink, mean ± SEM red). Gap detection thresholds were determined as the minimal duration of silent gaps in 70 dB background noise that were effective in significantly attenuating the amplitude of startle response elicited by 115 dB 12 kHz tone bursts (Mann–Whitney *U*-test followed by Bonferroni correction). Gap thresholds (squares) were elevated in *Otof*$^{I515T/I515T}$ mice (*P* = 0.04, Mann–Whitney *U*-test). In the control condition (no gap), the mean median startle amplitude for *Otof*$^{I515T/I515T}$ (0.07 ± 0.02) was identical to *Otof*$^{+/+}$ (0.07 ± 0.02; *P* = 0.99, *t*-test).

D   Two *Otof*$^{I515T/I515T}$ mice (red) and one *Otof*$^{+/+}$ mouse (black) learned to avoid drinking when they heard 12 kHz tone burst stimuli (400 ms, 3 Hz stimulus rate, 80 dB) during their visits to the soundproof corner of the "IntelliCage" operant conditioning system and drank water only when they did not perceive sounds. All three mice reacted to stimuli at 20 and 30 dB like for silence and for stimuli above 30 dB like for 80 dB, indicating comparable hearing thresholds near 35 dB for all three mice at the age of 14–21 weeks.

E   Subjective hearing thresholds in the same mice from (D) increased by approximately 5–15 dB when the mice were retested at an age of 42–53 weeks.

F   Behavioural gap detection did not show clear age-related changes in a wild-type mouse tested at 15–23 and 40–55 weeks.

**A**

```
human_e    163  PGEKSFR--------------RAGRSVFSAMKLGKNRSHKEEPQRPDEPAVLEMED  204
bos        163  SGEKSFR--------------RAGRSVFSAMKLGKNRPHKEEPQRQDEPAVLEMED  204
rat        163  PGEKSFR--------------RAGRSVFSAMKLGKTRSHKEEPQRQDEPAVLEMED  204
mouse var2 162  SGEKSFR--------------RAGRSVFSAMKLGKTRSHKEEPQRQDEPAVLEMED  203
mouse var4 162  SGEKSFR--------------RAGRSVFSAMKLGKTRSHKEEPQRQDEPAVLEMED  203
mouse var1 162  SGEKSFRSKGREKTKGGRDGEHKAGRSVFSAMKLGKTRSHKEEPQRQDEPAVLEMED  218
Xenopus    173  SGERAFK--------------RVGKGVFSAMKLGKTRPPKDESRKQDEPAVLETED  215
                .**::*:              :.*:.*********.*  *:* :: ******* **
```

**B**

```
human_e    1234  PDRSAPSWNTTVRLLRRCRVLCNGGSSSHSTGEVVVTMEPEVPIKKLETMVKLD  1287
human_b     487  PDRSAPSWNT-------------------TGEVVVTMEPEVPIKKLETMVKLD   520
bos        1234  PDRSAPNWNTSGRLLQGRRGLYSGGPSSRLTGEVVVSMEPEVPIKKLETMVKLD  1287
rat        1234  PDRSAANWNTTVRLLRGYHMLCNGGPSSCPTGEVVVSMEPEVPVKKLETLVKLD  1287
mouse var2 1233  PDRSAPNWNTTVRLLRGCHRLRNGGPSSRPTGEVVVSMEPEEPVKKLETMVKLD  1286
mouse var4 1233  PDRSAPNWNT-------------------TGEVVVSMEPEEPVKKLETMVKLD  1266
mouse var1 1248  PDRSAPNWNT-------------------TGEVVVSMEPEEPVKKLETMVKLD  1281
Xenopus    1246  PDKNSQQWTTAAKLMNGYLAMTNGRPRSRTTGEIVINMEPEAPVKKMETMVKLE  1299
                 **:.: .*.*                   ***:*:.**** *:**:**:***:
```

**C**



**Figure EV4.    Sequence variations in mouse and human otoferlin and comparison with other species.**

A  CLUSTAL Omega multiple sequence alignment for otoferlin homologues performed with the following sequences: Human otoferlin isoform e, NP_001274418.1; *Bos Taurus*, NP_001137579.1; *Rattus norvegicus*, NP_001263649; *Mus musculus* transcript variant 4, NM_001313767.1 (cDNA used in our experiments); *Mus musculus* transcript variant 1, NP_001093865.1; *Mus musculus* transcript variant 2, NP_114081.2; *Xenopus tropicalis*, XP_012826776.1. The presence of the 15 amino acid stretch SKG...GEH was tested in a PCR in (C).

B  Sequence alignment, also including human otoferlin isoform b, NP_004793. Focus on the amino acid region between $C_2D$ and $C_2E$ bearing an arginine-rich sequence in human otoferlin isoform e, including an RXR motif (in red). Labelled in yellow is the human sequence that was introduced by site-directed mutagenesis into the mouse variant 4 for experiments in Fig 5.

C  A PCR on mouse organ of Corti cDNA from P14 animals was performed to test for the expression of the mouse sequence variations. Left lane: using the primers AAGGACAGCCAGGAGACAGA and ATCTTGTCTTTGGGGCTCCT that bind before and after amino acid 168 in mouse variant 4 was used to distinguish between splice variants. For transcript variants 2 and 4, an amplicon of 155 bp was expected, whereas variant 1 should give rise to a 200-bp amplicon. The PCR indicates that almost exclusively the short variant is transcribed. Right lane: using primers TCATCTACCGACCTCCAGACC and CACATCCACCTTGACCACAGC binding before and after amino acid 1242 in mouse variant 4 expected to lead to an amplicon size of 148 bp for variants 1 and 4 or 208 bp for variant 2. The strong band at 148 bp indicates that the vast majority of cDNA molecules confirmed the expression of the short variant. In conclusion, our data indicate that transcript variant 4 seems to be the predominantly transcribed otoferlin isoform in mouse organs of Corti.

# <u>Appendix</u>

**<u>Table of content</u>**

**<u>Appendix Supplementary Figures and Figure legends</u>**
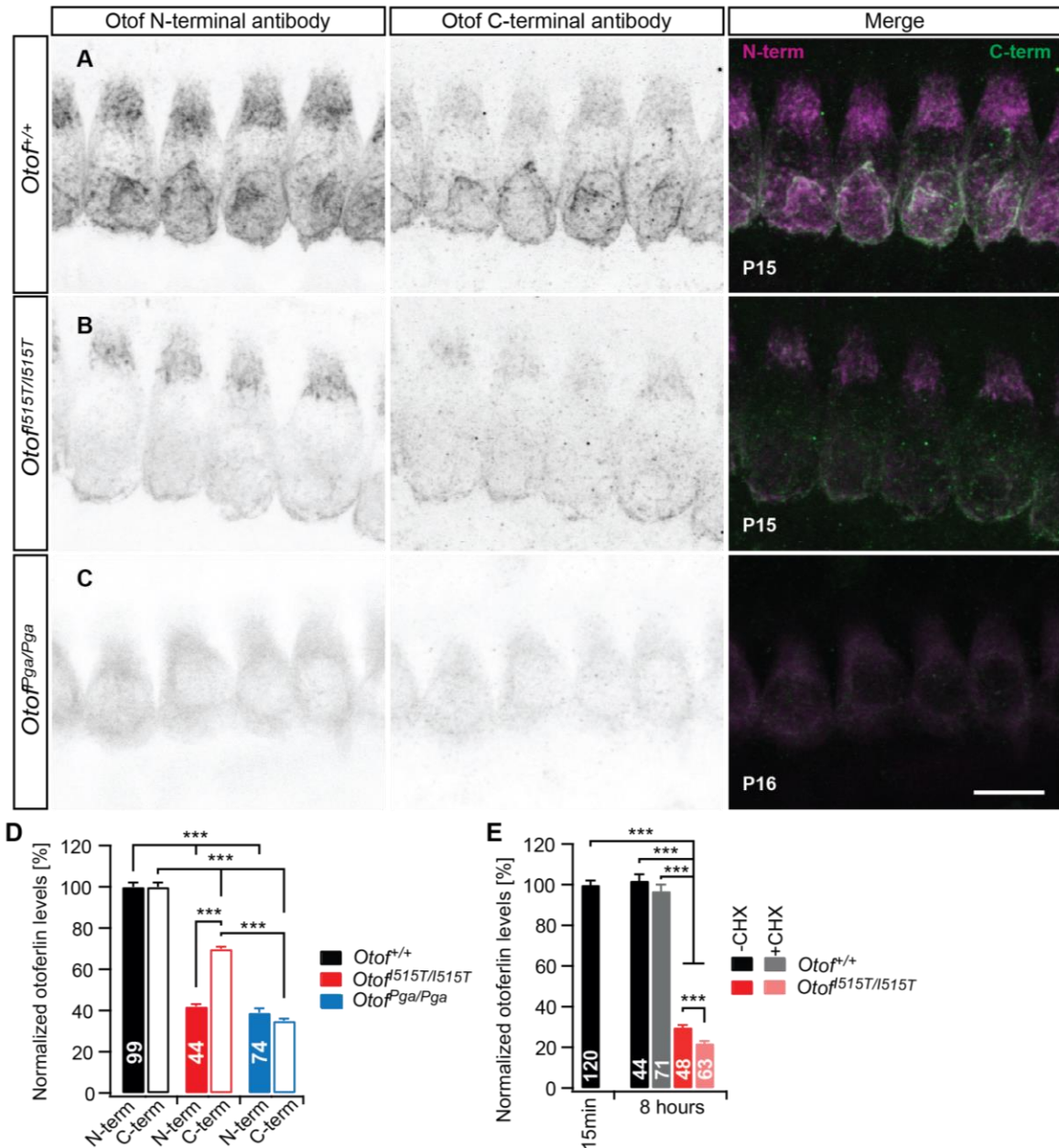
**Appendix Figure S1**
**Lower protein levels of otoferlin in $Otof^{I515T/I515T}$ and in $Otof^{Pga/Pga}$ IHCs.**
A-C, the reduction in cellular otoferlin levels were analyzed with two different anti-otoferlin antibodies: one binding an N-terminal epitope (Abcam, magenta), and one binding a very C-terminal epitope downstream of the transmembrane domain (Synaptic Systems, green). Both antibodies bind to plasma-membrane bound otoferlin in in $Otof^{+/+}$ and $Otof^{I515T/I515T}$. The N-terminal antibody displays a stronger intracellular staining than the C-terminal antibody, potentially due to binding to incompletely transcribed otoferlin fragments, and/or because the epitope of the C-terminal antibody might be less accessible. Scale bar, 10μm.
D, Quantification of otoferlin levels in P14 IHCs with the N-terminal (solid bars) and the C-terminal (open bars) antibodies both show a reduction in otoferlin levels in mutant IHCs. The stronger reduction in $Otof^{I515T/I515T}$ visualized by the N-terminal antibody might reflect a stronger decay in cytoplasmatic otoferlin while otoferlin at the plasma membrane seems better preserved (mean ± SEM, Kruskal-Wallis test).
E, protein biosynthesis was blocked by application of 50μg/ml cycloheximide (CHX) to determine protein degradation in explanted organs of Corti. In contrast to wild type otoferlin, Ile515Thr-otoferlin was significantly degraded in IHCs 8h after stop of protein biosynthesis, providing a potential reason for the chronically lower otoferlin levels in $Otof^{I515T/I515T}$ IHCs (mean ± SEM, Kruskal-Wallis test).

**Appendix Figure S2**
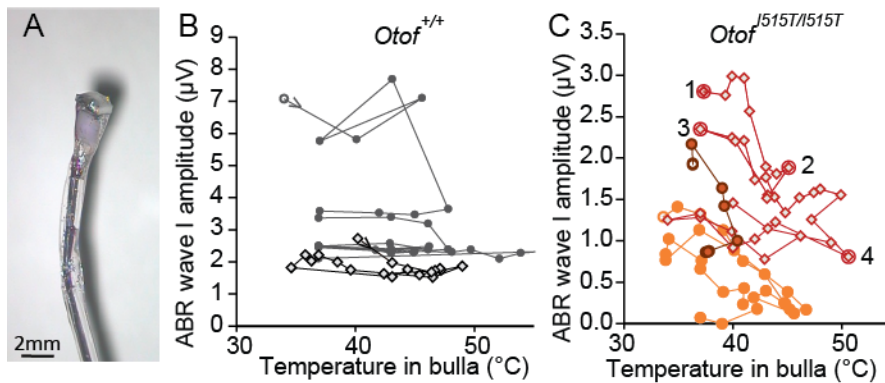


**Appendix Figure S2**

**Temporary and permanent reductions of ABR amplitudes upon local heating**

A, Custom-designed heat probe to be placed on the bulla during mouse ABR recordings: a small resistor and a temperature sensor were positioned on a glass capillary and embedded in heat-resistant glue. B, C, In a subset of the experiments partly shown Figure 5 B/C (same colors), ABR amplitudes remained irreversibly low after excessive heating.

**Appendix Figure S3**
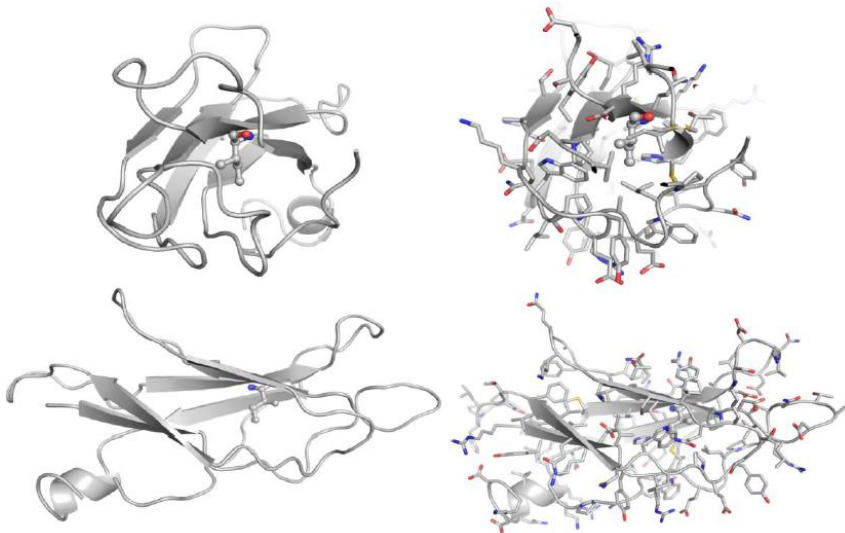


**Appendix Figure S3**

**The residue of isoleucine 515 is predicted to point towards the hydrophobic core of the $C_2C$ domain.**

Ile515 is depicted as ball and stick model within the $C_2C$ domain; two different perspectives without (left) and with (right) amino acid side chains. Homology modeling of $C_2C$ domain has been performed with Rosetta (Raman *et al*, 2009) package using the structure of a $C_2$ domain of a regulating synaptic membrane exocytosis protein 2 (PDB id: 2BWQ) as the template. The template has been identified using HHPRED search server (Söding *et al*, 2005) and shares with the target sequence 24% and 52.6% of sequence identity and similarity, respectively. The hydrophobic core has a strong contribution to the thermal stability of a protein domain due to the aggregation of the non-polar side chains in the interior of the protein. This favors the increase in entropy of the solvent molecules and decreases the conformational flexibility of the folded relative to the unfolded protein. Introducing the Ile515Thr mutation is suggested to result in an unfavorable placement and burial of the polar group in the hydrophobic core of the protein which likely decreases the protein stability. Models and images were kindly provided by Piotr Neumann, University of Goettingen.

**Appendix Figure S4**
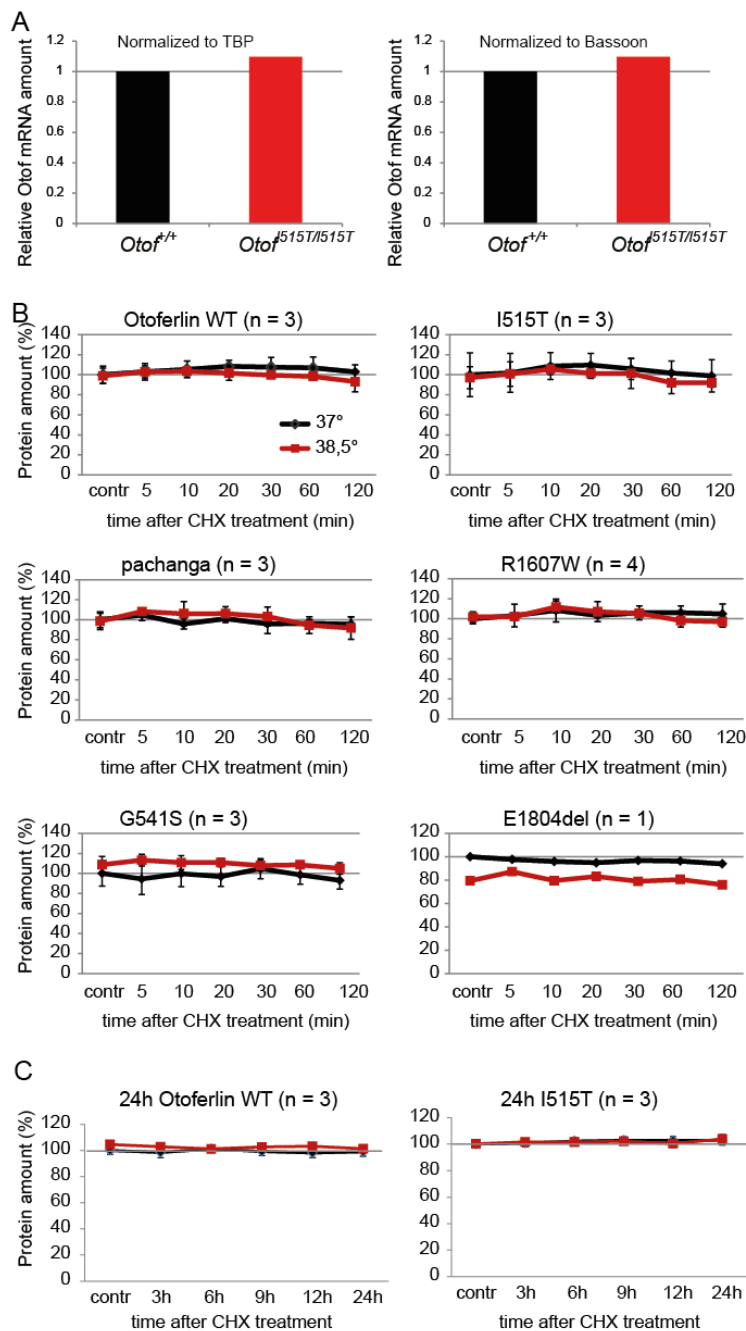
**Appendix Figure S4**
**No differences in mRNA expression levels and no fast degradation of mutated otoferlin in HEK cells.**
A, Quantitative PCR reveals no difference in expression levels of otoferlin mRNA in $Otof^{I515T/I515T}$ or $Otof^{+/+}$ organs of Corti. Otoferlin transcripts were quantified by a taqman based real-time PCR in three cDNA samples from $Otof^{+/+}$ organs of Corti and two cDNA samples from $Otof^{I515T/I515T}$ organs of Corti, prepared as described in Appendix Supplementary Methods. Otoferlin cDNA was normalized either to Tata-binding protein (TBP), which is expressed to a similar level in each cell (left panel), or to bassoon which is expressed in IHCs and spiral ganglion neurons but not in supporting cells or other epithelial cells in the organ of Corti (right panel). The Ile515Thr mutation did not lead to lower otoferlin mRNA levels in $Otof^{I515T/I515T}$ organs of Corti.
B, Protein degradation was quantified after expression of otoferlin cDNA and cycloheximide treatment in HEK293T cells (see Appendix Supplementary Methods). Mutations were selected as they were described to cause temperature dependent hearing loss in humans (Marlin *et al*, 2010; Matsunaga *et al*, 2012; Romanos *et al*, 2009; Varga *et al*, 2006; Wang *et al*, 2010). HEK cells were incubated either at 37°C or at 38.5°C, and samples were taken at indicated time points to quantify otoferlin protein levels by means of mass spectrometry (see Appendix Supplementary Methods). N-numbers in the figure indicate biological replicates (charges of transfected HEK cells), while each of these samples was quantified in mass spectrometry in triplicates. Protein amounts were normalized to the control sample at 37°C for each construct (in graphs: normalized mean ± standard deviation). If protein de-stabilization leading to protein degradation would be a major mechanism for the hearing loss, we would expect to see differences in protein stability between mutant and wild-type protein, especially at 38.5°C. However, mutant and wild-type otoferlin protein seem to be stable within two hours under both temperature conditions tested, thereby making it unlikely that fast protein degradation is a major mechanism contributing to deafening at higher temperature. C, Protein amounts within 24h for wild type otoferlin and Ile515Thr-otoferlin indicate no visible degradation in HEK cells during cycloheximide treatment. Nevertheless, we cannot exclude that elevated temperature leads to a fast unfolding of the protein which would not be visible in our experimental setting.

**Appendix Figure S5**



Vglut3 Triton

A

A'
IHC
Aff

Otoferlin Triton

B
IHC

B'
IHC
Aff

Otoferlin Saponin

C
IHC
IHC

C'
IHC

C''
IHC
Aff

500nm

200nm
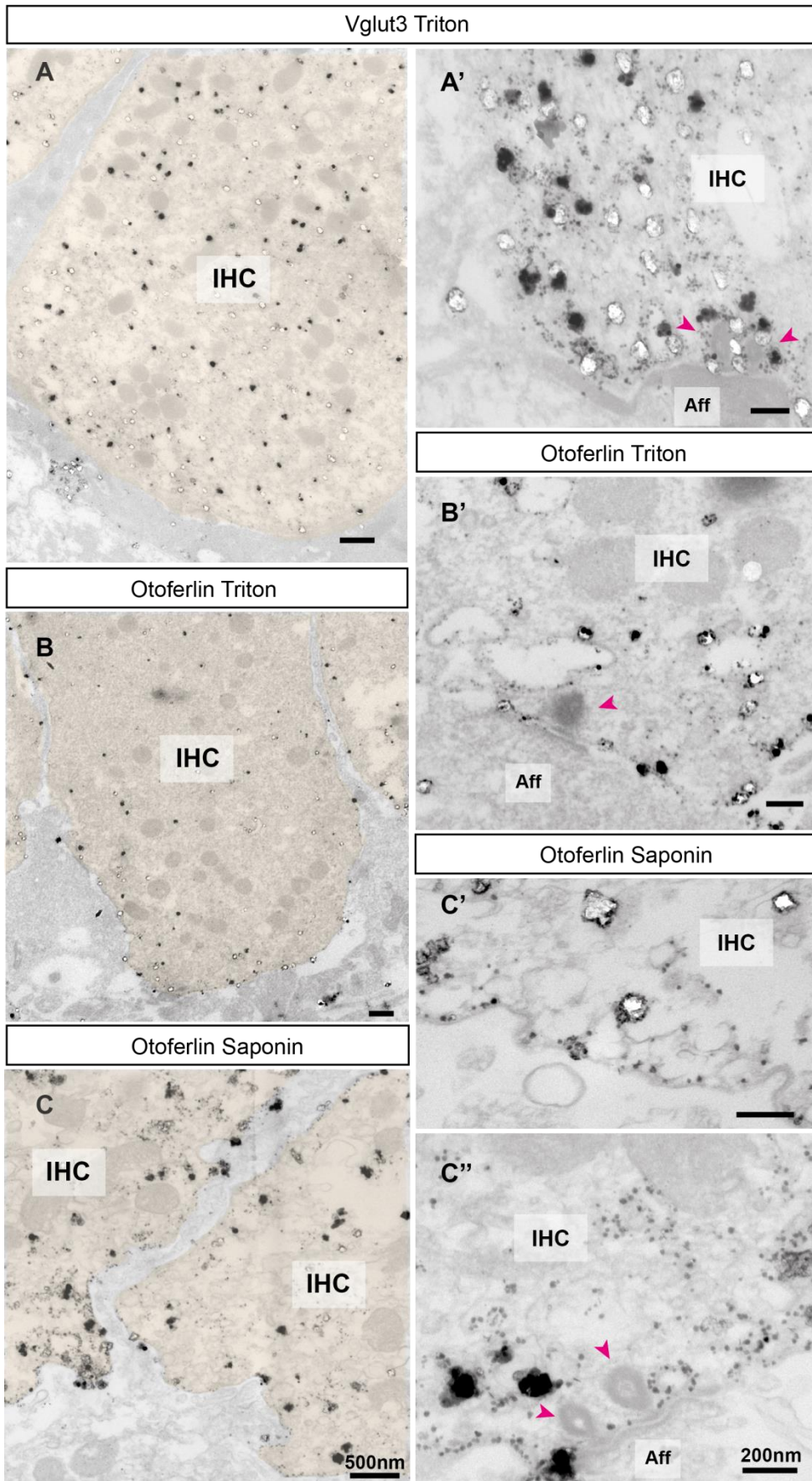
**Appendix Figure S5: Pre-embedding immunogold labeling**
A-B', Immunogold labelling of IHCs after Triton-X-100 treatment against Vglut3 (A,A') and otoferlin (B,B').
C-C'', Immunogold labelling of IHCs after Saponin treatment. A-C were processed in parallel. In both labelling
protocols otoferlin is clearly found in the plasma membrane, whereas Vglut3 staining is only found in the
cytoplasm. (Aff) Afferent bouton. Ribbons are indicated with magenta arrowheads, IHCs are highlighted in
beige. Scale bars left panel: 500 nm, scale bars right panel: 200 nm.

**Appendix Figure S6**
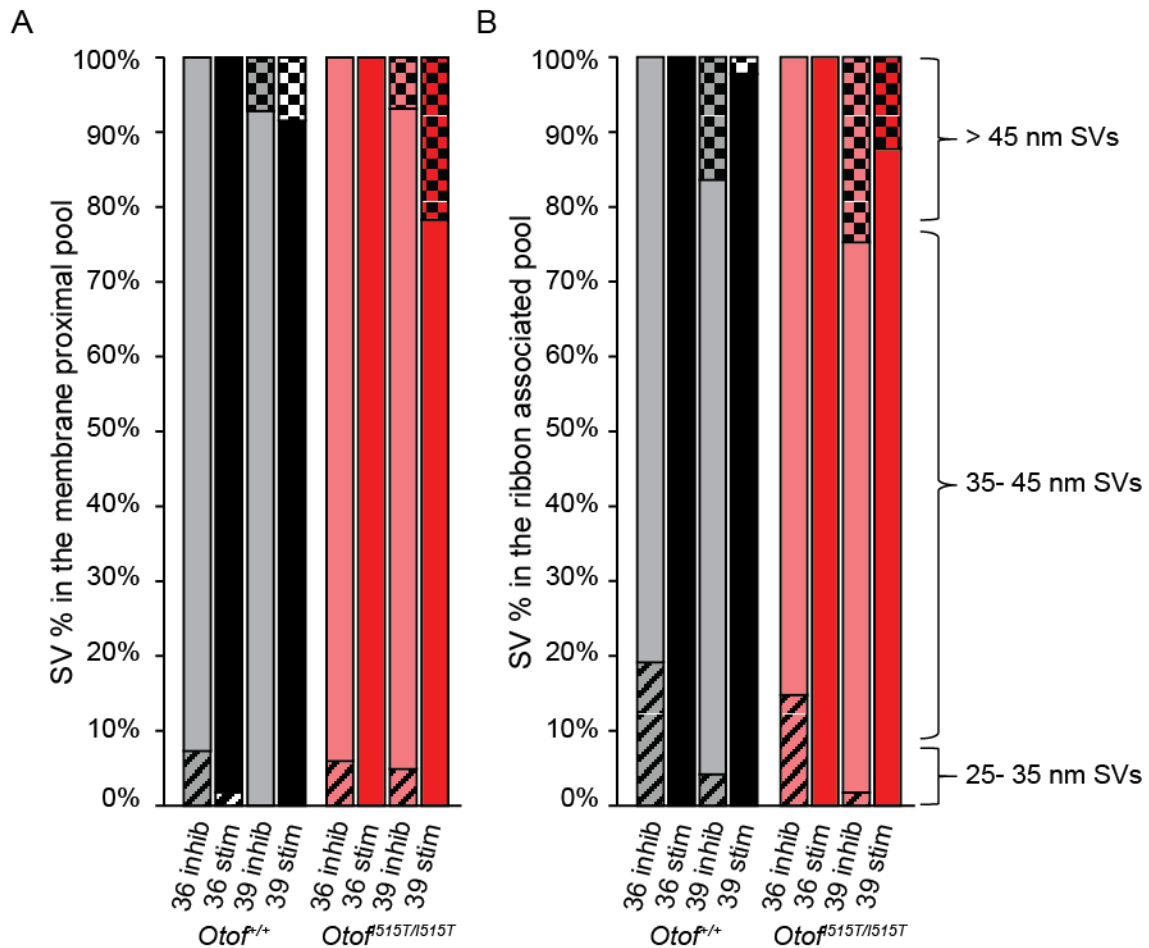


**Appendix Figure S6**
**Electron micrograph parameters for *Otof*[I515T/I515T] and *Otof*^{+/+} ribbon synapses**
A, Size distribution of membrane proximal vesicles for inhibitory and stimulatory conditions at 36°C and 39°C
in random sections, indicating that the majority of vesicles were of normal size (35-45 nm diameter). Larger
vesicles appeared only at 39°C.
B, Size distribution of ribbon-associated vesicles.

# Supplementary Table

**Appendix Table S1**

**Random section analysis of EM**

| | Conditions | $Otof^{+/+}$ | n | $Otof^{I515T/I515T}$ | n | p values |
|---|---|---|---|---|---|---|
| Number of synaptic vesicles in the **ribbon associated pool** | 36°C Inhibition | 8.6±0.5 | 36 | 9.3±0.7 | 21 | p > 0.05 * |
| | 36°C Stimulation | 8.8±0.7 | 25 | 9.9±0.5 | 34 | p > 0.05 * |
| | 39°C Inhibition | 8.9±0.6 | 24 | 9.6±0.5 | 36 | p > 0.05 * |
| | 39°C Stimulation | 8.4±0.6 | 27 | 8.6±0.5 | 21 | p > 0.05 * |
| Number of synaptic vesicles in the **membrane proximal pool** | 36°C Inhibition | 2.3±0.1 | | 2.4±0.2 | | p > 0.05 # |
| | 36°C Stimulation | 2.2±0.2 | | 3.5±0.3 | | p < 0.01 # |
| | 39°C Inhibition | 2.3±0.1 | | 2.8±0.1 | | p > 0.05 # |
| | 39°C Stimulation | 2.6±0.2 | | 4±0.3 | | p <0.05 # |
| Number of **large**(>45nm) vesicles in the **ribbon associated pool** | 36°C Inhibition | 0 | | 0 | | |
| | 36°C Stimulation | 0 | | 0 | | |
| | 39°C Inhibition | 1.5±0.2 | | 2.4±0.3 | | p > 0.05 * |
| | 39°C Stimulation | 0.2±0.1 | | 1.04±0.3 | | p < 0.05 * |
| Number of **large**(>45nm) vesicles in the **membrane proximal pool** | 36°C Inhibition | 0 | | 0 | | |
| | 36°C Stimulation | 0 | | 0 | | |
| | 39°C Inhibition | 0.2±0.1 | | 0.2±0.1 | | p > 0.05 # |
| | 39°C Stimulation | 0.2±0.1 | | 0.9±0.3 | | p < 0.05 # |

Data information: P values are calculated by one way ANOVA followed by Tukey's test (*) or Kruskal-Wallis test followed by non-parametric multiple comparisons test (#) reflecting differences between $Otof^{I515T/I515T}$ and $Otof^{+/+}$ under different treatment conditions. Data from 2 mice and *n* ribbon synapses for each genotype/condition were analyzed.

# Appendix Supplementary Methods

**Mouse genetics**

To generate $Otof^{I515T/I515T}$ mice, a targeting vector was constructed in which the codon coding for Ile515 (ATC) in exon 15 was replaced by a codon for threonine (ACA). The position 515 refers to the human protein sequence NP_001274418 and differs in the mouse protein sequence depending on the splice variant. In addition to the ATC to ACA replacement, a silent mutation was introduced 10 bp upstream of the new codon to introduce a KpnI restriction site for later screening. A neomycin selection cassette flanked by loxP sites was subcloned into the Pml1 restriction site in intron 15/16. The targeting construct consisted of 3- and 5.3-kb-long linkers for homologous recombination upstream of the point mutation and downstream of the loxP flanked neomycin cassette, respectively. A thymidine kinase cassette for negative selection was added after the 5.3-kb-long arm. This targeting construct was electroporated into 129ola embryonic stem cells, and cell colonies were picked after selection with G418 and ganciclovir. Homologous recombination was tested by Southern blot analysis after BclI digest using a BclI site upstream exon 11 and a newly introduced BclI site 5' of the neomycin cassette. Two clones were injected into mouse blastocysts, which both led to germ-line transmission in male chimeric mice. Heterozygous offspring from the chimeras were bred with an E2a cre-recombinase-expressing mouse line to excise the neomycin cassette. Mice were back-crossed with C57Bl6/N mice to out-breed the *Cre* recombinase.

For immunohistochemistry, cellular physiology and intellicage experiments, $Otof^{I515T/I515T}$ mice from a line that had been backcrossed for at least four generations with C57Bl6/N were used. For some experiments, $Otof^{I515T/I515T}$ mice were cross-bred with otoferlin knock-out mice (described in Reisinger *et al*, 2011). For single unit recordings and startle response measurements, we crossbred $Otof^{I515T/I515T}$ mice for five generations with CBA mice.

**Immunohistochemistry and fluorescence imaging**

Immunostaining was performed essentially as previously described (Khimich *et al*, 2005) with the following modifications: For acutely isolated organs of Corti at P14-P15, a major part of the bony shelf of the cochlea was removed and the round window was perforated to allow solutions to access the organ of Corti within the temporal bone. Fixation in 4% formaldehyde (FA) in PBS, blocking and antibody application was performed with the organ of Corti situated in the opened cochlea. Finally, the apical turn was excised from the cochlea and mounted in Moviol. For acute preparations at an age of 9-16 weeks, the temporal bone was locally perfused with 4% FA in PBS for 10 min, decalcified for 10 min in Morse's solution and the organ of Corti in the apical and basal turns were dissected. For incubations at different temperatures, organs of Corti at P7-P8 were excised from temporal bones in HEPES-buffered Hanks solution (Gibco) supplemented with 10μg/ml Penicillin G (Sigma-Aldrich) and 250 ng/ml Fungizone (Life Technologies). The tissue was then transferred to DMEM-F12 Glutamax 1 (1:1) medium (Life Technologies) with 5% fetal calf serum (Invitrogen) and mounted on coverslips coated with Cell-Tak™ (BD Biosciences). The organotypic cultures were allowed to settle for 24 hours and were then incubated at the indicated temperature.

For immunostainings, the following antibodies were used: mouse IgG1 anti-Ctbp2 (RRID:AB_399431, BD Biosciences, Heidelberg, Germany, 1:200), rabbit anti-GluR2 Clone 6C4 (RRID:AB_2113875, Chemicon/Merck Millipore, 1:200), mouse anti-otoferlin (RRID:AB_881807, Abcam, Cambridge, UK, 1:300), rabbit anti-otoferlin (Synaptic Systems, Göttingen, Germany, 1:300), rabbit anti-Vglut3 (RRID:AB_10015218, Synaptic Systems, 1:300), mouse anti-calbindin D28k (Swant, Switzerland, 1:1000) rabbit anti-sodium/potassium-ATPase α (Santa Cruz Biotechnology, Dallas, USA, 1:200), guinea pig anti-Parvalbumin (RRID:AB_1547406, Synaptic Systems, 1:200) and secondary Alexa Fluor®405, Alexa Fluor®488-, Alexa Fluor®568-, Alexa Fluor®594-, and AlexaFluor647-labeled antibodies (Invitrogen, 1:200). Confocal morphological images were acquired using a laser scanning confocal microscope (Leica TCS SP5, Leica Microsystems CMS GmbH, Mannheim, Germany) with a 63x Glycerol immersion objective (NA = 1.456) or a 100x oil immersion objective (NA = 1.3). Whole-mount preparations of the organ of Corti allowed analyzing several IHCs in a row (Khimich *et al*, 2005). For 3D reconstructions of the specimen, z-axis stacks of 2D images were taken with a step size of 0.5-0.8 μm. The number of synapses in 14-16 day old IHCs were counted using the cell counter plugin in *ImageJ* software as number of Ctbp2 spots adjacent to GluR2 spots. Synaptic ribbons in 9-16 week old animals were counted as Ctbp2-positive clusters within Parvalbumin-stained IHCs juxtaposed to NaK-ATPase-stained synaptic boutons using the ROI Manager plugin in *ImageJ*. Image analysis to determine fractional levels of membrane bound otoferlin is described in Figure 1. For analysis of organotypic cultures (Fig 6), the membrane position determined with the threshold method was always very close to the most basal peak value in subtracted fluorescence, which is why we took the maximum of the latter peak value for analysis. For IHCs after biolistic transfection (Fig 5), we used a threshold of 5 in summed fluorescence for quantification of the fractional membrane staining of otoferlin.

**Patch clamp recordings**

The pipette solutions for perforate-patch experiments contained (in mM): 130 Cs-gluconate, 10 Tetraethylammonium-chloride (TEA-Cl), 10 4-aminopyridine (4-AP, Merck, Darmstadt, Germany), 1 $MgCl_2$, 10 Cs-HEPES (pH adjusted to 7.17, osmolarity approx. 290 mOsm), 300 μg/ml amphotericin B (Calbiochem, La Jolla, CA). For flash photolysis of caged $Ca^{2+}$ we recorded in ruptured patch condition with a pipette solution containing (in mM) 120 Cs-gluconate, 20 TEA-Cl, 20 Cs-HEPES (pH adjusted to 7.2), 0.3 mag-fura-2 (Invitrogen, Karlsruhe, Germany), 10 DM-nitrophen (gift of A. Leonov and C. Griesinger, Göttingen), 5 DPTA (1,3-diaminopropan-2-ol-tetraacetic acid) and 10 $CaCl_2$. The extracellular solutions contained (in mM): 113 NaCl, 35 TEA-Cl, 2.8 KCl, 2 $CaCl_2$ (10 for flash-photolysis), 1 $MgCl_2$, 10 Na-HEPES, 1 CsCl, 11.1 D-glucose (pH adjusted to 7.2, osmolarity approx. 300 mOsm). All chemicals were obtained from Sigma-Aldrich (Taufkirchen, Germany) unless stated otherwise. EPC-9 or EPC-10 amplifiers (HEKA Electronics, Lambrecht, Germany), controlled by *Pulse* or *Patchmaster* software, were used to sample and filter currents at 20 kHz and at 5 kHz, respectively. We measured ΔCm as previously described using depolarizations of different durations to peak $Ca^{2+}$ current potential at intervals of 30 to 60 s (Beutner & Moser, 2001). All currents were leak-corrected using a P/6-protocol.

The vesicle replenishment rate was calculated as cell capacitance change during 100 ms depolarization minus the evoked release at 20 ms depolarization, divided by 45 aF per vesicle (Neef *et al*, 2007) to get the number of vesicles. Further, a number of 13 synapses per cell was used (Figure S4) to calculate the vesicle rate per active zone. This divided by 0.08 s gives the rate per second.

For $Otof^{+/+}$, ΔCm was 51.45 fF for 100 ms and 16.08 fF for 20 ms depolarization.

Replenishment rate = (51.45 fF – 16.08 fF)/0.045 fF/14 synapses/0.08s = 702 vesicles/s/active zone.

For $Otof^{I515T/I515T}$, ΔCm was 30.42 fF for 100 ms and 13.35 fF for 20 ms depolarization.

Replenishment rate = (30.42 fF-13.35 fF)/0.045 fF/14 synapses/0.08s = 339 vesicles/s/active zone.

Flash photolysis was performed as described (Beutner *et al*, 2001). If not otherwise indicated, recordings were performed at room temperature (20-25°C).

For recordings at elevated temperature, perforation solution and the objective lens were heated and the temperature was controlled by a miniature thermistor in ~1mm distance from the organ of Corti as described (Nouvian, 2007). Heating to 35-36.5°C took approximately 3-7 min. Recordings were started as soon as the temperature was at least 1 min between 35°C and 36.5°C. Similarly, recordings at higher temperature were performed as soon as the temperature was at 38.5-40°C.

**Quantification of single unit responses**

PSTHs were calculated as average spike rates using 200 presentations of 50ms tone bursts presented at CF, 30dB above threshold. Onset/peak rate was quantified as the largest bin of the PSTH (binwidth 0.5ms). Adapted rate was averaged in a window between 35 and 45ms following stimulus onset. Individual PSTHs were averaged after aligning for the time when they reached 30% of the difference between spontaneous and peak rate. Rate level functions were obtained using 50ms tone bursts presented at 5 Hz with 25 repetitions for each stimulus intensity. Threshold was interpolated from the rate level function as the intensity at which the spike rate increased by 20 Hz above spontaneous rate. The steepness was calculated as the increase in average spike rates for each 5 dB intensity increment. Dynamic range was calculated based on sigmoidal fits to the rate intensity function as described in (Taberner & Liberman, 2005). For analysis of forward masking data, spike numbers in a 5ms interval starting from response onset were determined and presented as the ratio of probe and masker responses for at least 25 repetitions for each interval. The adapted rate of the masker response was determined in a window 85-90ms following stimulus onset. The data was then normalized to 0 for the peak to adapted spike rate ratio and 1 for full recovery at the next masker onset. Then, the half time of recovery was determined from a logarithmic fit to the normalized recovery curve. For amplitude modulation analysis, the synchronization index, also called vector strength was calculated as described by (Goldberg & Brown, 1969). Synchronization indices were only considered significant when at least 15 spikes were present in a 3s recording interval and the Rayleigh statistic was below 13.8.

**Startle responses**

For measurements of startle responses, mice were placed in a custom-designed small cage on a mobile platform inside a sound-shielded box (Desone). To elicit startle responses, 12 kHz tone bursts or broadband white noise of 10 ms duration was administered at variable intensities using a high-frequency speaker system (ScanSpeak, Avisoft) mounted 15 cm above the cage. The minimal interval between two stimuli was randomly varied between 10 and 20 s. Stimuli were delayed by additional 5 s when mouse movements exceeded a manually set threshold during the pause. Stimulus generation and response recordings were performed using Tucker Davis System III and custom-written *Matlab* software. The summed integral output of accelerometers attached to the

cage in the x, y and z dimensions was analyzed in a time window of 9-20 ms following startle stimulus onset. For analysis of prepulse inhibition, 70 dB broadband noise was applied continuously, which was interrupted in 70 % of cases by a silent gap which preceded the startle stimulus (10 ms noise burst 115 dB) by 70 ms. Each stimulus condition was repeated at least 40 times in pseudorandom order. For analysis, we compared the distributions and median amplitudes of startle responses in the "no gap" condition with those of the different "gap" gap conditions and defined the gap detection threshold as the minimal gap duration which significantly reduced the startle response amplitude with all longer gaps also yielding a significant change (Mann-Whitney U test $p<0.007$, corresponding to a p value of 0.05 with Bonferroni correction for 7 comparisons).

**Operant conditioning**
Operant conditioning in the "Audiobox" was carried out essentially as described in (de Hoz & Nelken, 2014). Female mice were transponder-injected and habituated to the social cage environment which was enriched by houses and running wheels at an age of 4 weeks. During a habituation phase of at least 5 days, in which drinking was allowed at every visit in the sound-attenuated chamber while no sound (for threshold testing) or continuous 70 dB broadband noise (for gap detection) was played. We then introduced conditioned stimuli (80 dB 12 kHz tone bursts, 400 ms duration, 3 stimuli/second, or continuous 70 dB broadband noise interrupted by 3 90 ms gaps per second) in 5% of visits and punished drink attempts by air puffs to the back of the mouse, giving no water access. The fraction of conditioned stimuli was slowly increased to 20% over at least 3 weeks, depending on the discrimination performance of each mouse. In a subsequent generalization phase, the conditioned stimuli were varied in intensity (70-90 dB) or gap duration (70-90 ms), respectively. Finally, the experimental phase included rare interspersed stimuli of intermediate intensity or duration. Only data from mice that reached a discrimination performance of a difference of at least 0.3 between conditioned and unconditioned stimuli was used.
All loudspeaker systems were calibrated using a 1⁄4" microphone (D 4039, Bruel and Kjaer GmbH). For the Intellicage, an approximate average intensity detected in multiple locations within the corner with the water bottles was chosen for display.

**Cloning of full length otoferlin**
Full length otoferlin cDNA was subcloned from mouse organ of Corti cDNA by assembly of four fragments all amplified by PCR. The fragments were gained using oligonucleotides (all in 5'-3' direction) GAGAGAATTCGCCACCATGGCCCTGATTGTTCACCTC and CAGCAAAGAAGACTTGCACATAGG (1st fragment); GGTGAGAACAAGGACCTCGTC and GTGTCTCGTTTAGAACCTCAGTGC (2nd fragment); GCACTGAGGTTCTAAACGAGACAC and GGGTCCCTCCAGATATTGTAGC (3rd fragment), and CAGACCTATTCCATACATGGCTAC and GAGAGGTACCTCAGGCCCCTAGGAGCTT-CTTGACCATG (4th fragment). Fragments were assembled either with overlap PCR of with restriction enzyme cloning. Sanger Sequencing revealed a transcript variant that is now deposited under GeneBank accession No KX060996. The open reading frame sequence is congruent with reference sequence NM_001313767.1, termed otoferlin transcript variant 4.

**Cloning of the RXR motif**
By site-directed mutagenesis the human "RXR motif", comprising amino acids TVRLLRRCRVLCNGGSSSHS (amino acids 1244-1263 in NP_001274418) was subcloned into a pcDNA3 plasmid containing mouse otoferlin cDNA using overlap PCR. In addition, a site directed mutation for N1240S was included in the mouse sequence to mimic the human sequence (see Fig EV4). Oligonucleotides used were CGGCGCTGCCGTGTGCTGTGCAATGGGGGCTCCTCCTCTCACTCCACAGGGGAGGTTGTAGTAAGC (fwd) and CTCTTTACAGAGGCGTGTCAGG (rev) for one PCR and CAATGATTGACCGGAAAAA-TGGGG (fwd) and CACAGCACACGGCAGCGCCGGAGAAGCCTGACCGTGGTGTTCCAGCTGGGGGC-TGAGCGGTCTGG (rev) for the second PCR generating overlapping sequences including the codons for the inserted/mutated amino acids. The two amplicons were assembled by overlap PCR and sublconed into the original vector with SanDI and SfiI. The construct was verified by Sanger Sequencing, amplified and purified for biolistic transfection.

**Gene Gun transfection of otoferlin deficient mouse organs of Corti**
Gene Gun bullets were prepared according to the instructions of Woods and Zito (2008) with the following modifications: 25 mg gold with a diameter of 1 μm (Bio-Rad) were mixed with 100 μl 0.05M spermidine (Sigma-Aldrich), vortexed for 15 sec and sonified for 30 sec (Transsonic 820/H, Elma). 50 μg DNA (1 μg/μl) (90% pcDNA3-mOtof and 10% pEGFP-N1, w/w) in 50 μl H$_2$O were added to the solution and vortexed for 5 sec. 100 μl of 1 M CaCl$_2$ (Sigma-Aldrich) was added drop-wise to the mixture while vortexing. The mixture was incubated at RT for 10 min, while vortexing every 30 sec for 5 sec and centrifuged for 2 min (1000 g). Three wash (100% EtOH) and centrifugation steps (10 sec, 1000 g) followed. The mixture was resuspended in 3

ml Polyvinylpyrrolidone (PVP) (50 μg/ml) (Bio-Rad, USA) and vortexed for 15 sec. A 70-80 cm long Tefzel tubing (Bio-Rad) was dried using nitrogen (0.4 l/min) for at least 15 min in the tubing station (supplied with the Helios® Gene Gun System) and filled with the gold particle solution. The gold particles were distributed evenly inside the tubing piece as described in Woods and Zito, 2008. The tubing piece was left to dry by nitrogen flow (0.4 l/min, 5 min), cut into appropriate pieces using the supplied tubing chopper and stored desiccated at 4°C until further use.

For Gene Gun experiments, $Otof^{-/-}$ mice (Reisinger $et\ al$, 2011) at the age of P4 were used. The isolated organs were oriented with the basilar membrane facing upwards. The biolistic transfection was performed via the Helios® Gene Gun System (Bio-Rad, USA) with a pressure of 200-210 psi and a distance of 3.5 cm between the tissue and focusing nozzle. To reduce the amount of gold particles arriving at the tissue, two Falcon® 40 μm or 70 μm cell strainers (Corning, USA) were placed between the focusing nozzle and the sample (modified from Zhao $et\ al$, 2012). After biolistic transfection, medium with 1.5 μg/ml Ampicillin (Sigma-Aldrich) was added, then the stria vascularis was removed, and the organs were attached to the cover slips. The cultures were left to incubate for two days at 37°C before further experiments were conducted. EGFP fluorescence served to control for efficiency of transfection prior to immunohistochemistry. Cultures transfected with otoferlin RXR motif and Ile515Thr mutation were either incubated at 37°C or at 38.5°C for 30 min before fixation and immunostaining.

**Pre-embedding immunogold labeling**

Organs of Corti were isolated and immediately fixed on ice (4°C) for 35 minutes for saponin permeabilized (4 % PFA in PBS) and 90 minutes for Triton X-100 permeabilized samples (2 %PFA, 0.6% glutaraldehyde in 1X PEM solution (0.1 M PIPES, 2 mM EGTA, 1 mM MgSO$_4$x7H$_2$O)). For saponin permeabilization the samples were additionally incubated for 45 min in 0.05 % saponin (Carl Roth) diluted in PBS. Subsequently samples were blocked for 1 hour at RT in blocking solution (saponin permeabilization: 2 % BSA and 3 % NHS in PBS; Triton X-100 permeabilization: 2 % BSA, 3 % NHS, and 0.2 % TritonX-100 in PBS). The primary antibody incubation was performed overnight at 4°C after 1 hour incubation at RT. The secondary antibodies were applied to the samples for 2 hours at RT after three washing steps (saponin permeabilization: PBS; Triton X-100 permeabilization: 0.1 % TritonX-100 in PBS) and then left to wash again overnight at 4°C. The following primary antibodies were used; mouse anti-otoferlin antibody (N-terminal, Abcam, 1:300) in both pre-embedding protocols and rabbit anti-Vglut3 (Synaptic Systems, 1:300) in the Triton X-100 permeabilization protocol. As secondary antibodies the Nanogold® anti-mouse IgG antibody and the Nanogold® anti-rabbit IgG antibody (Bio Trend, Germany, 1:30) were used. All antibodies were diluted in PBS with 5% NHS for saponin permeabilized and PBS with 0.1% Triton X-100 for Triton X-100 permeabilized samples. The samples were washed once again afterwards for 30 min at RT, post-fixed for 30 min at RT with post-fixation solution (2% glutaraldehyde in PBS) and further washed four times at RT for 10 min in distilled water. The silver enhancement step was performed light protected for 2.5 min using the HQ Silver Enhancement kit (Nanoprobes, USA) according to the manufacturer's instructions. Four wash steps with distilled water at RT for 10 minutes followed. Next, samples were incubated in 2% OsO$_4$ (Sigma-Aldrich, USA) diluted in 0.1 M cacodylate buffer (pH 7.2) (Carl Roth, Germany) for 30 min, washed once for one hour and twice for 30 minutes in distilled water. After washing, several dehydration steps with ascending ethanol concentrations (5 min in 30% ethanol, 5 min in 50% ethanol, 10 min in 70% ethanol, two times for 10 min in 95% ethanol, and three times for 12 min in 100% ethanol) were performed. The organs of Corti were placed in a mixture of 100% ethanol and pure EPON (1:1) prepared from the EPON Agar 100-premix Kit (Plano, Germany) and incubated once for 30 minutes and once for 1.5 hours at RT. Subsequently, the solution was replaced by pure EPON and left to incubate once overnight and once for 6 hours. The polymerization of the samples was performed in pure EPON for two days at 70°C.

**Conventional embedding for transmission electron microscopy**

After stimulation or inhibition the samples were fixed immediately with 4% PFA and 0.5% glutaraldehyde. Samples were dehydrated, infiltrated and embedded in Epon resin as described previously (Wong $et\ al$, 2014). After embedding, 70 nm sections for 2D transmission electron microscopy and 250 nm sections for electron tomography were obtained on an Ultracut E ultramicrotome (Leica). Sections were applied to formvar-coated copper slot or mesh (tomography) grids and post-stained with 4% uranyl acetate and Reynold's lead citrate.

**Electron tomography**

10 nm gold particles (British Bio Cell) were applied to both sides of the stained mesh grids. Single tilt axis series were acquired at a JEOL JEM 2100 transmission electron microscope at 200 kV from -60 to +60 with 1° increment using the Serial-EM software. The tomograms were generated using the IMOD package etomo and models were rendered using 3dmod ($bio3d.colorado.edu/imod/$) as described (Wong $et\ al$, 2014; Vogl $et\ al$, 2015).

**EM Image analysis**

Quantitative image analysis for random ultrathin sections was done using the *ImageJ* software package. Two morphological vesicle pools at ribbon synapses were analyzed , (i) membrane proximal vesicles ($\leq$25 nm vesicle-to-membrane distance to the active zone membrane) and (ii) ribbon associated vesicles defined as all vesicles in the first row in $\leq$80 nm distance around the ribbon (excluding membrane proximal vesicles; see also Figure 7O). For calculation of the vesicle diameter in random sections, the average of the longest and the shortest axis was calculated. Image analyses for the tomograms were performed in *3dmod* (*bio3d.colorado.edu/imod/*). For ribbon-associated synaptic vesicles the first row of vesicles with a maximal distance of 80 nm from the ribbon to the vesicle membrane were counted per tomogram. Membrane-proximal synaptic vesicles were defined as vesicles with a membrane-to-membrane distance to the active zone of maximal 50 nm (Figure 8E) (Jung *et al*, 2015). Vesicle diameters were measured at the maximum projection for the round synaptic vesicles and the longest axis for the flattened vesicles. The height of the ribbons was determined as the maximum extent from the presynaptic density in both ultrathin and virtual sections.

The diameter of the otoferlin labeled structures was measured as described for the vesicle diameter measurement above. The number of anti-otoferlin gold clusters was counted over the length of the basal plasma membrane and indicated as gold clusters/µm. For quantifying the gold cluster amount within the IHC basal region, the clusters were counted within areas from 0-800 nm and 800-1600 nm distant to the plasma membrane and indicated as gold clusters/µm$^2$.

**Quantitative PCR**

Apical and midbasal turns of P9 organs of Corti were dissected from three $Otof^{+/+}$ and two $Otof^{I515T/I515T}$ mice. Tissue was homogenized in Trizol reagent (Life Technologies) and RNA was extracted according to the Trizol protocol. Precipitated RNA was dissolved in 13 µl H$_2$O, and 0.4 µl random hexamers (biomers.net; 0.5 µg/µl), 0.65 µl oligo dT primers (50 pmol/µl) and 1.3 µl dNTPs (10 mM each) were added. After incubation at 65°C for 5 min and cooling to 4°C, 5.3 µl first strand buffer, DTT (final concentration 1 mM), 260 U SuperScript® II (Invitrogen/Life Technologies) and 50 U RNAseOUT (Life Technologies) were added. Reverse transcriptase reaction was incubated for 10 min at room temperature, 30 min at 37°C and 1h at 42°C. Resulting cDNA was ethanol precipitated in presence of 1µg Glycogen and dissolved in 25µl H$_2$O. Real Time PCR was performed using Taqman assays Mm00453306 (Applied Biosystems) for amplification of otoferlin, Mm00446873_m1 for tata binding protein (TBP) and Mm00464451_m1 for bassoon on 2 µl of cDNA solution each.

To average (logarithmic) C$_t$ values from parallel experiments (same cDNA, same primers), first a linear value was calculated from C$_t$ values by

Lin(C$_t$) = 2^(42-C$_t$)

assuming that a single cDNA molecule would result in a C$_t$ of 42 (any deviations from this value would not change the overall result, as this is eliminated in the next step).

Lin(C$_t$) values were averaged, and back-calculated into "real" C$_t$ values by

C$_t$ = 42 − LN(Lin(C$_t$))/LN2

(Here the value of 42 is eliminated again, thus any other value could be assumed instead of the 42).

These averaged C$_t$ values were then used to calculate $\Delta$C$_t$ values for each cDNA sample by

$\Delta$Ct = C$_t$(Otof) − C$_t$(TBP).

Also, $\Delta$C$_t$ values from the individual cDNA preparations were averaged by calculating a linear value $\Delta$C$_t$ first which was averaged and back-calculated, as described for the C$_t$ values. Relative mRNA amount (equivalent to cDNA amount) in mutant vs wt cDNA is then calculated by

$\Delta\Delta$Ct = $\Delta$C$_t$ (mutant) − $\Delta$C$_t$ (wt)

Relative Otof mRNA amount = 2^-$\Delta\Delta$C$_t$.

**HEK cell transfection and mass spectrometric quantification of otoferlin levels**

Otoferlin cDNA (KX060996) was subcloned into pEGFP-N1 with a STOP codon such that no eGFP was transcribed from this plasmid. Mutations were introduced with overlap PCR and confirmed by Sanger sequencing. HEK293T cells between passages p3 up to p30 were used for experiments. Cells were transfected with desired plasmid DNA using Lipofectamine 2000 (Invitrogen / Life Technologies) according to the manufacturer's instructions and incubated overnight.

After 24h, 100 µg/ml cycloheximide was added to the cells and cells were incubated either at 37°C or at 38.5°C. Samples were taken at 0 min (control without cycloheximide), 5 min, 10 min, 20 min, 30 min, 60 min and 120 min, dissolved in 100 µl Laemmli Sample Buffer each (50 mM Tris pH 6.8, 20% SDS, 0.1% Bromophenol Blue, 10% glycerine, 100 µM DTT) and stored at -20°C until the last sample was taken. Samples were then thawed, sonified (3x20sec, Branson Sonifer 250) and 20 µl of each sample was loaded on an SDS PAGE consisting of 4% stacking gel and 6% running gel. The gel was stained in Coomassie Blue solution (10% acetic acid, 47.5% ethanol, 0.25% Coomassie Brilliant BlueR250) and destained in H$_2$O. Gel slices in the range of otoferlin size were cut out, washed, reduced with dithiothreitol (DTT), alkylated with 2-iodoacetamide and

digested with trypsin overnight. The resulting peptide mixtures were then extracted, dried in a SpeedVac, reconstituted in 2% acetonitrile/0.1% formic acid/ (v:v) and analyzed by nanoLC-MS/MS as described previously (Atanassov & Urlaub, 2013).

For mass spectrometric analysis samples were enriched on a self-packed reversed phase-C18 precolumn (0.15 mm ID x 20 mm, Reprosil-Pur120 C18-AQ 5 μm, Dr. Maisch, Ammerbuch-Entringen, Germany) and separated on an analytical reversed phase-C18 column (0.075 mm ID x 200 mm Picofrit 360-20-10-N, New Objective, Woburn/MA, USA, packed with Reprosil-Pur 120 C18-AQ, 3 μm) using a 37 min linear gradient of 5-35 % acetonitrile/0.1% formic acid (v:v) at 300 nl min$^{-1}$). The eluent was analyzed on a Q Exactive hybrid quadrupole/orbitrap mass spectrometer (ThermoFisher Scientific, Bremen) equipped with a FlexIon nanoSpray source and operated under Excalibur 2.2 software using a data-dependent acquisition method. Each experimental cycle was of the following form: one full MS scan across the 350-1600 $m/z$ range was acquired at a resolution setting of 70,000 FWHM, a target of $10e^6$ and a maximum fill time of 60 ms to select up to ten most abundant peptide precursors of charge states 2 to 5 above a $10e^4$ intensity threshold, at an isolation width of 2.0 $m/z$. Precursors were fragmented by Higher Collision Energy Dissociation (HCD) with nitrogen at a normalized collision energy setting of 25%, and their product ion spectra recorded using a start mass of 100 $m/z$, a resolution setting of 17,500 FWHM (full width, half maximum), a target of $2 \times 10e^5$ and a maximum fill time of 60 ms. Selected precursor $m/z$ values were then excluded for the following 15 s. Three technical replicates per sample were acquired.

The MS raw files were processed by MaxQuant (Cox & Mann, 2008) (version 1.5.2.8) and MS/MS spectra were searched against mouse database (UniProt, downloaded July 2014; 51,547 entries) supplemented with 245 frequently observed contaminants via the Andromeda search engine (Cox *et al*, 2011). Mass tolerance after recalibration of precursor mass and fragment ion mass were set as 6 and 20 ppm, respectively. Allowed variable modifications included protein N-terminal acetylation and methionine oxidation. Cysteine carbamidomethylation was defined as a fixed modification. Minimal peptide length was set to 7 amino acids with the maximum of two enzymatic mis-cleavages. The false discovery rate (FDR) was set to 1% for both peptide and protein identifications. For relative quantitation, intensities of all identified peptides were determined by the MaxQuant with the option of "match between runs" on. Intensity-based absolute quantification or iBAQ values (Schwanhäusser *et al*, 2011) of all identified proteins were then calculated to represent their quantity in the sample.

In order to eliminate possible system variations introduced during sample handling and during mass spectrometric analysis, we normalized the iBAQ value of otoferlin against that of stable background proteins, which were defined as those proteins showed most reproducible iBAQ values with relatively high abundance across all replicates. We carefully examined the abundance and iBAQ variations of all identified proteins over biological and technical replicates. To this end, four protein hits with the leading gene names as Spag9, Top2b, Brd4, and Uba52 were selected for following normalization.

**Supplementary References**

Atanassov I & Urlaub H (2013) Increased proteome coverage by combining PAGE and peptide isoelectric focusing: comparative study of gel-based separation approaches. *Proteomics* **13:** 2947–2955

Beutner D & Moser T (2001) The presynaptic function of mouse cochlear inner hair cells during development of hearing. *J Neurosci* **21:** 4593

Beutner D, Voets T, Neher E & Moser T (2001) Calcium dependence of exocytosis and endocytosis at the cochlear inner hair cell afferent synapse. *Neuron* **29:** 681–690

Cox J & Mann M (2008) MaxQuant enables high peptide identification rates, individualized p.p.b.-range mass accuracies and proteome-wide protein quantification. *Nature biotechnology* **26:** 1367–1372

Cox J, Neuhauser N, Michalski A, Scheltema RA, Olsen J V. & Mann M (2011) Andromeda: A peptide search engine integrated into the MaxQuant environment. *Journal of Proteome Research* **10:** 1794–1805

Goldberg JM & Brown PB (1969) Response of binaural neurons of dog superior olivary complex to dichotic tonal stimuli: some physiological mechanisms of sound localization. *J. Neurophysiol.* **32:** 613–636

de Hoz L & Nelken I (2014) Frequency tuning in the behaving mouse: different bandwidths for discrimination and generalization. *PLoS ONE* **9:** e91676

Jung S, Maritzen T, Wichmann C, Jing Z, Neef A, Revelo NH, Al-Moyed H, Meese S, Wojcik SM, Panou I, Bulut H, Schu P, Ficner R, Reisinger E, Rizzoli SO, Neef J, Strenzke N, Haucke V & Moser T (2015) Disruption of adaptor protein 2μ (AP-2μ) in cochlear hair cells impairs vesicle reloading of synaptic release sites and hearing. *EMBO J.* **34:** 2686–2702

Khimich D, Nouvian R, Pujol R, tom Dieck S, Egner A, Gundelfinger ED & Moser T (2005) Hair cell synaptic ribbons are essential for synchronous auditory signalling. *Nature* **434:** 889–894

Marlin S, Feldmann D, Nguyen Y, Rouillon I, Loundon N, Jonard L, Bonnet C, Couderc R, Garabedian EN, Petit C & Denoyelle F (2010) Temperature-sensitive auditory neuropathy associated with an otoferlin mutation: Deafening fever! *Biochem. Biophys. Res. Commun* **394:** 737–742

Matsunaga T, Mutai H, Kunishima S, Namba K, Morimoto N, Shinjo Y, Arimoto Y, Kataoka Y, Shintani T, Morita N, Sugiuchi T, Masuda S, Nakano A, Taiji H & Kaga K (2012) A prevalent founder mutation and genotype–phenotype correlations of OTOF in Japanese patients with auditory neuropathy. *Clinical Genetics* n/a–n/a

Neef A, Khimich D, Pirih P, Riedel D, Wolf F & Moser T (2007) Probing the mechanism of exocytosis at the hair cell ribbon synapse. *The Journal of Neuroscience* **27:** 12933–12944

Nouvian R (2007) Temperature enhances exocytosis efficiency at the mouse inner hair cell ribbon synapse. *The Journal of Physiology* **584:** 535–542

Raman S, Vernon R, Thompson J, Tyka M, Sadreyev R, Pei J, Kim D, Kellogg E, DiMaio F, Lange O, Kinch L, Sheffler W, Kim B-H, Das R, Grishin NV & Baker D (2009) Structure prediction for CASP8 with all-atom refinement using Rosetta. *Proteins* **77 Suppl 9:** 89–99

Reisinger E, Bresee C, Neef J, Nair R, Reuter K, Bulankina A, Nouvian R, Koch M, Bückers J, Kastrup L, Roux I, Petit C, Hell SW, Brose N, Rhee J-S, Kügler S, Brigande JV & Moser T (2011) Probing the functional equivalence of otoferlin and synaptotagmin 1 in exocytosis. *J. Neurosci.* **31:** 4886–4895

Robertson NG, Khetarpal U, Gutiérrez-Espeleta GA, Bieber FR & Morton CC (1994) Isolation of novel and known genes from a human fetal cochlear cDNA library using subtractive hybridization and differential screening. *Genomics* **23:** 42–50

Romanos J, Kimura L, Fávero ML, Izarra FAR, de Mello Auricchio MTB, Batissoco AC, Lezirovitz K, Abreu-Silva RS & Mingroni-Netto RC (2009) Novel OTOF mutations in Brazilian patients with auditory neuropathy. *J. Hum. Genet* **54:** 382–385

Schwanhäusser B, Busse D, Li N, Dittmar G, Schuchhardt J, Wolf J, Chen W & Selbach M (2011) Global quantification of mammalian gene expression control. *Nature* **473:** 337–342

Söding J, Biegert A & Lupas AN (2005) The HHpred interactive server for protein homology detection and structure prediction. *Nucleic Acids Res.* **33:** W244-248

Taberner AM & Liberman MC (2005) Response Properties of Single Auditory Nerve Fibers in the Mouse. *J Neurophysiol* **93:** 557–569

Varga R, Avenarius MR, Kelley PM, Keats BJ, Berlin CI, Hood LJ, Morlet TG, Brashears SM, Starr A, Cohn ES, Smith RJH & Kimberling WJ (2006) OTOF mutations revealed by genetic analysis of hearing loss families including a potential temperature sensitive auditory neuropathy allele. *J Med Genet* **43:** 576–581

Vogl C, Cooper BH, Neef J, Wojcik SM, Reim K, Reisinger E, Brose N, Rhee J-S, Moser T & Wichmann C (2015) Unconventional molecular regulation of synaptic vesicle replenishment in cochlear inner hair cells. *J. Cell. Sci.* **128:** 638–644

Wang D-Y, Wang Y-C, Weil D, Zhao Y-L, Rao S-Q, Zong L, Ji Y-B, Liu Q, Li J-Q, Yang H-M, Shen Y, Benedict-Alderfer C, Zheng Q-Y, Petit C & Wang Q-J (2010) Screening mutations of OTOF gene in

Chinese patients with auditory neuropathy, including a familial case of temperature-sensitive auditory neuropathy. *BMC Med. Genet* **11:** 79

Wong AB, Rutherford MA, Gabrielaitis M, Pangršič T, Göttfert F, Frank T, Michanski S, Hell S, Wolf F, Wichmann C & Moser T (2014) Developmental refinement of hair cell synapses tightens the coupling of Ca2+ influx to exocytosis. *EMBO J* **33:** 247–264

Woods G & Zito K (2008) Preparation of gene gun bullets and biolistic transfection of neurons in slice culture. *J Vis Exp*

Zhao H, Avenarius MR & Gillespie PG (2012) Improved Biolistic Transfection of Hair Cells. *PLoS One* **7** Available at: http://www.ncbi.nlm.nih.gov/pmc/articles/PMC3462194/ [Accessed December 14, 2012]

## 2.2 Establishing a dual-AAV vector approach to transfer the full-length otoferlin cDNA into auditory IHCs

### 2.2.1 Synopsis

The delivery of large genes associated with hearing loss and exceeding the packing capacity of a single AAV (~4.7 kb) (Grieger and Samulski, 2005; Chamberlain, Riyad and Weber, 2016; McClements and Maclaren, 2017) into the auditory sensory cells of the cochlea is challenging. Split-AAV vectors have been developed to circumvent this problem (Chamberlain, Riyad and Weber, 2016; McClements and Maclaren, 2017), but have not been established for inner ear gene transfer yet. In this project, I aimed to establish a dual-AAV gene therapy approach to transfer the 6 kb-long CDS of otoferlin into auditory IHCs and examined whether this technique can restore IHC and auditory function in deaf $Otof^{-/-}$ mice (Roux $et$ $al.$, 2006; Reisinger $et$ $al.$, 2011). For this purpose, the full-length otoferlin cDNA was split into two fragments and packaged into two sperate AAV2/6 viruses (5'-AAV2/6 and 3'-AAV2/6) (Al-Moyed $et$ $al.$, 2019: Fig. EV2). These dual-AAV half vectors were, then, co-injected through the RWM into the perilymph-filled scala tympani in the cochlea of P6-7 old $Otof^{-/-}$ mice. The organs of Corti (P18-30) from injected and non-injected ears were immunolabeled for the N-terminal and the C-terminal part of otoferlin via immunohistochemistry. Organs of Corti transduced with otoferlin dual-AAV2/6 trans-splicing (dual-AAV-TS) or dual-AAV2/6 hybrid (dual-AAV-Hyb) half vectors only showed full-length otoferlin (C-term otoferlin) immunofluorescent signal in auditory HCs, but not any other cochlear cell type (Al-Moyed $et$ $al.$, 2019: Fig. 1A, Appendix Fig. S1-S3). Non-injected contralateral ears, on the other hand, did not display any N-terminal or C-terminal otoferlin immunofluorescent signal (Al-Moyed $et$ $al.$, 2019: Appendix Fig. S1-S2). 12-51% of IHCs in dual-AAV-TS transduced and 5-34% of IHCs in dual-AAV-Hyb transduced $Otof^{-/-}$ cochleae exhibited a full-length (C-term otoferlin) otoferlin immunofluorescent signal and around 10% of transduced IHCs only showed an N-terminal otoferlin signal (Al-Moyed $et$ $al.$, 2019: Fig. 1D). Measuring the intensity of the C-terminal otoferlin immunofluorescent signal in transduced $Otof^{-/-}$ IHCs revealed that the dual-AAV approach was able to restore 31% of wild-type full-length otoferlin protein levels in dual-AAV-TS and 37% of wild-type levels in

dual-AAV-Hyb transduced IHCs (Al-Moyed *et al.*, 2019: Fig. 1E). *Otof*^{-/-} IHCs (P25-29) transduced with either dual-AAV strategy did not have significantly higher synaptic ribbon numbers than non-transduced IHCs from injected ears or non-injected contralateral ears (Al-Moyed *et al.*, 2019: Fig. 2A-B). Both transduced and non-transduced *Otof*^{-/-} IHCs had around 60% of their synaptic ribbons left at P25-29. To determine if otoferlin plays a role in IHC ribbon synapse development and maturation, I have assessed the number of ribbon synapses in P6 and P14 old *Otof*^{-/-} mice. The analysis revealed that *Otof*^{-/-} mice had higher synapse numbers than wild-type mice at P6 and similar numbers at P14 (Al-Moyed *et al.*, 2019: Fig. 2C-D). ABRs were further recorded from 3-4 weeks old dual-AAV treated *Otof*^{-/-} mice subjected to broadband click and tone burst (4 kHz, 6 kHz, 8 kHz, 12 kHz, 16 kHz, 24 kHz, 32 kHz) sound stimuli played with different sound pressure levels (SPL) (10-100 dB SPL; Al-Moyed *et al.*, 2019: Fig. 3, Fig. EV5). Dual-AAV mediated otoferlin gene transfer led to a partial recovery of ABR wave amplitudes in all treated *Otof*^{-/-} animals (Al-Moyed *et al.*, 2019: Fig. 3A-B, Fig. 3E, Fig. EV5A, Fig. EV5D-H). Non-transduced control *Otof*^{-/-} littermates (-AAV), in contrast, showed no ABR waves (Al-Moyed *et al.*, 2019: Fig. 3, Fig. EV5). *Otof*^{-/-} mice injected with either strategy had near wild-type broadband click sound-evoked ABR thresholds of 40-60 dB SPL (Al-Moyed *et al.*, 2019: Fig. 3C). Tones burst-induced ABR thresholds were more variable between individual animals and ranged between 50 dB SPL and no ABRs at all (Al-Moyed *et al.*, 2019: Fig. 3D, Fig. EV5B). The correlation analysis between IHC transduction rates and ABR wave amplitudes and click thresholds showed that ABR wave amplitudes, but not click thresholds, correlated with the number of full-length otoferlin (C-term otoferlin) expressing IHCs in transduced inner ears (Al-Moyed *et al.*, 2019: Fig. 3F, Fig. EV5C). Injecting otoferlin dual-AAV-TS half vectors into cochleae of wild-type control mice did not cause any detrimental effect on ABR thresholds, ABR wave latencies, and ABR wave I amplitudes (Al-Moyed *et al.*, 2019: Appendix Fig. S4).

## 2.2.2 Own contribution

I have performed experiments and analyzed data for the following figures in "Al-Moyed *et al.*, 2019":

- Figure 1: postnatal RWM injections, immunohistochemistry, confocal microscopy, data analysis, statistics, figure preparation.

- Figure 2A-D: postnatal RWM injections, immunohistochemistry, confocal microscopy, data analysis, statistics, figure preparation.

- Figure 3: postnatal RWM injections, broadband click and tone burst sound-evoked ABR recordings, data analysis, statistics, figure preparation.

- Figure EV1: postnatal RWM injections, immunohistochemistry, confocal microscopy, figure preparation.

- Figure EV2: cloning the two split-AAV-TS and the two split-AAV-Hyb half vector expression cassettes, figure preparation.

- Figure EV3: postnatal RWM injections, immunohistochemistry, confocal microscopy, figure preparation.

- Figure EV5: postnatal RWM injections, broadband click and tone burst sound-evoked ABR recordings, data analysis, statistics, figure preparation.

- Appendix Figure S1-S3: postnatal RWM injections, immunohistochemistry, confocal microscopy, figure preparation.

- Appendix Figure S4: RWM injections, broadband click and tone burst sound-evoked ABR recordings, data analysis, statistics, figure preparation.

The transduced $Otof^{-/-}$ inner ear depicted in Fig. 1A was injected by Dr. SangYong Jung (Institute for Auditory Neurosciences and InnerEarLab, University Medical Center Göttingen). The ABRs of a few dual-AAV-TS injected $Otof^{-/-}$ animals displayed in Fig. 3 and Fig. EV5 were measure by Stefan Thom (Department of Otorhinolaryngology, University Medical Center Göttingen). All AAVs used for the experiments in this thesis were packaged and produced by the Lab of Dr. Sebastian Kügler (Center Nanoscale Microscopy and Physiology of the Brain (CNMPB), Department of Neurology, University Medical Center Göttingen). All experiments and the subsequent data analysis were performed during the course of this thesis as described in the "materials and methods" section in "Al-Moyed *et al.*, 2019". The statistical analysis for all experiments was performed during my Ph.D. thesis as mentioned in "Al-Moyed *et al.*, 2019". The cloning of the two split-AAV-TS half vector

expression cassettes was started during my master thesis and later finished during the scope of this thesis. All figures mentioned above were prepared during this Ph.D. thesis as described in "Al-Moyed *et al.*, 2019". The manuscript for this publication was written, edited, and revised together with the other authors of the publication during the course of this thesis and published in 2019 (see the "authors contributions" section in "Al-Moyed *et al.*, 2019").

### 2.2.3  Publication

The results of this project were published by the "EMBO Molecular Medicine" journal in "Al-Moyed *et al.*, 2019" (see attached publication in "chapter 2.2.3").

Report

# A dual-AAV approach restores fast exocytosis and partially rescues auditory function in deaf otoferlin knock-out mice

Hanan Al-Moyed[1,2], Andreia P Cepeda[1,2] (iD), SangYong Jung[3,4], Tobias Moser[2,3,4] (iD), Sebastian Kügler[5,*] (iD) & Ellen Reisinger[1,**] (iD)

## Abstract

Normal hearing and synaptic transmission at afferent auditory inner hair cell (IHC) synapses require otoferlin. Deafness DFNB9, caused by mutations in the *OTOF* gene encoding otoferlin, might be treated by transferring wild-type otoferlin cDNA into IHCs, which is difficult due to the large size of this transgene. In this study, we generated two adeno-associated viruses (AAVs), each containing half of the otoferlin cDNA. Co-injecting these dual-AAV2/6 half-vectors into the cochleae of 6- to 7-day-old otoferlin knock-out ($Otof^{-/-}$) mice led to the expression of full-length otoferlin in up to 50% of IHCs. In the cochlea, otoferlin was selectively expressed in auditory hair cells. Dual-AAV transduction of $Otof^{-/-}$ IHCs fully restored fast exocytosis, while otoferlin-dependent vesicle replenishment reached 35–50% of wild-type levels. The loss of 40% of synaptic ribbons in these IHCs could not be prevented, indicating a role of otoferlin in early synapse maturation. Acoustic clicks evoked auditory brainstem responses with thresholds of 40–60 dB. Therefore, we propose that gene delivery mediated by dual-AAV vectors might be suitable to treat deafness forms caused by mutations in large genes such as *OTOF*.

## Introduction

Mutations in the *OTOF* gene cause profound congenital non-syndromic autosomal recessive hearing loss (DFNB9, Yasunaga *et al*, 1999). $Otof^{-/-}$ mice or animals with deleterious point

mutations in this gene are profoundly deaf (Roux *et al*, 2006; Longo-Guess *et al*, 2007; Pangrsic *et al*, 2010; Reisinger *et al*, 2011). The *OTOF* gene encodes otoferlin, a large multi-$C_2$-domain protein predominantly expressed in inner hair cells (IHCs), the genuine sensory cells in the cochlea. IHCs transform mechanical acoustic vibrations into a neural code via synaptic transmission to auditory neurons. Studies using $Otof^{-/-}$ and $Otof$ knock-in mouse models revealed that this protein plays an essential role in IHC exocytosis and vesicle replenishment, and is involved in vesicle reformation and endocytosis (Roux *et al*, 2006; Pangrsic *et al*, 2010; Duncker *et al*, 2013; Jung *et al*, 2015; Strenzke *et al*, 2016). To date, over one thousand pathogenic mutations have been identified within this gene, affecting 2.3–10% of patients from various ethnicities suffering from hereditary non-syndromic hearing loss (Rodríguez-Ballesteros *et al*, 2008; Choi *et al*, 2009; Iwasa *et al*, 2013; Van Camp & Smith). In contrast to many other deafness or Usher genes, otoferlin seems dispensable for auditory hair cell (HC) development (Roux *et al*, 2006). Given the normal inner ear morphology in these patients, a postnatal transfer of otoferlin cDNA into the inner ear is predicted to ameliorate this hearing loss. Gene therapy might outperform the otherwise necessary cochlear implantation, which transmits only part of the acoustic information. Cochlear implant users often report difficulties in speech understanding during noise and in perceiving vocal emotions, and typically cannot experience music as a person without hearing impairment (Fu *et al*, 1998; Nelson *et al*, 2003; McDermott, 2004; Luo *et al*, 2007; Most & Aviner, 2009; Oxenham & Kreft, 2014; Chatterjee *et al*, 2015; Paquette *et al*, 2018). Yet, no delivery method for large genes, like electroporation or viral transduction via adenoviruses, lentiviruses, or semliki forest viruses, transferred cDNA into HCs in the postnatal inner ear with high efficiency. Recombinant adeno-associated viruses (AAVs) are a safe and promising gene therapy tool to treat hearing impairment (reviewed in Ref. Géléoc & Holt, 2014). Prenatal injections of AAVs into the developing otocyst or postnatal cochlear injections have been proven

1 Molecular Biology of Cochlear Neurotransmission Group, Department of Otorhinolaryngology, University Medical Center Göttingen, and Collaborative Research Center 889, University of Göttingen, Göttingen, Germany
2 Göttingen Graduate School for Neurosciences, Biophysics, and Molecular Biosciences, University of Göttingen, Göttingen, Germany
3 Institute for Auditory Neurosciences and InnerEarLab, University Medical Center Göttingen, Göttingen, Germany
4 Synaptic Nanophysiology Group, Max Planck Institute for Biophysical Chemistry, Göttingen, Germany
5 Center Nanoscale Microscopy and Physiology of the Brain (CNMPB), Department of Neurology, University Medical Center Göttingen, Göttingen, Germany
*Corresponding author. Tel: +49 551 39 8351; E-mail: sebastian.kuegler@med.uni-goettingen.de
**Corresponding author. Tel: +49 551 39 9688; E-mail: ellen.reisinger@med.uni-goettingen.de

to efficiently transduce IHCs in animal models (Liu *et al*, 2005; Bedrosian *et al*, 2006). However, the limited AAV cargo capacity of approximately 4.7–5 kb presents an obstacle for the transfer of large coding sequences (CDS) such as the 6 kb-long otoferlin cDNA. Split-AAV vectors, each containing a fragment of the large transgene expression cassette, have been developed to circumvent this problem. This technique takes advantage of the intrinsic ability of the AAV genome to form tail-to-head concatemers by end-joining of its inverted terminal repeats (ITRs) (Duan *et al*, 1998). In the "trans-splicing (TS)" strategy, the ITRs are spliced out after transcription by introducing artificial splice donor (SD) and acceptor (SA) sites before and after the ITRs in the respective half-vectors. The reconstitution of the large transgene can also be mediated through homologous recombination of overlapping sequences placed at the 3′-end of the first AAV half-vector and at the 5′-end of the second in the "overlap" split-AAV strategy. The "hybrid" strategy is a combination of both previous strategies (Ghosh *et al*, 2008). The correct reassembly of the full-length expression cassette in the nuclei of target cells results in the production of full-length mRNA and protein (Yan *et al*, 2000; Duan *et al*, 2001; Chamberlain *et al*, 2016). To date, dual- and triple-AAV vectors have demonstrated efficacy in photoreceptors and muscle cells (Duan *et al*, 2001; Ghosh *et al*, 2008; Trapani *et al*, 2014; Maddalena *et al*, 2018), but have not been established for IHCs.

## Results and Discussion

In this study, we investigated whether the delivery of full-length otoferlin cDNA into IHCs via dual-AAV vectors can restore defective IHC and auditory functions in *Otof*$^{-/-}$ mice. We aimed for a rather late time point of treatment, since the early development of the inner ear does not seem to require otoferlin (Roux *et al*, 2006), making gene therapy of mature *Otof*$^{-/-}$ IHCs feasible in theory. AAVs were injected into the cochlea at postnatal day 6–7 (P6–7) because the auditory bulla structure covering the round window membrane (RWM) is still soft enough at this developmental stage to be penetrated well with an injection glass pipette. We chose AAVs with ITRs from serotype 2 and capsid proteins from serotype 6 (AAV2/6) as they can be produced with an excellent transducing-unit to vector-genome ratio (Grieger *et al*, 2016). This prevents administration of excess protein bolus into the delicate structure of the inner ear. To test whether this AAV serotype transduces IHCs efficiently, we injected single AAV2/6 viruses coding for eGFP through the RWM into the scala tympani of the left cochlea of CD1xC57BL/6N-F1 (CD1B6F1) wild-type mice. eGFP fluorescence was observed in IHCs, outer hair cells (OHCs), supporting cells, and spiral ganglion neurons (SGNs), indicating that the AAV2/6 has no specific IHC tropism and targets a variety of different cell types within the organ of Corti (Fig EV1A). 34–99% of IHCs (average = 77 ± 4%, mean ± standard error of the mean (s.e.m., *n* = 7 cochleae) exhibited eGFP fluorescence, revealing a high IHC transduction efficiency of the AAV2/6. This finding contrasts recent reports showing that AAV2/6 failed to transduce IHCs if injected at P1–2 (Shu *et al*, 2016). We assume that vector quality, titer, the injection procedure itself, and the animal age at the time of surgery are all factors influencing IHC transduction efficiency.

For gene replacement therapy in *Otof*$^{-/-}$ mice, we used mouse otoferlin transcript variant 4 cDNA (NM_001313767), coding for the

1977 amino acid-long protein and previously confirmed to be expressed endogenously in wild-type cochleae (Strenzke *et al*, 2016). We designed otoferlin dual-AAV-trans-splicing (dual-AAV-TS) and dual-AAV-hybrid (dual-AAV-Hyb) half-vectors, both containing the N-terminal otoferlin CDS in the 5′-AAV half-vector and the C-terminal CDS in the 3′-AAV vector (Fig EV2). Expression from the 5′AAV is driven by a human β actin promoter/CMV enhancer and additionally codes for a separately translated eGFP-fluorescent reporter to identify transduced cells in acutely isolated organs of Corti. These split-AAV vectors were co-injected through the RWM into the left cochlea of P6–7 CD1B6F1-*Otof*$^{-/-}$ mice. Organs of Corti from these animals were isolated at P18–30 and immunolabeled with two otoferlin antibodies, one binding within the N-terminal part of otoferlin and the other one binding after the transmembrane domain close to the C-terminus of otoferlin (Figs 1A–C and EV3, Appendix Fig S1–S3). Upon dual-AAV injection into *Otof*$^{-/-}$ cochleae, we found otoferlin immunofluorescence to be restricted to auditory HCs, with stronger expression in IHCs and much weaker in sparsely transduced OHCs (Appendix Fig S3), resembling otoferlin expression in wild-type animals (Roux *et al*, 2006; Beurg *et al*, 2008). eGFP fluorescence, on the contrary, was also found in other cell types (Figs 1A and EV1B, Appendix Fig S3), although the expression of both proteins is driven by the same promoter and they are translated from the same mRNA (Fig EV2). Neither eGFP nor otoferlin expression could be detected in contralateral non-injected ears (Fig 2A, Appendix Fig S1 and S2). We presume that a yet unknown mechanism such as post-transcriptional regulation or targeted protein degradation restricts the expression of otoferlin to auditory HCs. A similar finding was reported for AAV1 postnatal RWM injections (P1–3 and P10–12), where Vglut3 expression was found selectively in IHCs despite the broad cell type tropism of this AAV serotype (Akil *et al*, 2012). The restricted expression of otoferlin to HCs would be very beneficial for human gene therapy applications to avoid potential off-target effects due to expression of exogenous otoferlin in non-sensory cells in the inner ear.

The number of IHCs immunolabeled with both N-terminal and C-terminal otoferlin antibodies along the entire cochlea ranged from 12 to 51% in dual-AAV-TS (average: 30 ± 4%, *n* = 10 animals) and from 5 to 34% in dual-AAV-Hyb (average: 19 ± 3%, *n* = 9 animals) injected *Otof*$^{-/-}$ mice (Fig 1D). Approximately 10% of IHCs were solely labeled by the N-terminal otoferlin antibody, likely indicating no correct reassembly of the two virus half-vectors in on average one out of four transduced cells (Figs 1D and EV3). We did not find any IHC showing only a C-terminal otoferlin immunofluorescence signal, which was expected since the 3′-AAV half-vector does not contain a separate promoter. A previous study indicated that 70% of intact IHCs suffice for proper auditory function (Wang *et al*, 1997). Further studies will reveal if optimizing the virus administration procedure into the cochlea (e.g., as in ref. Yoshimura *et al*, 2018) might increase the otoferlin IHC transduction rate.

In order to examine whether the split full-length otoferlin expression cassette reassembled to produce the correct full-length mRNA in the target cells, we isolated mRNA from transduced *Otof*$^{-/-}$ organs of Corti (P26–29) and amplified otoferlin cDNA fragments spanning the dual-AAV split-site (Fig EV4). From dual-AAV-trans-duced *Otof*$^{-/-}$ organs of Corti and wild-type control samples, we amplified a PCR product with the size expected for full-length otoferlin cDNA (1,753 bp) that was absent in non-injected *Otof*$^{-/-}$
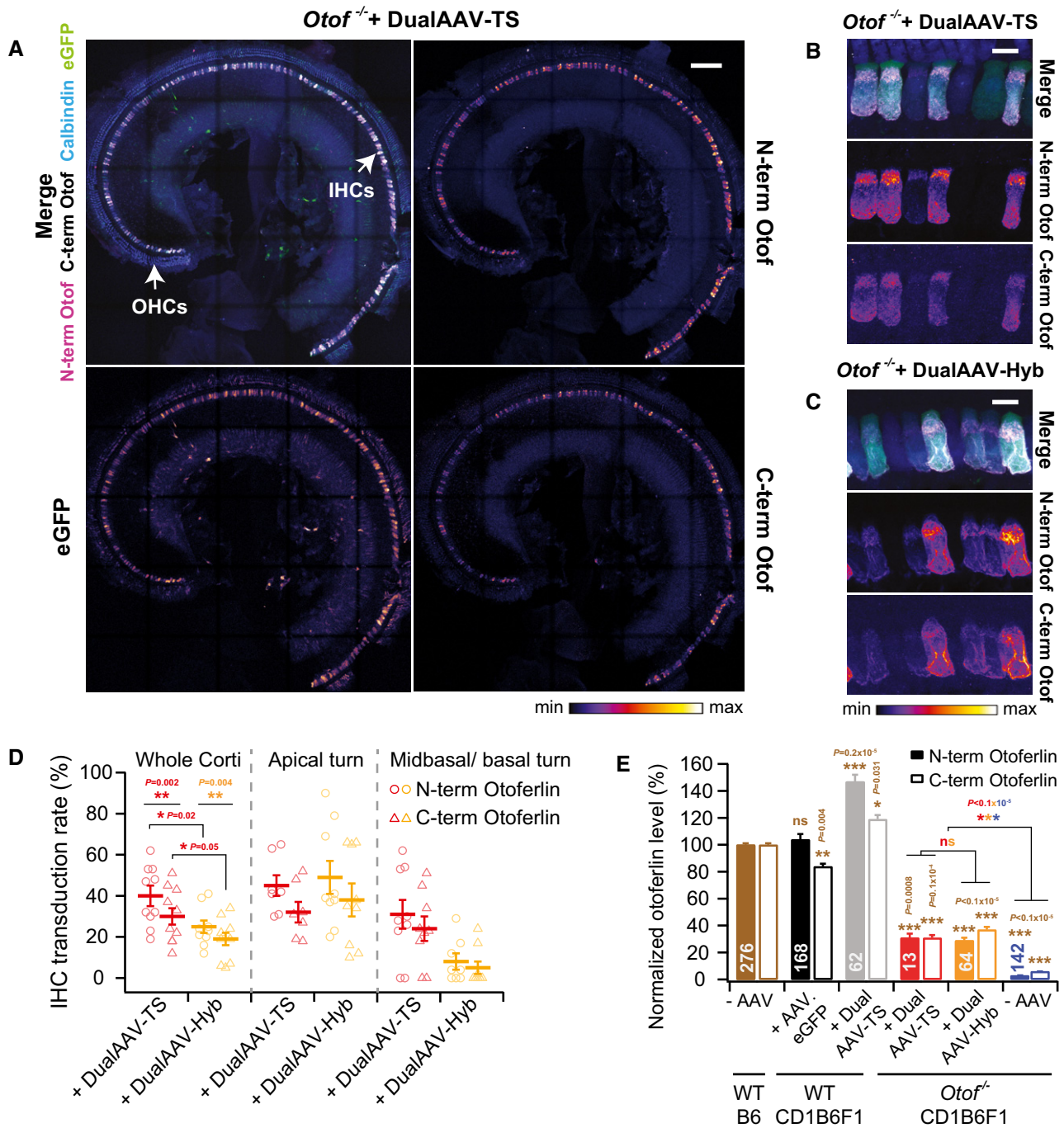
**Figure 1. Dual-AAV-mediated otoferlin expression is restricted to auditory hair cells in the cochlea.**

A    Low magnification views of a CD1-*Otof*⁻/⁻ organ of Corti (P23)-transduced with otoferlin dual-AAV-TS vectors. IHCs: inner hair cells, OHCs: outer hair cells.

B, C   High magnification views of CD1B6F1-*Otof*⁻/⁻ IHCs transduced with otoferlin dual-AAV-TS (P26) (B) and dual-AAV-Hyb (P26) (C) vectors. Individual eGFP and otoferlin immunostainings are depicted as color lookup tables in (A-C) with warmer colors representing higher pixel intensities. See Fig EV3 for comparison to wild-type IHCs.

D    Percentage of N- and C-terminal otoferlin labeled IHCs in dual-AAV-TS (*n* = 10 mice)- and dual-AAV-Hyb (*n* = 9 mice)-injected CD1B6F1-*Otof*⁻/⁻ mice (P18–30).

E    Average N-terminal and C-terminal otoferlin immunofluorescence levels in dual-AAV-transduced *Otof*⁻/⁻ and wild-type IHCs (P23–30). Otoferlin levels were normalized to immunofluorescence levels in non-transduced B6 wild-type IHCs for each antibody separately.

Data information: In (A–C), maximum intensity projections of confocal optical sections. Scale bars: 100 μm (A), 10 μm (B, C). In (D), individual animals are depicted with open symbols. In (E), the number of quantified IHCs is indicated inside the bars. In (D, E), data are displayed as mean ± s.e.m., ns *P* > 0.05; *$P \leq 0.05$; **$P \leq 0.01$; ***$P \leq 0.001$, [Wilcoxon matched-pair signed rank test (D), unpaired t-test with Welch's correction (D), and Kruskal–Wallis test followed by Dunn's multiple comparison test (E)].
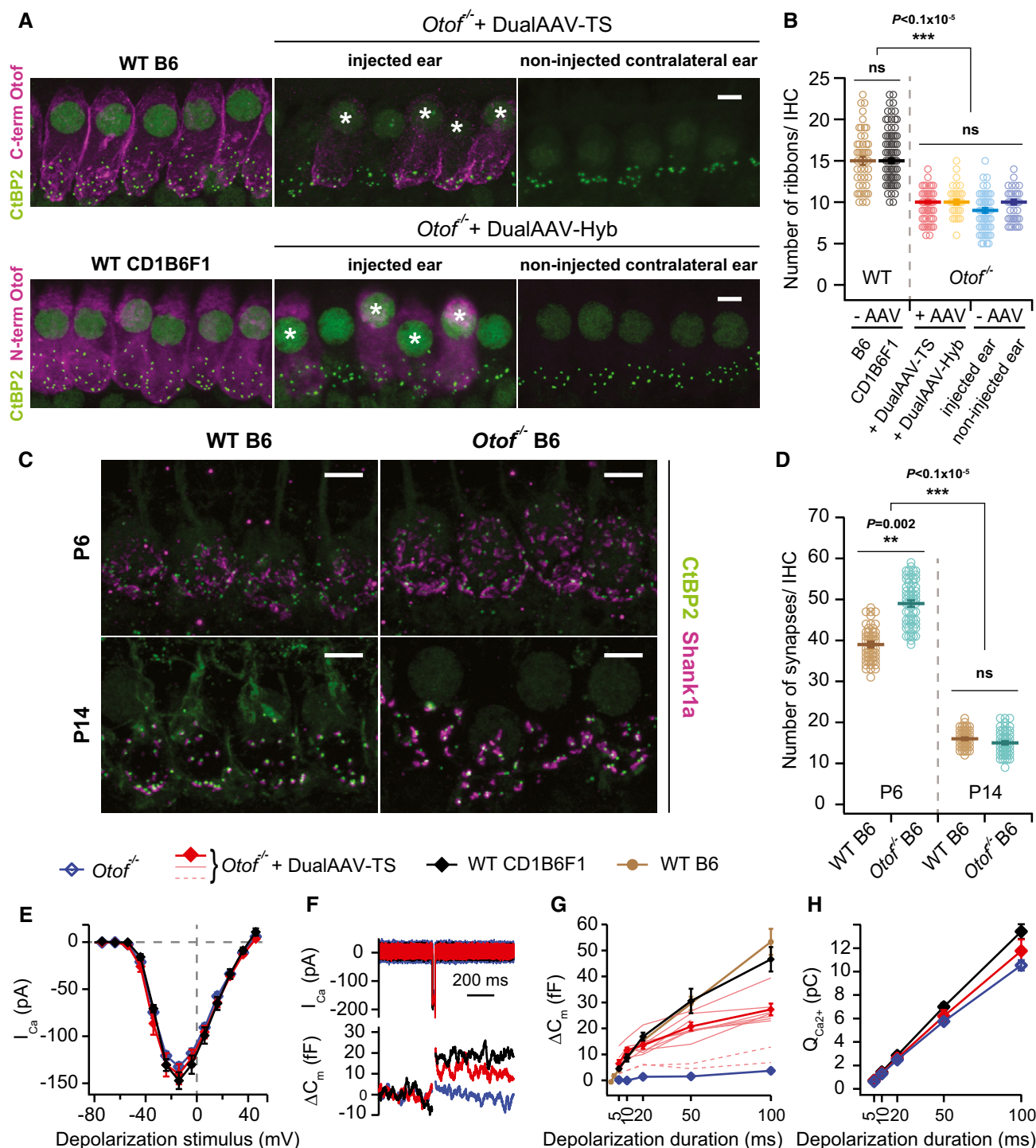
**Figure 2.**

organ of Corti samples (Fig EV4A and B). Amplicons from wild-type, control *Otof*$^{-/-}$, and dual-AAV-TS-transduced *Otof*$^{-/-}$ samples were subcloned and representative clones were subjected to Sanger sequencing (*n* = 2 clones/4 clones/5 clones, respectively; Fig EV4B and C). This confirmed the correct reconstitution of the full-length transgene from the two otoferlin AAV half-vectors and the presence of an artificially introduced AccIII restriction site found only in the dual-AAV-transduced *Otof*$^{-/-}$ samples (Fig EV4C). In cDNA

samples of dual-AAV-injected and non-treated *Otof*$^{-/-}$ organs of Corti, we amplified three otoferlin cDNA fragments of 1,379, 1,480, and 1,679 bp, all lacking exons 14 and 15 (Fig EV4B and C). The larger amplicons originate from incomplete splicing of the mutant mRNA (Fig EV4C). These splice variants might be translated into shorter fragments, the presence of which we assessed by Western blot (Fig EV4D). In wild-type organs of Corti, we detected two specific bands of ~210–230 kDa, likely corresponding to full-length

> **Figure 2.  Otoferlin dual-AAV injection at P6–7 partially restores synaptic function in *Otof*$^{-/-}$ IHCs.**
>
> A    High magnification views of IHCs immunolabeled for otoferlin and synaptic ribbons (CtBP2) from wild-type (B6: P27, CD1B6F1: P29), dual-AAV-injected CD1B6F1-*Otof*$^{-/-}$ (dualAAV-TS: P26, dualAAV-Hyb: P28), and their contralateral non-injected ears. (*) Transduced cells. Maximum intensity projections of optical confocal sections. Scale bars: 5 µm.
>
> B    Synaptic ribbon numbers quantified from IHCs in apical cochlear turns of wild-type (B6: *n* = 48 IHCs, CD1B6F1: *n* = 108 IHCs), transduced *Otof*$^{-/-}$ (dualAAV-TS: *n* = 59 IHCs, dualAAV-Hyb: *n* = 37 IHCs), and non-transduced *Otof*$^{-/-}$ IHCs from injected (-AAV-injected ear, *n* = 65 IHCs) and contralateral non-injected (-AAV non-injected ear, *n* = 46 IHCs) ears (P25–29).
>
> C    IHC synapses labeled with CtBP2 and the postsynaptic marker Shank1a in B6 wild-type and *Otof*$^{-/-}$ P6 and P14 organs of Corti. Maximum intensity projections of optical confocal sections. Scale bars: 5 µm.
>
> D    Synapse numbers quantified from IHCs in apical cochlear turns (C) of B6 wild-type (P6: *n* = 53 IHCs; P14: *n* = 73 IHCs) and B6-*Otof*$^{-/-}$ (P6: *n* = 62 IHCs; P14: *n* = 65 IHCs) mice at two different developmental stages (P6 and P14).
>
> E    Ca$^{2+}$-current–voltage relationship of control CD1B6F1 wild-type (*n* = 6 IHCs), dual-AAV-TS-transduced (*n* = 8 IHCs), and non-transduced CD1B6F1-*Otof*$^{-/-}$ (*n* = 10 IHCs) IHCs (P14–18).
>
> F    Representative Ca$^{2+}$-currents (I$_{ca}$) and IHC plasma membrane capacitance increments (ΔC$_m$) of a wild-type control, transduced, and non-transduced *Otof*$^{-/-}$ IHC in response to a 20 ms depolarization pulse at maximum Ca$^{2+}$-current potentials (typically −14 mV).
>
> G, H    Average exocytosis level measured as ΔC$_m$ (G) and corresponding Ca$^{2+}$-current integrals (Q$_{Ca2+}$) (H) in wild-type [CD1B6F1: *n* = 6 IHCs; B6: *n* = 11 IHCs (B6 data replotted from Strenzke *et al*, 2016)], dual-AAV-TS-transduced *Otof*$^{-/-}$ (*n* = 8 IHCs), and non-transduced (*n* = 11 IHCs) *Otof*$^{-/-}$ IHCs. Individual dual-AAV-TS transduced *Otof*$^{-/-}$ IHCs expressing eGFP, that had exocytosis (thinner red lines) and almost no exocytosis (broken red lines; not included into the average), are depicted.
>
> Data information: In (B, D), individual animals are depicted with open symbols. In (G), individual transduced *Otof*$^{-/-}$ IHCs are displayed with thinner or broken red lines. In (B, D, E, G, H), data are displayed as mean ± s.e.m., ns *P* > 0.05; **$P$ ≤ 0.01; ***$P$ ≤ 0.001 (Kruskal–Wallis test followed by Dunn's multiple comparison test).

otoferlin, which were absent in *Otof*$^{-/-}$ controls. However, due to a strong unspecific band at ~100 kDa, the presence of smaller otoferlin fragments that might interfere with the function of full-length otoferlin could not be excluded.

To quantify full-length otoferlin protein expression levels, we measured the fluorescence intensity of the C-terminal otoferlin antibody in transduced *Otof*$^{-/-}$ IHCs and normalized it to the C-terminal immunofluorescence in wild-type C57BL/6J (B6) IHCs (Figs 1E and EV3). Dual-AAV-mediated gene transfer into *Otof*$^{-/-}$ IHCs led to the expression of full-length otoferlin protein with 31–37% of wild-type levels (Fig 1E). We found the intracellular pattern of N- and C-terminal otoferlin immunolabeling in transduced *Otof*$^{-/-}$ IHCs to be similar to wild-type IHCs (Fig EV3). Non-transduced *Otof*$^{-/-}$ IHCs from contralateral non-injected ears displayed very weak N-terminal and C-terminal background otoferlin fluorescence signals of 3 ± 0.0% and 6 ± 0.0% of wild-type levels, respectively (Fig 1E, Appendix Fig S1 and S2). In dual-AAV-TS-transduced wild-type IHCs, the eGFP fluorescence signal was weaker than in those cells transduced with the single AAV2/6.eGFP virus (Figs EV1 and EV3).

An earlier study reported that *Otof*$^{-/-}$ IHCs have normal ribbon synapse numbers at P6, but only 60% of their synapses persist after P15 (Roux *et al*, 2006). By counting the number of CtBP2-labeled synaptic ribbons, we examined whether re-expressing otoferlin via dual-AAV vectors could reverse this loss (Fig 2A and B). At P26–29, *Otof*$^{-/-}$ IHCs from contralateral non-injected ears have 10 ± 0.3 synaptic ribbons (*n* = 46 IHCs), similar to non-transduced *Otof*$^{-/-}$ IHCs in injected ears (9 ± 0.3 ribbons, *n* = 65 IHCs). This is ~40% less than the 15 ± 0.3 synaptic ribbons in CD1B6F1 wild-type IHCs (*n* = 108 IHCs) and 15 ± 0.5 synaptic ribbons in B6 wild-type IHCs (*n* = 48 IHCs). Upon dual-AAV-mediated otoferlin expression, we found 10 ± 0.2 synaptic ribbons in dual-AAV-TS-transduced *Otof*$^{-/-}$ IHCs (*n* = 59 IHCs) and 10 ± 0.3 synaptic ribbons in dual-AAV-Hyb-transduced *Otof*$^{-/-}$ IHCs (*n* = 37 IHCs), which is virtually identical to the ribbon numbers in *Otof*$^{-/-}$ IHCs from contralateral non-injected ears. Thus, otoferlin gene delivery at P6–7 is apparently too late to prevent or reverse any synapse loss in *Otof*$^{-/-}$ IHCs. Accordingly, we re-assessed IHC synapse numbers in B6-*Otof*$^{-/-}$ and wild-type mice at P6 and P14 (Fig 2C and D). IHC synapses were identified as

CtBP2-labeled synaptic ribbons adjacent to Shank1a immunolabeled postsynaptic boutons (Huang *et al*, 2012). We found more synapses in P6 *Otof*$^{-/-}$ IHCs (49 ± 0.7 synapses; *n* = 62 IHCs) than in wild-type IHCs (39 ± 0.3 synapses; *n* = 53 IHCs). In the second postnatal week, synapse numbers decreased, reaching comparable numbers at P14 for *Otof*$^{-/-}$ mice (15 ± 0.3 synapses; *n* = 65 IHCs) and wild-type mice (16 ± 0.2 synapses; *n* = 73 IHCs, Fig 2D) pointing to a developmental delay in synapse loss compared to the *Otof*$^{-/-}$ mice assessed in Roux *et al* (2006). Notably, Shank1a labeled postsynaptic structures appeared larger in *Otof*$^{-/-}$ than in wild-type IHCs (Fig 2C). These findings, together with the failure to rescue synapse numbers by otoferlin re-expression from P6–7 on, point toward a yet undescribed role of otoferlin in IHC synapse maturation.

In rodents, SGNs diversify in the first four postnatal weeks into low, medium, and high spontaneous rate fibers to encode different sound intensities (Liberman & Liberman, 2016). In mature *Vglut3*$^{-/-}$ mice lacking ~40% of SGNs (Seal *et al*, 2008), almost all low spontaneous rate fibers and half of the medium rate fibers are missing (Shrestha *et al*, 2018). Similarly, aging or mild noise trauma result in the selective loss of low spontaneous rate fibers, which does not affect auditory thresholds, but likely impairs speech comprehension (Furman *et al*, 2013; Wu *et al*, 2018). It is currently unclear which type of auditory nerve fibers might be affected by the synapse loss in *Otof*$^{-/-}$ mice, whether synapse loss occurs at all in human patients and if so whether this would affect hearing after gene therapy. While SGN subtypes in *Otof*$^{-/-}$ mice could be identified by their molecular markers as in Shrestha *et al* (2018), future animal studies will be required to characterize spontaneous and sound-evoked firing rates of auditory nerve fibers in dual-AAV-treated *Otof*$^{-/-}$ mice. Co-administration of neurotrophic factors could additionally be tested to rescue these synapses (Wan *et al*, 2014; Suzuki *et al*, 2017).

By using cellular electrophysiological recordings, we investigated whether dual-AAV-mediated otoferlin gene transfer can rescue otoferlin-dependent fast exocytosis and synaptic vesicle replenishment in *Otof*$^{-/-}$ IHCs (Roux *et al*, 2006; Pangrsic *et al*, 2010; Fig 2E–H). Transduced IHCs in acutely isolated organs of Corti (P14–P18) were identified by their eGFP fluorescence and measured via perforated patch-clamp. Here, we found no difference in

voltage-gated Ca$^{2+}$-currents between dual-AAV-TS-transduced $Otof^{-/-}$ ($n = 8$ IHCs), non-transduced $Otof^{-/-}$ ($n = 10$ IHCs), and control CD1B6F1 wild-type IHCs ($n = 6$ IHCs, Fig 2E and H). Ca$^{2+}$-triggered exocytosis of the readily releasable synaptic vesicle pool (RRP) was measured as IHC plasma membrane capacitance increments ($\Delta C_m$) after short depolarization pulses (5–20 ms) eliciting Ca$^{2+}$ influx. Dual-AAV-mediated re-expression of otoferlin fully restored fast exocytosis of the RRP in $Otof^{-/-}$ IHCs (for 20 ms depolarization: wild-type CD1B6F1: 16.8 $\pm$ 1.4 fF, dual-AAV-TS-transduced $Otof^{-/-}$: 13.5 $\pm$ 1.3 fF; wild-type B6: 15.3 $\pm$ 1.6 fF (from Strenzke *et al*, 2016); $P = 0.3$, one-way ANOVA; non-transduced $Otof^{-/-}$: 1.4 $\pm$ 0.8 fF, $P = 1 \times 10^{-7}$, two-tailed t-test for transduced vs. non-transduced $Otof^{-/-}$ IHCs; Fig 2F and G). In agreement with our finding that around one out of four eGFP-fluorescent IHCs only expressed the N-terminal part of otoferlin (Figs 1D and EV3), we recorded two (out of ten) eGFP-expressing IHCs with hardly any Ca$^{2+}$-triggered exocytosis (broken red lines), similarly to non-transduced $Otof^{-/-}$ IHCs (Fig 2G). Presumably, the correct reassembly of the full-length otoferlin expression cassette in the right orientation did not take place in these two transduced IHCs. The lack of exocytosis in these cells is in agreement with earlier results (Reisinger *et al*, 2011), demonstrating that AAV-mediated co-expression of eGFP and synaptotagmin-1 neither rescued exocytosis in $Otof^{-/-}$ IHCs nor restored hearing in injected $Otof^{-/-}$ mice. Therefore, it can be ruled out that the AAV itself and/or the eGFP are able to recover exocytosis in the absence of otoferlin.

In contrast to the full rescue of fast exocytosis, sustained IHC exocytosis measured upon longer depolarization pulses (20–100 ms) and requiring otoferlin-dependent synaptic vesicle replenishment was only partially restored (Fig 2G). The estimated number of synaptic vesicles undergoing exocytosis between 20 and 100 ms of continuous depolarization in an average IHC synapse increased from 50 $\pm$ 13 synaptic vesicles/second/active zone (SV/s/AZ) in non-transduced $Otof^{-/-}$ ($n = 9$ IHCs) to 247 $\pm$ 20 SV/s/AZ in transduced $Otof^{-/-}$ IHCs ($n = 7$ IHCs) ($P < 0.0001$, two-tailed t-test). Still, these vesicle replenishment rates were 50 or 65% lower than in CD1B6F1 wild-type (522 $\pm$ 59 SV/s/AZ, $n = 5$ IHCs) or B6 wild-type IHCs (698 $\pm$ 60 SV/s/AZ, $n = 8$ IHCs) ($P = 0.0005$ for dual-AAV-TS vs. CD1B6F1 and $P < 0.0001$ for dual-AAV-TS vs. B6, Sidak's multiple comparisons test).

Otoferlin knock-out mice are profoundly deaf, and no auditory brainstem responses (ABRs) can be evoked by broadband click or tone burst sound stimuli (Roux *et al*, 2006; Pangrsic *et al*, 2010). Nevertheless, distortion product otoacoustic emissions (DPOAEs), measuring OHC amplification, and electrically evoked brainstem responses (eEBRs), measuring signal transmission through the afferent auditory pathway, are both normal in these mice and indicate that the impairment is specifically caused by a defect in the IHCs (Roux *et al*, 2006). We examined whether the dual-AAV strategy is able to restore auditory function in these animals by measuring ABRs in response to broadband clicks and tone bursts at different sound pressure levels (SPL) in 3- to 4-week-old (P23–30) dual-AAV-TS- ($n = 17$ mice) and dual-AAV-Hyb- ($n = 8$ mice) injected $Otof^{-/-}$ animals (Figs 3 and EV5). The characteristic ABR waveforms were partially rescued in all animals treated with otoferlin dual-AAV vectors (Figs 3A and B, and EV5A). Particularly, ABR waves II-V were clearly identifiable and served to determine ABR thresholds. In contrast, no ABRs could be elicited in non-treated

(-AAV) $Otof^{-/-}$ control littermates ($n = 38$ mice). Otoferlin dual-AAV injections restored auditory function with click-evoked ABR thresholds of 49 $\pm$ 1 dB SPL in dual-AAV-TS and 51 $\pm$ 1 dB SPL in dual-AAV-Hyb-transduced $Otof^{-/-}$ animals (range: 40–60 dB SPL; Fig 3C). In comparison, we measured click ABR thresholds of 32 $\pm$ 2 dB SPL in CD1B6F1 wild-type control animals injected with AAV2/6.eGFP ($n = 12$ mice) and 32 $\pm$ 2 dB SPL in otoferlin dual-AAV-TS-transduced wild-type mice ($n = 6$ mice; range: 20–40 dB SPL). In agreement with previous observations (Roux *et al*, 2006; Longo-Guess *et al*, 2007; Pangrsic *et al*, 2010; Reisinger *et al*, 2011), we recorded a prominent summating potential (SP) in non-treated $Otof^{-/-}$ mice evoked by the concerted depolarization of inner and outer HCs in response to broadband clicks (Figs 3A and B, and EV5A). The larger size of the SP compared to normal hearing animals is likely caused by the absence of efferent OHC inhibition, which requires auditory signal transmission along the afferent pathway (Fuchs & Lauer, 2018). In some dual-AAV-TS- and dual-AAV-Hyb-injected $Otof^{-/-}$ mice, the SP amplitude was similar to normal hearing mice, where AAV injection did not change the SP amplitude. Even though injection-induced HC loss cannot be excluded in $Otof^{-/-}$ mice, it seems plausible that the rescue of auditory signal transmission has activated the medial superior olivary nucleus (MSO), which hyperpolarizes OHCs by inhibitory synaptic contacts.

Tone burst ABR thresholds in dual-AAV-treated $Otof^{-/-}$ mice were generally much more variable between individual animals than click ABR thresholds (Figs 3D and EV5B). The discrepancy between consistently low ABR click thresholds compared to on average higher tone burst thresholds was also reported for $Vglut3^{-/-}$ mice rescued with a single AAV1 Vglut3-expressing virus (Akil *et al*, 2012). In our best mice, 8 and 12 kHz tone bursts of 50 dB SPL elicited ABRs (Figs 3D and EV5B). These frequencies are sensed in the apical half-turn of the mouse cochlea, where we found the highest IHC transduction rates (Fig 1D). The high variability can be explained as low SPL tone bursts induce a sharply tuned vibration of the basilar membrane only activating few IHCs that need to be transduced in order to evoke an ABR. Higher sound pressure levels cause a broader vibration peak of the basilar membrane and thus activate more IHCs, especially if the levels are high enough that OHC amplification is suppressed. In contrast, click sound stimuli contain a broadband of frequencies that activate IHCs along the entire cochlea, eliciting a measurable ABR as long as some IHCs have been transduced. In fact, we found no correlation between full-length otoferlin IHC transduction rates (entire cochlea, C-term otoferlin, Fig 1D) in dual-AAV-TS-treated animals and their individual click ABR thresholds ($n = 8$ mice; $r = -0.41$, $P = 0.5$, Spearman correlation test; Fig EV5C). Apparently, a click ABR threshold of ~50 dB can be established by very few dual-AAV-transduced IHCs. Improving dual-AAV vectors to gain higher otoferlin protein levels might result in even lower ABR thresholds, because synapses contacting low threshold SGNs might require a high vesicle replenishment rate, which correlates with the amount of otoferlin in IHCs (Strenzke *et al*, 2016).

Next, we quantified click ABR wave amplitudes in dual-AAV-treated $Otof^{-/-}$ mice, which were overall lower than in wild-type control mice (Figs 3E and EV5D–H). The ABR wave I amplitude, representing the summed activity of the auditory nerve, was very small and slightly delayed (Fig EV5D and I). This might be explained by the presence of fewer fully functional IHCs, fewer
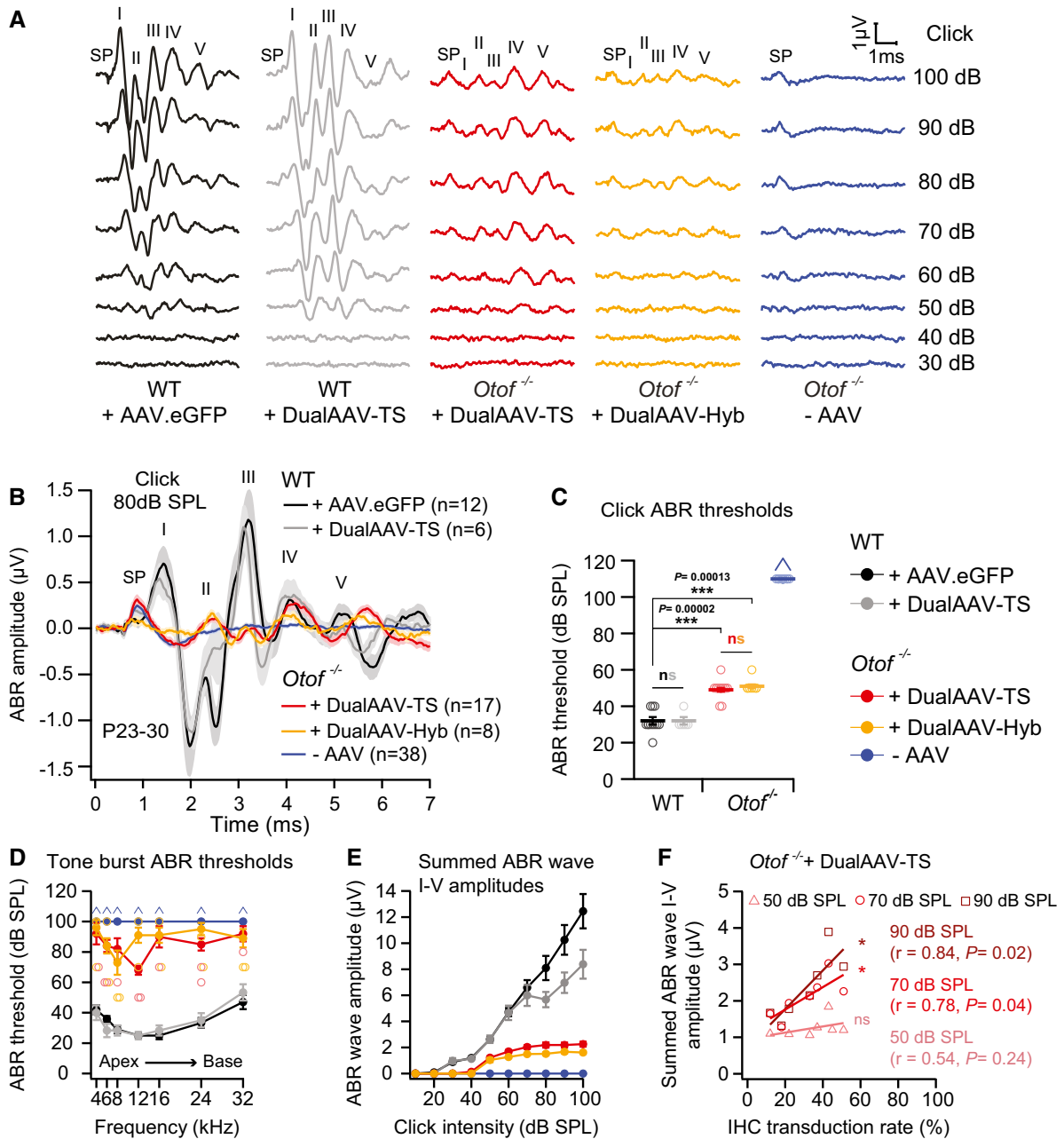
**Figure 3. Dual-AAV-mediated otoferlin gene delivery partially restores auditory function in deaf *Otof*^{−/−} mice.**

A    Representative ABR wave traces in response to broadband click sound stimuli from otoferlin dual-AAV-TS (P26) and dual-AAV-Hyb (P27)-injected CD1B6F1-*Otof*^{−/−} animals. AAV2/6.eGFP (+AAV.eGFP; P28) and dual-AAV-TS (P27)-injected CD1B6F1 wild-type, and non-injected control *Otof*^{−/−} littermate (-AAV; P26) mice served as controls. SP: summating potential; ABR waves are indicated from I–V.

B    Average ABRs evoked by 80 dB SPL click sound stimuli for 20 clicks/s.

C, D    ABR click sound (C) and tone burst (D) thresholds in otoferlin dual-AAV-treated *Otof*^{−/−} mice compared to wild-type and non-treated *Otof*^{−/−} control animals. In (D), the two best animals are depicted with open circles. Animals with thresholds exceeding the maximum loudspeaker output (arrows) of 100 dB SPL for clicks and 90 dB SPL for tone bursts were set to 110 dB SPL and 100 dB SPL, respectively. Apical and basal cochlear turns are indicated as Apex and Base, respectively.

E    Summed ABR wave I–V amplitudes at different click sound intensities in otoferlin dual-AAV-injected, non-injected *Otof*^{−/−}, and wild-type control mice.

F    Summed ABR wave I–V amplitudes of individual dual-AAV-TS-treated CD1B6F1-*Otof*^{−/−} animals (n = 8 animals; from Fig 3E) plotted against their full-length otoferlin IHC transduction rates (from Fig 1D, C-term otoferlin). r: correlation coefficient.

Data information: In (B–F), age of analyzed animals: P23–30. In (B, C, E), number of analyzed mice: CD1B6F1 wild-type animals (+AAV.eGFP: n = 12 mice, dualAAV-TS: n = 6 mice) and CD1B6F1-*Otof*^{−/−} animals (dualAAV-TS: n = 17 mice, dualAAV-Hyb: n = 8 mice, -AAV: n = 38 mice). In (D), number of analyzed mice is the same as for (B, C, E) except: CD1B6F1-*Otof*^{−/−} animals (dualAAV-TS: n = 16 mice). In (B–E), data are represented as mean ± s.e.m. In (C, D, F), individual animals are depicted with open symbols. In (F), r ≥ 0.5 positive correlation (70 dB SPL and 90 dB SPL: Pearson correlation test; 50 dB SPL: Spearman correlation test). In (C), ns P > 0.05; *P ≤ 0.05; ***P ≤ 0.001 (Kruskal–Wallis test followed by Dunn's multiple comparison test).

synapses in these cells, and lower otoferlin protein levels in treated $Otof^{-/-}$ compared to wild-type mice, the latter most likely reducing spike synchrony (Buran *et al*, 2010; Bourien *et al*, 2014; Strenzke *et al*, 2016). The normal ABR wave II-IV latencies (Fig EV5I) and the increase in ABR wave amplitudes along the auditory pathway (Fig EV5D–H) suggest some degree of central auditory compensation of the peripheral sound encoding. Higher full-length otoferlin IHC transduction rates (entire cochlea, C-term otoferlin; Fig 1D) correlated with higher overall ABR wave amplitudes ($n = 8$ mice, $r = 0.78$ at 70 dB SPL and $r = 0.84$ at 90 dB SPL; $P = 0.040$ and $P = 0.017$, Pearson correlation test; Fig 3F). Consequently, we expect that increasing the full-length otoferlin IHCs transduction rate, e.g., by optimizing the injection procedure, will further improve ABR wave amplitudes.

Injecting AAV2/6.eGFP or otoferlin dual-AAV-TS vectors into the cochleae of wild-type mice had hardly any detrimental effects on auditory function when compared to non-treated control CD1B6F1 wild-type mice ($n = 6$ mice, average click threshold: $30 \pm 0$ dB SPL; Fig 3, Appendix Fig S4). No difference between injected and non-injected contralateral wild-type ears was observed in ABR wave I amplitude and wave I–V latencies (Appendix Fig S4C,E). Even though we did not observe an apparent HC loss in our immunohistochemical analyses and click ABR thresholds were unaffected, a minor elevation of the 24 kHz ABR threshold (Appendix Fig S4B) might point to potential damage of HCs by the injection. The sensory cells of the inner ear are particularly sensitive to pressure and volume changes that might occur while injecting the virus solution into the cochlea (Yoshimura *et al*, 2018). In addition, we found a reduction in ABR wave II-V amplitudes in injected compared to non-injected ears (Appendix Fig S4A,D), the origin of which is unclear.

It is interesting to note the similarities in otoferlin protein levels, sustained IHC exocytosis levels, ABR thresholds, and ABR wave amplitudes between dual-AAV-treated $Otof^{-/-}$ mice and the mildly hearing impaired $Otof^{I515T/I515T}$ mice (Strenzke *et al*, 2016). Hence, the treatment of DFNB9 patients with otoferlin dual-AAV vectors might result in almost normal auditory thresholds, but also in impaired speech comprehension and auditory fatigue similar to the hearing phenotype found in DFNB9 patients with the p.Ile515Thr mutation (Varga *et al*, 2006; Wynne *et al*, 2013). Since sustained exocytosis and auditory function seem to scale with otoferlin protein levels (Strenzke *et al*, 2016), we assume that increasing otoferlin protein expression levels via optimized dual-AAV half-vectors would consequently improve vesicle replenishment rates and cochlear function. In order to achieve this goal, the process of joining the two vector genomes in the correct orientation, the transcription efficiency, and the translation of the full-length transcript will need to be enhanced, e.g., by using codon-optimized cDNA. Nevertheless, improving the large transgene reconstitution efficacy by simply increasing the amount of available vector genomes does not improve protein expression levels as shown for dual-AAV vectors in the retina (Carvalho *et al*, 2017). Since the IHC transduction rates of our single AAV2/6 eGFP-expressing virus reached 99%, it is unlikely that other AAV serotypes such as AAV2/Anc80 (Landegger *et al*, 2017; Suzuki *et al*, 2017) will increase the amount of fully functional otoferlin protein levels in IHCs.

Even though dual-AAV-mediated otoferlin expression currently reaches only one third of wild-type protein levels, this might already be sufficient to substantially ameliorate the disease phenotype (e.g.,

improve speech comprehension) of *OTOF* patients with residual otoferlin expression. However, otoferlin protein fragments, caused by mutations inducing a premature STOP codon or resulting from incomplete reconstitution of the two split-AAV half-vectors, might compete with full-length otoferlin and consequently inhibit its function.

In conclusion, we provide a proof of concept that dual-AAV vector systems are suitable for the delivery of large transgenes such as otoferlin into mammalian IHCs and can at least partially restore auditory function. Further refinement of the split-AAV vectors, testing which AAV serotypes are most suitable for human application, and optimization of the injection procedure will pave the way for future gene replacement therapies of recessively inherited deafness forms like DFNB9.

# Materials and Methods

### Study approval

Animal handling and experiments complied with national animal care guidelines and were approved by the board for animal welfare of the University of Göttingen and the animal welfare office of the state of Lower Saxony, Germany.

### Animals

CD1xC57BL/6N-F1 (CD1B6F1) $Otof^{-/-}$ mice were obtained by crossing CD1-$Otof^{-/-}$ female with C57BL/6N-$Otof^{-/-}$ male mice (Reisinger *et al*, 2011). For wild-type controls, we cross-bred CD1 wild-type female mice (Charles River) with B6 wild-type ($Otof^{+/+}$) male mice, or used C57BL/6J mice (B6). Animals of both genders were used for all experiments. The mice were housed in social groups in individually ventilated cage (IVC) racks in a specific pathogen-free facility with free access to food and water and 12-h/12-h light/dark cycles.

### Dual-AAV constructs

Both otoferlin dual-5′AAV-TS and 5′AAV-Hyb half-vectors contained the human beta-actin promoter (hbA), a cytomegalovirus enhancer ($CMV_e$), eGFP, a P2A peptide sequence inducing ribosome skipping (Kim *et al*, 2011), the first half of the otoferlin coding sequence (CDS), and a splice donor sequence (SD; Trapani *et al*, 2014) at the 3′-end (Fig EV2). The dual-3′AAV-TS and 3′AAV-Hyb half-vectors contained a splice acceptor sequence (SA; Trapani *et al*, 2014) at the 5′-end, the second half of the otoferlin CDS, a woodchuck hepatitis virus post-transcriptional regulatory element (WPRE), and a bovine growth hormone polyadenylation sequence (pA). The dual-5′AAV-Hyb and 3′AAV-Hyb half-vectors additionally contained a highly recombinogenic sequence derived from the F1 phage (AK; Trapani *et al*, 2014) downstream the SD and upstream the SA site (Fig EV2). The mouse organ of Corti full-length otoferlin cDNA (transcript variant 4, KX060996; identical with NM_001313767; Strenzke *et al*, 2016) was split at the exon 21–exon 22 junction site into two halves each containing three otoferlin $C_2$-domains ($C_2$A-$C_2$C in the dual-5′AAV half-vector and $C_2$D-$C_2$F in the dual-3′AAV half-vector). To distinguish between the otoferlin dual-AAV cDNA and the wild-type cDNA, a silent point mutation, generating an

artificial restriction site (AccIII; TCCGGA), was introduced into the otoferlin CDS downstream the SA site (Fig EV4A).

## Virus production

The otoferlin dual-AAV constructs and an eGFP-expressing control construct, containing an hbA promoter, a $CMV_e$ enhancer, a WPRE element, and a pA sequence were packaged into an AAV2/6 serotype. All viral vectors were produced by transient transfection of HEK293 cells in the presence of the helper plasmid pDP6. Viral particles were purified from cells harvested 2 days post-transfection by iodixanol step-gradient centrifugation and fast protein liquid chromatography (FPLC). Final virus preparations were dialyzed against PBS, and their purity was confirmed by SDS–gel electrophoresis. Virus genome (vg) titers were determined by qPCR.

## Postnatal injections

The virus solution was injected through the auditory bulla covering the round window membrane (RWM) into the scala tympani of the left cochlea at postnatal day 6–7 (P6–7) as described (Jung *et al*, 2015). All animals were anesthetized during the injection procedure via Isofluran (CONTRAfluran, ZeoSys) and locally anesthetized with Xylocain Pumpspray (AstraZeneca) before retroauricular incision. We used the following viral vectors for our experiments: AAV2/6.eGFP ($1.44 \times 10^{10}$ vg/µl), otoferlin dual-AAV2/6-TS half-vectors (1:1) ($1.2 \times 10^{10}$ vg/µl), and otoferlin dual-AAV2/6-Hyb half-vectors (1:1) ($1.38 \times 10^{10}$ vg/µl).

## RNA isolation, reverse transcription, PCR amplification, and sequencing

Total RNA was isolated from 3- to 4-week-old mice organs of Corti with the Invitrogen™ TRIzol™ Plus RNA Purification Kit (#12183555, Thermo Fisher Scientific) following the manufacturer's instructions. The SuperScript® IV First-Strand Synthesis System (#18091050, Thermo Fisher Scientific) served to synthesize cDNA. Otoferlin cDNA fragments spanning the split-site of the full-length otoferlin expression cassette were amplified from the cochlear cDNA using DreamTaq Polymerase (#EP0702, Thermo Fisher Scientific). The following primers were used for PCRs: 3′-CCCACAAGGC CAACGAGACGGATGAGGAC-5′ as forward and 3′-AAGAGGCTT CGGGCCTGATACATGTGTGCT-5′ as reverse primer. All PCR product bands were excised, TOPO TA cloned into a pCR2.1™-TOPO® vector using the TOPO® TA® Cloning Kit (#450641, Thermo Fisher Scientific), and transferred into One Shot™TOP10 Electrocomp™ *E. coli* cells (#C404050, Thermo Fisher Scientific). All clones were screened for the correct insert, and representative clones were subjected to Sanger sequencing.

## SDS–PAGE and Western blotting

Cochlear tissue from 3- to 4-week-old mice was lysed in RIPA buffer (50 mM Tris, 150 mM NaCl, 1% Triton X-100, 0.5% sodium deoxycholate, 0.1% SDS, pH 8.0) supplemented with protease inhibitors (cOmplete™, Mini, EDTA-free Protease Inhibitor Cocktail, Roche). Nuclei and cell debris were pelleted by low-speed centrifugation at 500 *g* for 5 min at 4°C, and the supernatant was used for Western

blotting. Protein concentration was determined with Pierce™ BCA Protein Assay Kit (#23227, Thermo Fisher Scientific).

Samples were separated by SDS–PAGE on NuPAGE™ 4–12% Bis–Tris Gels (Thermo Fisher Scientific) using Protein Marker VI (10–245) Prestained (Applichem USA) as a size marker and transferred onto nitrocellulose membranes (GE Healthcare Life Sciences). Membranes were probed with primary antibodies mouse IgG1 anti-otoferlin [13A9] (#ab53233, Abcam, 1:500) and rabbit anti-GAPDH (#247002, Synaptic Systems, 1:1,000) followed by incubation with secondary antibodies goat anti-mouse IgG-HRP (#115-035-146, Jackson ImmunoResearch, 1:2,000) and goat anti-rabbit IgG-HRP (#111-035-144, Jackson ImmunoResearch, 1:2,000). Pierce™ ECL Plus Western Blotting Substrate (#32132, Thermo Fisher Scientific) was used for detection.

## Patch-clamp electrophysiological recordings

Perforated patch-clamp recordings were used to measure $Ca^{2+}$-currents and plasma membrane capacitance increments ($\Delta C_m$) at room temperature in IHCs of acutely dissected apical turns of organs Corti (P14–18) as previously described (Moser & Beutner, 2000). The pipette solution contained the following: 130 mM Cs-gluconate, 10 mM tetraethylammonium chloride (TEA-Cl), 10 mM 4-amino-pyridine (Merck), 1 mM $MgCl_2$, 10 mM Cs-HEPES (pH 7.2, ~280 mOsm), and 300 µg/ml amphotericin B (Calbiochem). The extracellular solution contained the following: 110 mM NaCl, 35 mM TEA-Cl, 2.8 mM KCl, 2 mM $CaCl_2$, 1 mM $MgCl_2$, 10 mM Na-HEPES, 1 mM CsCl, and 11.1 mM D-glucose (pH 7.2, ~300 mOsm). All chemicals were purchased from Sigma-Aldrich, unless stated otherwise. An EPC-9 amplifier (HEKA Electronics) controlled by the *Pulse* software (HEKA Electronics) was used to filter low-pass currents at 5 kHz and sample them at 20 kHz. All recorded potentials were corrected for liquid-junction potentials (−14 mV). IHC recordings with a series resistance of > 30 MOhm or a leak conductivity of > 25 pS were excluded from analysis. Depolarization pulses were applied for different time periods with 30–60 s inter-stimulus intervals at peak $Ca^{2+}$-current potentials (usually at −14 mV) as described (Moser & Beutner, 2000). A P/6-protocol was used to correct for $Ca^{2+}$-current leak. The estimated average number of synaptic vesicles undergoing exocytosis during 0.08 ms (estimated average synaptic vesicle replenishment rate) was calculated from the $\Delta C_m$ difference between 100 ms and 20 ms depolarizations ($\Delta C_m100$ ms $- \Delta C_m20$ ms), 45 aF per vesicle (Neef *et al*, 2007), and the number of active zones per IHC at P14 according to the following equation:

$$\text{Vesicle replenishment rate } = [\Delta C_{m\,(100\,ms)} - \Delta C_{m\,(20\,ms)}]/0.08\,s/0.045\,fF/\text{synapse number.}$$

The number of active zones per IHC was determined by counting the CtBP2-immunolabeled synaptic ribbons adjacent to Shank1a-labeled postsynapses as depicted in Fig 2D (15 synapses/IHCs for $Otof^{-/-}$ IHCs and 16 synapses/IHCs for wild-type IHC).

## Immunohistochemistry

Cochlear whole mounts of injected and contralateral non-injected ears (P14–30) were immunostained as previously described

(Strenzke *et al*, 2016). The cochleae were perfused and fixed with 4% formaldehyde for 45 min at 4°C. Samples collected after ABR recordings from 3- to 4-week-old animals were additionally decalcified in Morse solution (10% sodium citrate, 22.5% formic acid) for 5 min or in 0.12 M EDTA (pH 8.0) for 2–3 days before the organs of Corti were dissected. The following primary antibodies were used: mouse IgG1 anti-otoferlin [13A9] (#ab53233, Abcam; 1:300) for labeling the N-terminal part of otoferlin, rabbit IgG anti-otoferlin (custom made; 1:100) for labeling the C-terminal part of otoferlin, goat IgG anti-calbindin D28K [C-20] (#sc-7691, Santa Cruz Biotechnology; 1:150) to visualize OHCs and IHCs, guinea pig anti-Vglut3 (#135204, Synaptic Systems; 1:300) to visualize IHCs, chicken IgY anti-GFP (#ab13970, Abcam, 1:500), rabbit IgG anti-Shank1a [C-terminal] (#RA19016, Neuromics; 1:300) for labeling the postsynaptic density, and goat IgG anti-CtBP2 [E-16] (#sc-5967, Santa Cruz Biotechnology; 1:100) and mouse IgG1 anti-CtBP2 [C-16] (#612044, BD Biosciences; 1:50) for labeling synaptic ribbons. The following secondary antibodies were used: Alexa Fluor 594- and Alexa Fluor 568-conjugated donkey anti-mouse IgG (#A21203, #A10037, Thermo Fisher Scientific, 1:200), Alexa Fluor 405-conjugated donkey anti-mouse IgG (#ab175658, Abcam, 1:200), Alexa Fluor 647- and Alexa Fluor 594-conjugated donkey anti-rabbit IgG (#A31573, #A21207, Thermo Fisher Scientific, 1:200), DyLight 405-conjugated donkey anti-goat IgG (#705-475-003, Jackson ImmunoResearch, 1:200), Alexa Fluor 594-conjugated donkey anti-goat IgG (#A11058, Thermo Fisher Scientific, 1:200), and Alexa Fluor 488-conjugated donkey anti-chicken IgY (#703-545-155, Jackson ImmunoResearch, 1:200). Confocal images were acquired using a laser scanning confocal microscope (Leica TCS SP5, Leica Microsystems GmbH) with a 10× air objective (NA = 0.40) for low and a 63× glycerol-immersion objective (NA = 1.3) for high magnifications images. Maximum intensity projections of optical confocal sections were generated using *ImageJ* (NIH, http://imagej.net/) and assembled in *Adobe Illustrator* (Adobe Systems).

The percentage of N-terminal and C-terminal otoferlin-positive IHCs were quantified from low magnification 3D images (3 µm z-stack step size) of apical, mid-basal, and basal turns of organs of Corti using the "Spots" tool in *Imaris 7.6.5* (Bitplane Scientific Software).

Protein expression levels were quantified from high magnification 3D IHC images (0.6 µm z-stack step size, 2× digital zoom) using a custom written *Matlab* (MathWorks) routine integrated into *Imaris 7.6.5* (Bitplane Scientific Software) as described (Strenzke *et al*, 2016).

Synaptic ribbon (immunolabeled with CtBP2) and synapse (co-immunolabeled with CtBP2 and Shank1a) numbers were counted from high magnification 3D IHC images (0.42 µm z-stack step size, 3× digital zoom) via the "Spots" tool in *Imaris 7.6.5* (Bitplane Scientific Software).

For IHC synapse and ribbon counting, images from apical cochlear turns were acquired, excluding the first 642.6 µm of the apex of the cochlea.

### Auditory brainstem response (ABR) recordings

Auditory brainstem responses were recorded from 3- to 4-week-old anesthetized mice subjected to 4, 6, 8, 12, 16, 24, 32 kHz tone burst (10 ms plateau, 1 ms $\cos^2$ rise/fall) or 0.03 ms broadband

### The paper explained

**Problem**

Congenital disabling hearing loss affects around one in 1000 newborns. Approximately, half of these cases are attributed to genetic causes in developed countries. More than 140 different deafness genes are known to date and more are expected to be characterized within the next years. Mutations in the gene *OTOF*, encoding the large protein otoferlin, lead to congenital recessive hearing loss DFNB9, addressed in this study. The acoustic signal transmission from auditory sensory hair cells to subsequent neurons is almost completely abolished in the absence of otoferlin. It is interesting to note that DFNB9 patients display no inner ear anomalies, which implies that reinstating the coding sequence of otoferlin into the cochlear sensory hair cells could restore hearing. However, a major challenge is the transfer of the long otoferlin coding sequence into these sensory cells. Viral vectors that can transport such large cDNAs are not suitable for gene delivery into hair cells and those vectors that are, have a limited transport capacity.

**Results**

In this study, the cargo limitation of adeno-associated viruses (AAVs) suitable for auditory sensory hair cell transduction was overcome by splitting otoferlin's cDNA into two halves and packaging them into two separate viruses. Co-injection of both viruses into cochleae of otoferlin knock-out mice led to the co-transduction of inner hair cells and to the reassembly and expression of the full-length mRNA and protein. Otoferlin protein levels reached about 30% of wild-type levels despite the predicted low efficiency of full-length transgene reassembly from two AAV half vectors. Fast inner hair cell exocytosis was completely restored and continuous vesicle replenishment partially recovered by the therapeutically reintroduced otoferlin. Auditory function in profoundly deaf otoferlin knock-out mice was partially rescued after split-AAV otoferlin treatment. Nonetheless, to ensure good speech comprehension in treated patients the split-AAV approach needs to be improved further to obtain higher otoferlin protein levels in auditory inner hair cells.

**Impact**

People with profound deafness usually receive cochlear implants, enabling them to understand spoken language, but have a limited hearing frequency resolution. Instead, gene therapy treatment has the potential to restore the full spectrum of hearing so that affected patients might be able to process vocal emotions, experience music, and understand speech in noisy environments like individuals without hearing impairment. This proof-of-concept study demonstrates that split viral vectors are suitable to partially restore hearing in otoferlin knock-out mice and, therefore, present a major step towards clinical gene therapy applications for this deafness form. Further optimization of these split-AAVs and their administration procedure might fully restore hearing in treated patients. Moreover, the split-AAV strategy can potentially rescue hearing in other forms of deafness caused by other large deafness genes.

click sound stimuli presented at 20 Hz as described (Jing *et al*, 2013). Injected ears were clogged with electrode gel while ABRs were recorded from contralateral non-injected ears. ABR click sound thresholds were determined as the lowest sound pressure levels necessary to evoke reproducible ABR wave responses and were measured in 10 dB SPL steps from 30 dB SPL to 100 dB SPL. Tone burst thresholds were recorded in 10 dB SPL steps from 10 dB SPL below the lowest reproducible ABR and up to 90 dB SPL. ABR wave I was defined as the first distinguishable peak between the summating receptor potential (SP) and the prominent ABR wave II peak. The amplitude of each ABR wave was

calculated as the difference between the highest point of a wave and the subsequent local minimum. The summed ABR wave I–V amplitude was calculated by adding up the individual amplitude values of ABR waves I–V.

### Statistics

We performed at least two independent experiments (e.g., animals) for our immunohistological analyses (e.g., synapse numbers in IHCs). For hearing function assessment, we measured at least 6 animals. For cellular electrophysiology, we recorded at least 6 cells, which originated from different animals and litters. All pups from a litter were treated the same way. We injected at least two litters for each condition/group, except for dual-AA-TS-treated wild-type mice, where only one litter was injected. All wild-type control and injected $Otof^{-/-}$ animals that showed reproducible ABR waveforms in response to click or tone burst sound stimuli were included into the analysis. However, around two thirds of injected $Otof^{-/-}$ animals showed neither any detectable ABR response nor transduced cells in immunostained organs of Corti at all, indicating that the virus solution did not enter into the cochlea. These animals were, thus, used as non-transduced $Otof^{-/-}$ controls.

Data averages are depicted as mean ± standard error of the mean (s.e.m.) and plotted using *Igor Pro 6* (WaveMetrics). Statistical analysis was performed via *GraphPad Prism 7.03* (GraphPad Software). The D'Agostino-Pearson omnibus and the Shapiro–Wilk tests were used to test for normality. The Brown–Forsythe test was used to test for equal variance in normally distributed data. The correlation coefficient ($r$) was calculated using the Pearson correlation test for parametric and the Spearman correlation test for non-parametric data (positive correlation $r \geq 0.5$; negative correlation $r \leq -0.5$). The Wilcoxon matched-pair signed rank test was used to test for statistical significance between two paired normally distributed data groups with unequal variance. The unpaired *t*-test with Welch's correction was used to test for statistical significance between two non-paired normally distributed data groups with unequal variance. The one-way ANOVA test followed by Tukey's or Sidak's multiple comparison test was used to test for statistical significance in parametric multiple comparisons. The Kruskal–Wallis test followed by the Dunn's multiple comparison test was used to test for statistical significance in non-parametric multiple comparisons (ns $P > 0.05$; *$P \leq 0.05$; **$P \leq 0.01$; ***$P \leq 0.001$). See Appendix Table S1 for exact *P*-values and statistical tests of individual experiments.

**Expanded View** for this article is available online.

### Author contributions

ER, SK, and HA-M designed the study. HA-M, SK, ER, and APC performed experiments and analyzed data. ER, HA-M, and SK wrote the manuscript. All authors revised the manuscript. SYJ and TM established inner ear injections.

### Conflict of Interest

The authors report being employees of University Medical Center Göttingen and co-inventors on a patent application for dual-AAV vectors to restore hearing. The University Medical Center Göttingen has licensed the rights to these parts of the patent exclusively to Akouos Inc., USA.

### For more information

(i)   https://omim.org/entry/601071.
(ii)  https://www.ncbi.nlm.nih.gov/books/NBK1251/.

### References

Akil O, Seal RP, Burke K, Wang C, Alemi A, During M, Edwards RH, Lustig LR (2012) Restoration of hearing in the VGLUT3 knockout mouse using virally mediated gene therapy. *Neuron* 75: 283–293

Bedrosian JC, Gratton MA, Brigande JV, Tang W, Landau J, Bennett J (2006) *In vivo* delivery of recombinant viruses to the fetal murine cochlea: transduction characteristics and long-term effects on auditory function. *Mol Ther* 14: 328–335

Beurg M, Safieddine S, Roux I, Bouleau Y, Petit C, Dulon D (2008) Calcium- and otoferlin-dependent exocytosis by immature outer hair cells. *J Neurosci* 28: 1798–1803

Bourien J, Tang Y, Batrel C, Huet A, Lenoir M, Ladrech S, Desmadryl G, Nouvian R, Puel J-L, Wang J (2014) Contribution of auditory nerve fibers to compound action potential of the auditory nerve. *J Neurophysiol* 112: 1025–1039

Buran BN, Strenzke N, Neef A, Gundelfinger ED, Moser T, Liberman MC (2010) Onset coding is degraded in auditory nerve fibers from mutant mice lacking synaptic ribbons. *J Neurosci* 30: 7587–7597

Carvalho LS, Turunen HT, Wassmer SJ, Luna-Velez MV, Xiao R, Bennett J, Vandenberghe LH (2017) Evaluating efficiencies of dual AAV approaches for retinal targeting. *Front Neurosci* 11: 503

Chamberlain K, Riyad JM, Weber T (2016) Expressing transgenes that exceed the packaging capacity of adeno-associated virus capsids. *Hum Gene Ther Methods* 27: 1–12

Chatterjee M, Zion DJ, Deroche ML, Burianek BA, Limb CJ, Goren AP, Kulkarni AM, Christensen JA (2015) Voice emotion recognition by cochlear-implanted children and their normally-hearing peers. *Hear Res* 322: 151–162

Choi BY, Ahmed ZM, Riazuddin S, Bhinder MA, Shahzad M, Husnain T, Riazuddin S, Griffith AJ, Friedman TB (2009) Identities and frequencies of mutations of the otoferlin gene (OTOF) causing DFNB9 deafness in Pakistan. *Clin Genet* 75: 237–243

Duan D, Sharma P, Yang J, Yue Y, Dudus L, Zhang Y, Fisher KJ, Engelhardt JF (1998) Circular intermediates of recombinant adeno-associated virus have defined structural characteristics responsible for long-term episomal persistence in muscle tissue. *J Virol* 72: 8568–8577

Duan D, Yue Y, Engelhardt JF (2001) Expanding AAV packaging capacity with trans-splicing or overlapping vectors: a quantitative comparison. *Mol Ther* 4: 383–391

Duncker SV, Franz C, Kuhn S, Schulte U, Campanelli D, Brandt N, Hirt B, Fakler B, Blin N, Ruth P *et al* (2013) Otoferlin couples to clathrin-mediated endocytosis in mature cochlear inner hair cells. *J Neurosci* 33: 9508–9519

Fu QJ, Shannon RV, Wang X (1998) Effects of noise and spectral resolution on vowel and consonant recognition: acoustic and electric hearing. *J Acoust Soc Am* 104: 3586 – 3596

Fuchs PA, Lauer AM (2018) Efferent inhibition of the cochlea. *Cold Spring Harb Perspect Med* https://doi.org/10.1101/cshperspect.a033530

Furman AC, Kujawa SG, Liberman MC (2013) Noise-induced cochlear neuropathy is selective for fibers with low spontaneous rates. *J Neurophysiol* 110: 577 – 586

Géléoc GSG, Holt JR (2014) Sound strategies for hearing restoration. *Science* 344: 1241062

Ghosh A, Yue Y, Lai Y, Duan D (2008) A hybrid vector system expands adeno-associated viral vector packaging capacity in a transgene-independent manner. *Mol Ther* 16: 124 – 130

Grieger JC, Soltys SM, Samulski RJ (2016) Production of recombinant adeno-associated virus vectors using suspension HEK293 cells and continuous harvest of vector from the culture media for GMP FIX and FLT1 clinical vector. *Mol Ther* 24: 287 – 297

Huang L-C, Barclay M, Lee K, Peter S, Housley GD, Thorne PR, Montgomery JM (2012) Synaptic profiles during neurite extension, refinement and retraction in the developing cochlea. *Neural Dev* 7: 1 – 17

Iwasa Y, Nishio S, Yoshimura H, Kanda Y, Kumakawa K, Abe S, Naito Y, Nagai K, Usami S (2013) OTOF mutation screening in Japanese severe to profound recessive hearing loss patients. *BMC Med Genet* 14: 95

Jing Z, Rutherford MA, Takago H, Frank T, Fejtova A, Khimich D, Moser T, Strenzke N (2013) Disruption of the presynaptic cytomatrix protein bassoon degrades ribbon anchorage, multiquantal release, and sound encoding at the hair cell afferent synapse. *J Neurosci* 33: 4456 – 4467

Jung S, Maritzen T, Wichmann C, Jing Z, Neef A, Revelo NH, Al-Moyed H, Meese S, Wojcik SM, Panou I *et al* (2015) Disruption of adaptor protein 2μ (AP-2μ) in cochlear hair cells impairs vesicle reloading of synaptic release sites and hearing. *EMBO J* 34: 2686 – 2702

Kim JH, Lee S-R, Li L-H, Park H-J, Park J-H, Lee KY, Kim M-K, Shin BA, Choi S-Y (2011) High cleavage efficiency of a 2A peptide derived from porcine teschovirus-1 in human cell lines, zebrafish and mice. *PLoS One* 6: e18556

Landegger LD, Pan B, Askew C, Wassmer SJ, Gluck SD, Galvin A, Taylor R, Forge A, Stankovic KM, Holt JR *et al* (2017) A synthetic AAV vector enables safe and efficient gene transfer to the mammalian inner ear. *Nat Biotechnol* 35: 280 – 284

Liberman LD, Liberman MC (2016) Postnatal maturation of auditory-nerve heterogeneity, as seen in spatial gradients of synapse morphology in the inner hair cell area. *Hear Res* 339: 12 – 22

Liu Y, Okada T, Sheykholeslami K, Shimazaki K, Nomoto T, Muramatsu S-I, Kanazawa T, Takeuchi K, Ajalli R, Mizukami H *et al* (2005) Specific and efficient transduction of cochlear inner hair cells with recombinant adeno-associated virus type 3 vector. *Mol Ther* 12: 725 – 733

Longo-Guess C, Gagnon LH, Bergstrom DE, Johnson KR (2007) A missense mutation in the conserved C2B domain of otoferlin causes deafness in a new mouse model of DFNB9. *Hear Res* 234: 21 – 28

Luo X, Fu Q-J, Galvin JJ (2007) Cochlear implants special issue article: vocal emotion recognition by normal-hearing listeners and cochlear implant users. *Trends Amplif* 11: 301 – 315

Maddalena A, Tornabene P, Tiberi P, Minopoli R, Manfredi A, Mutarelli M, Rossi S, Simonelli F, Naggert JK, Cacchiarelli D *et al* (2018) Triple vectors expand AAV transfer capacity in the retina. *Mol Ther* 26: 524 – 541

McDermott HJ (2004) Music perception with cochlear implants: a review. *Trends Amplif* 8: 49 – 82

Moser T, Beutner D (2000) Kinetics of exocytosis and endocytosis at the cochlear inner hair cell afferent synapse of the mouse. *Proc Natl Acad Sci USA* 97: 883 – 888

Most T, Aviner C (2009) Auditory, visual, and auditory-visual perception of emotions by individuals with cochlear implants, hearing aids, and normal hearing. *J Deaf Stud Deaf Educ* 14: 449 – 464

Neef A, Khimich D, Pirih P, Riedel D, Wolf F, Moser T (2007) Probing the mechanism of exocytosis at the hair cell ribbon synapse. *J Neurosci* 27: 12933 – 12944

Nelson PB, Jin S-H, Carney AE, Nelson DA (2003) Understanding speech in modulated interference: cochlear implant users and normal-hearing listeners. *J Acoust Soc Am* 113: 961 – 968

Oxenham AJ, Kreft HA (2014) Speech perception in tones and noise via cochlear implants reveals influence of spectral resolution on temporal processing. *Trends Hear* 18: Available at: http://tia.sagepub.com/cgi/doi/10.1177/2331216514553783 [Accessed July 13, 2015]

Pangrsic T, Lasarow L, Reuter K, Takago H, Schwander M, Riedel D, Frank T, Tarantino LM, Bailey JS, Strenzke N *et al* (2010) Hearing requires otoferlin-dependent efficient replenishment of synaptic vesicles in hair cells. *Nat Neurosci* 13: 869 – 876

Paquette S, Ahmed GD, Goffi-Gomez MV, Hoshino ACH, Peretz I, Lehmann A (2018) Musical and vocal emotion perception for cochlear implants users. *Hear Res* 370: 272 – 282

Reisinger E, Bresee C, Neef J, Nair R, Reuter K, Bulankina A, Nouvian R, Koch M, Bückers J, Kastrup L *et al* (2011) Probing the functional equivalence of otoferlin and synaptotagmin 1 in exocytosis. *J Neurosci* 31: 4886 – 4895

Rodríguez-Ballesteros M, Reynoso R, Olarte M, Villamar M, Morera C, Santarelli R, Arslan E, Medá C, Curet C, Völter C *et al* (2008) A multicenter study on the prevalence and spectrum of mutations in the otoferlin gene (OTOF) in subjects with nonsyndromic hearing impairment and auditory neuropathy. *Hum Mutat* 29: 823 – 831

Roux I, Safieddine S, Nouvian R, Grati M, Simmler M-C, Bahloul A, Perfettini I, Le Gall M, Rostaing P, Hamard G *et al* (2006) Otoferlin, defective in a human deafness form, is essential for exocytosis at the auditory ribbon synapse. *Cell* 127: 277 – 289

Seal RP, Akil O, Yi E, Weber CM, Grant L, Yoo J, Clause A, Kandler K, Noebels JL, Glowatzki E *et al* (2008) Sensorineural deafness and seizures in mice lacking vesicular glutamate transporter 3. *Neuron* 57: 263 – 275

Shrestha BR, Chia C, Wu L, Kujawa SG, Liberman MC, Goodrich LV (2018) Sensory neuron diversity in the inner ear is shaped by activity. *Cell* 174: 1229 – 1246.e17

Shu Y, Tao Y, Wang Z, Tang Y, Li H, Dai P, Gao G, Chen Z-Y (2016) Identification of adeno-associated viral vectors that target neonatal and adult mammalian inner ear cell subtypes. *Hum Gene Ther* 27: 687 – 699

Strenzke N, Chakrabarti R, Al-Moyed H, Müller A, Hoch G, Pangrsic T, Yamanbaeva G, Lenz C, Pan K-T, Auge E *et al* (2016) Hair cell synaptic dysfunction, auditory fatigue and thermal sensitivity in otoferlin Ile515Thr mutants. *EMBO J* 35: 2519 – 2535

Suzuki J, Hashimoto K, Xiao R, Vandenberghe LH, Liberman MC (2017) Cochlear gene therapy with ancestral AAV in adult mice: complete transduction of inner hair cells without cochlear dysfunction. *Sci Rep* 7: 45524

Trapani I, Colella P, Sommella A, Iodice C, Cesi G, de Simone S, Marrocco E, Rossi S, Giunti M, Palfi A *et al* (2014) Effective delivery of large genes to the retina by dual AAV vectors. *EMBO Mol Med* 6: 194 – 211

Van Camp G, Smith RJH. Hereditary Hearing Loss Homepage. Available at: http://hereditaryhearingloss.org

Varga R, Avenarius MR, Kelley PM, Keats BJ, Berlin CI, Hood LJ, Morlet TG, Brashears SM, Starr A, Cohn ES *et al* (2006) OTOF mutations revealed by

genetic analysis of hearing loss families including a potential temperature sensitive auditory neuropathy allele. *J Med Genet* 43: 576–581

Wan G, Gómez-Casati ME, Gigliello AR, Liberman MC, Corfas G (2014) Neurotrophin-3 regulates ribbon synapse density in the cochlea and induces synapse regeneration after acoustic trauma. *eLife* 3: e03564

Wang J, Powers N, Hofstetter P, Trautwein P, Ding D, Salvi R (1997) Effects of selective inner hair cell loss on auditory nerve fiber threshold, tuning and spontaneous and driven discharge rate. *Hear Res* 107: 67–82

Wu PZ, Liberman LD, Bennett K, de Gruttola V, O'Malley JT, Liberman MC (2018) Primary neural degeneration in the human cochlea: evidence for hidden hearing loss in the aging ear. *Neuroscience*. https://doi.org/10.1016/j.neuroscience.2018.07.053

Wynne DP, Zeng F-G, Bhatt S, Michalewski HJ, Dimitrijevic A, Starr A (2013) Loudness adaptation accompanying ribbon synapse and auditory nerve disorders. *Brain* 136: 1626–1638

Yan Z, Zhang Y, Duan D, Engelhardt JF (2000) Trans-splicing vectors expand the utility of adeno-associated virus for gene therapy. *Proc Natl Acad Sci USA* 97: 6716–6721

Yasunaga S, Grati M, Cohen-Salmon M, El-Amraoui A, Mustapha M, Salem N, El-Zir E, Loiselet J, Petit C (1999) A mutation in OTOF, encoding otoferlin, a FER-1-like protein, causes DFNB9, a nonsyndromic form of deafness. *Nat Genet* 21: 363–369

Yoshimura H, Shibata SB, Ranum PT, Smith RJH (2018) Enhanced viral-mediated cochlear gene delivery in adult mice by combining canal fenestration with round window membrane inoculation. *Sci Rep* 8: 2980

# Expanded View Figures
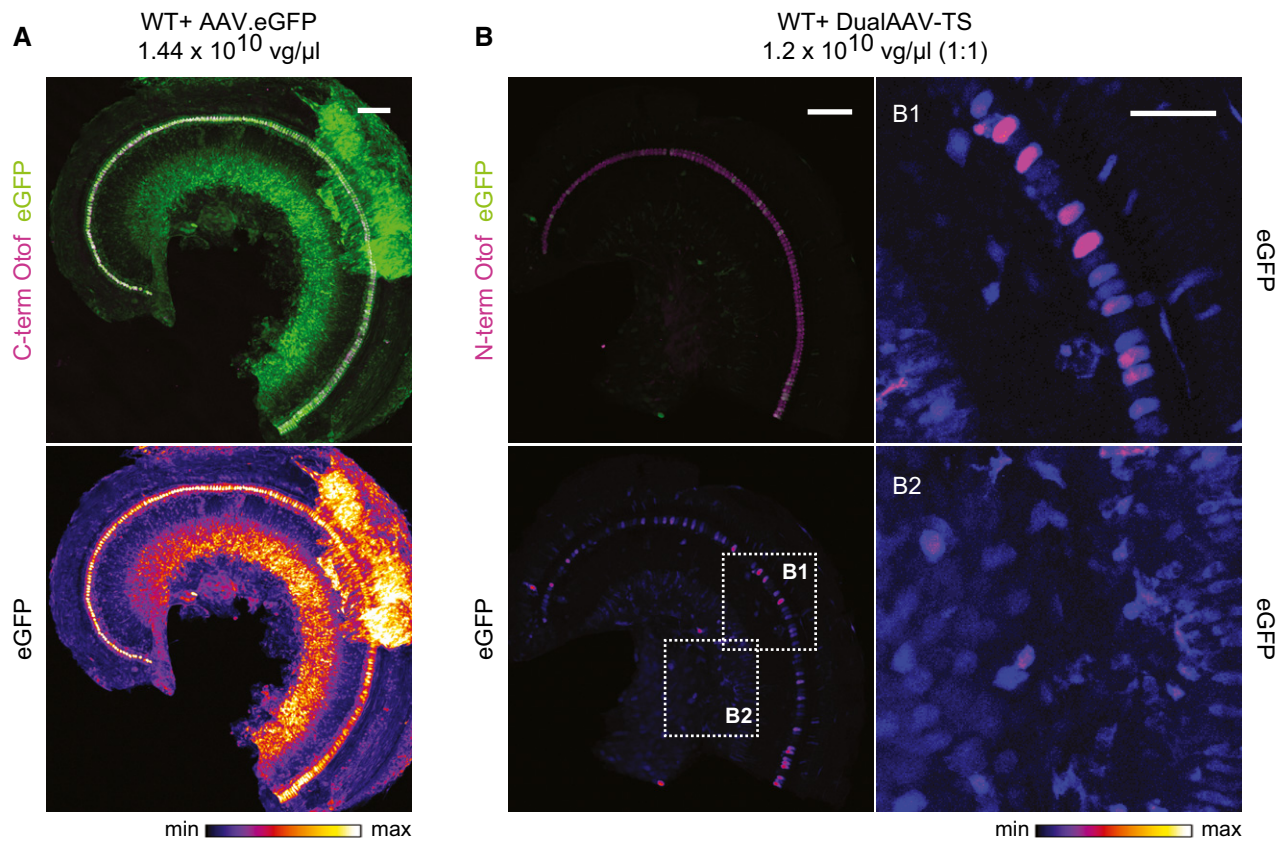


**Figure EV1.   AAV2/6 transduces various cell types in the inner ear.**

A, B   Low magnification views for eGFP immunofluorescence in CD1B6F1 wild-type organs of Corti transduced with AAV2/6 vectors, indicating a broad cell type tropism both for a single eGFP-expressing AAV2/6 (A; P23) and eGFP expressed from otoferlin dual-AAV-TS vectors (B; P27). Images were acquired and displayed with the same settings. Organs of Corti were co-immunolabeled for otoferlin (magenta) to visualize IHCs. (B1, B2) High magnification views of (B) displayed with higher intensity showing eGFP immunofluorescence in IHCs and supporting cells (B1) and in spiral ganglion neurons (B2) in dual-AAV-TS-treated wild-type mice. Individual eGFP immunostainings were depicted as color lookup tables with warmer colors representing higher pixel intensities (max). Maximum intensity projections of optical confocal sections. Vg, vector genomes. Scale bars: 100 μm (A, B), 50 μm (B1, B2).
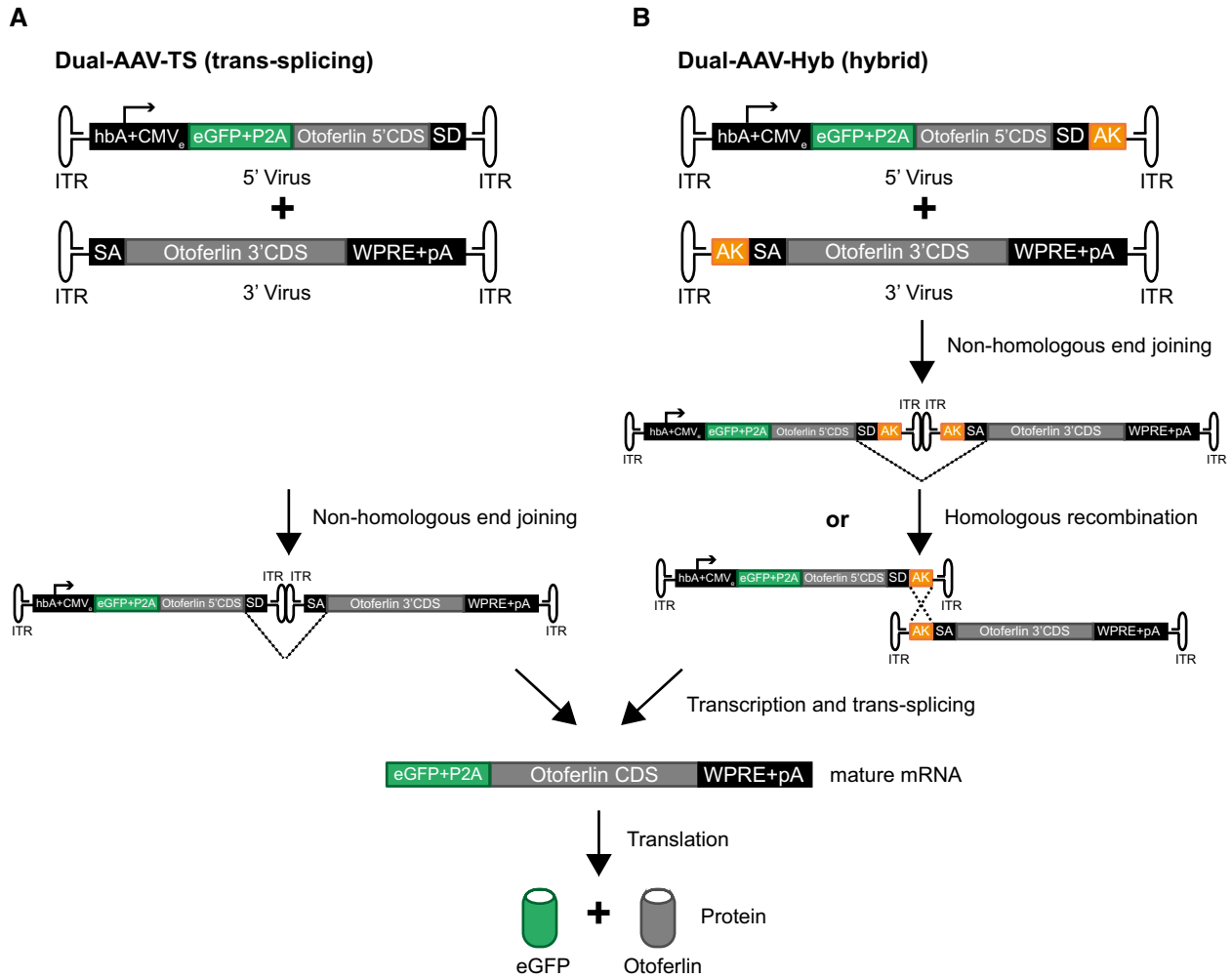
**Figure EV2.  Dual-AAV vector strategies for full-length otoferlin gene transfer.**

A, B   Schematic representation of the otoferlin dual-AAV-TS (A) and dual-AAV-Hyb (B) half-vectors used for postnatal cochlear injections. Both otoferlin dual-AAV half-vector systems contain the first half of the otoferlin coding sequence (CDS) in the 5′-AAV and the other half in the 3′-AAV half-vector. The correct reconstitution of the full-length otoferlin mRNA in the dual-AAV-TS strategy is mediated by non-homologous end joining of the inverted terminal repeats (ITRs). In the dual-AAV-Hyb strategy, the reassembly is mediated by non-homologous end joining of the ITRs and/or homologous recombination of the highly recombinogenic AK sequence. Splice donor (SD) and splice acceptor (SA) sites facilitate the excision of the ITRs via trans-splicing. The woodchuck hepatitis virus post-transcriptional regulatory element (WPRE) stabilizes the mRNA. To ensure the production of two separate proteins, a P2A peptide inducing ribosomal skipping is introduced between the eGFP and the otoferlin CDS. hbA: human beta-actin promoter, CMVe: cytomegalovirus enhancer, pA: polyadenylation signal.
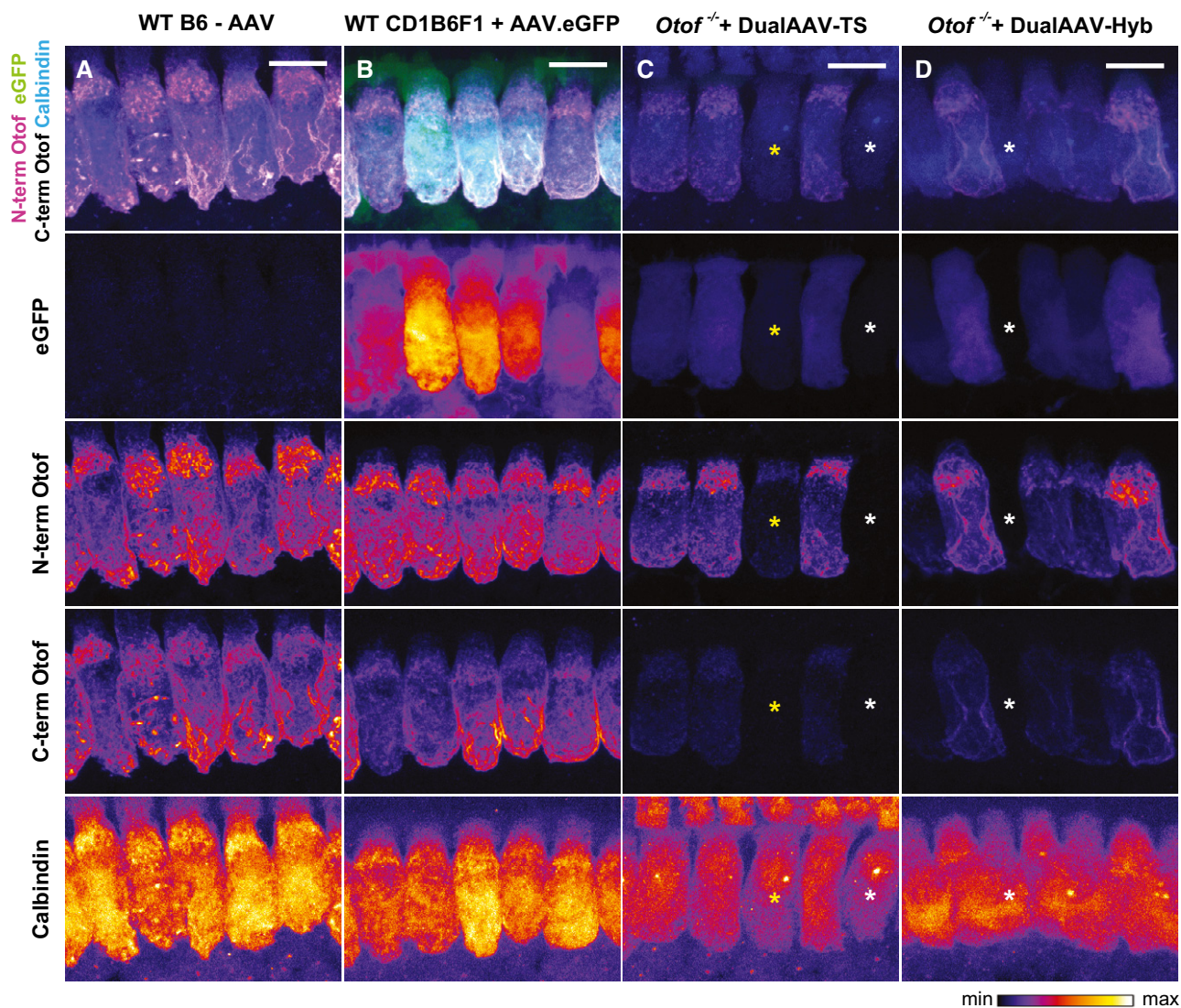
**Figure EV3.   Cellular localization of eGFP and otoferlin in dual-AAV-TS and dual-AAV-Hyb-transduced *Otof*^−/− IHCs compared to wild-type IHCs.**

A–D   High magnification views of dual-AAV-TS (C; P26) and dual-AAV-Hyb (D; P26)-transduced CD1B6F1-*Otof*^−/− IHCs depicted in Fig 1B and C and compared to AAV2/6.eGFP transduced CD1B6F1 wild-type (B; P28) and non-injected B6 wild-type (A; P27) IHCs. Successful virus transduction is monitored via eGFP immunofluorescence. Organs of Corti were immunolabeled against the N-terminal (magenta) and C-terminal (white) part of otoferlin. HCs were immunolabeled with calbindin. Individual eGFP, otoferlin, and calbindin immunostainings are depicted as color lookup tables with warmer colors representing higher pixel intensities. Non-transduced IHCs are labeled with white asterisks, and one transduced IHC displaying only eGFP and N-terminal otoferlin fluorescence, but hardly any C-terminal otoferlin fluorescence with a yellow asterisk. All samples were processed in parallel and acquired and displayed with the same settings. Maximum intensity projections of optical confocal sections. Scale bars: 10 µm.
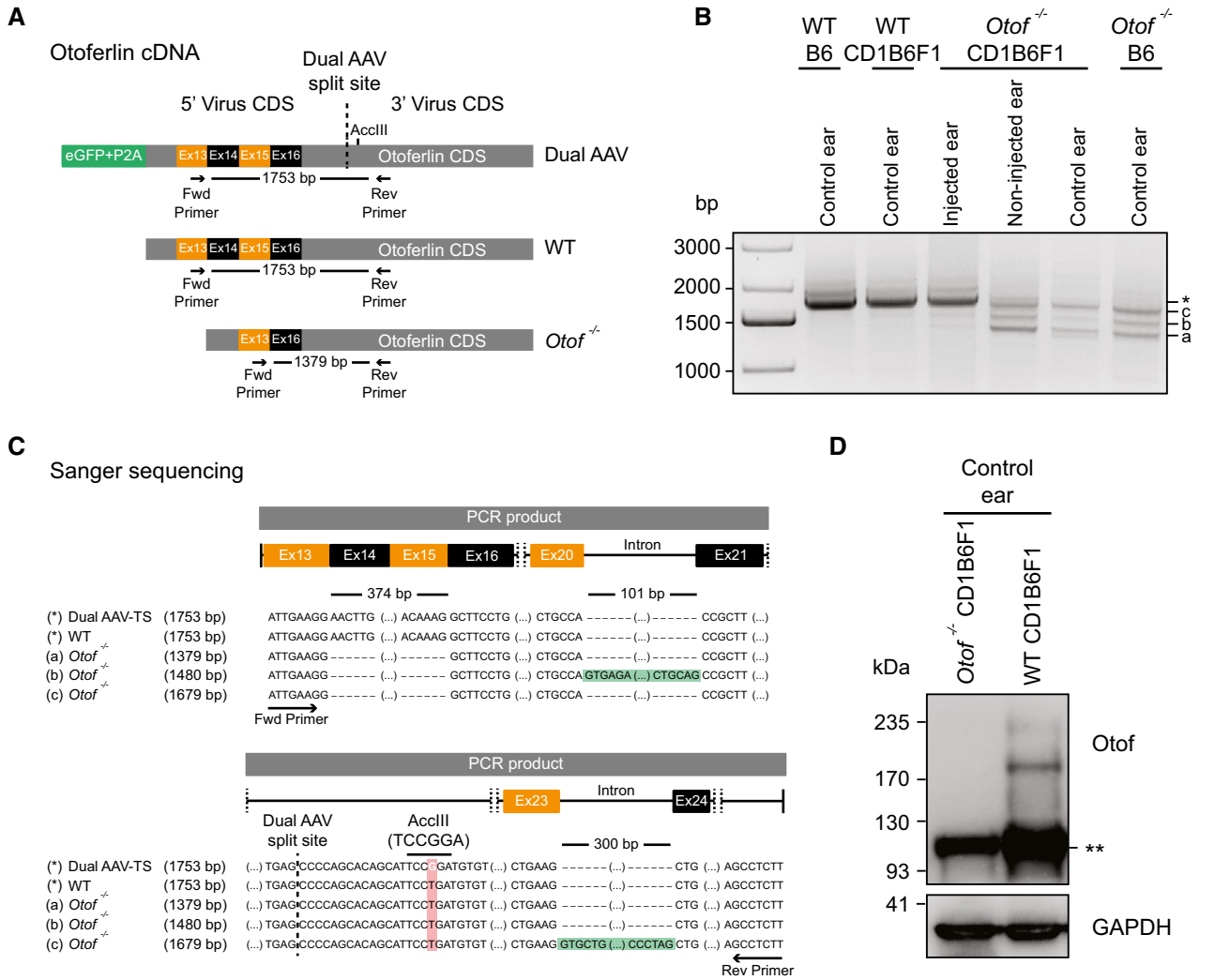
**Figure EV4. Otoferlin dual-AAV-TS-transduced *Otof*⁻/⁻ organs of Corti express full-length otoferlin mRNA.**

A   Schematic representation of otoferlin cDNA from otoferlin dual-AAV-transduced, wild-type, and *Otof*⁻/⁻ organs of Corti, displaying binding sites of primers used in PCRs to assess dual-AAV reassembly.

B   Otoferlin PCR amplicons from organ of Corti cDNA. A 1,753-bp-long amplicon (*), also present in non-injected wild-type controls (WTB6, WTCD1B6F1), indicates successful reassembly of the split otoferlin expression cassette in otoferlin dual-AAV-TS-transduced CD1B6F1-*Otof*⁻/⁻ organs of Corti (injected ear). In *Otof*⁻/⁻ samples, three shorter products were amplified (a, b and c).

C   Sanger sequencing confirmed correct dual-AAV split-site assembly (dashed line) as well as the presence of an artificial AccIII restriction site introduced in the dual-AAV-TS otoferlin cDNA, which is absent in the wild-type (WT) and *Otof*⁻/⁻ cDNA (a–c). Amplicons a-c from *Otof*⁻/⁻ organs of Corti all lack exons 14–15, while bands "b" (1,480 bp) and "c" (1,679 bp) still contain intron 20–21 (b) or intron 23–24 (c), respectively.

D   Western blotting on cell lysates of WT and *Otof*⁻/⁻ CD1B6F1 organs of Corti. Two bands of ~210–230 kDa, corresponding to full-length otoferlin, were detected in WT but absent in *Otof*⁻/⁻ ears. (**) refers to an unspecific band detected in both samples. GAPDH was used as loading control.

Data information: CDS: coding sequence, Ex: exon, TS: trans-splicing, Hyb: hybrid, control ear: non-treated ears, non-injected ear: contralateral non-injected *Otof*⁻/⁻ ears.
Source data are available online for this figure.
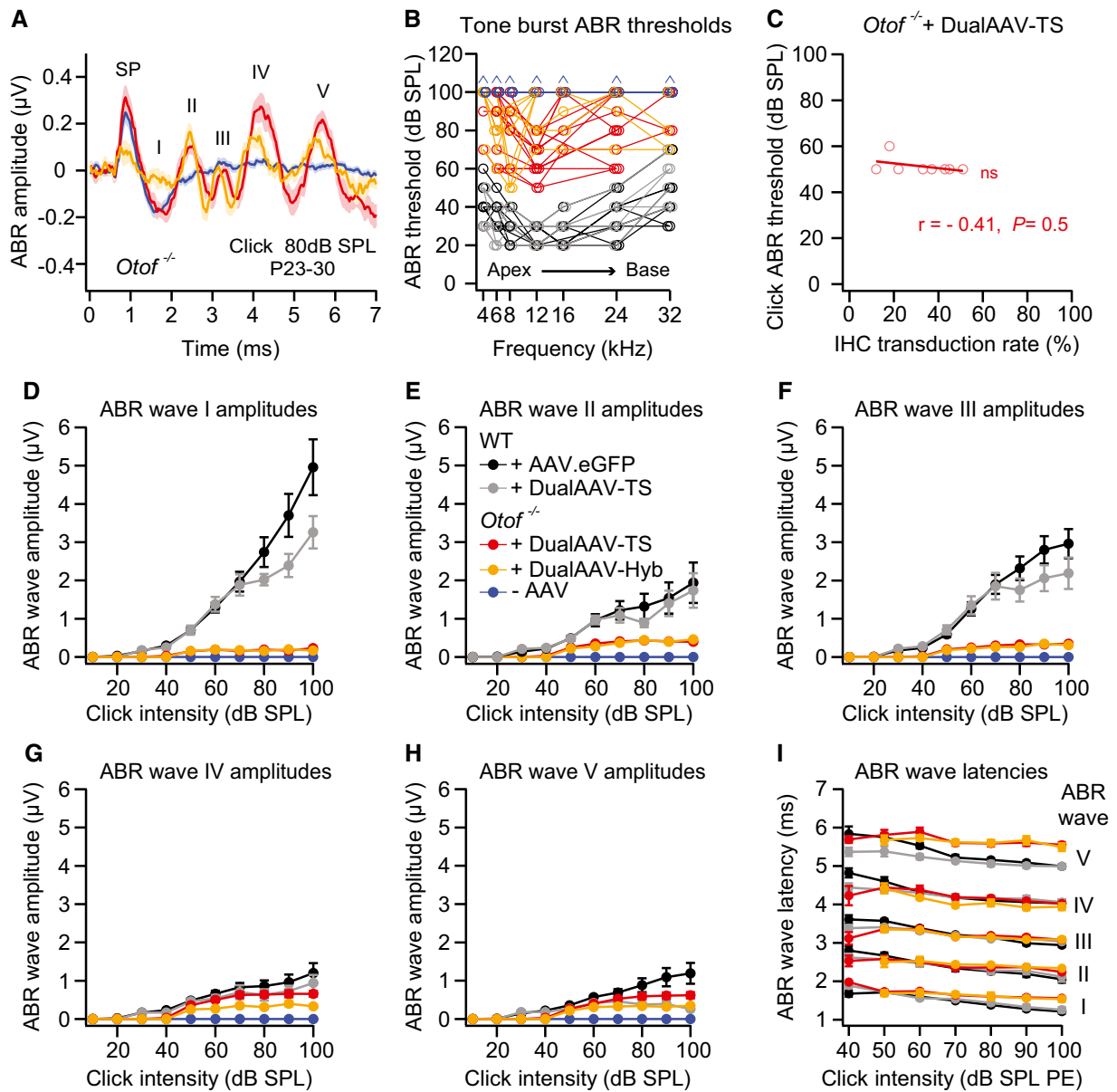
**Figure EV5. Otoferlin dual-AAV-treated *Otof*$^{-/-}$ mice show partially restored ABR wave amplitudes.**

A   Average ABR waves evoked by 80 dB SPL click sound stimuli in otoferlin dual-AAV-injected compared to non-injected deaf CD1B6F1 *Otof*$^{-/-}$ mice. SP: summating potential.

B   Tone burst ABR thresholds of individual otoferlin dual-AAV-treated *Otof*$^{-/-}$ mice compared to non-treated *Otof*$^{-/-}$ and wild-type control animals. Animals with thresholds exceeding the maximum loudspeaker output of 90 dB SPL were set to 100 dB SPL (arrows). Apical and basal cochlear turns are indicated as Apex and Base, respectively.

C   ABR click sound thresholds of individual dual-AAV-TS injected CD1B6F1-*Otof*$^{-/-}$ animals (n = 8 mice; from Fig 3C) plotted against their full-length otoferlin IHC transduction rates (from Fig 1D, C-term otoferlin). r: correlation coefficient.

D–H   ABR wave I (D), wave II (E), wave III (F), wave IV (G), and wave V (H) amplitudes, calculated as the difference between the local maximum and the subsequent local minimum, at different click sound intensities in otoferlin dual-AAV-injected and non-injected CD1B6F1-*Otof*$^{-/-}$ mice compared to AAV2/6.eGFP and dual-AAV-TS injected control CD1B6F1 wild-type (WT) animals. SPL: sound pressure level.

I   ABR wave I-V latencies at different click sound intensities in otoferlin dual-AAV-injected *Otof*$^{-/-}$ and injected CD1B6F1 wild-type control mice. PE: peak equivalent.

Data information: In (A–I), age of analyzed animals: P23–30. In (A, D–I), number of analyzed mice: CD1B6F1 wild-type animals (+AAV.eGFP: n = 12 mice, dualAAV-TS: n = 6 mice) and CD1B6F1-*Otof*$^{-/-}$ animals (dualAAV-TS: n = 17 mice, dualAAV-Hyb: n = 8 mice, -AAV: n = 38 mice). In (B), number of analyzed mice is the same as for (D–I) except: CD1B6F1-*Otof*$^{-/-}$ animals (dualAAV-TS: n = 16 mice). In (B, C), individual animals are depicted with open symbols. In (A, D–I), data are represented as mean ± s.e.m. In (C), 0.5 > r > −0.5 no correlation (Spearman correlation test).

# Appendix

# for

# *A dual-AAV approach restores fast IHC exocytosis and partially rescues auditory function in deaf otoferlin knock-out mice*

Hanan Al-Moyed[1,2], Andreia P. Cepeda[1,2], Sangyong Jung[3,4], Tobias Moser[2,3,4], Sebastian Kügler[5,*], Ellen Reisinger[1,*]

## Table of content

**Appendix Figure S1 - Contralateral non-injected *Otof*$^{-/-}$ ears do not show dual-AAV mediated eGFP and otoferlin expression**

**A,B** Low magnification views of organs of Corti from two CD1B6F1 *Otof*$^{-/-}$ mice treated with either otoferlin dual-AAV-TS (**A**; P28) or dual-AAV-Hyb (**B**; P26) half vectors. Both injected (**upper panels**) and contralateral non-injected ears (**lower panels**) of these animals were processed in parallel and acquired and displayed with the same settings. Organs of Corti were co-immunolabeled for calbindin (blue), eGFP (green), and the N-terminal (magenta) and C-terminal (white) part of otoferlin. Individual eGFP, N-terminal otoferlin, and C-terminal otoferlin immunostainings are depicted as color lookup tables with warmer colors representing higher pixel intensities. Maximum intensity projections of optical confocal sections. Scale bars: 100 μm.

**Appendix Figure S2 - OHCs and IHCs from contralateral non-injected *Otof*<sup>-/-</sup> ears do not show dual-AAV mediated eGFP and otoferlin expression**

**A,B** Higher magnification views of **Appedix Fig S1** showing OHCs and IHCs from two CD1B6F1 *Otof*<sup>-/-</sup> mice treated with either otoferlin dual-AAV-TS (**A**; P28) or dual-AAV-Hyb (**B**; P26) half vectors. Both injected (**left panels**) and contralateral non-injected ears (**right panels**) of these animals were processed in parallel and acquired and displayed with the same settings. Organs of Corti were co-immunolabeled for eGFP (green) and the N-terminal (magenta) and C-terminal (white) part of otoferlin. OHCs and IHCs were visualized via calbindin immunostaining (blue). Individual eGFP, N-terminal otoferlin, and C-terminal otoferlin immunostainings are depicted as color lookup tables with warmer colors representing higher pixel intensities. Maximum intensity projections of optical confocal sections. IHCs: inner hair cells, OHCs: outer hair cells. Scale bars: Scale bars: 10 µm.
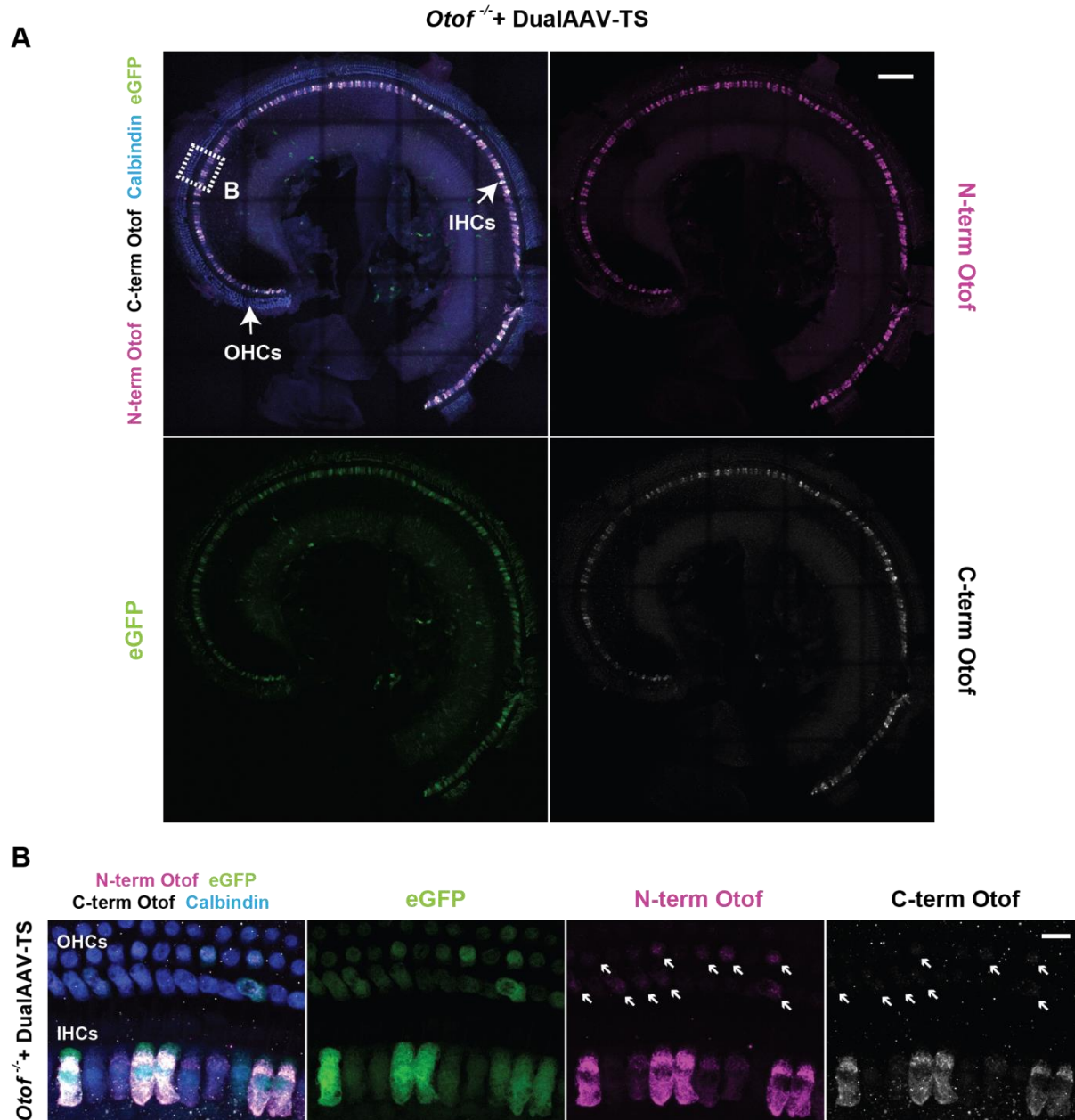
**Appendix Figure S3 – OHCs were sparsely transduced with dual-AAV vectors.**

**A** Low magnification views of a CD1 *Otof*$^{-/-}$ organ of Corti (P23) depicted in **Fig 1A** transduced with otoferlin dual-AAV-TS half vectors. The organ of Corti was co-immunolabeled for calbindin (blue), eGFP (green), and the N-terminal (magenta) and C-terminal (white) part of otoferlin.

**B** Higher magnification views of (**A**) showing OHCs expressing eGFP (green) and otoferlin (magenta, white, arrows) and IHCs transduced with otoferlin dual-AAV-TS half vectors.

Data information: Maximum intensity projections of optical confocal sections. IHCs: inner hair cells, OHCs: outer hair cells. Scale bars: 100µm (A), 10 µm (B).
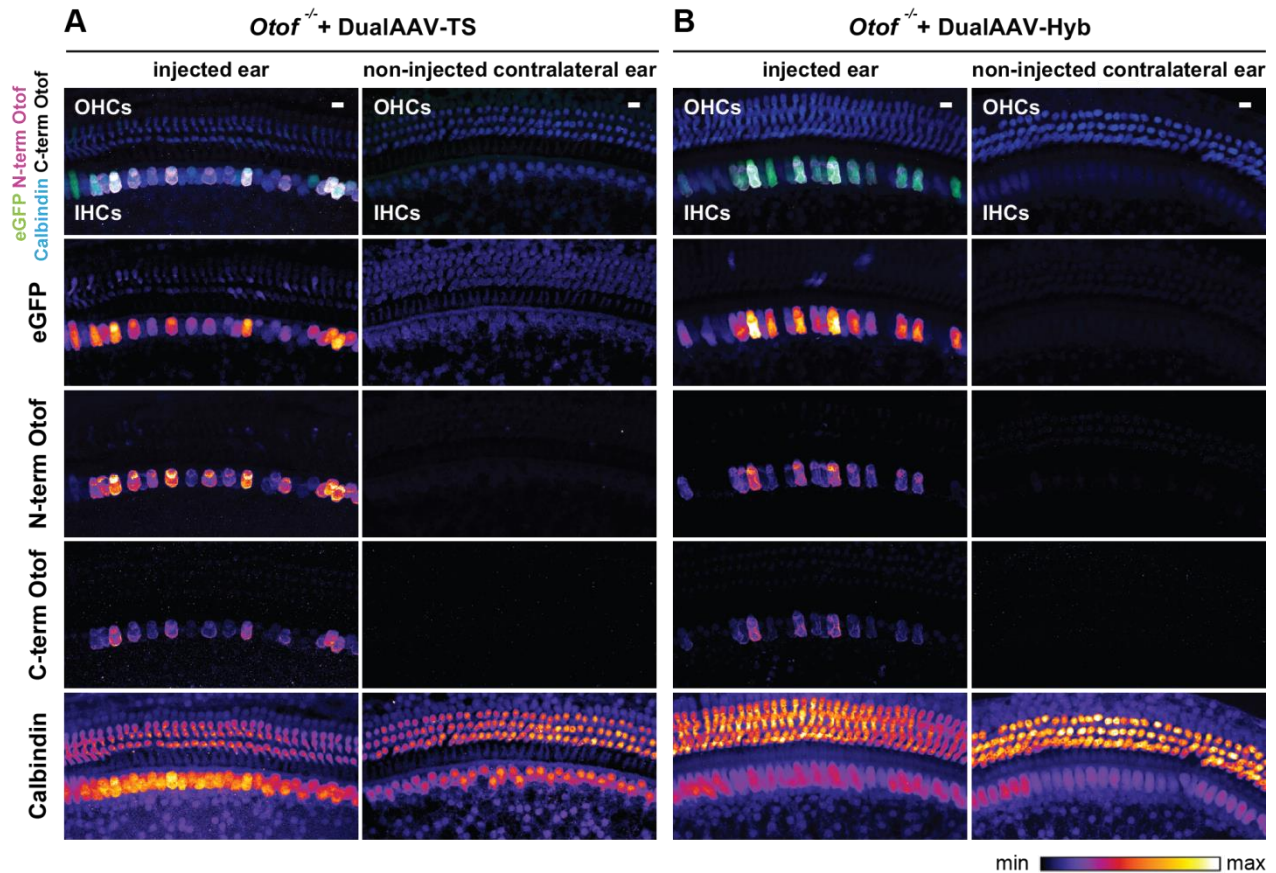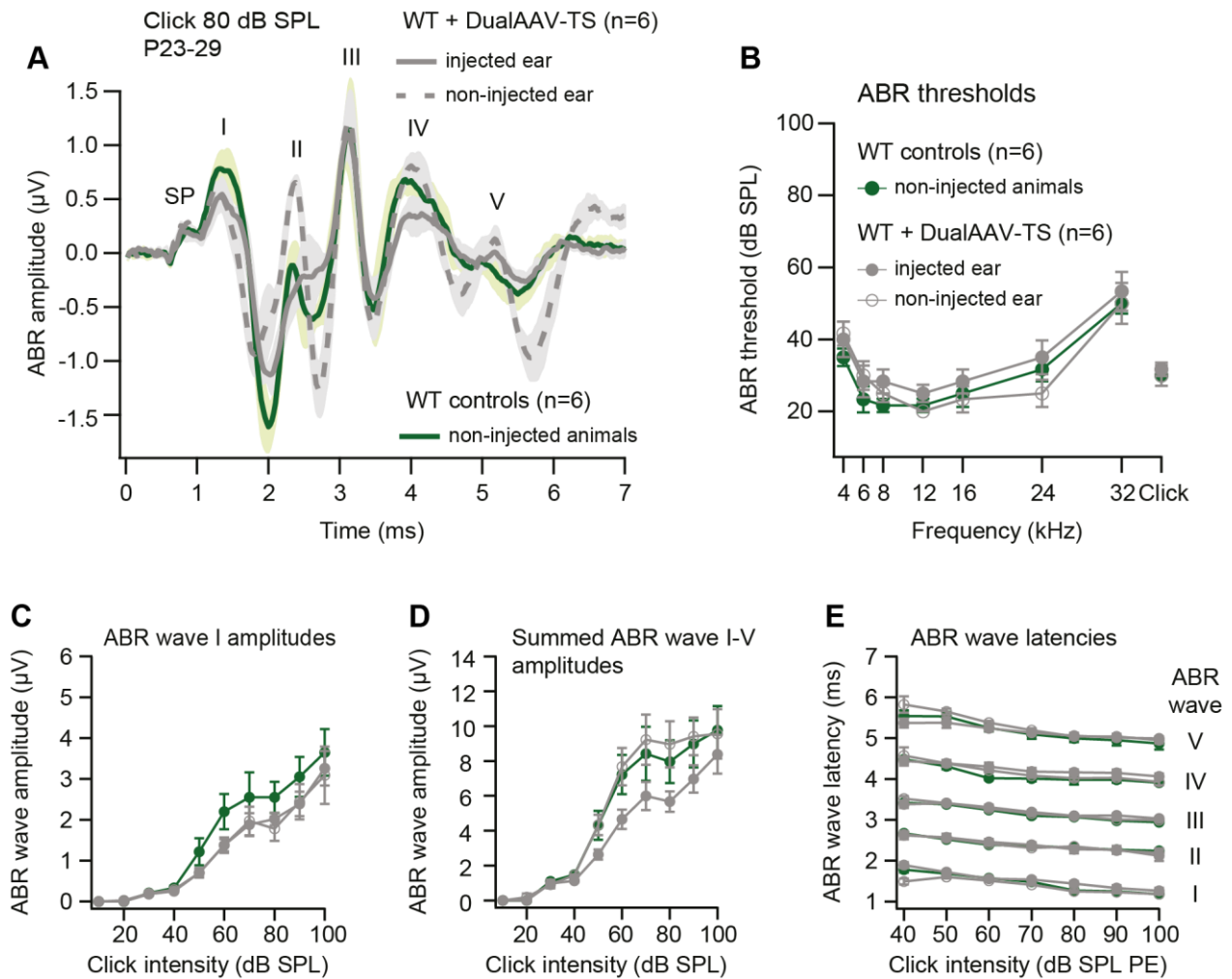
**Appendix Figure S4 - Otoferlin dual-AAV-TS injected and non-injected contralateral ears of wild-type mice did not differ in ABR thresholds and wave latencies.**

**A** Average ABR wave responses to 80dB SPL broadband click sound stimuli in otoferlin dual-AAV-TS injected and contralateral non-injected ears of CD1B6F1 wild-type mice (WT+ DualAAV-TS) compared to non-injected control CD1B6F1 wild-type animals (WT controls, P23-29). SP: summating receptor potential, wave I: auditory nerve activity, wave II: cochlear nucleus activity, wave III: superior olivary complex activity, wave IV-V: lateral lemniscus activity in the brainstem.

**B** ABR click sound (**right**) and tone burst (**left**) thresholds in otoferlin dual-AAV-TS injected and contralateral non-injected ears of wild-type animals compared to non-injected control wild-type mice.

**C, D** ABR wave I (**C**) and summed ABR wave I-V (**D**) amplitudes at different click sound intensities in otoferlin dual-AAV-TS injected and non-injected contralateral ears of wild-type mice. Non-injected wild-type mice served as controls.

**E** ABR wave I-V latencies at different click sound intensities measured from otoferlin dual-AAV-TS injected and non-injected contralateral ears of wild-type mice. SPL PE: sound pressure level peak equivalent.

Data information: In (A-E), data are presented as mean ± SEM.

## Appendix Table S1. Statistical tests and *P*-values

**Fig 1D.**

| Group compared | Statistical significance | *P* value | Statistical test |
|---|---|---|---|
| DualAAV-TS:<br>N-term Otoferlin<br>vs.<br>C-term Otoferlin | ** | 0.002 | Wilcoxon matched-pair singed rank test |
| DualAAV-Hyb:<br>N-term Otoferlin<br>vs.<br>C-term Otoferlin | ** | 0.004 | Wilcoxon matched-pair singed rank test |
| N-term Otoferlin:<br>DualAAV-TS<br>vs.<br>DualAAV-Hyb | * | 0.02 | Unpaired t-test with<br>Welch's correction |
| C-term Otoferlin:<br>DualAAV-TS<br>vs.<br>DualAAV-Hyb | * | 0.05 | Unpaired t-test with<br>Welch's correction |

**Fig 1E.**

| Group compared | Statistical significance | *P* value | Statistical test |
|---|---|---|---|
| N-term Otoferlin: | | | |
| WTB6 - AAV<br>vs.<br>WTCD1B6F1 + AAV.eGFP | ns | > 0.999999 | Kruskal-Wallis test followed by Dunn's multiple comparison test |
| WTB6 - AAV<br>vs.<br>WTCD1B6F1 + DualAAV-TS | *** | $2\times10^{-6}$ | Kruskal-Wallis test followed by Dunn's multiple comparison test |
| WTB6 - AAV<br>vs.<br>*Otof*^{-/-} CD1B6F1 + DualAAV-TS | *** | 0.0008 | Kruskal-Wallis test followed by Dunn's multiple comparison test |
| WTB6 - AAV<br>vs.<br>*Otof*^{-/-} CD1B6F1 + DualAAV-Hyb | *** | $< 1\times10^{-6}$ | Kruskal-Wallis test followed by Dunn's multiple comparison test |
| WTB6 - AAV<br>vs.<br>*Otof*^{-/-} CD1B6F1 - AAV | *** | $< 1\times10^{-6}$ | Kruskal-Wallis test followed by Dunn's multiple comparison test |
| *Otof*^{-/-} CD1B6F1 + DualAAV-TS<br>vs.<br>*Otof*^{-/-} CD1B6F1 + DualAAV-Hyb | ns | > 0.999999 | Kruskal-Wallis test followed by Dunn's multiple comparison test |
| *Otof*^{-/-} CD1B6F1 + DualAAV-TS<br>vs.<br>*Otof*^{-/-} CD1B6F1 - AAV | *** | $< 1\times10^{-6}$ | Kruskal-Wallis test followed by Dunn's multiple comparison test |
| *Otof*^{-/-} CD1B6F1 + DualAAV-Hyb<br>vs.<br>*Otof*^{-/-} CD1B6F1 - AAV | *** | $< 1\times10^{-6}$ | Kruskal-Wallis test followed by Dunn's multiple comparison test |

| C-term Otoferlin: | | | |
|---|---|---|---|
| WTB6 - AAV vs. WTCD1B6F1 + AAV.eGFP | ** | 0.004 | Kruskal-Wallis test followed by Dunn's multiple comparison test |
| WTB6 - AAV vs. WTCD1B6F1 + DualAAV-TS | * | 0.031 | Kruskal-Wallis test followed by Dunn's multiple comparison test |
| WTB6 - AAV vs. $Otof^{/-}$ CD1B6F1 + DualAAV-TS | *** | $1\times10^{-5}$ | Kruskal-Wallis test followed by Dunn's multiple comparison test |
| WTB6 - AAV vs. $Otof^{/-}$ CD1B6F1 + DualAAV-Hyb | *** | $< 1\times10^{-6}$ | Kruskal-Wallis test followed by Dunn's multiple comparison test |
| WTB6 - AAV vs. $Otof^{/-}$ CD1B6F1 - AAV | *** | $< 1\times10^{-6}$ | Kruskal-Wallis test followed by Dunn's multiple comparison test |
| $Otof^{/-}$ CD1B6F1 + DualAAV-TS vs. $Otof^{/-}$ CD1B6F1 + DualAAV-Hyb | ns | > 0.999999 | Kruskal-Wallis test followed by Dunn's multiple comparison test |
| $Otof^{/-}$ CD1B6F1 + DualAAV-TS vs. $Otof^{/-}$ CD1B6F1 - AAV | *** | $< 1\times10^{-6}$ | Kruskal-Wallis test followed by Dunn's multiple comparison test |
| $Otof^{/-}$ CD1B6F1 + DualAAV-Hyb vs. $Otof^{/-}$ CD1B6F1 - AAV | *** | $< 1\times10^{-6}$ | Kruskal-Wallis test followed by Dunn's multiple comparison test |

**Fig 2B.**

| Group compared | Statistical significance | *P* value | Statistical test |
|---|---|---|---|
| WTB6 vs. WTCD1B6F1 +AAV | ns | > 0.999999 | Kruskal-Wallis test followed by Dunn's multiple comparison test |
| WTB6 vs. $Otof^{/-}$ + DualAAV-TS | *** | $< 1\times10^{-6}$ | Kruskal-Wallis test followed by Dunn's multiple comparison test |
| WTB6 vs. $Otof^{/-}$ + DualAAV-Hyb | *** | $< 1\times10^{-6}$ | Kruskal-Wallis test followed by Dunn's multiple comparison test |
| WTB6 vs. $Otof^{/-}$ - AAV injected ear | *** | $< 1\times10^{-6}$ | Kruskal-Wallis test followed by Dunn's multiple comparison test |
| WTB6 vs. $Otof^{/-}$ - AAV non-injected ear | *** | $< 1\times10^{-6}$ | Kruskal-Wallis test followed by Dunn's multiple comparison test |
| WTCD1B6F1 + AAV vs. $Otof^{/-}$ + DualAAV-TS | *** | $< 1\times10^{-6}$ | Kruskal-Wallis test followed by Dunn's multiple comparison test |

| Group compared | Statistical significance | P value | Statistical test |
|---|---|---|---|
| WTCD1B6F1 + AAV<br>vs.<br>$Otof^{-/-}$ + DualAAV-Hyb | *** | < $1 \times 10^{-6}$ | Kruskal-Wallis test followed by Dunn's multiple comparison test |
| WTCD1B6F1 + AAV<br>vs.<br>$Otof^{-/-}$ - AAV<br>injected ear | *** | < $1 \times 10^{-6}$ | Kruskal-Wallis test followed by Dunn's multiple comparison test |
| WTCD1B6F1 + AAV<br>vs.<br>$Otof^{-/-}$ - AAV<br>non-injected ear | *** | < $1 \times 10^{-6}$ | Kruskal-Wallis test followed by Dunn's multiple comparison test |
| $Otof^{-/-}$ + DualAAV-TS<br>vs.<br>$Otof^{-/-}$ + DualAAV-Hyb | ns | > 0.999999 | Kruskal-Wallis test followed by Dunn's multiple comparison test |
| $Otof^{-/-}$ + DualAAV-TS<br>vs.<br>$Otof^{-/-}$ - AAV<br>injected ear | ns | > 0.999999 | Kruskal-Wallis test followed by Dunn's multiple comparison test |
| $Otof^{-/-}$ + DualAAV-TS<br>vs.<br>$Otof^{-/-}$ - AAV<br>non-injected ear | ns | > 0.999999 | Kruskal-Wallis test followed by Dunn's multiple comparison test |
| $Otof^{-/-}$ + DualAAV-Hyb<br>vs.<br>$Otof^{-/-}$ - AAV<br>injected ear | ns | 0.32 | Kruskal-Wallis test followed by Dunn's multiple comparison test |
| $Otof^{-/-}$ + DualAAV-Hyb<br>vs.<br>$Otof^{-/-}$ - AAV<br>non-injected ear | ns | > 0.999999 | Kruskal-Wallis test followed by Dunn's multiple comparison test |
| $Otof^{-/-}$ - AAV<br>injected ear<br>vs.<br>$Otof^{-/-}$ - AAV<br>non-injected ear | ns | > 0.999999 | Kruskal-Wallis test followed by Dunn's multiple comparison test |

**Fig 2D.**

| Group compared | Statistical significance | P value | Statistical test |
|---|---|---|---|
| WT B6 P6<br>vs.<br>$Otof^{-/-}$ B6 P6 | ** | 0.002 | Kruskal-Wallis test followed by Dunn's multiple comparison test |
| WT B6 P6<br>vs.<br>WT B6 P14 | *** | < $1 \times 10^{-6}$ | Kruskal-Wallis test followed by Dunn's multiple comparison test |
| WT B6 P6<br>vs.<br>$Otof^{-/-}$ B6 P14 | *** | < $1 \times 10^{-6}$ | Kruskal-Wallis test followed by Dunn's multiple comparison test |

| Otof$^{-/-}$ B6 P6 vs. WT B6 P14 | *** | < 1x10$^{-6}$ | Kruskal-Wallis test followed by Dunn's multiple comparison test |
|---|---|---|---|
| Otof$^{-/-}$ B6 P6 vs. Otof$^{-/-}$ B6 P14 | *** | < 1x10$^{-6}$ | Kruskal-Wallis test followed by Dunn's multiple comparison test |
| WT B6 P14 vs. Otof$^{-/-}$ B6 P14 | ns | 0.37 | Kruskal-Wallis test followed by Dunn's multiple comparison test |

**Fig 2G.**

| 20 ms depolarization | | | |
|---|---|---|---|
| Group compared | Statistical significance | *P* value | Statistical test |
| WTB6 vs. WTCD1B6F1 vs. Otof$^{-/-}$+ DualAAV-TS | ns | 0.3 | One-way ANOVA |
| Otof$^{-/-}$+ DualAAV-TS vs. Otof$^{-/-}$ | *** | <1x10$^{-4}$ | t-test (unpaired, two-tailed) |
| 20-100ms vesicle replenishment rate | | | |
| Otof$^{-/-}$+ DualAAV-TS vs. Otof$^{-/-}$ | *** | < 1x10$^{-4}$ | t-test (two-tailed, unpaired) |
| WTCD1B6F1 vs. Otof$^{-/-}$+ DualAAV-TS | *** | 0.0005 | One-way ANOVA followed by Sidak's multiple comparisons test |
| WTB6 vs. Otof$^{-/-}$+ DualAAV-TS | *** | <1x10$^{-4}$ | One-way ANOVA followed by Sidak's multiple comparisons test |

**Fig 3C.**

| Group compared | Statistical significance | *P* value | Statistical test |
|---|---|---|---|
| WT + AAV.eGFP vs. WT + DualAAV-TS | ns | > 0.999999 | Kruskal-Wallis test followed by Dunn's multiple comparison test |
| WT + AAV.eGFP vs. Otof$^{-/-}$ + DualAAV-TS | *** | 0.00002 | Kruskal-Wallis test followed by Dunn's multiple comparison test |
| WT + AAV.eGFP vs. Otof$^{-/-}$ + DualAAV-Hyb | *** | 0.00013 | Kruskal-Wallis test followed by Dunn's multiple comparison test |
| Otof$^{-/-}$ + DualAAV-TS vs. Otof$^{-/-}$ + DualAAV-Hyb | ns | > 0.999999 | Kruskal-Wallis test followed by Dunn's multiple comparison test |

**Fig 3F.**

| Group | Statistical significance | P value + correlation coefficient | Correlation test |
|---|---|---|---|
| 50 dB SPL | ns | $P$ = 0.24<br>r = 0.54 | Spearman correlation test |
| 70 dB SPL | * | $P$ = 0.04<br>r = 0.78 | Pearson correlation test |
| 90 dB SPL | * | $P$ = 0.02<br>r = 0.84 | Pearson correlation test |

**Fig EV5C.**

| Group | Statistical significance | P value + correlation coefficient | Correlation test |
|---|---|---|---|
| $Otof^{-/-}$ + DualAAV-TS | ns | $P$ = 0.50<br>r = - 0.41 | Spearman correlation test |

## 2.3 Optimizing the dual-AAV approach to increase otoferlin IHC transduction rates

From the previous chapter it becomes clear that otoferlin dual-AAV half vectors need to be developed further to achieve wild-type like or near wild-type ABR wave amplitudes and thresholds in treated $Otof^{-/-}$ mice. The correlation analysis between IHC transduction rates and ABR wave amplitudes in dual-AAV2/6-TS injected $Otof^{-/-}$ mice revealed, in particular, that the number of full-length otoferlin expressing IHCs needs to be increased in order to reach higher ABR wave amplitudes (Al-Moyed et al., 2019: Fig. 3F). One possibility to increase the number of transduced IHCs is to use AAVs with capsid proteins from different serotypes given that several research groups have obtained different IHC transduction success rates with various AAV serotypes such AAV1 (Akil et al., 2012; Askew et al., 2015; Shu et al., 2016), AAV8 (Chien et al., 2016; Geng et al., 2017), AAV9 (Yoshimura et al., 2018), and AAVAnc80L65 (Landegger et al., 2017; Pan et al., 2017; Suzuki et al., 2017; Yoshimura et al., 2018).

### 2.3.1 Testing AAVs with capsid proteins from different serotypes

For this purpose, I have tested whether AAVs with capsid proteins from serotype 8 (AAV2/8) and Anc80L65 (AAV2/ Anc80) as well as an AAV with chimeric capsid proteins from serotype 1 and 2 (AAV2/1-2) can target more IHCs than the AAV2/6 serotype used for the proof of concept study in "chapter 2.2" The same control eGFP expression cassette used in "chapter 2.2" (see "materials and methods" section in "Al-Moyed et al., 2019") was packed into single AAV2/8 (AAV2/8.eGFP) and AAV2/Anc80 (AAV2/Anc80.eGFP) viruses to test the auditory IHC targeting efficiency of these two AAV serotypes. The AAV2/1-2 serotype, in turn, was already successfully used to transfer synaptotagmin 1 and eGFP into auditory IHCs by my research group (Reisinger et al., 2011). The two split-otoferlin trans-splicing expression cassettes (5'-AAV-TS and 3'-AAV-TS) used in "chapter 2.2" (see "materials and methods" section in "Al-Moyed et al., 2019") were, therefore, packaged directly into two sperate AAV2/1-2 viruses (dual-AAV2/1-2-TS). All viruses used for the experiments in this thesis were packaged and produced by the Lab of Dr. Sebastian Kügler (Center Nanoscale Microscopy and Physiology of the Brain (CNMPB), Department of

Neurology, University Medical Center Göttingen). The different AAV serotypes were, then, injected through the RWM into the scala tympani (see introduction "Figure 1.6") of the left cochlea of P6-8 wild-type control or $Otof^{-/-}$ mice as described in (Jung *et al.*, 2015; Al-Moyed *et al.*, 2019). Note that all experiments and the subsequent data and statistical analysis mentioned in "chapter 2.3" was performed by me as described in "Al-Moyed *et al.*, 2019" unless stated otherwise.
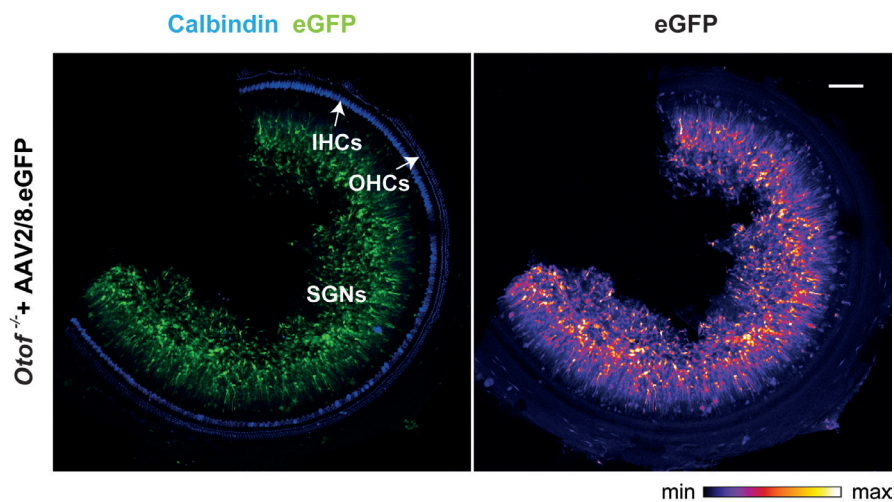


**Figure 2.1:**

**The AAV2/8 serotype does not target auditory HCs.**

Low magnification views of an organ of Corti from a CD1B6F1-$Otof^{-/-}$ mouse (P16) injected with a single eGFP-expressing AAV2/8 virus (AAV2/8.eGFP) at P7. The organ of Corti was immunolabeled for the auditory HC marker Calbindin (blue) and eGFP (green). The individual eGFP immunostaining is illustrated as a color lookup table with warmer colors representing higher pixel intensities (max) and depicted with the same settings as the merged image (left panel). All images are maximum intensity projections of optical confocal sections. IHCs, inner hair cells. OHCs, outer hair cells, SGNs, spiral ganglion neurons. Scale bar, 100 μm.

CD1xC57BL/6N-F1 (CD1B6F1)-$Otof^{-/-}$ organs of Corti transduced with the control AAV2/8.eGFP virus and immunolabeled for eGFP showed no eGFP fluorescent signal in auditory HCs, but in SGNs (Figure 2.1). Cochleae of CD1-$Otof^{-/-}$ mice (n = 3 cochleae) that were co-injected with otoferlin dual-AAV2/1-2-TS half vectors by Dr. SangYong Jung

(Institute for Auditory Neurosciences and InnerEarLab, University Medical Center Göttingen) and immunolabeled for otoferlin only displayed an N-terminal otoferlin immunofluorescent signal in a few IHCs and no C-terminal otoferlin signal (Figure 2.2). In this regard, two otoferlin antibodies were used to visualize otoferlin expression in transduced organs of Corti. One of the antibodies binds within the N-terminal region of otoferlin and was used to immunolabel N-terminal otoferlin fragments and the N-terminal part of the full-length protein. The other antibody binds to the C-terminal part of otoferlin after the transmembrane domain and was used to immunolabel full-length otoferlin.
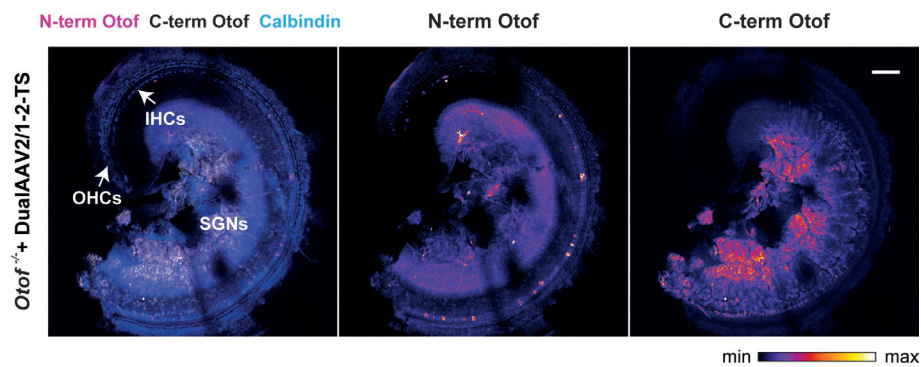


**Figure 2.2:**

**Otoferlin dualAAV2/1-2-TS half vectors have an extremely low IHC targeting efficiency.**

Low magnification views of an organ of Corti from a CD1B6F1-*Otof*^{-/-} mouse (P24) co-injected with otoferlin dual-AAV2/1-2-TS half vectors at P6. The organ of Corti was immunolabeled for the auditory HC marker Calbindin (blue) and the N-terminal part (N-term Otof, magenta) and C-terminal part (C-term Otof, white) of otoferlin. Individual otoferlin immunostainings are illustrated as color lookup tables with warmer colors representing higher pixel intensities (max) and depicted with the same settings as the merged image (left panel). All images are maximum intensity projections of optical confocal sections. IHCs, inner hair cells. OHCs, outer hair cells, SGNs, spiral ganglion neurons. Scale bar, 100 µm.

Organs of Corti from CD1B6F1-wild-type mice (n = 6 cochleae) inoculated with the control AAV2/Anc80.eGFP virus showed an eGFP fluorescent signal in IHCs, OHCs, supporting cells, and SGNs (Figure 2.3A). To further determine the IHC targeting rate of this AAV serotype, I have counted the number of eGFP immunolabeled IHCs in apical cochlear
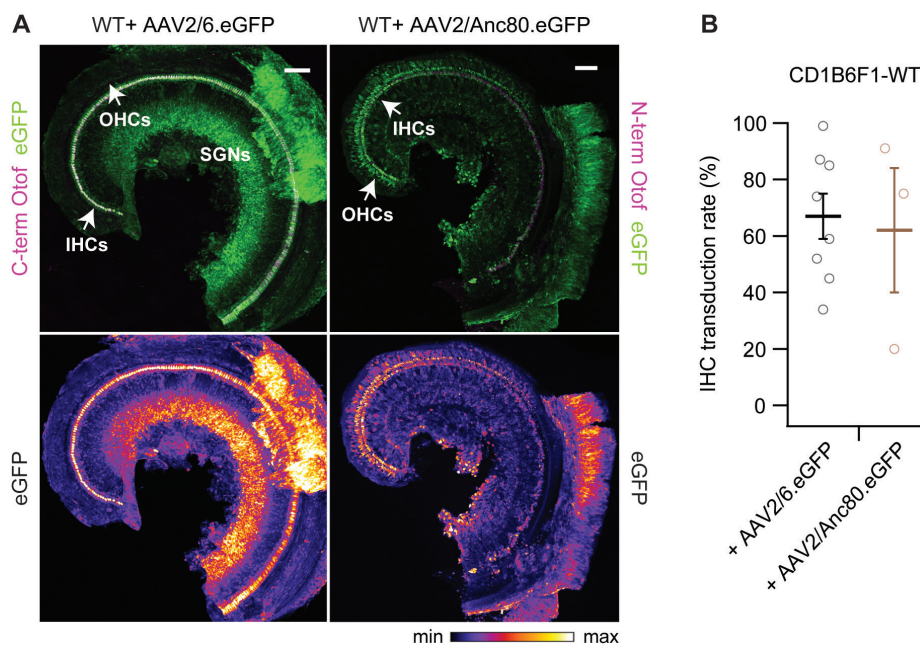
**Figure 2.3:**

**The AAV2/Anc80L65 serotype has a similar IHC transduction efficiency as the AAV2/6 serotype**

**A** Low magnification views of organs of Corti from CD1B6F1-wild-type mice injected with a single eGFP-expressing AAV2/6 virus (AAV2/6.eGFP; P23; virus titer: $1.44 \times 10^{10}$ vg/µl) at P6 or a single eGFP-expressing AAV2/Anc80L65 virus (AAV2/Anc80.eGFP; P30; virus titer: $1.11 \times 10^{9}$ vg/µl) at P8. The organ of Corti was immunolabeled for eGFP (green) and the N-terminal part (N-term Otof) or C-terminal part (C-term Otof) of otoferlin (magenta). Individual eGFP immunolabelings are illustrated as color lookup tables with warmer colors representing higher pixel intensities (max) and depicted with the same settings as the merged image (top panels). All images are maximum intensity projections of optical confocal sections. IHCs, inner hair cells. OHCs, outer hair cells, SGNs, spiral ganglion neurons. Scale bars, 100 µm.

**B** Percentage of eGFP immunolabeled IHCs in apical cochlear turns of AAV2/6.eGFP (n = 8 mice) and AAV2/Anc80.eGFP (n = 3 mice) injected CD1B6F1-wild-type mice (P30). Transduction rates of individual animals are depicted with open symbols. The average transduction rates are displayed as mean ± s.e.m.

turns of AAV2/Anc80.eGFP injected wild-type ears (P30). 20-91% of IHCs in these injected cochleae exhibited an eGFP fluorescent signal (average: 62 ± 22%, mean ± standard error of the mean (s.e.m.), n = 3 mice) (Figure 2.3B). These IHC targeting rates were on average like the transduction rates seen in apical cochlear turns of AAV2/6.eGFP transduced CD1B6F1-wild-type mice (range: 34-99%, average: 67 ± 8%, n = 8 mice, P23-28) (Figure 2.3).

## 2.3.2 Using the AAV2/Anc80L65 serotype for dual-AAV mediated otoferlin gene delivery

Other research groups have reported a high IHC transduction efficiency for the AAVAnc80L65 serotype (Landegger *et al.*, 2017; Suzuki *et al.*, 2017; Yoshimura *et al.*, 2018) and the results from "chapter 2.3.1" clearly show that the AAV2/Anc80.eGFP virus seems to have on average an equally high IHC targeting rate as the AVV2/6.eGFP virus (see results "chapter 2.3.1"). This means that the AAV2/Anc80 serotype could potentially be used for dual-AAV mediated otoferlin gene transfer. The two split-otoferlin trans-splicing expression cassettes (5'-AAV-TS and 3'-AAV-TS) described in "chapter 2.2" (see "materials and methods" section in "Al-Moyed *et al.*, 2019") were, therefore, packed into two separate AAV2/Anc80 viruses (dual-AAV2/Anc80-TS) and subsequently co-injected through the RWM into the scala tympani (see introduction "Figure 1.6") of the left cochlea of P5-6 CD1B6F1-*Otof*$^{-/-}$ mice (n = 6 cochleae) as described in (Jung *et al.*, 2015; Al-Moyed *et al.*, 2019).

Organs of Corti from injected and non-injected contralateral ears were isolated at P29-31 and immunolabeled for eGFP, calbindin, and the N-terminal (N-term Otof) and C-terminal (C-term Otof) parts of otoferlin as described in "Al-Moyed et al., 2019". IHCs and OHCs were visualized via the HC marker calbindin. The eGFP immunostaining was used to monitor for successful virus transduction. Dual-AAV2/Anc80-TS injected Otof-/- inner ears only showed an otoferlin immunofluorescent signal in IHCs and few OHCs (Figure 2.4, upper panel; Figure 2.6A) similar to the observations made in dual-AAV2/6-TS or dual-AAV2/6-Hyb injected cochleae (see results "chapter 2.2"). eGFP immunofluorescence, on the other hand, was also detected in other cell types like e.g. SGNs (Figure 2.4, upper panel). Only a few non-injected contralateral cochleae showed an eGFP and otoferlin immunofluorescent signal in a few IHCs (Figure 2.4, lower panel). The other non-injected contralateral ears, however, did not exhibit any eGFP or otoferlin immunofluorescence.
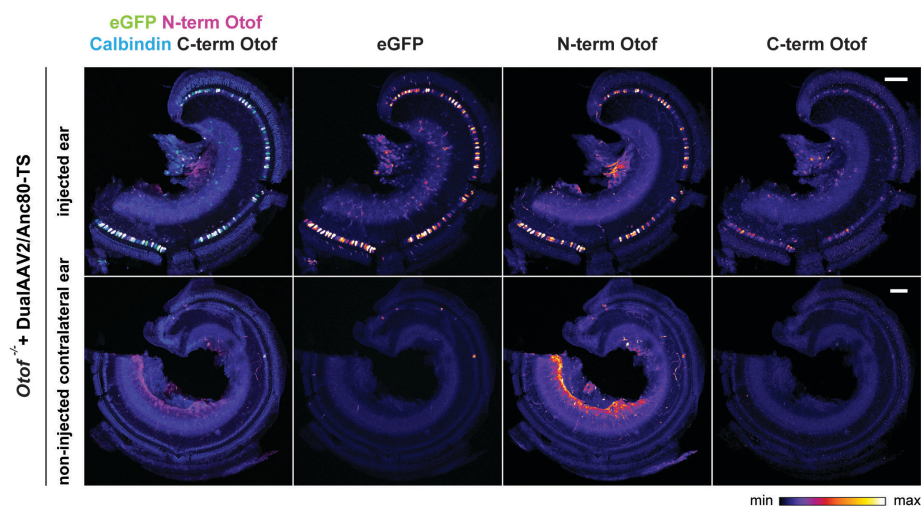
**Figure 2.4:**

**Otoferlin dualAAV2/Anc80-TS transduced *Otof*$^{-/-}$ organs of Corti show the same otoferlin expression pattern as dualAAV2/6 transduced *Otof*$^{-/-}$ inner ears.**

Low magnification views of organs of Corti from a CD1B6F1-*Otof*$^{-/-}$ mouse (P29) co-injected with otoferlin dual-AAV2/Anc80-TS half vectors at P5. The organs of Corti of injected (upper panel) and non-injected contralateral ears (lower panel) were immunolabeled in parallel for the auditory HC marker calbindin (blue), eGFP (green), and the N-terminal part (N-term Otof, magenta) and C-terminal part (C-term Otof, white) of otoferlin. Individual eGFP and otoferlin immunostainings are illustrated as color lookup tables with warmer colors representing higher pixel intensities (max) and depicted with the same settings as the merged image (top left and bottom left). All images are maximum intensity projections of optical confocal sections acquired with the same settings. Scale bars, 100 µm.

To examine if dual-AAV2/Anc80-TS half vectors can lead to higher full-length otoferlin transduction rates than the dual-AAV2/6-TS or dual-AAV2/6-Hyb vectors used in "chapter 2.2", I have counted the number of IHCs showing N-terminal and C terminal otoferlin immunofluorescent signal in the entire cochlea of dual-AAV2/Anc80-TS injected mice (P29-31). The number of IHCs immunolabeled with the C-terminal (C-term) otoferlin antibody ranged from 3-36% (average: 15 ± 5%, n = 6 mice) and those immunolabeled with the N-terminal (N-term) antibody ranged from 4-53% (average: 24 ± 7%) (Figure 2.5). Some of the transduced IHCs only showed N-terminal otoferlin immunofluorescent signal, but no C-terminal signal. However, I did not detect any IHC that displayed C-terminal otoferlin signal

without N-terminal signal. This quantification also clearly demonstrated that the full-length otoferlin (C-term otoferlin) IHC transduction rates were higher in the apical cochlear turn (C-term otoferlin: average: 19 ± 5%, range: 3-36%) than in the midbasal and basal turns (C-term otoferlin: average: 7 ± 1%, range: 2-11%) (Figure 2.5).
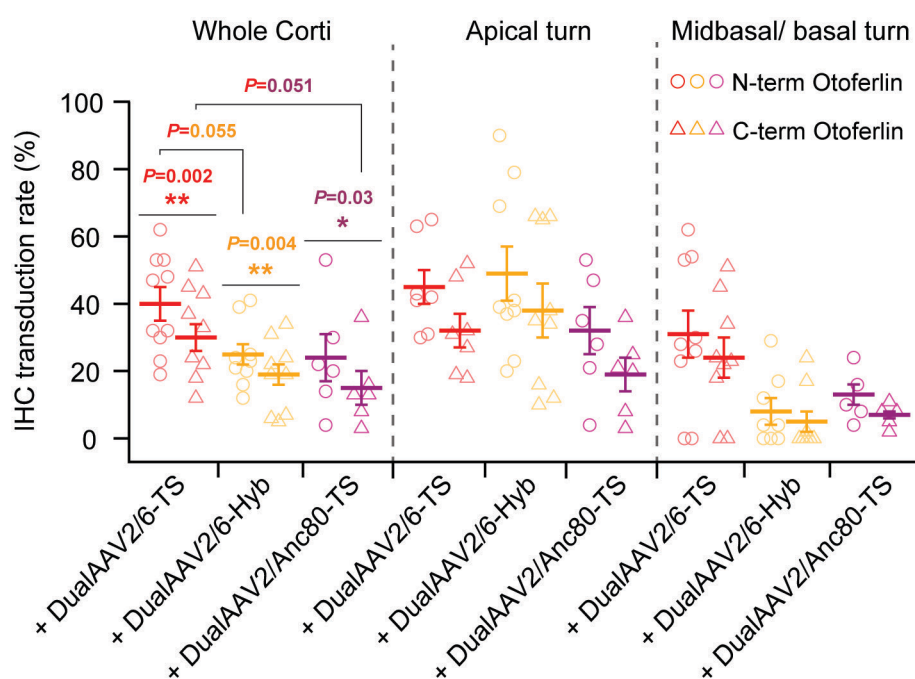


**Figure 2.5:**

**Otoferlin dual-AAV2/Anc80-TS transduced *Otof^-/-* cochleae had slightly lower full-length otoferlin IHC transduction rates than dual-AAV2/6-TS transduced cochleae.**

Percentage of auditory IHCs showing an N-terminal (N-term Otoferlin) or a C-terminal (C-term Otoferlin) otoferlin immunofluorescent signal along the cochlea of dual-AAV2/6-TS injected (n = 10 mice), dual-AAV2/6-Hyb injected (n = 9 mice), and dual-AAV2/Anc80-TS injected (n = 6 mice) CD1B6F1-*Otof^-/-* mice (P18-31). Transduction rates of individual animals are depicted with open symbols. The average IHC transduction rates are displayed as mean ± s.e.m., ns *P* > 0.05; **P* ≤ 0.05; ***P* ≤ 0.01, Wilcoxon matched-pair signed rank test and Tukey's multiple comparisons test (see "Appendix Table S1" for exact *P*-values).
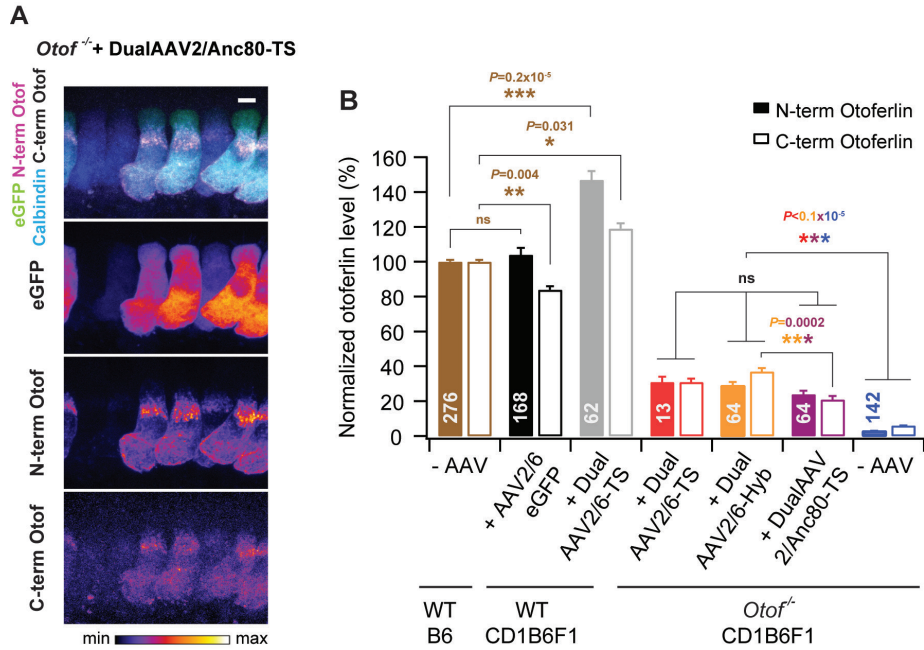
**Figure 2.6:**

*Otof⁻/⁻* **IHCs transduced with otoferlin dual-AAV2/Anc80-TS half vectors have on average slightly lower full-length otoferlin protein levels than dual-AAV2/6 transduced IHCs.**

**A** High magnification views of otoferlin dual-AAV2/Anc80-TS transduced CD1B6F1-*Otof⁻/⁻* IHCs (P31) co-immunolabeled for the auditory HC marker Calbindin (blue), eGFP (green), and the N-terminal part (N-term Otof, magenta) and C-terminal part (C-term Otof, white) of otoferlin. Individual eGFP and otoferlin immunostainings are illustrated as color lookup tables with warmer colors representing higher pixel intensities (max) and depicted with the same settings as the merged image (top panel). All images are maximum intensity projections of optical confocal sections. Scale bar, 5 μm.

**B** Average N-terminal (N-term Otoferlin, closed bars) and C-terminal (C-term Otoferlin, open bars) otoferlin immunofluorescent intensity levels in transduced (+AAV2/6.eGFP, +DualAAV2/6-TS, +DualAAV2/6-Hyb, +DualAAV2/Anc80-TS) and non-transduced (-AAV) CD1B6F1-*Otof⁻/⁻* and CD1B6F1-wild-type IHCs (P23-30). The N-terminal and C-terminal otoferlin intensity levels were normalized to the otoferlin intensity levels of each corresponding antibody separately in non-transduced control B6-wild-type IHCs (-AAV WTB6). The number of analyzed IHCs is displayed inside the bars. Average otoferlin protein levels are depicted as mean ± s.e.m., ns $P > 0.05$; *$P \leq 0.05$; **$P \leq 0.01$; ***$P \leq 0.001$, Kruskal–Wallis test followed by Dunn's multiple comparison test (see "Appendix Table S1" for exact $P$-values).

I have further quantified overall otoferlin protein levels in these dual-AAV2/Anc80-TS transduced $Otof^{-/-}$ IHCs by measuring the fluorescence intensity of the N-terminal and C-terminal otoferlin signals and compared these levels to the protein levels in dual-AAV2/6 transduced $Otof^{-/-}$, non-transduced $Otof^{-/-}$, and wild-type control IHCs (Figure 2.6). The immunofluorescence intensity of each antibody was normalized to the corresponding N-terminal or C-terminal otoferlin fluorescence intensity in non-transduced C57BL/6J (B6) wild-type IHCs as described in "Strenzke *et al.*, 2016" and "Al-Moyed *et al.*, 2019". Dual-AAV2/Anc80-TS transduced $Otof^{-/-}$ IHCs had slightly lower overall otoferlin protein levels (N-term: average: $24 \pm 2\%$; C-term: average: $21 \pm 2\%$) than dual-AAV2/6-TS (N-term: average: $31 \pm 3\%$; C-term: average: $31 \pm 2\%$) or dual-AAV2/6-Hyb (N-term: average: $29 \pm 2\%$; C-term: average: $37 \pm 2\%$) transduced $Otof^{-/-}$ IHCs (Figure 2.6B).

As mentioned in "chapter 2.2", otoferlin dual-AAV2/6-TS and dual-AAV2/6-Hyb vectors were unable to prevent the ~40% of synaptic ribbon loss in $Otof^{-/-}$ mice (Roux *et al.*, 2006; Al-Moyed *et al.*, 2019: Fig. 2A-B). I have counted the number of synaptic ribbons in IHCs from dual-AAV2/Anc80-TS injected $Otof^{-/-}$ mice as described in "Al-Moyed *et al.*, 2019" to examine whether these half vectors could rescue synaptic ribbons in $Otof^{-/-}$ mutants (Figure 2.7). The synaptic ribbons were visualized via immunohistochemistry as in Khimich *et al.*, 2005 using an antibody against the transcriptional repressor carboxy-terminal binding protein 2 (CtBP2) that is transcribed from the same gene as the major synaptic ribbon component ribeye and only differs from ribeye in 20 amino acids in the B-domain. Dual-AAV2/Anc80-TS $Otof^{-/-}$ IHCs (P30; n = 4 IHCs) had on average $11 \pm 0.8$ synaptic ribbons, which was comparable to the average ribbon numbers in dual-AAV2/6 transduced IHCs (dual-AAV2/6-TS: $10 \pm 0.2$ synaptic ribbons, n = 59 IHCs; dual-AAV2/6-Hyb: $10 \pm 0.3$ synaptic ribbons, n = 37 IHCs).
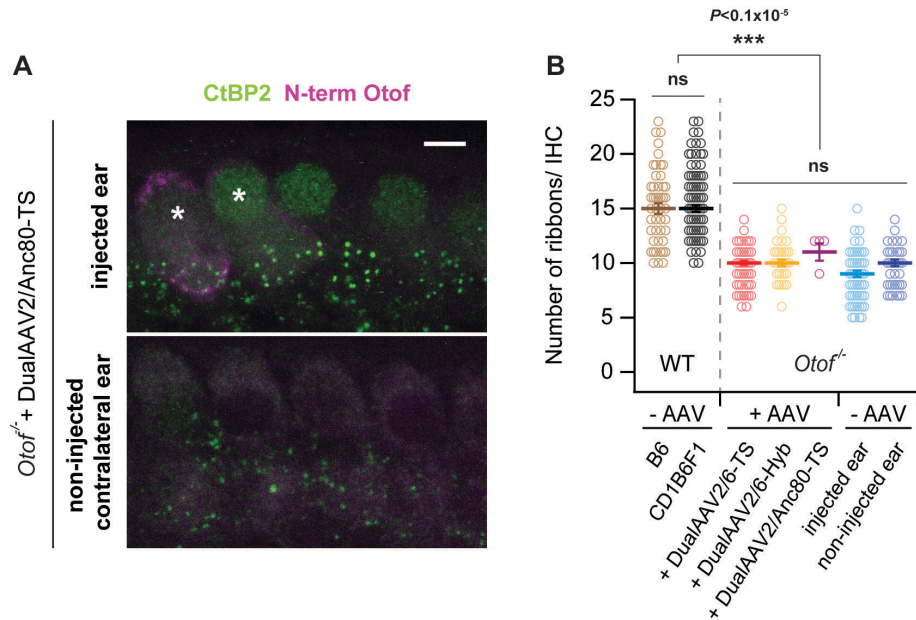
**Figure 2.7:**

**The dual-AAV2/Anc80-TS approach does not prevent synaptic ribbon loss in *Otof⁻/⁻* mice.**

**A** High magnification views of IHCs immunolabeled for otoferlin (N-term Otof, magenta) and the synaptic ribbon marker CtBP2 (green) from an otoferlin dual-AAV2/Anc80-TS injected CD1B6F1-*Otof⁻/⁻* mouse (P30). All images are maximum intensity projections of optical confocal sections and depicted with the same settings. Organs of Corti from the injected (top panel) and the non-injected contralateral ear (lower panel) were processed in parallel and imaged with the same settings. Transduced IHCs are labeled with an asterisk (*). Scale bar, 5 μm.

**B** Synaptic ribbons numbers assessed from IHCs in apical cochlear turns of non-transduced wild-type control IHCs (B6: n = 48 IHCs, CD1B6F1: n = 108 IHCs), dual-AAV transduced CD1B6F1-*Otof⁻/⁻* (+DualAAV2/6-TS: n = 59 IHCs, +DualAAV2/6-Hyb: n = 37 IHCs, +DualAAV2/Anc80-TS: n = 4 IHCs), and non-transduced CD1B6F1-*Otof⁻/⁻* IHCs from injected (-AAV injected ear, n = 65 IHCs) and non-injected contralateral (-AAV non-injected ear, n = 46 IHCs) ears (P25-30). Synaptic ribbon numbers of individual IHCs are indicated with open symbols. Average synaptic ribbon numbers are depicted as mean ± s.e.m., ns $P > 0.05$; ***$P ≤ 0.001$, Kruskal–Wallis test followed by Dunn's multiple comparison test (see "Appendix Table S1" for exact $P$-values). The data from die dualAAV2/Anc80-TS transduced IHCs were not taken into the statistical analysis.
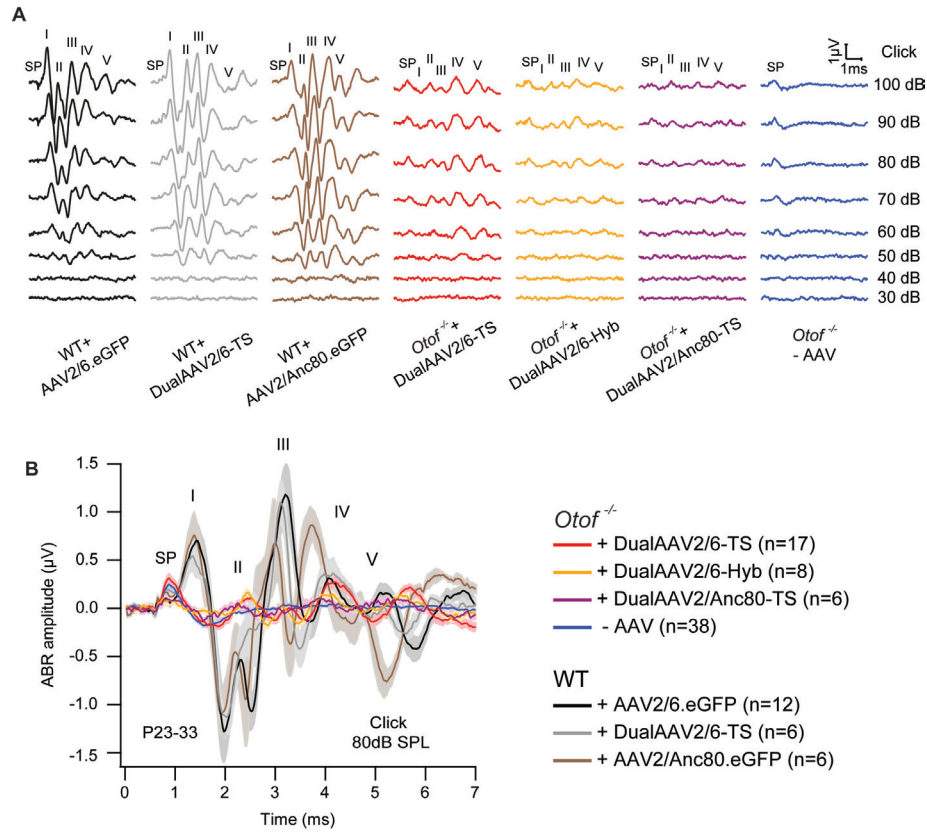
**Figure 2.8:**

**Otoferlin dual-AAV2/Anc80-TS half vectors can partially restore the auditory function in deaf *Otof⁻ᐟ⁻* mice.**

**A** Representative ABR wave traces measured from dual-AAV treated (+DualAAV2/6-TS: P26; +DualAAV2/6-Hyb: P27; +DualAAV2/Anc80-TS: P29) CD1B6F1-*Otof⁻ᐟ⁻* and non-treated (-AAV: P26) control littermate mice in response to broadband click sound stimuli played with different sound pressure levels (30-100 dB SPL) and a stimulation frequency of 20 Hz/s. CD1B6F1-wild-type mice injected with an AAV2/6.eGFP virus (+AAV2/6.eGFP, P28), an AAV2/Anc80.eGFP virus (+AAV2/Anc80.eGFP, P32), or otoferlin dual-AAV2/6-TS half vectors (+DualAAV2/6-TS: P27) served as controls. Individual ABR waves are depicted from wave I-V. SP, summating potential.

**B** Average ABR waves in responses to 80 dB SPL broadband click sound stimuli played for 20 clicks/s and measured from CD1B6F1-wild-type control, dual-AAV treated CD1B6F1-*Otof⁻ᐟ⁻* and non-treated CD1B6F1-*Otof⁻ᐟ⁻* control littermate mice (P23-33). The number of analyzed animals is depicted in the figure. All average ABRs are displayed as mean ± s.e.m.

To determine if otoferlin dual-AAV2/Anc80-TS half vectors can rescue auditory function in deaf *Otof*^(-/-) mice (Roux *et al.*, 2006; Pangrsic *et al.*, 2010; Reisinger *et al.*, 2011) and increase ABR wave amplitudes, I measured ABRs in 3-4 weeks old (P26-33) CD1B6F1-*Otof*^(-/-) mice treated with these half vectors (+DualAAV2/Anc80-TS; n = 6 mice). Non-injected *Otof*^(-/-) littermates (-AAV) as well as CD1B6F1-wild-type mice injected with the AAV2/Anc80.eGFP virus (+AAV2/Anc80.eGFP; n = 6 mice) served as controls (Figure 2.8). All animals used for ABR recordings were subjected to broadband click and tone burst (4 kHz, 6 kHz, 8 kHz, 12 kHz, 16 kHz, 24 kHz, 32 kHz) sound stimuli played with different sound pressure levels (SPL) from 10-100 dB SPL. Dual-AAV2/Anc80-TS injected animals showed a partial rescue of ABR waves like the rescue seen in dual-AAV2/6-Hyb *Otof*^(-/-) injected mice (+DualAAV2/6-Hyb) (Figure 2.8; Figure 2.10A).
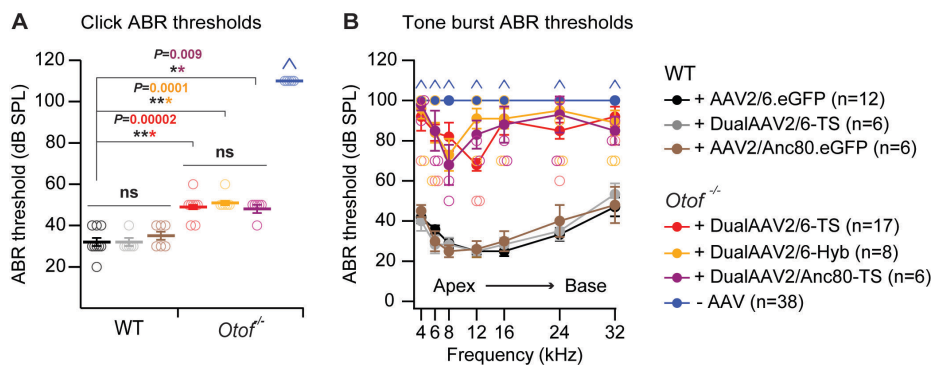


**Figure 2.9:**

*Otof*^(-/-) **mice treated with otoferlin dual-AAV2/Anc80-TS half vectors have near wild-type click sound-evoked ABR thresholds and improved tone burst-induced ABR thresholds.**

**A** Broadband click sound-induced ABR thresholds of otoferlin dual-AAV treated CD1B6F1-*Otof*^(-/-) and non-treated CD1B6F1-*Otof*^(-/-) and wild-type control mice (P23-33). All animals with click ABR thresholds exceeding the maximum loudspeaker output of 100 dB SPL are set to 110 dB SPL (arrows).

**B** Tone burst sound-evoked ABR thresholds in dual-AAV treated CD1B6F1-*Otof*^(-/-) compared to CD1B6F1-wild-type and non-treated CD1B6F1-*Otof*^(-/-) control mice (P23-33). All animals with tone burst ABR thresholds exceeding the maximum loudspeaker output of 90 dB SPL are set to 100 dB SPL (arrows).

**Data information**: In (A-B), ABR thresholds of individual animals are displayed with open circles and the number of analyzed animals is depicted in the figure. Average ABR thresholds are indicated as mean ± s.e.m. In (A), ns $P > 0.05$; **$P ≤ 0.01$; ***$P ≤ 0.001$, Kruskal–Wallis test followed by Dunn's multiple comparison test (see "Appendix Table S1" for exact *P*-values).
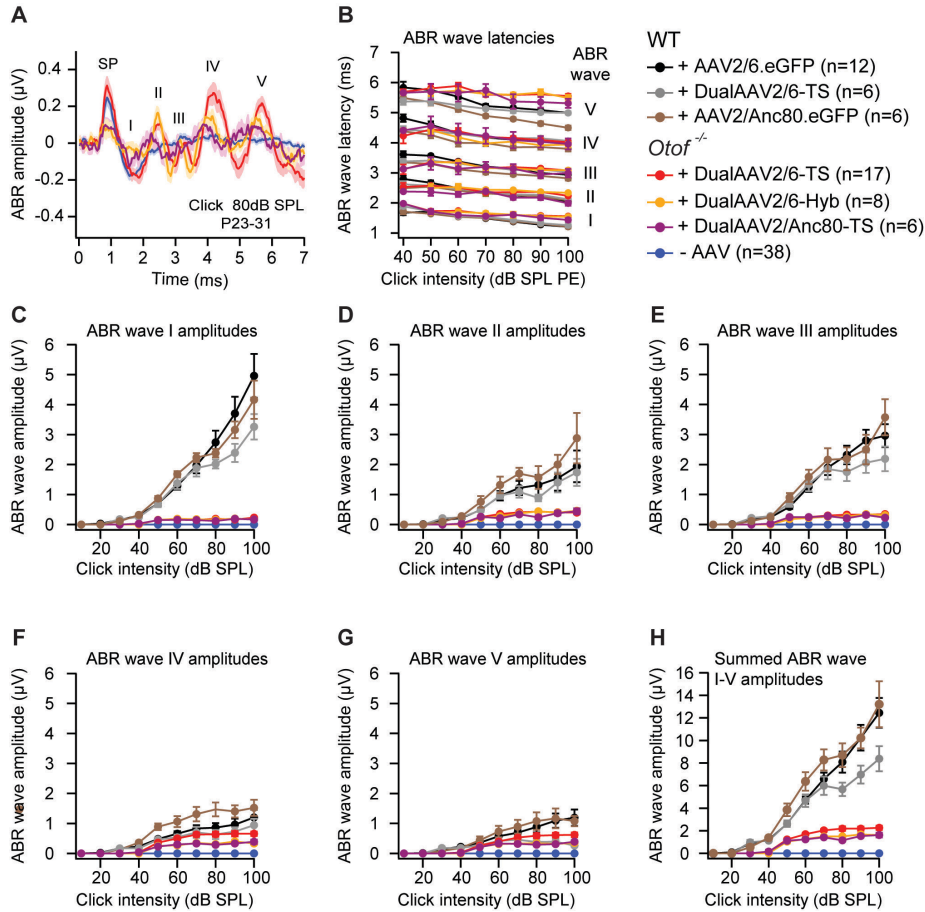
**Figure 2.10:**

**Dual-AAV2/Anc80 injected *Otof*^{-/-} mice have comparable ABR wave amplitudes to otoferlin dual-AAV2/6-Hyb treated *Otof*^{-/-} mice.**

**A** Average ABR waves in responses to 80 dB SPL broadband click sound stimuli measured in otoferlin dual-AAV treated CD1B6F1-*Otof*^{-/-} and non-treated CD1B6F1-*Otof*^{-/-} control littermate mice (P23-31).

**B** Average ABR wave I-V latencies in response to broadband click sound stimuli played at 20 Hz/s and different click sound pressure levels quantified from CD1B6F1-wild-type control, otoferlin dual-AAV treated CD1B6F1-*Otof*^{-/-} and non-treated control CD1B6F1- *Otof*^{-/-} littermate mice (P23-33). SPL, sound pressure level. PE, peak equivalent.

**C-H** Average ABR wave I (C), wave II (D), wave III (E), wave IV (F), wave V (G), and the summed wave I-V (H) amplitudes at different broadband click sound intensities measured in otoferlin dual-AAV injected CD1B6F1-*Otof*^{-/-} mice compared to CD1B6F1-wild-type and non-treated CD1B6F1-*Otof*^{-/-} control animals (P23-33).

**Data information**: In (A-H), average ABR wave traces, latencies, and amplitudes are depicted as mean ± s.e.m. The number of analyzed animals is displayed in the figure.

The click sound-evoked ABR thresholds in dual-AAV2/Anc80-TS treated animals were close to wild-type control thresholds and ranged between 40-50 dB SPL (average: 48 ± 2 dB SPL) (Figure 2.9A). AAV2/Anc80.eGFP injected control wild-type animals had, in comparison, click ABR thresholds between 30-40 dB SPL (average: 35 ± 2 dB SPL) (Figure 2.9A). Tone burst-induced ABR thresholds, on the other hand, were less improved than click ABR thresholds (range: 50 dB SPL to no ABRs at all) and comparable to the thresholds measured in dual-AAV2/6-Hyb $Otof^{-/-}$ injected mice (Figure 2.9B). Dual-AAV2/Anc80-TS injected $Otof^{-/-}$ animals had generally better tone burst ABR thresholds at lower sound frequencies (6 kHz, 8 kHz, 12 kHz) with the best threshold measured at 8 kHz and 50 dB SPL (Figure 2.9B).

The ABR wave amplitudes in these injected $Otof^{-/-}$ mice were smaller than in wild-type control animals, but similar to the amplitudes quantified in dual-AAV2/6-Hyb injected $Otof^{-/-}$ animals (Figure 2.10C-H). The amplitude of an ABR wave was defined as the difference between the local maximum of a wave and the subsequent minimum (see "materials and methods" section in "Al-Moyed *et al.*, 2019"). Additionally, the latencies of ABR waves I and V were delayed when compared to wild-type control mice (Figure 2.10B).

The tone burst ABR thresholds, ABR wave amplitudes, and ABR wave latencies, apart from ABR wave V, of AAV2/Anc80.eGFP injected control wild-type mice were not different from those measured in other wild-type control animals (Figure 2.8; Figure 2.9; Figure 2.10).

In summary, otoferlin dual-AAV2/Anc80-TS half vectors can partially restore full-length otoferlin protein levels in $Otof^{-/-}$ IHCs and auditory function in $Otof^{-/-}$ mice. Nonetheless, these split-AAV vectors did not result in higher full-length otoferlin IHC transduction rates or ABR wave amplitudes than otoferlin dual-AAV2/6-TS or dual-AAV2/6-Hyb half vectors.

## 2.4     Investigating the role of otoferlin in IHC synapse maturation

Roux *et al.*, 2006, who first characterized an *Otof*<sup>-/-</sup> mouse model, has found that P15 old animals have around 40% less ribbon synapses than P15 wild-type control mice. In an attempt to understand if this decrease in synapse numbers is caused by a developmental defect in these animals, Roux *et al.*, 2006 counted the number of ribbon synapses in P6 old animals and found no difference between *Otof*<sup>-/-</sup> and wild-type control mice. The authors of this study have, therefore, concluded that ribbon synapses develop normally in *Otof*<sup>-/-</sup> mice (Roux *et al.*, 2006). However, the administration of otoferlin dual-AAV half vectors into the cochleae of P5-6 *Otof*<sup>-/-</sup> mice could not prevent or reverse the loss of synaptic ribbons in these mutants as mentioned earlier in "chapter 2.2 and 2.3.2" (Al-Moyed *et al.*, 2019: Fig. 2A-B; Figure 2.7). My results rather indicate that re-introducing otoferlin at as early as P5 into *Otof*<sup>-/-</sup> IHCs is already too late to stop the synaptic ribbon loss in these mutants and further points towards a possible yet undescribed role for otoferlin in IHC synapse maturation.

To investigate whether *Otof*<sup>-/-</sup> mice have altered synapse maturation, I assessed the number of ribbon synapses in B6-wild-type and B6-*Otof*<sup>-/-</sup> mice from two different litters between the ages of P4 and P14 (P4, P6, P8, P10, P12, P14) via immunohistochemistry (Figure 2.11). The afferent IHC synapses were visualized by immunostaining for synaptic ribbons via an anti-CtBP2 antibody as in Khimich *et al.*, 2005 and for the postsynaptic density of afferent auditory nerve boutons via an anti-Shank1a antibody as in Huang *et al.*, 2012. Only intact synapses with closely juxtaposed immunofluorescent synaptic ribbon and afferent bouton spots were used for quantification purposes. Orphan ribbons or afferent post-synaptic terminals that did not have an adjacent pre-synaptic fluorescent signal were not included into the assessment. The experiments and data analysis mentioned in this chapter were performed by me as described in "Al-Moyed *et al.*, 2019".

The quantitative analysis showed that the number of ribbon synapses gradually decreased during IHC maturation within the first two postnatal weeks in both *Otof*<sup>-/-</sup> and control wild-type mice (Figure 2.12). At P4, wild-type IHCs (45 ± 0.8 synapses, n = 38 IHCs) and *Otof*<sup>-/-</sup> IHCs (49 ± 0.6 synapses, n = 56 IHCs) still had comparable ribbon synapse
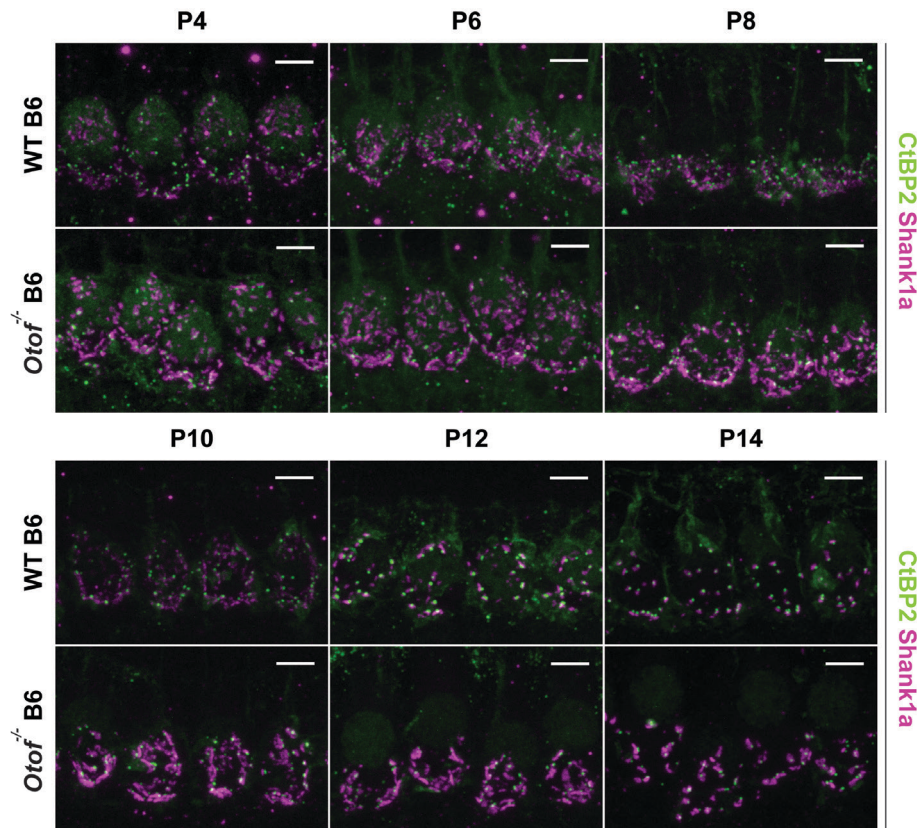
**Figure 2.11:**

*Otof^{-/-}* **mice have abnormally enlarged post-synaptic afferent nerve terminal compared to wild-type control mice.**

High magnification views of IHCs from P4-14 old B6-*Otof^{-/-}* and B6-wild-type control mice immunolabeled for the synaptic ribbon marker CtBP2 (green) and the post-synaptic density marker Shank1a (magenta). All images are maximum intensity projections of optical confocal sections displayed with the same settings. Scale bars, 5 μm.

numbers ($P > 0.999$, Kruskal–Wallis test followed by Dunn's multiple comparison test). The most prominent reduction in wild-type IHC synapses was seen in the first postnatal week between P4-8 (P6: 39 ± 0.6 synapses, n = 53 IHCs; P8: 28 ± 0.4 synapses, n = 49 IHCs). The synapse numbers continued to decrease further during the second postnatal week until they reached an almost stable number around the onset of hearing at P12 (Mikaelian and Ruben, 1965; Ehret, 1985) (P10: 25 ± 0.5 synapses, n = 51 IHCs; P12: 17 ± 0.4 synapses, n = 57 IHCs). In contrast, the decline in *Otof^{-/-}* IHC synapse numbers seemed to be delayed

during the first postnatal week compared to wild-type controls (P6: 49 ± 0.7 synapses, n = 62 IHCs; P8: 43 ± 0.6 synapses, n = 59 IHCs). After P8, the synapse numbers in *Otof*^{-/-} mutants started to decrease until P14 (P10: 32 ± 0.5 synapses, n = 56 IHCs; P12: 22 ± 0.4 synapses, n = 57 IHCs). At P14, both wild-type (16 ± 0.2 synapses, n = 73 IHCs) and *Otof*^{-/-} mice (15 ± 0.3 synapses, n = 65 IHCs) showed no significant difference in synapse numbers (*P* > 0.999, Kruskal–Wallis test followed by Dunn's multiple comparison test).
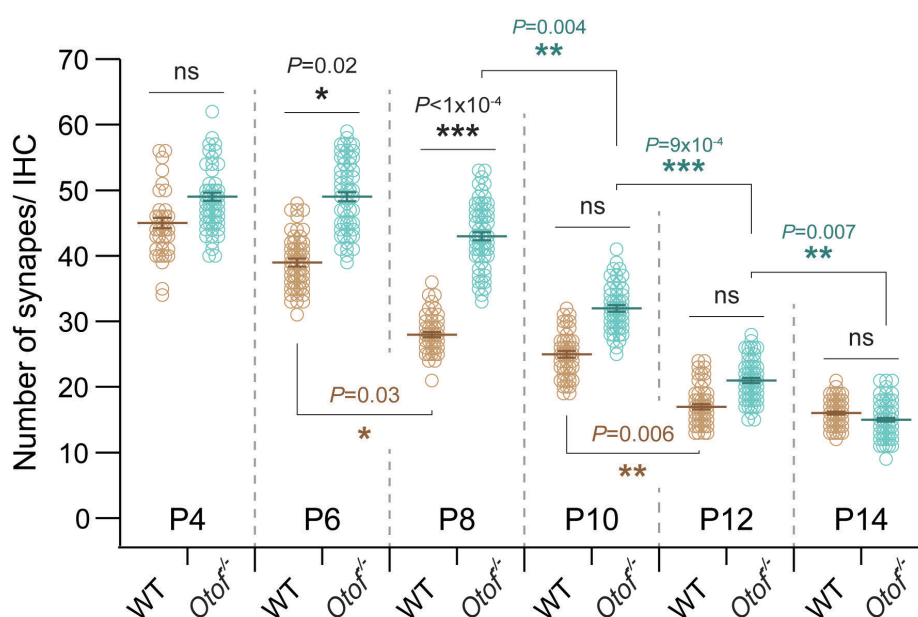


**Figure 2.12:**

**IHC ribbon synapse maturation during the first two postnatal weeks seems to be altered and delayed in *Otof*^{-/-} mice.**

IHC ribbon synapse numbers quantified from IHCs in apical cochlear turns of P4-14 old B6-wild-type (P4: n = 38 IHCs; P6: n = 53 IHCs; P8: n = 49 IHCs; P10: n = 51 IHCs; P12: n = 57 IHCs; P14: n = 73 IHCs) and B6-*Otof*^{-/-} mice (P4: n = 56 IHCs; P6: n = 62 IHCs; P8: n = 59 IHCs; P10: n = 56 IHCs; P12: n = 57 IHCs; P14: n = 65 IHCs). Synapse numbers of individual IHCs are depicted with open symbols. Average synapse numbers are represented as mean ± s.e.m., ns *P* > 0.05; ; *\**P* ≤ 0.05; *\*\**P* ≤ 0.01; *\*\*\**P* ≤ 0.001, Kruskal–Wallis test followed by Dunn's multiple comparison test (see "Appendix Table S1" for exact *P*-values).

Another striking observation in all immunolabeled *Otof*^{-/-} organs of Corti was the abnormal shape of the post-synaptic density immunofluorescent signal (Figure 2.11,

magenta). While the shape of Shank1a-labelled post-synaptic structures seemed to get smaller with increasing age in wild-type control mice, it stayed enlarged in $Otof^{-/-}$ mice across all analyzed age groups.

In conclusion, the number of IHC ribbon synapses decreases during IHC maturation within the first two postnatal weeks in both wild-type and $Otof^{-/-}$ IHCs. This reduction, however, seemed to be delayed in $Otof^{-/-}$ mutants and the shape of the immunolabeled post-synaptic terminals was enlarged across all analyzed age groups. The synaptic ribbon numbers continue to decline further with increasing age in $Otof^{-/-}$ mice until only around 60% of ribbons are left at P25-30 while the ribbon numbers stay stable in wild-type animals as shown in "chapter 2.3.2".

# 3 Discussion

Otoferlin is a large multi-$C_2$ domain protein crucial for hearing and auditory IHC synaptic transmission (Roux *et al.*, 2006; Pangršič, Reisinger and Moser, 2012). Similar to other ferlin family members, otoferlin is a multi-functional protein involved in many cellular processes (Lek *et al.*, 2012; Pangršič, Reisinger and Moser, 2012; Pangrsic and Vogl, 2018). Studies have shown that this protein plays an essential role in IHC exocytosis by acting as a $Ca^{2+}$ sensor facilitating SV priming, SV fusion, SV tethering, and SV replenishment to refill the RRP at the AZ release sites (Roux *et al.*, 2006; Pangrsic *et al.*, 2010; Pangršič, Reisinger and Moser, 2012; Vogl *et al.*, 2015; Michalski *et al.*, 2017; Chakrabarti, Michanski and Wichmann, 2018). This protein is further involved in exocytosis-endocytosis coupling by regulating IHC AZ release site clearance, clathrin-mediated endocytosis, SV recycling, SV formation, and SV transport towards the synaptic ribbons (Duncker *et al.*, 2013; Jung *et al.*, 2015; Strenzke *et al.*, 2016; Michalski *et al.*, 2017; Chakrabarti, Michanski and Wichmann, 2018). This Ph.D. thesis has contributed to the efforts towards the understanding of otoferlin's diverse roles in auditory IHCs and the disease mechanisms underlying *OTOF*-related deafness. Furthermore, this work represents the first successful split-AAV mediated gene therapy application to transfer large genes into the inner ear, partially restoring auditory function in a deaf DFNB9 mutant mouse model, thus being a great step towards human DFNB9 gene therapy.

## 3.1 The relationship between otoferlin protein levels and IHC function in different otoferlin mutant mouse models

Mutations in the *OTOF* gene, encoding otoferlin, have been linked to prelingual autosomal recessive non-syndromic hearing loss DFNB9 (Yasunaga *et al.*, 1999, 2000; Varga, 2003; Shearer and Smith, 2015). The severity of the hearing impairment ranges from mild to profound deafness depending on the pathogenic *OTOF* variant the patient is carrying (Varga, 2003; Varga *et al.*, 2006; Rodríguez-Ballesteros *et al.*, 2008; Marlin *et al.*, 2010). These mutations are believed to affect the function and the interaction of otoferlin

with phospholipids and other proteins (Pangršič, Reisinger and Moser, 2012). Nonetheless, the exact impact of these human *OTOF* mutations on otoferlin's stability, cellular distribution, ultrastructural subcellular localization, protein expression levels and how these factors influence the disease mechanism underlying DFNB9 is unknown.

### 3.1.1 Plasma membrane-bound otoferlin levels scale with IHC exocytosis and auditory function

Several otoferlin mutant mouse models have been generated to study the functions of otoferlin and to understand the disease mechanisms underlying DFNB9. Three otoferlin mutant mouse models with different degrees of IHC function and hearing impairment were investigated during the scope of this thesis. $Otof^{-/-}$ mice have almost completely abolished IHC exocytosis despite normal $Ca^{2+}$ currents (Roux *et al.*, 2006; Reisinger *et al.*, 2011; Al-Moyed *et al.*, 2019) and show no characteristic ABR wave responses to sound stimuli (Roux *et al.*, 2006; Reisinger *et al.*, 2011; Al-Moyed *et al.*, 2019: Fig. 3, Fig. EV5). $Otof^{Pga/Pga}$ mutant mice, carrying the p.Asp1767Gly missense mutation that affects the $C_2F$ domain of otoferlin (Schwander *et al.*, 2007), are also profoundly deaf, but their IHCs still show normal fast and severely reduced sustained IHC exocytosis (see introduction "chapter 1.3") (Pangrsic *et al.*, 2010). In contrast, $Otof^{I515T/I515T}$ otoferlin knock-in mice, carrying the human p.Ile515Thr missense mutation that affects $C_2C$ domain of otoferlin (Mirghomizadeh *et al.*, 2002; Varga *et al.*, 2006), only display a moderate hearing impairment and their sustained IHC exocytosis levels are between the levels of wild-type and $Otof^{Pga/Pga}$ IHCs (Strenzke *et al.*, 2016).

Several studies as well as this work have shown that otoferlin is distributed throughout the cytoplasm of auditory IHCs and found at the IHC plasma membrane (Roux *et al.*, 2006; Pangrsic *et al.*, 2010; Strenzke *et al.*, 2016: Fig. 1A, Fig. 1D, Appendix Fig. S1A). $Otof^{-/-}$ IHCs lack otoferlin expression (Roux *et al.*, 2006; Reisinger *et al.*, 2011; Strenzke *et al.*, 2016: Fig. 7C; Al-Moyed *et al.*, 2019: Fig. 1E, Fig. 2A, Appendix Fig. S1, Appendix Fig. S2), which, in turn, leads to the complete loss of auditory function and almost abolished IHC exocytosis in these mice (Roux *et al.*, 2006; Reisinger *et al.*, 2011; Al-Moyed *et al.*, 2019). $Otof^{Pga/Pga}$ IHCs still have an overall otoferlin protein expression level of approximately 31% compared

to protein levels in wild-type IHCs (Strenzke *et al.*, 2016: Fig. 1G), but have only 3% of membrane-bound otoferlin in their basolateral plasma membrane left (Strenzke *et al.*, 2016: Fig. 1D-F, Fig. 1I-J). A previous study that quantified cellular otoferlin protein levels in *Otof^{Pga/Pga}* IHCs using a different analysis routine than mine has found comparable overall otoferlin levels of around 27% in these mutants (Pangrsic *et al.*, 2010). *Otof^{I515T/I515T}* IHCs, on the other hand, have similar overall otoferlin protein levels (~35% of wild-type levels) as *Otof^{Pga/Pga}* IHCs (Strenzke *et al.*, 2016: Fig. 1G), but have higher membrane-bound otoferlin levels (~34% of wild-type levels) than *Otof^{Pga/Pga}* mutants (Strenzke *et al.*, 2016: Fig. 1D-F, Fig. 1I-J). This decrease in otoferlin levels in *Otof^{I515T/I515T}* IHCs was additionally verified via pre-embedding immunogold EM microscopy (Strenzke *et al.*, 2016: Fig. 7L, Fig. 7M). Cellular otoferlin protein levels reduced even further with increasing age from 30% in P19 *Otof^{I515T/I515T}* mice (2-3 weeks) to 15% in P99 animals (14-15 weeks) (Strenzke *et al.*, 2016: Fig. EV1D). This finding might explain the progressive deterioration in ABR wave amplitudes and hearing thresholds observed in older mice (8-25 weeks) (Strenzke *et al.*, 2016). The defective IHC exocytosis and moderate hearing loss phenotype seen in *Otof^{I515T/I515T}* mutants could also not be ascribed to a decrease in IHC synapse numbers as these were not different from synapse numbers in wild-type IHCs (Strenzke *et al.*, 2016: Fig. EV1F). All of these findings suggest that the reduced plasma membrane-bound otoferlin protein levels found in these different mutant mouse models seem to scale with their sustained IHC exocytosis levels, and consequently with their ABR wave amplitudes and ABR thresholds (Roux *et al.*, 2006; Pangrsic *et al.*, 2010; Strenzke *et al.*, 2016; Al-Moyed *et al.*, 2019).

Impaired IHC exocytosis can be caused by defects in one or several steps of the SV cycle like SV tethering (Vogl *et al.*, 2015; Chakrabarti, Michanski and Wichmann, 2018), SV priming, SV fusion, RRP replenishment (Roux *et al.*, 2006; Pangrsic *et al.*, 2010; Vogl *et al.*, 2015; Strenzke *et al.*, 2016; Michalski *et al.*, 2017; Chakrabarti, Michanski and Wichmann, 2018), AZ release site clearance (Duncker *et al.*, 2013; Jung *et al.*, 2015; Chakrabarti, Michanski and Wichmann, 2018), endocytosis (Neef *et al.*, 2014; Jung *et al.*, 2015), the correct formation of fusion-competent SVs (Strenzke *et al.*, 2016), and SV transport from cellular compartments towards the synaptic ribbon (Strenzke *et al.*, 2016; Michalski *et al.*,

2017; Chakrabarti, Michanski and Wichmann, 2018). The fast component of IHC exocytosis is measured via patch-clamp electrophysiological recordings as IHC plasma membrane capacitance increments upon short IHC depolarization (see introduction "chapter 1.2"). These capacitance changes are thought to reflect the fusion of the RRP SVs (Moser and Beutner, 2000; Beutner and Moser, 2001). The presence of at least 30% of overall otoferlin protein levels in both *Otof^{Pga/Pga}* and *Otof^{I515T/I515T}* mutants appears to be still sufficient to ensure RRP SV priming, docking, and fusion at the AZ membrane in these mutants (Pangrsic *et al.*, 2010; Strenzke *et al.*, 2016). This, however, is not the case in *Otof^{-/-}* IHCs that lack otoferlin (Roux *et al.*, 2006; Pangrsic *et al.*, 2010; Strenzke *et al.*, 2016; Al-Moyed *et al.*, 2019).

The sustained component of IHC exocytosis measured upon longer IHC depolarization is believed to represent the constant replenishment of the RRP SVs (see introduction "chapter 1.2") (Moser and Beutner, 2000; Beutner and Moser, 2001; Frank *et al.*, 2010; Pangrsic *et al.*, 2010). This process is considered to be $Ca^{2+}$ dependent (Schnee *et al.*, 2011) and requires the presence of otoferlin (Pangrsic *et al.*, 2010; Strenzke *et al.*, 2016; Michalski *et al.*, 2017). Although the overall otoferlin protein levels were not significantly different between *Otof^{Pga/Pga}* and *Otof^{I515T/I515T}* IHCs (Strenzke *et al.*, 2016: Fig. 1G), *Otof^{I515T/I515T}* mice showed a lower reduction in sustained IHC exocytosis levels and a less severe hearing loss phenotype than *Otof^{Pga/Pga}* mutants (Pangrsic *et al.*, 2010; Strenzke *et al.*, 2016). This difference between the two mutant mouse models is likely due to the almost abolished plasma membrane-bound otoferlin levels in *Otof^{Pga/Pga}* IHCs, but not in *Otof^{I515T/I515T}* mutants (Strenzke *et al.*, 2016: Fig. 1D-F, Fig. 1I-J). In fact, the amount of plasma membrane-bound otoferlin seems to influence the RRP replenishment rates in IHCs (Pangrsic *et al.*, 2010; Strenzke *et al.*, 2016) since these rates ranged between ~700 SVs/s/AZ in wild-type IHCs, ~340 SVs/s/AZ in *Otof^{I515T/I515T}* IHCs with 34% of membrane-bound otoferlin, and ~200 SVs/s/AZ in *Otof^{Pga/Pga}* IHCs with 3% of membrane-bound otoferlin (Pangrsic *et al.*, 2010; Strenzke *et al.*, 2016).

A recent study has further reported that the exocytosis steps following tethering and docking seem to be slowed down in *Otof^{Pga/Pga}* IHCs, leading to the accumulation of multiple-tethered and docked SVs at the presynaptic AZ membrane upon IHC stimulation

(Chakrabarti, Michanski and Wichmann, 2018). Wild-type IHCs, on the contrary did not show such a SV accumulation (Chakrabarti, Michanski and Wichmann, 2018). The authors of this study have, therefore, proposed that this accumulation in $Otof^{Pga/Pga}$ IHCs is caused by an impaired AZ membrane release site clearance (Chakrabarti, Michanski and Wichmann, 2018). This, in turn, is thought to slow down the process of SV resupply to refill the RRP at the AZ membrane and thereby contributes to the reduced sustained IHC exocytosis levels in these mutants (Pangrsic *et al.*, 2010; Chakrabarti, Michanski and Wichmann, 2018). The almost absent otoferlin levels in the plasma membrane of $Otof^{Pga/Pga}$ IHCs (Strenzke *et al.*, 2016: Fig. 1D-F, Fig. 1I-J) might explain the SV accumulation and AZ membrane clearance defect seen in this mutant given that otoferlin can interact with the endocytic protein AP-2, which is involved in AZ membrane clearance (see introduction "chapters 1.2 and 1.3") (Duncker *et al.*, 2013; Jung *et al.*, 2015). Since $Otof^{I515T/I515T}$ IHCs have plasma membrane-bound otoferlin levels (~34% of wild-type levels) that are between the levels of wild-type and $Otof^{Pga/Pga}$ IHCs (Strenzke *et al.*, 2016: Fig. 1D-F, Fig. 1I-J), it is possible that such a SV accumulation and AZ release site clearance dysfunction also occurs in $Otof^{I515T/I515T}$ mutants, but not as pronounced as in $Otof^{Pga/Pga}$ IHCs. Further ultrastructural analysis of $Otof^{I515T/I515T}$ IHC ribbon synapses upon IHC stimulation is needed to test this theory.

Another factor that potentially contributes to the differences between the sustained IHC exocytosis levels in $Otof^{Pga/Pga}$ and $Otof^{I515T/I515T}$ mutants, is the cellular distribution of otoferlin throughout their IHCs (Strenzke *et al.*, 2016: Fig. 1A-C, Appendix Fig. S1A-C). Otoferlin and Vglut3 are slightly more localized to the basal region below the IHC nucleus in $Otof^{I515T/I515T}$ IHCs compared to wild-type IHCs (Strenzke *et al.*, 2016: Fig. 1H). In contrast, both proteins were found to be more concentrated in the apical IHC region above the nucleus in $Otof^{Pga/Pga}$ IHCs (Strenzke *et al.*, 2016: Fig. 1H). This finding might point towards a defect in otoferlin and Vglut3 trafficking from the apical IHC region in $Otof^{Pga/Pga}$ mutants, where those two proteins are being produced, to the IHC synapse at the basal region. Padmanarayana *et al.*, 2014 has demonstrated that the $C_2C$ and $C_2F$ domains of otoferlin can interact with the phospholipid [PI(4,5)P2] *in vitro*. This interaction is thought to regulate the preferential targeting of otoferlin towards membranes and cellular

compartments with a specific lipid content. Thus, the p.Asp1767Gly and perhaps also the p.Ile515Thr mutation might possibly alter the interaction of these two $C_2$ domains with phospholipids and other proteins involved in SV trafficking (Pangrsic *et al.*, 2010; Strenzke *et al.*, 2016). The different membrane-bound otoferlin levels in both mutants (Strenzke *et al.*, 2016: Fig. 1D-F, Fig. 1I-J) further indicate that the $C_2F$ domain, in particular, seems to play a more prominent role in membrane targeting than the $C_2C$ domain of otoferlin. *Otof*$^{-/-}$ IHCs transfected *in vitro* with an otoferlin cDNA construct that lacks the $C_2F$ domain via biolistic Gene Gun transfection showed hardly any otoferlin immunofluorescence staining in the plasma membrane, which further supports this assumption (Müller, 2016). There is increasing evidence that otoferlin does not only regulate AZ release site clearance to generate new docking spots for arriving RRP SVs (Duncker *et al.*, 2013; Jung *et al.*, 2015; Chakrabarti, Michanski and Wichmann, 2018), but might also be involved in $Ca^{2+}$-dependent assembly of membrane-trafficking complexes and cellular trafficking events like other ferlins (Lek *et al.*, 2012; Johnson, 2017). Since otoferlin can interact with MyoVI and Rab8 that are involved in cargo sorting and endosomal trans-Golgi networking (Heidrych *et al.*, 2008, 2009; Roux *et al.*, 2009; Pangrsic and Vogl, 2018) it could potentially be that otoferlin regulates the transport of Vglut3 carrying endosomal structures to more basal IHC regions or newly formed SVs to refill the ribbon-associated SV pool at the synaptic ribbon (see introduction "chapter 1.3") (Heidrych *et al.*, 2008, 2009; Roux *et al.*, 2009; Duncker *et al.*, 2013; Jung *et al.*, 2015; Vincent *et al.*, 2015; Michalski *et al.*, 2017). The more apical otoferlin and Vglut3 distribution seen in *Otof*$^{Pga/Pga}$ mutants might point towards a defect in the transport of newly formed SVs to refill the ribbon-associated SV pool since less otoferlin is present in basal IHC regions to ensure efficient SV trafficking. This hypothesis is further strengthened by the observations of another study that reported fewer ribbon-associated SVs at the ribbons of *Otof*$^{Pga/Pga}$ IHCs upon continuous IHC stimulation, especially at the upper distal half of the synaptic ribbon (Chakrabarti, Michanski and Wichmann, 2018).

The structural changes caused by the p.Ile515Thr and the p.Asp1767Gly mutation are thought to have an impact on the stability of otoferlin (Pangrsic *et al.*, 2010; Strenzke *et al.*, 2016). In fact, predictions of otoferlin's 3D $C_2C$ domain structure have indicated that

exchanging the isoleucine at position 515 that points towards the hydrophobic core of this domain with a more hydrophilic threonine can reduce the stability of otoferlin (Strenzke *et al.*, 2016). Since organs of Corti from *Otof*<sup>Pga/Pga</sup> and *Otof*<sup>I515T/I515T</sup> mice did not have lower otoferlin mRNA levels than wild-type organs of Corti, it can be ruled out that the lower protein levels in their IHCs result from less transcription or mRNA decay (Pangrsic *et al.*, 2010; Strenzke *et al.*, 2016). Inhibiting protein biosynthesis in *Otof*<sup>I515T/I515T</sup> IHCs via cycloheximide led to an even further decrease in overall otoferlin levels, which could not be detected in wild-type IHCs (Strenzke *et al.*, 2016: Appendix Fig. S1E). This result clearly suggests that the mutated otoferlin form in these IHCs is more unstable and degrades faster than wild-type otoferlin, which would explain the overall reduced otoferlin levels in these mutants. It is possible that the p.Asp1767Gly mutation decreases the stability of otoferlin as well given the reduced overall otoferlin protein levels and normal otoferlin mRNA levels in *Otof*<sup>Pga/Pga</sup> IHCs (Pangrsic *et al.*, 2010).

### 3.1.2 Temperature elevation further reduces otoferlin protein levels in *Otof*<sup>I515T/I515T</sup> mice

DFNB9 patients carrying the p.Ile515Thr mutation suffer from a temporary hearing loss once their core body temperature rises up to 38.1°C and higher (Varga *et al.*, 2006). Incubating explanted *Otof*<sup>I515T/I515T</sup> organs of Corti (P7-8) at 38.5°C for 24 hours led to a further reduction in overall otoferlin protein levels from 29% at 37°C to 21% at 38.5°C (Strenzke *et al.*, 2016: Fig. 6H-J, Fig. 6K). Such a reduction in otoferlin levels was not observed in wild-type IHCs at 38.5°C (Strenzke *et al.*, 2016: Fig. 6H-J, Fig. 6K). The plasma membrane-bound otoferlin levels in *Otof*<sup>I515T/I515T</sup>, in particular, seemed to be affected by these temperature shifts and decreased further with increasing temperature (Strenzke *et al.*, 2016: Fig. 6M-N). At 38.5°C, *Otof*<sup>I515T/I515T</sup> mice had only 12% of total membrane-bound otoferlin levels left in their IHCs (Strenzke *et al.*, 2016: Fig. 6N). This reduction in otoferlin protein levels in *Otof*<sup>I515T/I515T</sup> IHCs was consistent with a further decrease in sustained IHC exocytosis levels at higher temperatures (38.5-40°C) (Strenzke *et al.*, 2016). These mutants additionally showed a slower exocytosis recovery to baseline levels when the temperature was reduced from 38.5°C-40°C to 29°C in comparison to wild-type IHCs (Strenzke *et al.*,

2016). Interestingly, increasing the temperature did not only affect otoferlin expression levels, but also changed the cellular distribution of otoferlin in these mutants. $Otof^{I515T/I515T}$ IHCs had a more apical distribution of otoferlin and Vglut3 at 38.5°C (Strenzke *et al.*, 2016: Fig. 6L) similar to the distribution of both proteins seen in $Otof^{Pga/Pga}$ mutants under normal experimental conditions (Strenzke *et al.*, 2016: Fig. 1H). The extremely reduced amount of membrane-bound otoferlin and the more apical distribution of both otoferlin and Vglut3 likely explain the impaired sustained IHC exocytosis at higher temperatures and poorer exocytosis recovery from temperature shifts in $Otof^{I515T/I515T}$ mutants.

The findings of Strenzke *et al.*, 2016, who studied the physiology of $Otof^{I515T/I515T}$ IHCs in more detail, indicate that otoferlin is generally a heat-sensitive protein and that some pathogenic *OTOF* mutations like the p.Ile515Thr mutation seem to increase the heat instability of this protein even further (Strenzke *et al.*, 2016). It is also possible that heat does not only affect the stability of otoferlin, but also changes the folding of this protein and thereby alters the interaction of its $C_2$ domains with phospholipids at the IHC plasma membrane and other cellular compartments. My results further imply that both the $C_2C$ and the $C_2F$ domains of this protein play a role in targeting and/or integrating otoferlin into membranes. Strenzke *et al.*, 2016 has, therefore, suggested that an increase in the body temperature of patients suffering from *OTOF*-related temperature-sensitive hearing loss reduces the amount of correctly folded otoferlin protein at the IHC plasma membrane below the critical level needed for proper IHC functioning and synaptic sound encoding.

### 3.1.3 The p.Ile515Thr mutation affects the membrane turnover in endosomal IHC structures

Further ultrastructural analysis of both wild-type and in $Otof^{I515T/I515T}$ IHCs via pre-embedding immunogold electron microscopy revealed no difference in the subcellular localization between the two genotypes. Otoferlin immunogold labelling was found distributed throughout the cytoplasm and at the plasma membrane, especially at the AZ membrane (Strenzke *et al.*, 2016: Fig. 7A-B, Fig. 7D-G, Appendix Fig. S5B-C), which was consistent with the reports from a previous study (Roux *et al.*, 2006). In comparison, Vglut3 labeling was found as clusters, most likely representing SVs, surrounding synaptic ribbons

and distributed throughout the cytosol (Strenzke *et al.*, 2016: Fig. 7H, Appendix Fig. S5A-A'). Interestingly, otoferlin did not localize to the SVs surrounding the ribbon in both genotypes (Strenzke *et al.*, 2016: Fig. 7D-G, Appendix Fig. S5B', Appendix Fig. S5C'') as previously reported by Roux *et al.*, 2006. This discrepancy between both studies might be due to using different immunogold embedding EM procedures, otoferlin antibodies, or the inaccessibility of the otoferlin epitope the antibody binds to.

Otoferlin was specifically found at plasma membrane invaginations and different vesicular structures within IHCs in both genotypes (Strenzke *et al.*, 2016: Fig. 7A-B, Fig. 7D-G, Fig. 7I-J, Appendix Fig. S5B-C). These vesicular structures are most probably of endosomal origin since these cellular compartments contained clathrin-coated pits (Strenzke *et al.*, 2016: Fig. 7A-B, Fig. 7I-J red arrows, Appendix Fig. S5B-C), involved budding off SV from endosomal (see introduction "chapter 1.2" and "Figure 1.4"). This observation is in agreement with a previous report that found otoferlin to co-localize with endosomal compartments via STED microscopy imaging (Revelo *et al.*, 2014). Measuring the outer diameter of these structures revealed that they were larger than the size of an average SV (average diameter: 30-45 nm according to Neef *et al.*, 2007; Chapochnikov *et al.*, 2014; Strenzke *et al.*, 2016; Chakrabarti, Michanski and Wichmann, 2018). Moreover, $Otof^{I515T/I515T}$ IHCs had on average larger vesicular structures (average: 210 ± 13 nm, range: 51-625 nm) than wild-type IHCs (average: 151 ± 8nm, range: 52-423nm) (Strenzke *et al.*, 2016: Fig. 7K). A recent study also reported the presence of more endosome-like vacuoles with diameters larger than 70 nm after IHC stimulation with high $K^+$ concentrations in $Otof^{Pga/Pga}$ IHCs (Chakrabarti, Michanski and Wichmann, 2018). The larger diameter of these endosomal compartments in $Otof^{I515T/I515T}$ and $Otof^{Pga/Pga}$ IHCs likely indicate a general defect in membrane turn-over in these mutants. This assumption is further corroborated by the presence of enlarged membrane-proximal and ribbon-associated SVs in both mutants (Strenzke *et al.*, 2016; Chakrabarti, Michanski and Wichmann, 2018). Based on these findings it was proposed that otoferlin plays a role in membrane retrieval and the formation of correctly sized fusion-competent SVs from endosome-like vacuoles and membrane invaginations (Strenzke *et al.*, 2016; Chakrabarti, Michanski and Wichmann,

2018). The larger endosomal compartments and enlarged SVs in $Otof^{I515T/I515T}$ and $Otof^{Pga/Pga}$ IHCs point towards a defect in SV formation in these mutant mouse models.

Otoferlin is thought to play a role in SV recycling by interacting with phospholipids and proteins involved in this process like the AP-2 complex (Duncker *et al.*, 2013; Jung *et al.*, 2015), which also plays a role in SV reformation in IHCs (Jung *et al.*, 2015), and other yet unidentified proteins (see introduction "chapter 1.3"). These proteins are believed to form a larger protein complex termed the otoferlin interactome that can facilitate SVs to pinch off from larger endosomal vacuoles and plasma membrane invaginations (Duncker *et al.*, 2013; Kononenko *et al.*, 2014; Jung *et al.*, 2015; Strenzke *et al.*, 2016; Chakrabarti, Michanski and Wichmann, 2018; Pangrsic and Vogl, 2018). It is also interesting to note that the $C_2C$ and $C_2F$ domains of otoferlin can be phosphorylated by the $Ca^{2+}$/calmodulin-dependent serine/threonine kinase CaMKIIδ, transforming the $C_2C$ domain from a non-$Ca^{2+}$ binding into a $Ca^{2+}$ binding domain and decreasing the $Ca^{2+}$ binding affinity of the $C_2F$ domain (Meese *et al.*, 2017). The $Ca^{2+}$ dependent phosphorylation of otoferlin by CaMKIIδ and/or other kinases was suggested to regulate the function of otoferlin in exocytosis, SV replenishment, and/or membrane retrieval at endosomal compartments near synaptic ribbons to ensure continuous high SV release rates at IHC synapses (Meese *et al.*, 2017). Thus, it is possible that the p.Ile515Thr and the p.Asp1767Gly mutations change the folding of the protein so that otoferlin is less accessible for CaMKIIδ and/ or any other otoferlin interactome protein involved in SV recycling or reformation, leading to the membrane turnover defects and enlarged SVs observed in $Otof^{I515T/I515T}$ and $Otof^{Pga/Pga}$ IHCs (Strenzke *et al.*, 2016: Fig. 7K; Chakrabarti, Michanski and Wichmann, 2018). The p.Asp1767Gly mutation additionally seems to interfere with the $Ca^{2+}$ binding ability of otoferlin's $C_2F$ domain (Meese, 2015), which might alter the membrane targeting of otoferlin towards these cellular compartment (Strenzke *et al.*, 2016: Fig. 1H) and/or its interaction with other otoferlin interactome proteins involved in membrane retrieval like AP-2 (Duncker *et al.*, 2013; Jung *et al.*, 2015).

In conclusion, sustained IHC exocytosis levels and auditory function in different otoferlin mutant mouse models seem to correlate with the amount of plasma membrane-bound otoferlin in their IHCs. The structural changes caused by the p.Ile515Thr and the

p.Asp1767Gly mutation likely decrease the stability of otoferlin, leading to reduced overall protein levels in IHCs of $Otof^{I515T/I515T}$ and $Otof^{Pga/Pga}$ otoferlin mutant mice. These reduced protein levels and/or the structural changes in otoferlin further influence SV replenishment, AZ release site clearance, and SV reformation from larger endosome-like vacuoles in these two mutant mouse models. The p.Asp1767Gly, in particular, altered the cellular distribution of otoferlin and appeared to affect the membrane targeting ability of its $C_2F$ domain, causing an impairment in SV trafficking towards the ribbons in $Otof^{Pga/Pga}$ mice. Temperature elevation lowered the levels of plasma membrane-bound otoferlin even further and also changed the cellular distribution of otoferlin in $Otof^{I515T/I515T}$ IHCs, thus, providing a potential explanation for the temperature-sensitive hearing loss seen in individuals carrying this $OTOF$ mutation.

## 3.2 Dual-AAV mediated full-length otoferlin cDNA transfer into auditory IHCs

DFNB9 patients would be an interesting target group for gene replacement therapies since they usually have no inner ear anomalies and the only available treatment option for these individuals are cochlear implants at the moment (Eppsteiner *et al.*, 2012; Shearer and Smith, 2015; Nishio and Usami, 2017). Even though cochlear implants have proven over the years to be very effective in improving the hearing quality of these patients (Eppsteiner *et al.*, 2012; Shearer and Smith, 2015; Nishio and Usami, 2017), these devices still have major drawbacks in frequency resolution and speech understanding during noise despite constant improvement (Bruns, Mürbe and Hahne, 2016; Huang *et al.*, 2017; Lee and Park, 2018). Gene replacement therapies are, therefore, considered to be a better alternative for treating hearing loss than cochlear implants (see introduction "chapter 1.7") (Géléoc and Holt, 2014; Ahmed, Shubina-Oleinik and Holt, 2017; Lee and Park, 2018). However, developing a gene therapy approach to transfer the 6 kb-long full-length otoferlin CDS into auditory IHCs is challenging since IHCs are terminally differentiated cells and tightly embedded into the surrounding tissue in the organ of Corti. To date, the only successful full-length otoferlin *in vivo* rescue of hearing and balance was achieved in otoferlin knock-down zebrafish by microinjecting a full-length otoferlin plasmid into zebrafish embryos at

the one-cell stage (Chatterjee *et al.*, 2015). Other efforts to transfer foreign full-length otoferlin cDNA into auditory IHCs of other animals models such as *Otof*^{-/-} mice were only successful *in vitro* via biolistic gene gun transfection of explanted organs of Corti (Strenzke *et al.*, 2016). Lentiviruses, retroviruses, or Semliki Forest viruses, commonly used to transport large genes with a size up to 8 kb, target IHCs with an extremely low efficiency and can potentially integrate into the host genome (Bedrosian *et al.*, 2006; Wang and Chang, 2013; Ahmed, Shubina-Oleinik and Holt, 2017). Adenoviruses, on the other hand, can deliver foreign cDNA with a size up to 36 kb and are able to transduce IHCs to some degree, but can result in a strong immune response in the target tissue (Ahmed, Shubina-Oleinik and Holt, 2017). An earlier attempt using adenoviruses to transfer full-length otoferlin cDNA into IHCs of *Otof*^{-/-} mice led to severe malformations within the inner ear (Reuter, 2011). Thus, it is necessary to develop a viral transduction method that enables the delivery of large transgenes such as the otoferlin CDS into auditory IHCs with high efficacy and minimum side effects.

Gene delivery mediated by recombinant AAVs is considered to be a promising tool to treat several inherited disorders like blindness and deafness due to their high safety profile and efficacy in targeting terminally differentiated cells compared to other viral vectors (see introduction "chapter 1.7") (Géléoc and Holt, 2014; Ahmed, Shubina-Oleinik and Holt, 2017; McClements and Maclaren, 2017; Lee and Park, 2018). The limited capacity of recombinant AAVs to transfer genes exceeding the size of its wild-type genome (~4.7 kb) (Grieger and Samulski, 2005; McClements and Maclaren, 2017) hinders the efficient transport of large transgenes such as otoferlin with a CDS of about 6 kb. Dual- and triple-AAV vectors have been developed to circumvent this obstacle and have shown efficacy in delivering large transgenes into various cell types including photoreceptors, which are also terminally differentiated cells like auditory IHCs (see introduction "chapter 1.8") (Zhang *et al.*, 2013; Colella *et al.*, 2014; Trapani *et al.*, 2014; Kodippili *et al.*, 2017). Nevertheless, split-AAV vectors have not been established for gene transfer into auditory or vestibular HCs yet (Ahmed, Shubina-Oleinik and Holt, 2017; Lee *et al.*, 2018). Within the scope of this thesis I have, therefore, investigated whether dual-AAV half vectors are suitable to transport the

full-length otoferlin cDNA into auditory IHCs and are able to restore IHC and auditory function in deaf *Otof*^{-/-} mice (Roux *et al.*, 2006; Reisinger *et al.*, 2011).

### 3.2.1 AAV2/6 targets auditory IHCs with high efficiency

The AAV serotype chosen for this proof-of-concept study was an AAV with ITRs from serotype 2 and capsid proteins from serotype 6 (AAV2/6). This serotype can be produced with a high vector-genome to transducing-unit ratio (Grieger, Soltys and Samulski, 2016), crucial for attaining good transduction rates without administering too many non-functional virus particles into the cochlea. Injecting a control eGFP-expressing AAV2/6 virus through the RWM (see introduction "Figure 1.6") into the left cochlea of CD1B6F1-wild-type mice at P6-7 showed that this serotype targets various cell types within the organ of Corti including auditory IHCs (Al-Moyed *et al.*, 2019: Fig. EV1A). This AAV serotype was also able to transduce up to 99% of auditory IHCs (average: ~67%) in the apical cochlear turn of injected animals (Figure 2.3). These results indicate that the AAV2/6 serotype is suitable for transgene transport into auditory IHCs contrary to a previous report, where this AAV serotype failed to transduce P1-2 IHCs (Shu *et al.*, 2016).

The injection time point of P5-8 was chosen as a compromise between two factors. Firstly, the inner ear of mice fully matures within the first two weeks after birth while humans are already born with mature inner ears (Kelly and Chen, 2009; Yoshimura *et al.*, 2018). This means that viral vectors need to be administered to at least two-week-old animals rather than neonatal mice (P0-2) to translate this type of treatment to human gene replacement therapy. The age between P5-8 is the closest developmental time point to the mature inner ear stage, where the injection glass pipette can still penetrate the auditory bulla structure covering the RWM without the need to create an additional opening in the bulla and cause unnecessary tissue damage. Secondly, Roux *et al.*, 2006, who first characterized an *Otof*^{-/-} mouse model, has reported that otoferlin is not essential for IHC development and survival, implying that otoferlin can be reintroduced at a later developmental stage like P5-8 without disrupting the inner ear development.

## 3.2.2 The dual-AAV trans-splicing and hybrid strategies are suitable for inner ear gene therapy

Since the dual-AAV trans-splicing and hybrid strategies had the best therapeutic outcomes upon co-injection into the retina (Colella *et al.*, 2014; Trapani *et al.*, 2014), I have tested the efficacy of these two strategies to deliver the full-length otoferlin cDNA into auditory IHCs in vivo (Al-Moyed *et al.*, 2019: Fig. EV2). For this purpose the full-length otoferlin cDNA, coding for the 1977 amino acid-long protein (transcript variant 4, NM_001313767) (Strenzke *et al.*, 2016), was split into two fragments and packed into two sperate AAV2/6 viruses. Co-injecting otoferlin dual-AAV2/6 half vectors (5'-AAV2/6 + 3'-AAV2/6) of either split-AAV strategy into cochleae of CD1B6F1-Otof$^{-/-}$ mice (P6-7) led to the transcription of the correct full-length otoferlin mRNA (Al-Moyed *et al.*, 2019) and the expression of eGFP and full-length otoferlin protein (C-term otoferlin) (Al-Moyed *et al.*, 2019: Fig. 1A–C, Fig. EV3, Appendix Fig. S1–S3). On the contrary, the non-injected contralateral ears of these mice did not show any eGFP or otoferlin expression (Al-Moyed *et al.*, 2019: Fig: 2A, Appendix Fig. S1-S2). Full-length otoferlin could be detected by using an antibody that binds after the transmembrane domain at the C-terminus of the protein (C-term otoferlin) (see introduction "Figure 1.5"). Another antibody binds within the N-terminal region of otoferlin (N-term otoferlin), present in truncated N-terminal otoferlin fragments and the full-length protein. Both eGFP and otoferlin were produced separately in transduced cells (Al-Moyed *et al.*, 2019: Fig. EV3, Appendix Fig. S3B) since a P2A sequence that induces ribosomal skipping was placed between the CDSs of eGFP and otoferlin in the 5'-AAV half vector (Al-Moyed *et al.*, 2019: Fig. EV2). Although otoferlin and eGFP were expressed under the same promoter and translated from the same mRNA (Al-Moyed *et al.*, 2019: Fig. EV2), the expression otoferlin was restricted to auditory HCs (Al-Moyed *et al.*, 2019: Fig. 1A-C, Appendix Fig. S1-S3) while eGFP could also be detected in other cell types throughout the cochlea (Al-Moyed *et al.*, 2019: Fig. 1A, Fig. EV1B, Appendix Fig. S3). The otoferlin immunofluorescent signal in these transduced organs of Corti was stronger in IHCs and a much weaker in OHCs (Al-Moyed *et al.*, 2019: Appendix Fig. S3). This otoferlin fluoresce intensity difference between IHCs and OHCs in transduced Otof$^{-/-}$ inner ears can also be seen between IHCs and OHCs in non-transduced wild-type control organs

of Corti (Roux *et al.*, 2006; Beurg *et al.*, 2008). A previous study has reported a similar restricted Vglut3 expression to auditory IHCs after AAV1-mediated Vglut3 gene delivery into Vglut3$^{-/-}$ organs of Corti upon postnatal RWM injections (P1–3 and P10–12) even though Vglut3 mRNA could be detected in other cell types (Akil *et al.*, 2012). Thus, it is very likely that otoferlin mRNA is also present in other cell types than HCs, especially those expressing eGFP. The restricted Vglut3 (Akil *et al.*, 2012) and otoferlin expression to auditory HCs suggests that there must be some sort of a post-transcriptional regulatory mechanism that leads to the selective expression of HC proteins in HCs and not in other cell types. Some of these mechanisms might be microRNA inactivation (Elkan-Miller *et al.*, 2011), targeted protein degradation (Cheng, Tong and Edge, 2016), or another yet to be identified regulatory process.

The analysis of the transduction rates throughout the entire cochlea revealed that 12-51% of IHCs in dual-AAV-TS injected and 5-34% of IHCs in dual-AAV-Hyb injected animals expressed full-length otoferlin (C-term otoferlin) (Al-Moyed *et al.*, 2019: Fig. 1D). Interestingly, the full-length otoferlin IHC transduction rates were higher in apical cochlear turns than in midbasal and basal regions of the cochlea. Since IHC maturation seems to progress in a gradient from the base to the apex of the cochlea (Kelly and Chen, 2009; Lelli *et al.*, 2009), it would mean that IHCs in more basal cochlear regions are already in a more mature developmental stage and might, therefore, express less cell surface receptors the AAV2/6 needs for cell entry than IHCs in more apical regions. Another reason could be that the anatomical properties of the scala tympani canal together with the diffusion kinetics of the virus solution led to the accumulation of more virus particles at the apex of the cochlea upon RWM injections than at the base close to the entry point of the injection pipette. About 10% of transduced IHCs only showed an N-terminal otoferlin immunolabeling, but no C-terminal immunolabeling in mice injected with either strategy (Al-Moyed *et al.*, 2019: Fig. 1D, Fig. EV3). This observation suggests that either only the 5'-AAV otoferlin half vector transduced these IHCs or the full-length otoferlin transgene did not reassemble correctly in these cells. Both possibilities would consequently lead to the production of N-terminal otoferlin fragments in these transduced IHCs (see discussion "chapter 3.2.7" for more details). As predicted, there were no IHCs showing C-terminal otoferlin antibody

immunolabeling without N-terminal immunolabeling since the 3'-AAV transgene did not contain a promoter sequence that could potentially drive protein expression. Nevertheless, the production of truncated C-terminal otoferlin fragments cannot be excluded as ITRs seem to have a weak promoter activity (Flotte *et al.*, 1992) (see discussion "chapter 3.2.7" for more details).

Further quantification of overall full-length otoferlin protein levels (C-term otoferlin) revealed that dual-AAV mediated large gene transfer can restore full-length otoferlin protein levels in transduced Otof$^{-/-}$ IHCs to an average of 31-37% of wild-type protein levels (Al-Moyed *et al.*, 2019: Fig. 1E, Fig. EV3). Non-transduced Otof$^{-/-}$ IHCs from contralateral non-injected ears only showed very faint background signal in comparison (Al-Moyed *et al.*, 2019: Fig. 1E, Appendix Fig. S1-2). Wild-type IHCs also transduced with dual-AAV-TS vectors showed an increase of around 30% in full-length protein levels as well (Al-Moyed *et al.*, 2019: Fig. 1E, Fig. EV3). Restoring 31-37% of full-length otoferlin levels in Otof$^{-/-}$ IHCs was sufficient to rescue fast exocytosis and significantly improve sustained exocytosis and RRP replenishment in these IHCs (Al-Moyed *et al.*, 2019). The partial rescue of synaptic transmission in these transduced IHCs is not surprising given that sustained IHC exocytosis levels scale with the amount of otoferlin in IHCs, especially at the plasma membrane as discussed earlier in "chapter 3.1.1".

### 3.2.3   Otoferlin seems to play a role in IHC synapse maturation

Roux *et al.*, 2006 has reported a 40% reduction in ribbon synapse numbers in P15 *Otof$^{-/-}$* IHCs. My results showed that dual-AAV transduced *Otof$^{-/-}$* IHCs (P26-29) did not have significantly different synaptic ribbon numbers than non-transduced IHCs, which only had approximately 60% of their ribbons left (Al-Moyed *et al.*, 2019: Fig. 2A-B). This finding shows that re-introducing full-length otoferlin into IHCs of P6-7 *Otof$^{-/-}$* mice did not rescue the synaptic ribbon loss in these animals.

Since otoferlin gene delivery at P6-7 seems to be too late to reverse or prevent synaptic ribbon loss in these mutant IHCs, it might be possible that otoferlin plays a role in IHCs synapse maturation. Assessing the number of IHC ribbon synapses in wild-type and *Otof$^{-/-}$*

mice between the age of P4 and 14 (P4, P6, P8, P10, P12, P14) revealed that $Otof^{-/-}$ mutants had significantly more synapses during the first postnatal week between P6-P8 than wild-type controls (Figure 2.11; Figure 2.12). This observation was non-compliant with the findings of Roux *et al.*, 2006, who reported normal synapse numbers in P6 $Otof^{-/-}$ mice. Nevertheless, it should be mentioned that in Roux *et al.*, 2006 ribbon synapse numbers were assessed at P6 via electron microscopy and not via immunohistochemistry as I did, which might explain the discrepancy between the two results. Additionally, the authors of the previous study h ave used a different $Otof^{-/-}$ mouse line than the one generated by Reisinger *et al.*, 2011 and that I used for my experiments. The IHC synapse loss defect in the mouse line I used might have been delayed in comparison to the mouse line assessed by Roux *et al.*, 2006.

The synapse numbers continued to decline in both genotypes with increasing age until both $Otof^{-/-}$ and wild-type animals had similar average synapse numbers of 15-16 synapses per IHC at P14 (Al-Moyed *et al.*, 2019: Fig. 2C-D; Figure 2.11; Figure 2.12). However, while in wild-type mice the number of IHC synapses already started to decrease in the first postnatal week from P6 until it reached an almost stable number of synapses at P12, this synapse degradation only seemed to start during the second postnatal week at P8 in $Otof^{-/-}$ animals and continued even after P14 (Figure 2.11; Figure 2.12). After P14, the number of IHC synapses stayed stable in wild-type mice with increasing age whereas the synapse number declined further to approximately 10 synapses per IHC in P26-29 old $Otof^{-/-}$ mice (Al-Moyed *et al.*, 2019: Fig. 2B). My results point towards a delay in IHC synapse maturation in $Otof^{-/-}$ mice. The comparable synapse numbers between both genotypes (wild-type: 16 synapses; $Otof^{-/-}$: 15 synapses) at P14 might also explain the normal $Ca^{2+}$ currents recorded from $Otof^{-/-}$ IHCs (P14-18) (Al-Moyed *et al.*, 2019).

Shank1 (SH3 and multiple ankyrin repeat domains protein 1) is a post-synaptic density scaffolding protein located in afferent auditory nerve boutons and is known to regulate the structure and function of synapses during development by arranging other post-synaptic density proteins (Huang *et al.*, 2012). The shape of the Shank1a-labeled post-synaptic terminals seemed to decrease within the first two postnatal weeks in wild-type IHCs, which is in line with previous observations made by (Huang *et al.*, 2012). In $Otof^{-/-}$ animals,

however, the shape of these structures stayed enlarged across all analyzed age groups (Al-Moyed *et al.*, 2019: Fig. 2C; Figure 2.11). This observation is in agreement with a previous report from Roux *et al.*, 2006, who found structurally abnormal postsynaptic contacts via electron microscopy in P15 *Otof*$^{-/-}$ IHCs, but not in wild-type cells. All these results imply that otoferlin is involved in IHC ribbon synapse maturation and that an earlier injection time point like P4 or younger might prevent the synapse loss seen in *Otof*$^{-/-}$ mice. Further analysis using STED microscopy imaging and electron microscopy might additionally be helpful to understand the altered IHC synapse development and the abnormal shape of the post-synaptic density in afferent auditory nerve boutons in *Otof*$^{-/-}$ animals.

Afferent auditory never fibers of SGNs can be classified into high-spontaneous rate low threshold, medium-spontaneous rate intermediate threshold, and low-spontaneous rate high threshold fibers (Liberman, 1978; Liberman and Liberman, 2016; Fettiplace, 2017). Mature *Vglut3*$^{-/-}$ mice, which are also deaf, lose approximately 40% of their SGNs (Seal *et al.*, 2008). Single-cell RNA sequencing revealed that half of the medium-spontaneous rate and almost all of the low-spontaneous rate fibers are lost in these knock-out animals (Shrestha *et al.*, 2018). The loss of low-spontaneous rate fibers due to noise-induced hearing loss or aging is predicted to affect speech perception, but not auditory thresholds (Furman, Kujawa and Liberman, 2013; Wu *et al.*, 2018). It is unknown whether *Otof*$^{-/-}$ mice also lose their auditory nerve fibers like *Vglut3*$^{-/-}$ animals, which is very likely given the fact that they lose almost half of their synaptic ribbons during maturation (Al-Moyed *et al.*, 2019: Fig. 2A-B).  Future studies will be needed to characterize the SGN subgroups present in *Otof*$^{-/-}$ mice and if otoferlin dual-AAV treatment can prevent auditory nerve fiber loss, possibly in combination with neurotrophic factor administration (Suzuki *et al.*, 2017).

It is also unclear whether DFNB9 patients have a similar reduction in IHC ribbon synapse numbers as *Otof*$^{-/-}$ (Roux *et al.*, 2006; Al-Moyed *et al.*, 2019: Fig. 2A-B) or *pachanga* otoferlin mutant mice (Pangrsic *et al.*, 2010). Since *Otof*$^{I515T/I515T}$ mutant mice have normal synapse numbers (see discussion "chapter 3.1.1") (Strenzke *et al.*, 2016: Fig. EV1E-F) it is likely that individuals carrying this mutation or affected by a moderate hearing loss form have normal synapse numbers as well. Preventing IHC synapse loss via dual-AAV otoferlin gene delivery would not be necessary in this case.

### 3.2.4 Otoferlin dual-AAV half vectors can partially rescue auditory function in *Otof*<sup>-/-</sup> mice

*Otof*<sup>-/-</sup> mice show no ABR waves when subjected to broadband click or tone burst (4 kHz, 6 kHz, 8 kHz, 12 kHz, 16 kHz, 24 kHz, 32 kHz) sound stimuli played with different sound pressure levels (SPL) (see introduction "Figure 1.2") (Roux *et al.*, 2006; Pangrsic *et al.*, 2010; Reisinger *et al.*, 2011). These mice, however, still have normal electrically evoked brainstem responses (eEBRs), measuring the signal transmission through the afferent auditory pathway, and DPOAEs that measure OHC function (Roux *et al.*, 2006). The profound deafness in these mice, therefore, likely results from an impaired IHC function and not from a defect in the OHCs, the auditory nerve, or the auditory centers in the brain stem (Roux *et al.*, 2006).

The administration of dual-AAV half vectors partially restored auditory function in the injected ear of *Otof*<sup>-/-</sup> mice (P23–30; +DualAAV-TS and +DualAAV-Hyb) (Al-Moyed *et al.*, 2019: Fig. 3A-B, Fig. EV5A). Ears of non-treated *Otof*<sup>-/-</sup> control littermates (-AAV), on the other hand, showed no characteristic ABR wave forms in response to broadband click or tone burst sound stimuli at all (Al-Moyed *et al.*, 2019: Fig. 3A-B, Fig. EV5A). Non-injected control animals only displayed a prominent summating potential (SP), which arises from the concentrated sound-induced depolarization of IHCs and OHCs, similar to previous reports (Roux *et al.*, 2006; Longo-Guess *et al.*, 2007; Pangrsic *et al.*, 2010; Reisinger *et al.*, 2011). The bigger SP amplitude in treated and non-treated *Otof*<sup>-/-</sup> ears compared to wild-type ears is probably due to the missing efferent OHC inhibition, which has to be activated through feedback from the afferent auditory pathway and thereby leading to OHC hyperpolarization (Fuchs and Lauer, 2018). An earlier study has demonstrated that co-expressing eGFP and synaptotagmin 1 via a single AAV2/1-2 did not restore exocytosis or auditory function in injected *Otof*<sup>-/-</sup> mice (Reisinger *et al.*, 2011). It is, therefore, unlikely that the partial rescue in IHC exocytosis and auditory function in dual-AAV treated *Otof*<sup>-/-</sup> mice is caused by the co-expressed eGFP in transduced IHCs.

The dual-AAV approach was able to restore broadband click-evoked ABR thresholds (40-60 dB SPL) in treated animals to near wild-type thresholds (20-40 dB SPL) (Al-Moyed *et*

*al.*, 2019: Fig. 3C). Tone burst-induced ABR thresholds, in comparison, could not be rescued that well as click ABR thresholds (Al-Moyed *et al.*, 2019: Fig. 3D, Fig. EV5B), which was also reported for AAV1-medaited Vlgut3 rescue in *Vglut3^-/-* mice (Akil *et al.*, 2012). In general, the best tone burst ABR thresholds could be observed for lower frequency tone bursts (6-12 kHz) that activate IHCs in more apical regions of the cochlea (Al-Moyed *et al.*, 2019: Fig. 3D, Fig. EV5B). This finding is in agreement with the higher full-length otoferlin IHC transduction rates in apical cochlear turns (Al-Moyed *et al.*, 2019: Fig. 1D). Each sound frequency generates a traveling wave that reaches its peak at a specific basilar membrane region along the cochlear turn and activates the IHCs in that specific location (see introduction "chapter 1.1") (Fettiplace, 2017). The IHCs in that frequency specific region of the cochlea, thus, need to be transduced in order to transmit the acoustic signal and generate an ABR. This would explain the high variability of tone burst ABR thresholds between individual injected animals (Al-Moyed *et al.*, 2019: Fig. EV5B). In addition, high sound pressure levels elicit a broader vibration of the basilar membrane that activates more IHCs than lower sound pressure levels, which only cause a narrow basilar membrane vibration and activate fewer IHCs. Unlike tone burst sound stimuli, click sound stimuli consist of a broadband of different frequencies that can activate several IHCs selective for those frequencies along the entire cochlea and evoke an ABR even if only a few IHCs have been transduced. This notion is further supported as there appears to be no correlation (Al-Moyed *et al.*, 2019: Fig. 1EV5C) between click ABR thresholds (Al-Moyed *et al.*, 2019: Fig. 3C) and full-length otoferlin IHC transduction rates (Al-Moyed *et al.*, 2019: Fig. 1D C-term otoferlin in entire cochlea) in dual-AAV-TS injected cochleae. These results show that only very few transduced IHCs expressing full-length otoferlin are needed to induce a click ABR response with a threshold at 50 dB.

The click ABR wave amplitudes were generally smaller in treated animals than in wild-type control mice (Al-Moyed *et al.*, 2019: Fig. 3E, Fig. EV5D-H). Specially the amplitude of ABR wave I that reflects the compound action potential of the auditory nerve was very small and slightly delayed in dual-AAV treated *Otof^-/-* mice (Al-Moyed *et al.*, 2019: Fig. EV5D, Fig. EV5I). It seems that lower otoferlin protein levels (Al-Moyed *et al.*, 2019: Fig. 1E), fewer fully functional IHCs in injected *Otof^-/-* ears (Al-Moyed *et al.*, 2019: Fig. 1D), and their

reduced synapse numbers (Al-Moyed *et al.*, 2019: Fig. 2B) are all factors that likely contribute to the reduced synchronous spike discharges of the auditory nerve fibers in these treated *Otof*$^{-/-}$ animals (Buran *et al.*, 2010; Bourien *et al.*, 2014; Strenzke *et al.*, 2016). The gradual increase in ABR wave amplitudes from ABR wave II to wave V and the normal latencies of these waves, apart from wave I and V, point towards some degree of compensation within the auditory brain stem, especially in the superior olivary complex, the lateral lemniscus, and the cochlear nucleus (see introduction "Figure 1.2"). The full-length otoferlin IHC transduction rates (Al-Moyed *et al.*, 2019: Fig. 1D C-term otoferlin in entire cochlea) appear to correlate with the amplitude of all ABR waves in treated animals (Al-Moyed *et al.*, 2019: Fig. 3F). This finding implies that the more IHCs express full-length otoferlin upon dual-AAV treatment the higher the ABR wave amplitudes measured for those ears.

Injecting the dual-AAV-TS half vectors into the cochleae of wild-type control mice showed no evident negative effects on auditory function in these animals. The ABR thresholds, ABR wave latencies, and ABR wave I amplitudes in injected ears were comparable to those measured from non-injected contralateral ears and ears of non-treated wild-type control mice (Al-Moyed *et al.*, 2019: Appendix Fig. S4). It is unclear why the amplitudes of ABR waves II, IV, and V are smaller in injected ears than in non-injected contralateral ears even though the amplitudes of ABR wave I were similar in both ears. It should additionally be pointed out that there was generally a variability in ABR thresholds, ABR wave amplitudes, and ABR wave V latencies among wild-type control animals with some animals having a better auditory function than others (Al-Moyed *et al.*, 2019: Fig. 3, Fig. EV5, Appendix Fig. S4). Nevertheless, potential injection related HC damage caused by the injection procedure and/or the amount of virus solution injected into the delicate cochlea structure (Lee and Park, 2018; Lee *et al.*, 2018; Yoshimura *et al.*, 2018) (see introduction "chapter 1.6") cannot be excluded despite no evident HCs loss in injected inner ears (Al-Moyed *et al.*, 2019: Fig. 1A, Appendix Fig. S1-3).

Developing the otoferlin dual-AAV vector design further to achieve higher full-length protein expression levels is necessary since otoferlin protein levels, especially at the plasma membrane, scale with sustained IHC exocytosis levels and cochlear function as seen in dual-

AAV treated $Otof^{-/-}$ mice (Al-Moyed $et$ $al.$, 2019) or in $Otof^{I515T/I515T}$ and $Otof^{Pga/Pga}$ otoferlin mutant mouse models (Strenzke $et$ $al.$, 2016). Increasing sustained IHC exocytosis levels in dual-AAV treated animals might even lead to lower ABR thresholds as high-spontaneous rate low threshold SGNs are believed to require high SV replenishment rates and sustained exocytosis levels (Strenzke $et$ $al.$, 2016).

The moderately hearing impaired $Otof^{I515T/I515T}$ mutant mouse model (see discussion "chapter 3.1") has comparable otoferlin protein levels, sustained IHC exocytosis levels, ABR wave amplitudes, and ABR thresholds as the dual-AAV treated $Otof^{-/-}$ mice (Strenzke $et$ $al.$, 2016; Al-Moyed $et$ $al.$, 2019). DFNB9 patients carrying the same mutation are predicted to have some residual otoferlin protein expression left (Shearer and Smith, 2015), which might be similar to the levels in $Otof^{I515T/I515T}$ mutant mice (Strenzke $et$ $al.$, 2016). These individuals would, therefore, benefit significantly from a ≥ 30% increase in overall otoferlin protein levels upon dual-AAV transduction. These patients also suffer from mildly elevated pure tone thresholds, auditory fatigue, severely impaired speech comprehension, and temperature-sensitive hearing loss (see introduction "chapter 1.5") (Varga $et$ $al.$, 2006; Wynne $et$ $al.$, 2013). The elevated otoferlin protein levels might, thus, be sufficient to fully restore the auditory and IHC function in these patients. In addition, treating $Otof^{I515T/I515T}$ mutant mice with otoferlin dual-AAV vectors is necessary to determine if the dual-AAV approach can fully restore hearing in these animals and to study possible negative side effects of mutated endogenous otoferlin on the re-introduced wild-type protein.

## 3.2.5 Using the AAV2/Anc80L65 serotype to improve dual-AAV mediated otoferlin gene delivery

From the previous chapter it becomes clear that the ABR wave amplitudes in dual-AAV treated $Otof^{-/-}$ mice, especially ABR wave I, need to be increased substantially to move towards otoferlin gene replacement therapy in humans (see discussion "chapter 3.2.4"). Since ABR wave amplitudes seem to correlate with the number of full-length otoferlin expressing IHCs in transduced inner ears (Al-Moyed $et$ $al.$, 2019: Fig. 3F), it is crucial to further increase IHC transduction rates to achieve higher ABR wave amplitudes.

One possibility to increase the number of full-length otoferlin expressing IHCs in transduced organs of Corti is to use AAVs with capsid proteins from other serotypes than serotype 6. Some of the AAV serotypes that were demonstrated to successfully target auditory IHCs are AAV8 (Chien *et al.*, 2016; Geng *et al.*, 2017), AAV2/1-2 (Reisinger *et al.*, 2011), and AAVAnc80L65 (Landegger *et al.*, 2017; Pan *et al.*, 2017; Suzuki *et al.*, 2017; Yoshimura *et al.*, 2018). The artificial AAVAnc80L65 serotype, in particular, was reported to target auditory IHCs with a transduction efficiency of almost 100% according to some publications (Landegger *et al.*, 2017; Suzuki *et al.*, 2017) and thus seems very promising for dual-AAV mediated inner ear gene therapy. The AAV2/8 and AAV2/Anc80L65 serotypes were first tested by injecting single eGFP-expressing AAV2/8 (AAV2/8.eGFP) and AAV2/Anc80L65 (AAV2/Anc80.eGFP) control viruses into the cochlea of wild-type or *Otof*$^{-/-}$ animals since my research group had no previous experience with the IHC transduction efficiency of these two AAV serotypes. In comparison, the AAV2/1-2 serotype was successfully used before to transfer synaptotagmin 1 and eGFP into auditory *Otof*$^{-/-}$ IHCs by my research group (Reisinger *et al.*, 2011) and was, therefore, used directly for dual-AAV gene delivery.

Injecting the AAV2/8.eGFP virus into the cochlea of wild-type control mice (P6-8) revealed that this AAV serotype did not target IHCs or OHCs at all, but rather SGNs (Figure 2.1), making this AAV serotype unsuitable for otoferlin inner ear gene delivery. The otoferlin dual-AAV2/1-2-TS half vectors targeted IHCs with an extremely low efficacy with only a few IHCs per injected ear showing an N-terminal otoferlin immunofluorescent signal (Figure 2.2). This means that this AAV serotype is also not efficient enough for otoferlin gene transfer. The single AAV2/Anc80.eGFP control virus, in contrast, had on average equally good IHC targeting rates (average: ~62%) as the single AAV2/6.eGFP virus (average: ~67%) even though the AAV2/Anc80.eGFP (1.11 x 10$^9$ vg/µl) was administered with a lower virus titer than the AAV2/6.eGFP virus (1.44 x 10$^{10}$ vg/µl) (Figure 2.3). This result suggests that this AAV serotype would be applicable for dual-AAV mediated otoferlin gene delivery into auditory IHCs.

Since the AAV2/Anc80L65 serotype had comparable IHC transduction rates to the AAV2/6 serotype, the two split-AAV trans-splicing otoferlin expression cassettes (5'-AAV-

TS + 3'-AAV-TS) were packaged into two separate AAV2/Anc80L65 viruses (dual-AAV2/Anc80-TS). The trans-splicing dual-AAV strategy was chosen because the transduction rates (Al-Moyed *et al.*, 2019: Fig. 1D) and ABR wave amplitudes (Al-Moyed *et al.*, 2019: Fig. 3A-B, Fig. 3E, Fig. EV5A, Fig. EV5D-H) measured from otoferlin dual-AAV2/6-TS injected *Otof$^{-/-}$* mice were slightly better than those measured from dual-AAV2/6-Hyb treated animals.

Transduced organs of Corti from otoferlin dual-AAV2/Anc80-TS injected *Otof$^{-/-}$* mice showed eGFP expression in various cell types including HCs. Otoferlin immunostaining, on the other hand, could only be detected in IHCs and in very few OHCs (Figure 2.4). This otoferlin immunostaining pattern (Figure 2.4; Figure 2.6) was similar to the pattern found in dual-AAV2/6-TS and dual-AAV2/6-Hyb transduced cochleae (Al-Moyed *et al.*, 2019: Fig. 1A–C, Fig. EV3, Appendix Fig. S1–S3). This observation suggests that the restricted otoferlin expression to auditory HCs is independent of the AAV serotype used for otoferlin gene delivery. The contralateral non-injected ears of some *Otof$^{-/-}$* mice injected with dual-AAV2/Anc80-TS vectors at P5 showed an eGFP and otoferlin immunofluorescent signal in very few HCs (Figure 2.4). Such an AAV spread into the non-injected ear could either occur through the temporal bone marrow space (Kho *et al.*, 2000) or the cochlear aqueduct (Pan *et al.*, 2017) that might still be connected between both ears at P5, but not at later injection time points. Other research groups have also reported virus diffusion to the non-injected contralateral upon RWM injections at P0-3 (Pan *et al.*, 2017).

Full-length otoferlin IHC transduction rates were slightly lower (average: ~15%) in dual-AAV2/Anc80-TS transduced organs of Corti than in dual-AAV2/6-TS or dual-AAV2/6-Hyb injected ears (Figure 2.5). It cannot be ruled out that lower amounts of virus solution were inoculated into the cochlea of these mice because the opening of the injection pipette could have been partially clogged/obstructed, which might explain the lower IHC targeting rates of the dual-AAV2/Anc80-TS vectors. Another explanation might be the lower virus titer of these vectors or possible lower amounts of the 3'-AAV2/Anc80 virus particles in the final injection solution (see discussion "chapter 3.2.6" for more details). The number of IHCs showing an N-terminal otoferlin immunofluorescent signal (N-term otoferlin) without any C-terminal fluorescent signal (C-term otoferlin) was similar to the number in dual-

AAV2/6 transduced organs of Corti (Figure 2.5). This finding clearly indicates that the production of truncated N-terminal otoferlin fragments in approximately 10% of transduced IHCs is independent of the AAV serotype used for the large transgene delivery. The limited ability of the two split-AAV vectors to combine their genomes or an unequal 5'-AAV2/Anc80-TS to 3'-AAV2/Anc80-TS virus particle ratio in the injection solution might rather explain this result (see "chapter 3.2.6" for more details). Full-length otoferlin protein levels were also lower in dual-AAV2/Anc80-TS transduced IHCs (average: ~21%) than in dual-AAV2/6 transduced $Otof^{-/-}$ IHCs (dual-AAV2/6-TS: ~31%; dual-AAV2/6-Hyb: ~37%) (Figure 2.6B). It seems in general that the reconstitution of the correct full-length otoferlin transgene form the two half vectors was less efficient in theses six otoferlin dual-AAV2/Anc80-TS injected mice based on their lower full-length otoferlin (C-term otoferlin) transduction rates and protein levels. As expected, otoferlin dual-AAV2/Anc80-TS vectors were also not able to recover the synaptic ribbon loss in the few analyzed IHCs of $Otof^{-/-}$ mice injected at P5-6 (Figure 2.7).

Nonetheless, the full-length otoferlin IHC transduction rates and protein levels in these transduced $Otof^{-/-}$ organs of Corti were still sufficient to generate ABR waves in response to broadband click and tone burst sound stimuli (Figure 2.8; Figure 2.9; Figure 2.10). Click-evoked ABR thresholds in these animals were not significantly different from those observed in $Otof^{-/-}$ mice treated with otoferlin dual-AAV2/6 half vectors (Figure 2.9A). The ABR wave amplitudes and tone burst thresholds were generally comparable to those measured in dual-AAV2/6-Hyb injected $Otof^{-/-}$ animals (Figure 2.9B; Figure 2.10C-H). Dual-AAV2/Anc80-TS transduced $Otof^{-/-}$ mice further showed a similar delay in ABR wave I and V as dual-AAV2/6 treated animals (Figure 2.10B).

Otoferlin dual-AAV2/6-TS ($1.2x10^{10}$ vg/μl) and dual-AAV2/6-Hyb ($1.38x10^{10}$ vg/μl) transduced $Otof^{-/-}$ IHCs did not have significantly different full-length otoferlin levels (Figure 2.6, C-term otoferlin). Dual-AAV2/6-Hyb injected $Otof^{-/-}$ ears, however, had slightly lower full-length otoferlin IHC transduction rates (Figure 2.5, C-term otoferlin entire cochlea) and overall ABR amplitudes (Figure 2.10H) than dual-AAV2/6-Hyb injected animals. Moreover, dual-AAV2/6-Hyb ($1.38x10^{10}$ vg/μl) transduced $Otof^{-/-}$ organs of Corti had significantly higher full-length otoferlin levels than dual-AAV2/Anc80-TS ($9x10^9$ vg/μl) transduced inner

ears (Figure 2.6, C-term otoferlin), but comparable full-length otoferlin IHC targeting rates (Figure 2.5, C-term otoferlin entire cochlea) and ABR wave amplitudes (Figure 2.10H). These findings imply that the dual-AAV hybrid strategy is not more efficient than the trans-splicing strategy in reassembling the full-length otoferlin transgene. This result was quite surprising as the reconstitution of the large transgene in the split-AAV hybrid approach can be facilitated by homologous recombination or non-homologous ITR end-joining unlike the trans-splicing strategy (Al-Moyed *et al.*, 2019: Fig. EV2), which is only mediated by ITR concatemerization (Chamberlain, Riyad and Weber, 2016; McClements and Maclaren, 2017).

## 3.2.6 Different factors that might influence dual-AAV mediated otoferlin gene therapy

All these findings show that changing the AAV serotype does not substantially increase the number of full-length otoferlin expressing IHCs nor does it considerably influence the amount of full-length protein expressed in transduced cells. The AAV serotype does also not account for the partial rescue of IHC exocytosis and auditory function in dual-AAV treated $Otof^{-/-}$ mice since both AAV2/6 and AAV2/Anc80L65 had comparable otoferlin rescue results. Thus, the AAV serotype seems not to be the determining factor for obtaining high full-length otoferlin IHC transduction rates or protein levels.

Otoferlin dual-AAV2/Anc80-TS half vectors ($9x10^9$ vg/µl) were injected with a 25% lower titer than dual-AAV2/6-TS vectors ($1.2x10^{10}$ vg/µl). This might partially explain the lower number of full-length otoferlin expressing IHCs in dual-AAV2/Anc80-TS injected cochleae (Figure 2.5). However, the titer of the AAV virus does not seem to play a major role in gaining high full-length otoferlin IHC transduction rates either since dual-AAV2/6-Hyb vectors ($1.38x10^{10}$ vg/µl) targeted fewer IHCs along the cochlea than dual-AAV2/6-TS vectors ($1.2x10^{10}$ vg/µl) although inoculated with a 13% higher titer than dual-AAV2/6-TS vectors (Al-Moyed *et al.*, 2019: Fig. 1D; Figure 2.5). Moreover, the control AAV2/Anc80.eGFP virus ($1.11x10^9$ vg/µl) was inoculated into the scala tympani with an approximately 9-fold lower titer than the otoferlin dual-AAV2/Anc80-TS half vector mix ($9x10^9$ vg/µl) and could still transduce up to 91% of IHCs (Figure 2.3; Figure 2.5).

Discussion

The AAV virus quality and the ratio between the 5'-AAV and 3'-AAV virus particles in the injection solution are also factors that could theoretically contribute to the success of the dual-AAV gene therapy approach. The otoferlin 5'-AAV and 3'-AAV viruses I used for my experiments were produced with high quality and purified by iodixanol step-gradient centrifugation and fast protein liquid chromatography (FPLC) from equal amounts of transfected HEK293 (see "materials and methods" section in "Al-Moyed *et al.*, 2019"). Both otoferlin dual-AAV2/6-Hyb and dual-AAV2/Anc80-TS half vectors were, however, not purified separately as done for the dual-AAV2/6-TS half vectors, but the 5'-AAV and 3'-AAV virus particles were pooled in a 1:1 ratio and purified together. It is, therefore, possible that the final virus injection solution of these two otoferlin dual-AAV vectors did not contain the 5'-AAV and 3'-AAV virus particles in a 1:1 ratio like the final dual-AAV2/6-TS injection solution. Furthermore, the team of Dr. Sebastian Kügler (Center Nanoscale Microscopy and Physiology of the Brain (CNMPB), Department of Neurology, University Medical Center Göttingen), who produced all viruses for my experiments, found it difficult to produce the otoferlin dual-AAV2/Anc80-TS half vectors with high titers. This could, therefore, explain the lower IHC transduction rates in organs of Corti transduced with dual-AAV2/6-Hyb or dual-AAV2/Anc80-TS half vectors (Figure 2.5). In fact, measuring the virus titers of otoferlin 5'-AAV2/6-TS and 3'-AAV2/6-TS virus preparations that were produced and purified separately from equal amounts of transfected HEK293 cells revealed that the 3'-AAV2/6-TS virus preparation had a lower titer than the 5'-AAV2/6-TS virus preparation. Dual-AAV virus solutions with different 5'-AAV:3'-AAV virus particle ratios (e.g. 5'-AAV:3'-AAV in a 1:2, 1:3, 1:5 ratio) should be tested in the future to determine the ratio that yields the best full-length otoferlin transduction rates and protein levels.

Another factor that could potentially influence IHC transduction rates is the age of the animal at the time point of the injection procedure. Although I did not systematically study the impact of this factor on the outcome of dual-AAV otoferlin gene transfer and postnatal RWM injections in general, I found little difference between mice injected at P5-8 in terms of IHC transduction rates, otoferlin protein levels, and ABR results. Nevertheless, whether RWM injections at an earlier developmental stage like P0-3 (Akil *et al.*, 2012; Askew *et al.*, 2015; Chien *et al.*, 2016; Pan *et al.*, 2017) or a later more mature stage like P14 and older

(Suzuki *et al.*, 2017; Yoshimura *et al.*, 2018) can substantially increase or decrease IHC transduction rates and ABR amplitudes has to be examined. This is especially important in respect to otoferlin dual-AAV human gene therapy application as humans are already born with mature inner ears unlike mice (Kelly and Chen, 2009; Yoshimura *et al.*, 2018). Inoculating P4 or younger mice might also be interesting to see if an earlier injection time point could prevent IHC ribbon synapse loss in *Otof*$^{-/-}$ mice since P6 animals already seem to have an altered IHC synapse maturation (Figure 2.11; Figure 2.12).

The injection procedure itself might also affect full-length otoferlin IHC transduction rates. The diameter of the injection glass pipette opening, the amount of virus solution injected into the scala tympani, the injection route itself (see introduction "chapter 1.6"), the pressure pulses applied by the injector to inoculate the virus solution into the cochlea, and the diffusion properties of the solution that carries the virus particles are all factors that seem to influence the outcome of the injection procedure to some degree. Different research labs have gained diverse IHC transduction rates by using different AAV administration routes (Wang and Chang, 2013; Suzuki *et al.*, 2017) or modified postnatal RWM injection protocols (Yoshimura *et al.*, 2018). In this study I have used a glass pipette with a 15-20 µm tip opening to inject approximately 5-9 shots (~0.5-1 µl) of virus solution with a pico-injector (PL1–100, Harvard Apparatus) at around 0.129 bar through the RWM membrane into the perilymph-filled scala tympani (see introduction "Figure 1.6") (Jung *et al.*, 2015: Fig. EV2B; Al-Moyed *et al.*, 2019: see 'materials and methods' section). Inoculating too much virus solution into the cochlea or applying too much pressure while injecting can cause severe damage to the extremely sensitive organ of Corti tissue. Optimizing the injecting procedure further by changing one of these variables or using hydrogels (Lee *et al.*, 2018) with different diffusion properties instead of PBS to carry the virus particles are two options that might substantially enhance IHC targeting rates. Postnatal RWM injections in combination with semi-circular canal fenestration, in particular, appeared to substantially increase the IHC transduction efficiency according to Yoshimura *et al.*, 2018 and should also be tested in the future.

Around 70% of IHCs need to be fully functional in order to achieve normal hearing (Wang *et al.*, 1997), which means that not all IHCs have to be transduced to restore or at

least substantially improve auditory function in *Otof*^{-/-} mice and DFNB9 patients. These transduction rates can be achieved by further optimizing the injection procedure, finding the best 5'-AAV:3'-AAV virus particle ratios in the injection solution, and potentially increasing the reconstitution efficiency of the large transgene.

### 3.2.7 Improving full-length otoferlin transgene reassembly

Otoferlin gene replacement therapy does not only depend on IHC transduction with both AAV half vectors, but also requires efficient reconstitution of the full-length transgene upon dual-AAV gene delivery. For this purpose, the reassembly, the transcription, and the translation of the correct full-length otoferlin transgene have to be optimized further. Carvalho *et al.*, 2017 reported that increasing the number of AAV genome copies in transduced cells by using higher virus titers increased the co-transduction efficacy of the two half vectors in the target tissue but had little effect on the reconstitution of the large transgene. In addition, Carvalho *et al.*, 2017 found that co-transduced cells had much higher levels of full-length mRNA than actual full-length protein as the mRNA stability seems to decrease with increasing mRNA length. These findings highlight the fact that the major bottleneck of this gene therapy technique is the recombination of the 5'-AAV and the 3'-AAV genomes in the right orientation to form the correct full-length transgene.

Several studies have demonstrated that the reconstitution of the two split-AAV genomes largely depends on the ITR sequences and/or the recombinogenic properties of the overlapping sequences in the two AAV half vector genomes (Trapani *et al.*, 2015; Chamberlain, Riyad and Weber, 2016; McClements and Maclaren, 2017). The efficacy of the three dual-AAV strategies also appears to depend on the nature of the transgene itself (Zhang and Duan, 2012 and) and the targeted cell type as different cell types might utilize tissue specific mechanisms to reassemble the large transgene (Huertas, 2010; McClements and Maclaren, 2017). The dual-AAV overlap strategy, for example, leads to higher full-length protein expression levels for dysferlin and mini-dystrophin in muscle cells than the other two dual-AAV strategies (Zhang and Duan, 2012; Zhang *et al.*, 2013; Pryadkina *et al.*, 2015; Kodippili *et al.*, 2017). The dual-AAV hybrid strategy, on the other hand, was more efficient in the reconstitution of the full-length ABCA4 transgene in photoreceptors (Colella

*et al.*, 2014; Trapani *et al.*, 2014, 2015). It might, therefore, be possible that dual-AAV-OV vectors with optimized complementary regions in the 5'-AAV and the 3'-AAV transgenes can lead to more efficient full-length otoferlin reassembly in auditory IHCs than the other two split-AAV strategies.

There are several ways to improve the vector design of the 5'-AAV and 3'-AAV viruses to enhance the reassembly of the large transgene. One approach would to use dual-AAV-Hyb vectors with a highly recombinogenic region from another foreign gene than the AK sequence used in this study like e.g. from the alkaline phosphatase (AP) gene as in Trapani *et al.*, 2014. Several research groups have also tried to boost the orientation-directed ITR concatemerization of the two split-AAV transgenes in the trans-splicing strategy by using heterologous ITRs. These attempts improved large transgene reconstitution to some degree in skeletal muscles (Yan *et al.*, 2005, 2006), but had little effect in the retina (Trapani *et al.*, 2015). Trapani *et al.*, 2015 additionally reported that dual-AAV-TS vectors with heterologous ITRs were difficult to produce with high virus titers. It is, therefore, unlikely that otoferlin dual-AAV-TS vectors with heterologous ITRs would substantially improve full-length otoferlin reconstitution in auditory IHCs. Another option to improve otoferlin dual-AAV-TS vectors is to use optimized splice sites since the splicing efficacy is different for each splice element (Lai *et al.*, 2005). Nonetheless, whether splice sites with synthetic sequences or natural splice junctions from the same gene (Lai *et al.*, 2006; Lostal *et al.*, 2010) are better suited for this purpose needs to be tested further. The structure of the concatemerized virus genomes is also a factor that can inhibit or enhance the splicing process and should, therefore, be taken into account while designing the two dual-AAV transgene expression cassettes (McClements and Maclaren, 2017).

The production of truncated otoferlin protein fragments as a result of incomplete full-length transgene reassembly upon dual-AAV transduction is an important aspect that has to be considered while further developing the sequence design of dual-AAV half vectors. A 5'-AAV genome that did not recombine with the 3'-AAV genome can be transformed into an episomal dsDNA structure that can produce truncated transcripts and protein fragments. Although such truncated transcripts are expected to be highly unstable because of the missing polyA and mRNA stabilizing element signals (WRPE) in the 5'-AAV transgene,

several studies could still detect truncated protein products in dual-AAV transduced tissue (Dyka *et al.*, 2014; Trapani *et al.*, 2015). These observations imply that such truncated transcripts survive long enough to be translated into protein fragments and/or short peptides due to possible cryptic polyA sites and/or stop codons in the 5'-AAV transgene sequence (McClements and Maclaren, 2017). Since these truncated protein products were only detected upon dual-AAV trans-splicing and hybrid transduction and not dual-AAV-OV transduction, it was suggested that some dual-AAV strategies are more likely to facilitate the production of these protein fragments than other strategies (Dyka *et al.*, 2014). However, another study did not detect such truncated protein products in the retina upon *in vivo* dual-AAV injection, but only *in vitro* in cell culture (Trapani *et al.*, 2015). Undesired truncated protein fragments are less frequently expressed from the 3'-AAV half vector (Li *et al.*, 2008; Trapani *et al.*, 2015) as this transgene does not contain any decided promoter sequence. The presence of the polyA signal in the 3'-AAV transgene sequence could, however, potentially drive protein expression from the 3'-AAV vector (McClements and Maclaren, 2017). The 5'-ITR sequence located in the 3'-AAV transgene might also mediate this transcription as ITRs seem to have a weak promoter activity (Flotte *et al.*, 1992). It is likely that the majority of such truncated protein products are non-functional and are degraded upon production, resulting in the expression of very low amounts of these fragments in transduced cells (Reits *et al.*, 2004; Saric, Graef and Goldberg, 2004). Around 10% of IHCs transduced with either dual-AAV strategy *in vivo* showed an N-terminal otoferlin immunofluorescence signal (Al-Moyed *et al.*, 2019: Fig. 1A, Fig. 1D, Fig. EV3, Appendix Fig. S3; Fig. 2.3.5). It is likely that these transduced IHCs express truncated N-terminal otoferlin fragments as result of incomplete full-length otoferlin reconstitution. The safety and potential negative side effects of these fragments that might inhibit or outcompete the re-introduced wild-type full-length otoferlin in transduced IHCs need to be investigated in depth before any clinical application. One possibility to reduce the production of such protein products is to introduce an in-frame degradation signal like the CL1 sequence at the 3'-end of the 5'-AAV vector as successfully demonstrated by Trapani *et al.*, 2015. Thus, optimizing the split-transgene sequences of dual-AAV half vectors e.g. through codon optimization (Fischer *et al.*, 2017) is critical to eliminate any cryptic genetic signals that might lead to the expression of undesired truncated otoferlin fragments.

### 3.2.8 Outlook

Treating profoundly deaf or severely hearing impaired DFNB9 patients with optimized otoferlin dual-AAV half vectors has the potential to restore or substantially ameliorate the auditory function in these individuals. Even if the here presented gene replacement therapy was only able to restore hearing to similar levels as in older individuals without hearing impairment or patients suffering from a more moderate form of DFNB9, the sound quality would still be better than the quality achieved via cochlear implants (see introduction "chapter 1.6" and discussion "chapter 3.2"). Specially DFNB9 patients suffering from temperature-sensitive deafness or moderate hearing impairment (Varga *et al.*, 2006; Wynne *et al.*, 2013) will benefit from such a gene therapy approach, given that cochlear implants are still not able to fully restore speech comprehension and musical sound perception deficits in these patients (see introduction "chapter 1.5" and discussion "chapter 3.2.4") (Shearer and Smith, 2015). Nevertheless, these dual-AAV half vectors need to be developed further by enhancing the reassembly of the two split-AAV genomes and increasing the number of full-length otoferlin expressing IHCs to obtain higher clinically relevant otoferlin levels and ABR wave amplitudes (see discussion "chapters 3.2.4, 3.2.6, and 3.2.7"). Additionally, full-length otoferlin expression and auditory function must be monitored in dual-AAV treated $Otof^{-/-}$ mice over a longer time frame to determine if this approach is suitable for long-term large gene expression. Future studies will also need to examine whether the dual-AAV approach can restore other hearing properties like temporal coding, gap detection, and sound adaptation in treated $Otof^{-/-}$ mice. These hearing properties can be studied via different tests like pre-pulse inhibition of the acoustic startle response or operant conditioning in an Audiobox as described in "Strenzke *et al.*, 2016".

In summary, dual-AAV half vectors can be used to deliver large deafness-related genes with a CDS that exceeds the packaging capacity of a single AAV like *OTOF* into murine IHCs. Establishing such a split-AAV approach for inner ear large gene delivery is crucial since over 35% of genetic deafness cases are estimated to be caused by mutations in large genes (Holt and Geleoc, 2018) such as myosin VIIA (CDS: ~6.7 kb) and cadherin-23 (CDS: ~10.1 kb) (Raviv, Dror and Avraham, 2010; Dyka *et al.*, 2014; Maddalena *et al.*, 2018).

Discussion

Transducing organs of Corti of *Otof*^{-/-} mice with either otoferlin dual-AAV-TS or dual-AAV-Hyb half vectors led to the production of full-length otoferlin in auditory HCs, but not any other cell type. This restricted otoferlin expression is especially beneficial for human gene therapy application as it reduces potential off-target effects that might arise from otoferlin expression in other non-sensory cells in the cochlea. Re-introducing wild-type full-length otoferlin into IHCs of *Otof*^{-/-} mice completely rescued fast IHC exocytosis and partially restored sustained exocytosis and auditory function. This work further showed that the AAV serotype is just one of many factors that can influence the outcome of dual-AAV mediated otoferlin gene delivery and is not the determining factor for obtaining high full-length otoferlin IHC transduction rates or protein levels in transduced IHCs.

# References

Ahmed, H., Shubina-Oleinik, O. and Holt, J. R. (2017) 'Emerging Gene Therapies for Genetic Hearing Loss', *JARO - Journal of the Association for Research in Otolaryngology*. Journal of the Association for Research in Otolaryngology, pp. 1–22. doi: 10.1007/s10162-017-0634-8.

Akil, O. *et al.* (2012) 'Restoration of Hearing in the VGLUT3 Knockout Mouse Using Virally Mediated Gene Therapy', *Neuron*, 75(2), pp. 283–293. doi: 10.1016/j.neuron.2012.05.019.

Al-Moyed, H. *et al.* (2019) 'A dual-AAV approach restores fast exocytosis and partially rescues auditory function in deaf otoferlin knock-out mice', *EMBO Molecular Medicine*, 11(1), p. e9396. doi: 10.15252/emmm.201809396.

Anson, D. S. (2004) 'The use of retroviral vectors for gene therapy-what are the risks? A review of retroviral pathogenesis and its relevance to retroviral vector-mediated gene delivery', *Genetic Vaccines and Therapy*, 2, pp. 1–13. doi: 10.1186/1479-0556-2-9.

Askew, C. *et al.* (2015) 'Tmc gene therapy restores auditory function in deaf mice', *Science translational medicine*, 7(295), pp. 1–12. doi: 10.1126/scitranslmed.aab1996.

Bedrosian, J. C. *et al.* (2006) 'In Vivo Delivery of Recombinant Viruses to the Fetal Murine Cochlea : Transduction Characteristics and Long-Term Effects on Auditory Function', *Molecular Therapy*. The American Society of Gene Therapy, 14(3), pp. 328–335. doi: 10.1016/j.ymthe.2006.04.003.

Beurg, M. *et al.* (2008) 'Calcium- and Otoferlin-Dependent Exocytosis by Immature Outer Hair Cells', *Journal of Neuroscience*, 28(8), pp. 1798–1803. doi: 10.1523/JNEUROSCI.4653-07.2008.

Beurg, M. *et al.* (2010) 'Control of exocytosis by synaptotagmins and otoferlin in auditory hair cells', *The Journal of Neuroscience*, 30(40), pp. 13281–13290. doi:

# References

10.1523/JNEUROSCI.2528-10.2010.

Beutner, D. *et al.* (2001) 'Calcium dependence of exocytosis and endocytosis at the cochlear inner hair cell afferent synapse', *Neuron*, 29(3), pp. 681–690. doi: 10.1016/S0896-6273(01)00243-4.

Beutner, D. and Moser, T. (2001) 'The presynaptic function of mouse cochlear inner hair cells during development of hearing', *The Journal of neuroscience : the official journal of the Society for Neuroscience*, 21(13), pp. 4593–9. doi: 21/13/4593 [pii].

Bourien, J. *et al.* (2014) 'Contribution of auditory nerve fibers to compound action potential of the auditory nerve', *Journal of Neurophysiology*, 112(5), pp. 1025–1039. doi: 10.1152/jn.00738.2013.

Brandt, A., Striessnig, J. and Moser, T. (2003) 'Ca&lt;sub&gt;V&lt;/sub&gt;1.3 Channels Are Essential for Development and Presynaptic Activity of Cochlear Inner Hair Cells', *The Journal of Neuroscience*, 23(34), pp. 10832 LP – 10840. Available at: http://www.jneurosci.org/content/23/34/10832.abstract.

Bruns, L., Mürbe, D. and Hahne, A. (2016) 'Understanding music with cochlear implants', *Scientific Reports*. Nature Publishing Group, 6(August), pp. 1–14. doi: 10.1038/srep32026.

Buran, B. N. *et al.* (2010) 'Onset Coding Is Degraded in Auditory Nerve Fibers from Mutant Mice Lacking Synaptic Ribbons', *Journal of Neuroscience*, 30(22), pp. 7587–7597. doi: 10.1523/JNEUROSCI.0389-10.2010.

Carvalho, L. S. *et al.* (2017) 'Evaluating Efficiencies of Dual AAV Approaches for Retinal Targeting', *Frontiers in Neuroscience*, 11(September), pp. 1–8. doi: 10.3389/fnins.2017.00503.

Chakrabarti, R., Michanski, S. and Wichmann, C. (2018) 'Vesicle sub-pool organization at inner hair cell ribbon synapses', *EMBO reports*, p. e44937. doi: 10.15252/embr.201744937.

Chamberlain, K., Riyad, J. M. and Weber, T. (2016) 'Expressing Transgenes That Exceed the

## References

---

Packaging Capacity of Adeno-Associated Virus Capsids', *Human Gene Therapy Methods*, 27(1), pp. 1–12. doi: 10.1089/hgtb.2015.140.

Chapochnikov, N. M. *et al.* (2014) 'Uniquantal release through a dynamic fusion pore is a candidate mechanism of hair cell exocytosis', *Neuron*, 83(6), pp. 1389–1403. doi: 10.1016/j.neuron.2014.08.003.

Chatterjee, P. *et al.* (2015) 'Otoferlin Deficiency in Zebrafish Results in Defects in Balance and Hearing: Rescue of the Balance and Hearing Phenotype with Full-Length and Truncated Forms of Mouse Otoferlin', *Molecular and Cellular Biology*, 35(6), pp. 1043–1054. doi: 10.1128/MCB.01439-14.

Cheng, Y. F., Tong, M. and Edge, A. S. B. (2016) 'Destabilization of Atoh1 by E3 ubiquitin ligase Huwe1 and casein kinase 1 is essential for normal sensory hair cell development', *Journal of Biological Chemistry*, 291(40), pp. 21096–21109. doi: 10.1074/jbc.M116.722124.

Chien, W. W. *et al.* (2016) 'Gene therapy restores hair cell stereocilia morphology in inner ears of deaf whirler mice', *Molecular Therapy*, 24(1), pp. 17–25. doi: 10.1038/mt.2015.150.

Chiu, Y. H. *et al.* (2010) 'Mutations in the OTOF gene in Taiwanese patients with auditory neuropathy', *Audiology and Neurotology*, 15(6), pp. 364–374. doi: 10.1159/000293992.

Choi, B. Y. *et al.* (2009) 'Identities and frequencies of mutations of the otoferlin gene (OTOF) causing DFNB9 deafness in Pakistan', *Clinical Genetics*, 75(3), pp. 237–243. doi: 10.1111/j.1399-0004.2008.01128.x.

Colella, P. *et al.* (2014) 'Efficient gene delivery to the cone-enriched pig retina by dual AAV vectors', *Gene Therapy*. Nature Publishing Group, 21(4), pp. 450–456. doi: 10.1038/gt.2014.8.

Dong, B., Nakai, H. and Xiao, W. (2010) 'Characterization of genome integrity for oversized recombinant AAV vector', *Molecular Therapy*. Nature Publishing Group, 18(1), pp. 87–92. doi: 10.1038/mt.2009.258.

## References

Duan, D. *et al.* (1998) 'Circular intermediates of recombinant adeno-associated virus have defined structural characteristics responsible for long-term episomal persistence in muscle tissue.', *Journal of virology*, 72(11), pp. 8568–77. doi: 10.1128/jvi.75.15.6969-6976.2001.

Duncker, S. V. *et al.* (2013) 'Otoferlin Couples to Clathrin-Mediated Endocytosis in Mature Cochlear Inner Hair Cells', *Journal of Neuroscience*, 33(22), pp. 9508–9519. doi: 10.1523/JNEUROSCI.5689-12.2013.

Dyka, F. M. *et al.* (2014) 'Dual Adeno-Associated Virus Vectors Result in Efficient *In Vitro* and *In Vivo* Expression of an Oversized Gene, *MYO7A*', *Human Gene Therapy Methods*, 25(2), pp. 166–177. doi: 10.1089/hgtb.2013.212.

Ehret, G. (1985) 'Behavioural studies on auditory development in mammals in relation to higher nervous system functioning', *Acta Oto-Laryngologica*, 99(S421), pp. 31–40. doi: 10.3109/00016488509121754.

Elkan-Miller, T. *et al.* (2011) 'Integration of transcriptomics, proteomics, and microRNA analyses reveals novel microrna regulation of targets in the mammalian inner ear', *PLoS ONE*, 6(4), pp. 1–12. doi: 10.1371/journal.pone.0018195.

Eppsteiner, R. W. *et al.* (2012) 'Prediction of cochlear implant performance by genetic mutation: The spiral ganglion hypothesis', *Hearing Research*. Elsevier B.V., 292(1–2), pp. 51–58. doi: 10.1016/j.heares.2012.08.007.

Fettiplace, R. (2017) 'Hair cell transduction, tuning, and synaptic transmission in the mammalian cochlea', *Comprehensive Physiology*, 7(4), pp. 1197–1227. doi: 10.1002/cphy.c160049.

Fischer, M. D. *et al.* (2017) 'Codon-Optimized RPGR Improves Stability and Efficacy of AAV8 Gene Therapy in Two Mouse Models of X-Linked Retinitis Pigmentosa', *Molecular Therapy*. Elsevier Ltd., 25(8), pp. 1854–1865. doi: 10.1016/j.ymthe.2017.05.005.

Flotte, T. R. *et al.* (1992) 'Gene expression from adeno-associated virus vectors in airway epithelial cells.', *American journal of respiratory cell and molecular biology*, 7(3), pp. 349–

## References

356. doi: 10.1165/ajrcmb/7.3.349.

Frank, T. *et al.* (2010) 'Bassoon and the synaptic ribbon organize Ca2+channels and vesicles to add release sites and promote refilling', *Neuron*, 68(4), pp. 724–738. doi: 10.1016/j.neuron.2010.10.027.

Fuchs, P. A. and Lauer, A. M. (2018) 'Efferent Inhibition of the Cochlea', *Cold Spring Harbor Perspectives in Medicine*, p. a033530. doi: 10.1101/cshperspect.a033530.

Furman, A. C., Kujawa, S. G. and Liberman, M. C. (2013) 'Noise-induced cochlear neuropathy is selective for fibers with low spontaneous rates', *Journal of Neurophysiology*, 110(3), pp. 577–586. doi: 10.1152/jn.00164.2013.

Géléoc, G. S. G. and Holt, J. R. (2014) 'Sound strategies for hearing restoration', *Science*, 344(6184). doi: 10.1126/science.1241062.

Geng, R. *et al.* (2017) 'Modeling and preventing progressive hearing loss in usher syndrome III', *Scientific Reports*. Springer US, 7(1), pp. 1–15. doi: 10.1038/s41598-017-13620-9.

Ghosh, A. *et al.* (2008) 'A hybrid vector system expands adeno-associated viral vector packaging capacity in a transgene-independent manner', *Molecular Therapy*. The American Society of Gene Therapy, 16(1), pp. 124–130. doi: 10.1038/sj.mt.6300322.

Ghosh, A. *et al.* (2009) 'Systemic Trans-splicing adeno-associated viral delivery efficiently transduces the heart of adult mdx mouse, a model for duchenne muscular dystrophy.', *Human gene therapy*, 20(11), pp. 1319–28. doi: 10.1089/hum.2009.058.

Glowatzki, E. and Fuchs, P. A. (2002) 'Transmitter release at the hair cell ribbon synapse', *Nature Neuroscience*, 5(2), pp. 147–154. doi: 10.1038/nn796.

Graydon, C. W. *et al.* (2014) 'Passive Diffusion as a Mechanism Underlying Ribbon Synapse Vesicle Release and Resupply', *Journal of Neuroscience*, 34(27), pp. 8948–8962. doi: 10.1523/JNEUROSCI.1022-14.2014.

Grieger, J. C. and Samulski, R. J. (2005) 'Packaging Capacity of Adeno-Associated Virus

# References

Serotypes: Impact of Larger Genomes on Infectivity and Postentry Steps', *Journal of Virology*, 79(15), pp. 9933–9944. doi: 10.1128/JVI.79.15.9933-9944.2005.

Grieger, J. C., Soltys, S. M. and Samulski, R. J. (2016) 'Production of recombinant adeno-associated virus vectors using suspension HEK293 cells and continuous harvest of vector from the culture media for GMP FIX and FLT1 clinical vector', *Molecular Therapy*. American Society of Gene & Cell Therapy, 24(2), pp. 287–297. doi: 10.1038/mt.2015.187.

Hall, J. W. (2007) *New handbook of auditory evoked responses*. Boston: Pearson.

Hams, N. *et al.* (2017) 'Otoferlin is a multivalent calcium-sensitive scaffold linking SNAREs and calcium channels', *Proceedings of the National Academy of Sciences*, 114(30), pp. 8023–8028. doi: 10.1073/pnas.1703240114.

Harsini, F. M. *et al.* (2018) 'FerA is a Membrane-Associating Four-Helix Bundle Domain in the Ferlin Family of Membrane-Fusion Proteins', *Scientific Reports*. Springer US, 8(1), pp. 1–11. doi: 10.1038/s41598-018-29184-1.

Heidrych, P. *et al.* (2008) 'Rab8b GTPase, a protein transport regulator, is an interacting partner of otoferlin, defective in a human autosomal recessive deafness form', *Human Molecular Genetics*, 17(23), pp. 3814–3821. doi: 10.1093/hmg/ddn279.

Heidrych, P. *et al.* (2009) 'Otoferlin interacts with myosin VI: Implications for maintenance of the basolateral synaptic structure of the inner hair cell', *Human Molecular Genetics*, 18(15), pp. 2779–2790. doi: 10.1093/hmg/ddp213.

Helfmann, S. *et al.* (2011) 'The crystal structure of the C2A domain of otoferlin reveals an unconventional top loop region', *Journal of Molecular Biology*. Elsevier Ltd, 406(3), pp. 479–490. doi: 10.1016/j.jmb.2010.12.031.

Holt, J. R. and Geleoc, G. S. (2018) 'Split otoferlins reunited', *EMBO Molecular Medicine*, p. e9995. doi: 10.15252/emmm.201809995.

Hosoya, M. *et al.* (2018) 'Elongated EABR wave latencies observed in patients with auditory

neuropathy caused by *OTOF* mutation', *Laryngoscope Investigative Otolaryngology*, 3(5), pp. 388–393. doi: 10.1002/lio2.210.

Huang, J. *et al.* (2017) 'Electro-tactile stimulation enhances cochlear implant speech recognition in noise', *Scientific Reports*. Springer US, 7(1), pp. 1–5. doi: 10.1038/s41598-017-02429-1.

Huang, L. C. *et al.* (2012) 'Synaptic profiles during neurite extension, refinement and retraction in the developing cochlea', *Neural Development*, 7(1), pp. 1–17. doi: 10.1186/1749-8104-7-38.

Huertas, P. (2010) 'DNA resection in eukaryotes: Deciding how to fix the break', *Nature Structural and Molecular Biology*. Nature Publishing Group, 17(1), pp. 11–16. doi: 10.1038/nsmb.1710.

Jean, P. *et al.* (2018) 'The synaptic ribbon is critical for sound encoding at high rates and with temporal precision', *eLife*. Edited by C. Petit and A. J. King. eLife Sciences Publications, Ltd, 7, p. e29275. doi: 10.7554/eLife.29275.

Jing, Z. *et al.* (2013) 'Disruption of the Presynaptic Cytomatrix Protein Bassoon Degrades Ribbon Anchorage, Multiquantal Release, and Sound Encoding at the Hair Cell Afferent Synapse', *Journal of Neuroscience*, 33(10), pp. 4456–4467. doi: 10.1523/JNEUROSCI.3491-12.2013.

Johnson, C. P. (2017) 'Emerging Functional Differences between the Synaptotagmin and Ferlin Calcium Sensor Families', *Biochemistry*, 56(49), pp. 6413–6417. doi: 10.1021/acs.biochem.7b00928.

Johnson, C. P. and Chapman, E. R. (2010) 'Otoferlin is a calcium sensor that directly regulates SNARE-mediated membrane fusion', *Journal of Cell Biology*, 191(1), pp. 187–197. doi: 10.1083/jcb.201002089.

Jung, S. *et al.* (2015) 'Disruption of adaptor protein 2 l ( AP- 2 l ) in cochlear hair cells impairs vesicle reloading of synaptic release sites and hearing', 34(21).

# References

Kaga, K. (2016) 'Auditory nerve disease and auditory neuropathy spectrum disorders', *Auris Nasus Larynx*. Elsevier Ireland Ltd, 43(1), pp. 10–20. doi: 10.1016/j.anl.2015.06.008.

Kantardzhieva, A. *et al.* (2012) 'Protein composition of immunoprecipitated synaptic ribbons', *Journal of Proteome Research*, 11(2), pp. 1163–1174. doi: 10.1021/pr2008972.

Kantardzhieva, A., Liberman, M. C. and Sewell, W. F. (2013) 'Quantitative analysis of ribbons, vesicles, and cisterns at the cat inner hair cell synapse: Correlations with spontaneous rate', *Journal of Comparative Neurology*, 521(14), pp. 3260–3271. doi: 10.1002/cne.23345.

Kelly, M. C. and Chen, P. (2009) 'Development of form and function in the mammalian cochlea', *Current Opinion in Neurobiology*, 19(4), pp. 395–401. doi: 10.1016/j.conb.2009.07.010.

Khimich, D. *et al.* (2005) 'Hair cell synaptic ribbons are essential for synchronous auditory signalling', *Nature*. Macmillan Magazines Ltd., 434, p. 889. Available at: http://dx.doi.org/10.1038/nature03418.

Kho, S. T. *et al.* (2000) 'Safety of adeno-associated virus as cochlear gene transfer vector: Analysis of distant spread beyond injected cochleae', *Molecular Therapy*. American Society for Gene Therapy, 2(4), pp. 368–373. doi: 10.1006/mthe.2000.0129.

Kiang, N. Y. S. (2011) 'Peripheral Neural Processing of Auditory Information', *Comprehensive Physiology*, pp. 639–674. doi: 10.1002/cphy.cp010315.

Kodippili, K. *et al.* (2017) 'Dual AAV gene therapy for Duchenne muscular dystrophy with a 7-kb mini-dystrophin gene in the canine model', *Human Gene Therapy*, p. hum.2017.095. doi: 10.1089/hum.2017.095.

Kononenko, N. L. *et al.* (2014) 'Clathrin/AP-2 mediate synaptic vesicle reformation from endosome-like vacuoles but are not essential for membrane retrieval at central synapses', *Neuron*. Elsevier Inc., 82(5), pp. 981–988. doi: 10.1016/j.neuron.2014.05.007.

## References

Koo, T. *et al.* (2014) 'Triple Trans-Splicing Adeno-Associated Virus Vectors Capable of Transferring the Coding Sequence for Full-Length Dystrophin Protein into Dystrophic Mice', *Human Gene Therapy*, 25(2), pp. 98–108. doi: 10.1089/hum.2013.164.

Kroll, J. *et al.* (2019) 'Endophilin-A regulates presynaptic Ca 2+ influx and synaptic vesicle recycling in auditory hair cells', *The EMBO Journal*, p. e100116. doi: 10.15252/embj.2018100116.

Lai, Y. *et al.* (2005) 'Efficient in vivo gene expression by trans-splicing adeno-associated viral vectors.', *Nature biotechnology*, 23(11), pp. 1435–9. doi: 10.1038/nbt1153.

Lai, Y. *et al.* (2006) 'Synthetic Intron Improves Transduction Efficiency of *Trans* -Splicing Adeno-Associated Viral Vectors', *Human Gene Therapy*, 17(10), pp. 1036–1042. doi: 10.1089/hum.2006.17.1036.

Lai, Y., Yue, Y. and Duan, D. (2010) 'Evidence for the failure of adeno-associated virus serotype 5 to package a viral genome ≥8.2kb', *Molecular Therapy*. Nature Publishing Group, 18(1), pp. 75–79. doi: 10.1038/mt.2009.256.

Landegger, L. D. *et al.* (2017) 'A synthetic AAV vector enables safe and efficient gene transfer to the mammalian inner ear', *Nature Biotechnology*, 35(3). doi: 10.1038/nbt.3781.

Lee, J.-H. *et al.* (2018) 'Auditory disorders and future therapies with delivery systems', *Journal of Tissue Engineering*, 9, p. 204173141880845. doi: 10.1177/2041731418808455.

Lee, M. Y. and Park, Y. H. (2018) 'Potential of Gene and Cell Therapy for Inner Ear Hair Cells', *BioMed Research International*. Hindawi, 2018. doi: 10.1155/2018/8137614.

Lek, A. *et al.* (2012) 'Ferlins: Regulators of Vesicle Fusion for Auditory Neurotransmission, Receptor Trafficking and Membrane Repair', *Traffic*, 13(2), pp. 185–194. doi: 10.1111/j.1600-0854.2011.01267.x.

Lek, A. *et al.* (2013) 'Calpains, Cleaved Mini-DysferlinC72, and L-Type Channels Underpin Calcium-Dependent Muscle Membrane Repair', *Journal of Neuroscience*, 33(12), pp. 5085–

# References

5094. doi: 10.1523/JNEUROSCI.3560-12.2013.

Lelli, A. *et al.* (2009) 'Tonotopic Gradient in the Developmental Acquisition of Sensory Transduction in Outer Hair Cells of the Mouse Cochlea', *Journal of Neurophysiology*, 101(6), pp. 2961–2973. doi: 10.1152/jn.00136.2009.

Li, J. *et al.* (2008) 'Protein *Trans* -Splicing as a Means for Viral Vector-Mediated *In Vivo* Gene Therapy', *Human Gene Therapy*, 19(9), pp. 958–964. doi: 10.1089/hum.2008.009.

Liberman, L. D. and Liberman, M. C. (2016) 'Postnatal maturation of auditory-nerve heterogeneity, as seen in spatial gradients of synapse morphology in the inner hair cell area', *Hearing Research*. Elsevier Ltd, 339, pp. 12–22. doi: 10.1016/j.heares.2016.06.002.

Liberman, M. C. (1978) '<Liberman1978.pdf>', pp. 442–455.

Longo-Guess, C. *et al.* (2007) 'A missense mutation in the conserved C2B domain of otoferlin causes deafness in a new mouse model of DFNB9', *Hearing Research*, 234(1–2), pp. 21–28. doi: 10.1016/j.heares.2007.09.005.

Lostal, W. *et al.* (2010) 'Efficient recovery of dysferlin deficiency by dual adeno-associated vector-mediated gene transfer', *Human Molecular Genetics*, 19(10), pp. 1897–1907. doi: 10.1093/hmg/ddq065.

Lostal, W. *et al.* (2014) 'Full-Length Dystrophin Reconstitution with Adeno-Associated Viral Vectors', *Human Gene Therapy*, 25(6), pp. 552–562. doi: 10.1089/hum.2013.210.

Maddalena, A. *et al.* (2018) 'Triple Vectors Expand AAV Transfer Capacity in the Retina', *Molecular Therapy*. Elsevier Ltd., 26(2), pp. 524–541. doi: 10.1016/j.ymthe.2017.11.019.

Maritzen, T. and Haucke, V. (2017) 'Coupling of exocytosis and endocytosis at the presynaptic active zone', *Neuroscience Research*. Elsevier Ireland Ltd and Japan Neuroscience Society, 127, pp. 45–52. doi: 10.1016/j.neures.2017.09.013.

Marlin, S. *et al.* (2010) 'Temperature-sensitive auditory neuropathy associated with an otoferlin mutation: Deafening fever!', *Biochemical and Biophysical Research*

# References

*Communications*. Elsevier Inc., 394(3), pp. 737–742. doi: 10.1016/j.bbrc.2010.03.062.

Matsunaga, T. *et al.* (2012) 'A prevalent founder mutation and genotype-phenotype correlations of OTOF in Japanese patients with auditory neuropathy', *Clinical Genetics*, 82(5), pp. 425–432. doi: 10.1111/j.1399-0004.2012.01897.x.

McClements, M. E. *et al.* (2016) 'A Fragmented Adeno-Associated Viral Dual Vector Strategy for Treatment of Diseases Caused by Mutations in Large Genes Leads to Expression of Hybrid Transcripts', *Journal of Genetic Syndromes & Gene Therapy*, 7(5). doi: 10.4172/2157-7412.1000311.

McClements, M. E. *et al.* (2018) 'An AAV dual vector strategy ameliorates the Stargardt phenotype in adult Abca4-/- mice', *Human Gene Therapy*, pp. 1–31. doi: 10.1089/hum.2018.156.

McClements, M. E. and Maclaren, R. E. (2017) 'Adeno-associated virus (AAV) dual vector strategies for gene therapy encoding large transgenes', *Yale Journal of Biology and Medicine*, 90(4), pp. 611–623.

Meese, S. (2015) 'Biochemical studies of the synaptic protein otoferlin', *Georg-August University School of Science (GAUSS)*.

Meese, S. *et al.* (2017) 'Activity-Dependent Phosphorylation by CaMKIIδ Alters the Ca2+ Affinity of the Multi-C2-Domain Protein Otoferlin', *Frontiers in Synaptic Neuroscience*, 9(October), p. 13. doi: 10.3389/fnsyn.2017.00013.

Meyer, A. C. *et al.* (2009) 'Tuning of synapse number, structure and function in the cochlea', *Nature Neuroscience*, 12(4), pp. 444–453. doi: 10.1038/nn.2293.

Michalski, N. *et al.* (2017) 'Otoferlin acts as a Ca2+sensor for vesicle fusion and vesicle pool replenishment at auditory hair cell ribbon synapses', *eLife*, 6, pp. 1–34. doi: 10.7554/eLife.31013.

Migliosi, V. (2002) 'Q829X, a novel mutation in the gene encoding otoferlin (OTOF), is

frequently found in Spanish patients with prelingual non-syndromic hearing loss', *Journal of Medical Genetics*, 39(7), pp. 502–506. doi: 10.1136/jmg.39.7.502.

Mikaelian, D. and Ruben, R. J. (1965) 'Development of Hearing in the Normal Cba-J Mouse: Correlation of Physiological Observations with Behavioral Responses and with Cochlear Anatomy', *Acta Oto-Laryngologica*. Taylor & Francis, 59(2–6), pp. 451–461. doi: 10.3109/00016486509124579.

Mirghomizadeh, F. *et al.* (2002) 'Substitutions in the Conserved C2C Domain of Otoferlin Cause DFNB9, a Form of Nonsyndromic Autosomal Recessive Deafness', *Neurobiology of Disease*, 10(2), pp. 157–164. doi: 10.1006/nbdi.2002.0488.

Morton, C. C. and Nance, W. E. (2006) 'Newborn Hearing Screening — A Silent Revolution', *New England Journal of Medicine*, 354(20), pp. 2151–2164. doi: 10.1056/NEJMra050700.

Moser, T. and Beutner, D. (2000) 'Kinetics of exocytosis and endocytosis at the cochlear inner hair cell afferent synapse of the mouse', *Proceedings of the National Academy of Sciences*, 97(2), pp. 883–888. doi: 10.1073/pnas.97.2.883.

Moser, T., Predoehl, F. and Starr, A. (2013) 'Review of Hair Cell Synapse Defects in Sensorineural Hearing Impairment', *Otology & Neurotology*, 34(6), pp. 995–1004. doi: 10.1097/MAO.0b013e3182814d4a.

Moser, T. and Starr, A. (2016) 'Auditory neuropathy-neural and synaptic mechanisms', *Nature Reviews Neurology*. Nature Publishing Group, 12(3), pp. 135–149. doi: 10.1038/nrneurol.2016.10.

Müller, A. (2016) 'Molecular studies of the synaptic protein otoferlin submitted by', *Ph.D. Thesis, Georg-August Universität Göttingen*.

Muresan, V., Lyass, A. and Schnapp, B. J. (1999) 'The Kinesin Motor KIF3A Is a Component of the Presynaptic Ribbon in Vertebrate Photoreceptors', *The Journal of Neuroscience*, 19(3), pp. 1027–1037. doi: 10.1523/JNEUROSCI.19-03-01027.1999.

## References

Narayan, S. S. (1998) 'Frequency Tuning of Basilar Membrane and Auditory Nerve Fibers in the Same Cochleae', *Science*, 282(5395), pp. 1882–1884. doi: 10.1126/science.282.5395.1882.

Neef, A. *et al.* (2007) 'Probing the Mechanism of Exocytosis at the Hair Cell Ribbon Synapse', *Journal of Neuroscience*, 27(47), pp. 12933–12944. doi: 10.1523/JNEUROSCI.1996-07.2007.

Neef, J. *et al.* (2014) 'Modes and Regulation of Endocytic Membrane Retrieval in Mouse Auditory Hair Cells', *The Journal of Neuroscience*, 34(3), pp. 705–716. doi: 10.1523/JNEUROSCI.3313-13.2014.

Nishio, S. Y. and Usami, S. I. (2017) 'Outcomes of cochlear implantation for the patients with specific genetic etiologies: a systematic literature review', *Acta Oto-Laryngologica*. Informa UK Limited, trading as Taylor 8 Francis Group, 137(7), pp. 730–742. doi: 10.1080/00016489.2016.1276303.

Nouvian, R. *et al.* (2006) 'Structure and Function of the Hair Cell Ribbon Synapse', *Journal of Membrane Biology*, 209(2–3), pp. 153–165. doi: 10.1007/s00232-005-0854-4.

Nouvian, R. *et al.* (2011) 'Exocytosis at the hair cell ribbon synapse apparently operates without neuronal SNARE proteins.', *Nature neuroscience*. Nature Publishing Group, 14(4), pp. 411–413. doi: 10.1038/nn.2774.

Olds, C. and Oghalai, J. S. (2015) 'Audiologic impairment associated with bilirubin-induced neurologic damage', *Seminars in Fetal and Neonatal Medicine*. Elsevier Ltd, 20(1), pp. 42–46. doi: 10.1016/j.siny.2014.12.006.

Padmanarayana, M. *et al.* (2014) 'Characterization of the lipid binding properties of Otoferlin reveals specific interactions between PI(4,5)P2 and the C2C and C2F domains.', *Biochemistry*, 53(30), pp. 5023–33. doi: 10.1021/bi5004469.

Pan, B. *et al.* (2017) 'Gene therapy restores auditory and vestibular function in a mouse model of Usher syndrome type 1c', *Nature Biotechnology*, 35(3). doi: 10.1038/nbt.3801.

# References

Pangrsic, T. *et al.* (2010) 'Hearing requires otoferlin-dependent efficient replenishment of synaptic vesicles in hair cells.', *Nature neuroscience*. Nature Publishing Group, 13(7), pp. 869–876. doi: 10.1038/nn.2578.

Pangršič, T., Reisinger, E. and Moser, T. (2012) 'Otoferlin: A multi-C2domain protein essential for hearing', *Trends in Neurosciences*, 35(11), pp. 671–680. doi: 10.1016/j.tins.2012.08.002.

Pangrsic, T. and Vogl, C. (2018) 'Balancing presynaptic release and endocytic membrane retrieval at hair cell ribbon synapses', *FEBS Letters*, pp. 1–18. doi: 10.1002/1873-3468.13258.

Petit, C. (1996) 'Genes responsible for human hereditary deafness: symphony of a thousand', *Nature Genetics*. Nature Publishing Group, 14, p. 385. Available at: https://doi.org/10.1038/ng1296-385.

Plontke, S. K. and Salt, A. N. (2018) 'Local drug delivery to the inner ear: Principles, practice, and future challenges', *Hearing Research*. Elsevier B.V., 368, pp. 1–2. doi: 10.1016/j.heares.2018.06.018.

Pryadkina, M. *et al.* (2015) 'A comparison of AAV strategies distinguishes overlapping vectors for efficient systemic delivery of the 6.2 kb Dysferlin coding sequence', *Molecular Therapy — Methods & Clinical Development*, 2(January), p. 15009. doi: 10.1038/mtm.2015.9.

Ramakrishnan, N. A. *et al.* (2014) 'Calcium regulates molecular interactions of otoferlin with soluble NSF attachment protein receptor (SNARE) proteins required for hair cell exocytosis', *Journal of Biological Chemistry*, 289(13), pp. 8750–8766. doi: 10.1074/jbc.M113.480533.

Ramakrishnan, N. A., Drescher, M. J. and Drescher, D. G. (2009) 'Direct interaction of otoferlin with syntaxin 1A, SNAP-25, and the L-type voltage-gated calcium channel Cav1.3', *Journal of Biological Chemistry*, 284(3), pp. 1364–1372. doi: 10.1074/jbc.M803605200.

References

Raviv, D., Dror, A. a. and Avraham, K. B. (2010) 'Hearing loss: A common disorder caused by many rare alleles', *Annals of the New York Academy of Sciences*, 1214(1), pp. 168–179. doi: 10.1111/j.1749-6632.2010.05868.x.

Reisinger, E. *et al.* (2011) 'Probing the functional equivalence of otoferlin and synaptotagmin 1 in exocytosis', *The Journal of neuroscience : the official journal of the Society for Neuroscience*, 31(13), pp. 4886–4895. doi: 10.1523/JNEUROSCI.5122-10.2011.

Reits, E. *et al.* (2004) 'A major role for TPPII in trimming proteasomal degradation products for MHC class I antigen presentation', *Immunity*, 20(4), pp. 495–506. doi: 10.1016/S1074-7613(04)00074-3.

Reuter, K. (2011) 'Biochemistry and physiological role of otoferlin', *Ph.D. Thesis, Georg-August Universität Göttingen*, (August).

Revelo, N. H. *et al.* (2014) 'A new probe for super-resolution imaging of membranes elucidates trafficking pathways', *Journal of Cell Biology*, 205(4), pp. 591–606. doi: 10.1083/jcb.201402066.

Rodríguez-Ballesteros, M. *et al.* (2008) 'A multicenter study on the prevalence and spectrum of mutations in the otoferlin gene (OTOF) in subjects with nonsyndromic hearing impairment and auditory neuropathy', *Human Mutation*, 29(6), pp. 823–831. doi: 10.1002/humu.20708.

Romanos, J. *et al.* (2009) 'Novel OTOF mutations in Brazilian patients with auditory neuropathy', *Journal of Human Genetics*, 54(7), pp. 382–385. doi: 10.1038/jhg.2009.45.

Roux, I. *et al.* (2006) 'Otoferlin, Defective in a Human Deafness Form, Is Essential for Exocytosis at the Auditory Ribbon Synapse', *Cell*, 127(2), pp. 277–289. doi: 10.1016/j.cell.2006.08.040.

Roux, I. *et al.* (2009) 'Myosin VI is required for the proper maturation and function of inner hair cell ribbon synapses', *Human Molecular Genetics*, 18(23), pp. 4615–4628. doi: 10.1093/hmg/ddp429.

# References

Ruel, J. *et al.* (2008) 'Impairment of SLC17A8 Encoding Vesicular Glutamate Transporter-3, VGLUT3, Underlies Nonsyndromic Deafness DFNA25 and Inner Hair Cell Dysfunction in Null Mice', *American Journal of Human Genetics*, 83(2), pp. 278–292. doi: 10.1016/j.ajhg.2008.07.008.

Safieddine, S., El-Amraoui, A. and Petit, C. (2012) 'The Auditory Hair Cell Ribbon Synapse: From Assembly to Function', *Annual Review of Neuroscience*, 35(1), pp. 509–528. doi: 10.1146/annurev-neuro-061010-113705.

Safieddine, S. and Wenthold, R. J. (1999) 'SNARE complex at the ribbon synapses of cochlear hair cells: Analysis of synaptic vesicle- and synaptic membrane-associated proteins', *European Journal of Neuroscience*, 11(3), pp. 803–812. doi: 10.1046/j.1460-9568.1999.00487.x.

Santarelli, R. *et al.* (2015) 'Audibility, speech perception and processing of temporal cues in ribbon synaptic disorders due to OTOF mutations', *Hearing Research*. Elsevier B.V. doi: 10.1016/j.heares.2015.07.007.

Saric, T., Graef, C. I. and Goldberg, A. L. (2004) 'Pathway for degradation of peptides generated by proteasomes: A key role for thimet oligopeptidase and other metallopeptidases', *Journal of Biological Chemistry*, 279(45), pp. 46723–46732. doi: 10.1074/jbc.M406537200.

Schnee, M. E. *et al.* (2011) 'Calcium-Dependent Synaptic Vesicle Trafficking Underlies Indefatigable Release at the Hair Cell Afferent Fiber Synapse', *Neuron*, 70(2), pp. 326–338. doi: 10.1016/j.neuron.2011.01.031.

Schwander, M. *et al.* (2007) 'A Forward Genetics Screen in Mice Identifies Recessive Deafness Traits and Reveals That Pejvakin Is Essential for Outer Hair Cell Function', *Journal of Neuroscience*, 27(9), pp. 2163–2175. doi: 10.1523/JNEUROSCI.4975-06.2007.

Seal, R. P. *et al.* (2008) 'Sensorineural Deafness and Seizures in Mice Lacking Vesicular Glutamate Transporter 3', *Neuron*. Elsevier, 57(2), pp. 263–275. doi: 10.1016/j.neuron.2007.11.032.

## References

Shearer, A. E. and Smith, R. J. (2015) *OTOF-Related Deafness*, *GeneReviews®*. University of Washington, Seattle. Available at: http://www.ncbi.nlm.nih.gov/pubmed/20301429 (Accessed: 14 November 2018).

Shrestha, B. R. *et al.* (2018) 'Sensory Neuron Diversity in the Inner Ear Is Shaped by Activity', *Cell*. Elsevier Inc., 174(5), pp. 1229-1246.e17. doi: 10.1016/j.cell.2018.07.007.

Shu, Y. *et al.* (2016) 'Identification of Adeno-Associated Viral Vectors That Target Neonatal and Adult Mammalian Inner Ear Cell Subtypes', *Human Gene Therapy*, 27(9), pp. 687–699. doi: 10.1089/hum.2016.053.

Sondergaard, P. C. *et al.* (2015) 'AAV.Dysferlin Overlap Vectors Restore Function in Dysferlinopathy Animal Models', *Annals of Clinical and Translational Neurology*, 2(3), pp. 256–270. doi: 10.1002/acn3.172.

Starr, A. *et al.* (1996) 'Auditory neuropathy', *Brain*, 119, pp. 741–753. doi: 10.1097/00020840-199810000-00008.

Strenzke, N. *et al.* (2009) 'Complexin-I Is Required for High-Fidelity Transmission at the Endbulb of Held Auditory Synapse', *Journal of Neuroscience*, 29(25), pp. 7991–8004. doi: 10.1523/JNEUROSCI.0632-09.2009.

Strenzke, N. *et al.* (2016) 'Hair cell synaptic dysfunction, auditory fatigue and thermal sensitivity in otoferlin Ile515Thr mutants.', *The EMBO journal*, pp. 1–17. doi: 10.15252/embj.201694564.

Suzuki, J. *et al.* (2017) 'Cochlear gene therapy with ancestral AAV in adult mice: complete transduction of inner hair cells without cochlear dysfunction.', *Scientific reports*. Nature Publishing Group, 7(March), p. 45524. doi: 10.1038/srep45524.

Tertrais, M. *et al.* (2019) 'Viral transfer of mini-otoferlins partially restores The fast component of exocytosis And uncovers ultrafast endocytosis In auditory hair cells of otoferlin knock-out mice', *Journal of Neuroscience*, in press.

## References

Tom Dieck, S. *et al.* (2005) 'Molecular dissection of the photoreceptor ribbon synapse: Physical interaction of Bassoon and RIBEYE is essential for the assembly of the ribbon complex', *Journal of Cell Biology*, 168(5), pp. 825–836. doi: 10.1083/jcb.200408157.

Trapani, I. *et al.* (2014) 'Effective delivery of large genes to the retina by dual AAV vectors', *EMBO Molecular Medicine*, 6(2), pp. 194–211. doi: 10.1002/emmm.201302948.

Trapani, I. *et al.* (2015) 'Improved dual AAV vectors with reduced expression of truncated proteins are safe and effective in the retina of a mouse model of Stargardt disease', *Human Molecular Genetics*, 24(23), pp. 6811–6825. doi: 10.1093/hmg/ddv386.

Tretiakova, A. P. *et al.* (2018) 'Realizing the promise of gene therapy through collaboration and partnering : Pfizer ' s view', *Pfizer Inc.*

Uthaiah, R. C. and Hudspeth, A. J. (2010) 'Molecular Anatomy of the Hair Cell's Ribbon Synapse', *Journal of Neuroscience*, 30(37), pp. 12387–12399. doi: 10.1523/JNEUROSCI.1014-10.2010.

Varga, R. (2003) 'Non-syndromic recessive auditory neuropathy is the result of mutations in the otoferlin (OTOF) gene', *Journal of Medical Genetics*, 40(1), pp. 45–50. doi: 10.1136/jmg.40.1.45.

Varga, R. *et al.* (2006) 'OTOF mutations revealed by genetic analysis of hearing loss families including a potential temperature sensitive auditory neuropathy allele.', *Journal of medical genetics*, 43(August), pp. 576–581. doi: 10.1136/jmg.2005.038612.

Vincent, P. F. Y. *et al.* (2014) 'Exocytotic Machineries of Vestibular Type I and Cochlear Ribbon Synapses Display Similar Intrinsic Otoferlin- Dependent Ca 2 ε Sensitivity But a Different Coupling to Ca 2 ε Channels', 34(33), pp. 10853–10869. doi: 10.1523/JNEUROSCI.0947-14.2014.

Vincent, P. F. Y. *et al.* (2015) 'A synaptic F-actin network controls otoferlin-dependent exocytosis in auditory inner hair cells', *eLife*, 4(NOVEMBER2015), pp. 1–13. doi: 10.7554/eLife.10988.001.

# References

Vincent, P. F. Y. *et al.* (2017) 'Different Ca ᵥ 1.3 Channel Isoforms Control Distinct Components of the Synaptic Vesicle Cycle in Auditory Inner Hair Cells', *The Journal of Neuroscience*, 37(11), pp. 2960–2975. doi: 10.1523/JNEUROSCI.2374-16.2017.

Vogl, C. *et al.* (2015) 'Unconventional molecular regulation of synaptic vesicle replenishment in cochlear inner hair cells', *Journal of Cell Science*, 128(4), pp. 638–644. doi: 10.1242/jcs.162099.

Wang, D. Y. *et al.* (2010) 'Screening mutations of OTOF gene in Chinese patients with auditory neuropathy, including a familial case of temperature-sensitive auditory neuropathy', *BMC Medical Genetics*, 11(1), pp. 3–5. doi: 10.1186/1471-2350-11-79.

Wang, J. *et al.* (1997) 'E ¡ ects of selective inner hair cell loss on auditory nerve ¢ ber threshold , tuning and spontaneous and driven discharge rate', 107.

Wang, Y. *et al.* (2018) 'Novel *OTOF* gene mutations identified using a massively parallel DNA sequencing technique in DFNB9 deafness', *Acta Oto-Laryngologica*, 6489, pp. 1–6. doi: 10.1080/00016489.2018.1476777.

Wang, Y. and Chang, Q. (2013) 'Early postnatal virus inoculation into the scala media achieved extensive expression of exogenous green fl uorescent protein in the inner ear and preserved auditory brainstem response thresholds', (January), pp. 123–133. doi: 10.1002/jgm.

Wichmann, C. and Moser, T. (2015) 'Relating structure and function of inner hair cell ribbon synapses', *Cell and Tissue Research*, 361(1), pp. 95–114. doi: 10.1007/s00441-014-2102-7.

Wu, P. Z. *et al.* (2018) 'Primary Neural Degeneration in the Human Cochlea: Evidence for Hidden Hearing Loss in the Aging Ear', *Neuroscience*, pp. 1–13. doi: 10.1016/j.neuroscience.2018.07.053.

Wu, W. *et al.* (2015) 'Function coupling of otoferlin with GAD65 acts to modulate GABAergic activity', *Journal of Molecular Cell Biology*, 7(2), pp. 168–179. doi: 10.1093/jmcb/mjv011.

# References

Wu, Z., Yang, H. and Colosi, P. (2010) 'Effect of genome size on AAV vector packaging', *Molecular Therapy*. Nature Publishing Group, 18(1), pp. 80–86. doi: 10.1038/mt.2009.255.

Wynne, D. P. *et al.* (2013) 'Loudness adaptation accompanying ribbon synapse and auditory nerve disorders', *Brain*, 136(5), pp. 1626–1638. doi: 10.1093/brain/awt056.

Yan, Z. *et al.* (2005) 'Inverted Terminal Repeat Sequences Are Important for Intermolecular Recombination and Circularization of Adeno-Associated Virus Genomes', *Society*, 79(1), pp. 364–379. doi: 10.1128/JVI.79.1.364-379.2005.

Yan, Z. *et al.* (2006) 'Hybrid Adeno-Associated Virus Bearing Nonhomologous Inverted Terminal Repeats Enhances Dual-Vector Reconstruction of Minigenes *In Vivo*', *Human Gene Therapy*, 0(0), p. 061221035427001. doi: 10.1038/nri2807.

Yasunaga, S. *et al.* (1999) 'A mutation in OTOF, encoding otoferlin, a FER-1-like protein, causes DFNB9, a nonsyndromic form of deafness.', *Nature genetics*, 21(4), pp. 363–9. doi: 10.1038/7693.

Yasunaga, S. *et al.* (2000) 'OTOF encodes multiple long and short isoforms: genetic evidence that the long ones underlie recessive deafness DFNB9.', *American journal of human genetics*, 67(3), pp. 591–600. doi: 10.1086/303049.

Yildirim-Baylan, M. *et al.* (2014) 'Evidence for genotype-phenotype correlation for OTOF mutations', *International Journal of Pediatric Otorhinolaryngology*. Elsevier Ireland Ltd, 78(6), pp. 950–953. doi: 10.1016/j.ijporl.2014.03.022.

Yoshimura, H. *et al.* (2018) 'Enhanced viral-mediated cochlear gene delivery in adult mice by combining canal fenestration with round window membrane inoculation', *Scientific Reports*. Springer US, 8(1), pp. 1–10. doi: 10.1038/s41598-018-21233-z.

Zhang, Y. *et al.* (2013) 'Dual AAV therapy ameliorates exercise-induced muscle injury and functional ischemia in murine models of Duchenne muscular dystrophy', *Human Molecular Genetics*, 22(18), pp. 3720–3729. doi: 10.1093/hmg/ddt224.

# References

Zhang, Y. and Duan, D. (2012) 'Novel Mini–Dystrophin Gene Dual Adeno-Associated Virus Vectors Restore Neuronal Nitric Oxide Synthase Expression at the Sarcolemma', *Human Gene Therapy*, 23(1), pp. 98–103. doi: 10.1089/hum.2011.131.

XXX

# Appendix

*Appendix table S1. Statistical analysis*

## Chapter 2.3

**Figure 2.5**

| Compared group | Statistical significance | *P*-value | Statistical test |
|---|---|---|---|
| DualAAV2/6-TS: N-term Otoferlin vs. C-term Otoferlin | ** | 0.002 | Wilcoxon matched-pairs singed rank test |
| DualAAV2/6-Hyb: N-term Otoferlin vs. C-term Otoferlin | ** | 0.004 | Wilcoxon matched-pairs singed rank test |
| DualAAV2/Anc80-TS: N-term Otoferlin vs. C-term Otoferlin | * | 0.03 | Wilcoxon matched-pairs singed rank test |
| N-term Otoferlin: DualAAV2/6-TS vs. DualAAV2/6-Hyb | ns | 0.055 | Tukey's multiple comparisons test |
| C-term Otoferlin: DualAAV2/6-TS vs. DualAAV2/6-Hyb | ns | 0.11 | Tukey's multiple comparisons test |
| N-term Otoferlin: DualAAV2/6-TS vs DualAAV2/Anc80-TS | ns | 0.08 | Tukey's multiple comparisons test |
| C-term Otoferlin: DualAAV2/6-TS vs DualAAV2/Anc80-TS | ns | 0.051 | Tukey's multiple comparisons test |
| N-term Otoferlin: DualAAV2/6-Hyb vs. | ns | 0.99 | Tukey's multiple comparisons test |

| DualAAV2/Anc80-TS | | | |
|---|---|---|---|
| C-term Otoferlin: DualAAV2/6-Hyb vs. DualAAV2/Anc80-TS | ns | 0.83 | Tukey's multiple comparisons test |

**Figure 2.6B**

| Compared group | Statistical significance | *P*-value | Statistical test |
|---|---|---|---|
| N-term Otoferlin: | | | |
| WTB6 - AAV vs. WTCD1B6F1 + AAV2/6.eGFP | ns | > 0.999999 | Kruskal-Wallis test followed by Dunn's multiple comparison test |
| WTB6 - AAV vs. WTCD1B6F1 + DualAAV2/6-TS | *** | $0.2 \times 10^{-5}$ | Kruskal-Wallis test followed by Dunn's multiple comparison test |
| WTB6 - AAV vs. $Otof^{-/-}$ CD1B6F1 + DualAAV2/6-TS | *** | 0.0008 | Kruskal-Wallis test followed by Dunn's multiple comparison test |
| WTB6 - AAV vs. $Otof^{-/-}$ CD1B6F1 + DualAAV2/6-Hyb | *** | $< 0.1 \times 10^{-5}$ | Kruskal-Wallis test followed by Dunn's multiple comparison test |
| WTB6 - AAV vs. $Otof^{-/-}$ CD1B6F1 + DualAAV2/Anc80-TS | *** | $< 0.1 \times 10^{-5}$ | Kruskal-Wallis test followed by Dunn's multiple comparison test |
| WTB6 - AAV vs. $Otof^{-/-}$CD1B6F1 - AAV | *** | $< 0.1 \times 10^{-5}$ | Kruskal-Wallis test followed by Dunn's multiple comparison test |
| $Otof^{-/-}$ CD1B6F1 + DualAAV2/6-TS vs. $Otof^{-/-}$ CD1B6F1 + DualAAV2/6-Hyb | ns | > 0.999999 | Kruskal-Wallis test followed by Dunn's multiple comparison test |
| $Otof^{-/-}$ CD1B6F1 + DualAAV2/6-TS vs. $Otof^{-/-}$ CD1B6F1 + DualAAV2/Anc80-TS | ns | > 0.999999 | Kruskal-Wallis test followed by Dunn's multiple comparison test |

| | | | |
|---|---|---|---|
| *Otof*^{-/-} CD1B6F1 + DualAAV2/6-TS vs. *Otof*^{-/-} CD1B6F1 - AAV | *** | < 0.1x10$^{-5}$ | Kruskal-Wallis test followed by Dunn's multiple comparison test |
| *Otof*^{-/-} CD1B6F1 + DualAAV2/6-Hyb vs. *Otof*^{-/-} CD1B6F1 + DualAAV2/Anc80-TS | ns | > 0.999999 | Kruskal-Wallis test followed by Dunn's multiple comparison test |
| *Otof*^{-/-} CD1B6F1 + DualAAV2/6-Hyb vs. *Otof*^{-/-} CD1B6F1 - AAV | *** | < 0.1x10$^{-5}$ | Kruskal-Wallis test followed by Dunn's multiple comparison test |
| *Otof*^{-/-} CD1B6F1 + DualAAV2/Anc80-TS vs. *Otof*^{-/-} CD1B6F1 - AAV | *** | < 0.1x10$^{-5}$ | Kruskal-Wallis test followed by Dunn's multiple comparison test |
| C-term Otoferlin: | | | |
| WTB6 - AAV vs. WTCD1B6F1 + AAV2/6.eGFP | ** | 0.004 | Kruskal-Wallis test followed by Dunn's multiple comparison test |
| WTB6 - AAV vs. WTCD1B6F1 + DualAAV2/6-TS | * | 0.031 | Kruskal-Wallis test followed by Dunn's multiple comparison test |
| WTB6 - AAV vs. *Otof*^{-/-} CD1B6F1 + DualAAV2/6-TS | *** | 0.1x10$^{-4}$ | Kruskal-Wallis test followed by Dunn's multiple comparison test |
| WTB6 - AAV vs. *Otof*^{-/-} CD1B6F1 + DualAAV2/6-Hyb | *** | < 0.1x10$^{-5}$ | Kruskal-Wallis test followed by Dunn's multiple comparison test |
| WTB6 - AAV vs. *Otof*^{-/-} CD1B6F1 + DualAAV2/Anc80-TS | *** | < 0.1x10$^{-5}$ | Kruskal-Wallis test followed by Dunn's multiple comparison test |
| WTB6 - AAV vs. *Otof*^{-/-} CD1B6F1 - AAV | *** | < 0.1x10$^{-5}$ | Kruskal-Wallis test followed by Dunn's multiple comparison test |
| *Otof*^{-/-} CD1B6F1 + DualAAV2/6-TS vs. *Otof*^{-/-} CD1B6F1 + DualAAV2/6-Hyb | ns | > 0.999999 | Kruskal-Wallis test followed by Dunn's multiple comparison test |

| | | | |
|---|---|---|---|
| *Otof*<sup>-/-</sup> CD1B6F1 + DualAAV2/6-TS vs. *Otof*<sup>-/-</sup> CD1B6F1 + DualAAV2/Anc80-TS | ns | 0.211 | Kruskal-Wallis test followed by Dunn's multiple comparison test |
| *Otof*<sup>-/-</sup>CD1B6F1 + DualAAV2/6-TS vs. *Otof*<sup>-/-</sup> CD1B6F1 - AAV | *** | < 0.1x10<sup>-5</sup> | Kruskal-Wallis test followed by Dunn's multiple comparison test |
| *Otof*<sup>-/-</sup> CD1B6F1 + DualAAV2/6-Hyb vs. *Otof*<sup>-/-</sup> CD1B6F1 + DualAAV2/Anc80-TS | *** | 0.0002 | Kruskal-Wallis test followed by Dunn's multiple comparison test |
| *Otof*<sup>-/-</sup>CD1B6F1 + DualAAV2/6-Hyb vs. *Otof*<sup>-/-</sup>CD1B6F1 - AAV | *** | < 0.1x10<sup>-5</sup> | Kruskal-Wallis test followed by Dunn's multiple comparison test |
| *Otof*<sup>-/-</sup> CD1B6F1 + DualAAV2/Anc80-TS vs. *Otof*<sup>-/-</sup> CD1B6F1 - AAV | *** | < 0.1x10<sup>-5</sup> | Kruskal-Wallis test followed by Dunn's multiple comparison test |

**Figure 2.7B.**

| Compared group | Statistical significance | *P*-value | Statistical test |
|---|---|---|---|
| WTB6 vs. WTCD1B6F1 | ns | > 0.999999 | Kruskal-Wallis test followed by Dunn's multiple comparison test |
| WTB6 vs. *Otof*<sup>-/-</sup>+ DualAAV2/6-TS | *** | < 0.1x10<sup>-5</sup> | Kruskal-Wallis test followed by Dunn's multiple comparison test |
| WTB6 vs. *Otof*<sup>-/-</sup> + DualAAV2/6-Hyb | *** | < 0.1x10<sup>-5</sup> | Kruskal-Wallis test followed by Dunn's multiple comparison test |
| WTB6 vs. *Otof*<sup>-/-</sup> - AAV injected ear | *** | < 0.1x10<sup>-5</sup> | Kruskal-Wallis test followed by Dunn's multiple comparison test |
| WTB6 vs. *Otof*<sup>-/-</sup> - AAV non-injected ear | *** | < 0.1x10<sup>-5</sup> | Kruskal-Wallis test followed by Dunn's multiple comparison test |

| | | | |
|---|---|---|---|
| WTCD1B6F1<br>vs.<br>*Otof*$^{-/-}$ + DualAAV2/6-TS | *** | < 0.1x10$^{-5}$ | Kruskal-Wallis test<br>followed by Dunn's<br>multiple comparison test |
| WTCD1B6F1<br>vs.<br>*Otof*$^{-/-}$ + DualAAV2/6-Hyb | *** | < 0.1x10$^{-5}$ | Kruskal-Wallis test<br>followed by Dunn's<br>multiple comparison test |
| WTCD1B6F1<br>vs.<br>*Otof*$^{-/-}$ - AAV<br>injected ear | *** | < 0.1x10$^{-5}$ | Kruskal-Wallis test<br>followed by Dunn's<br>multiple comparison test |
| WTCD1B6F1<br>vs.<br>*Otof*$^{-/-}$ - AAV<br>non-injected ear | *** | < 0.1x10$^{-5}$ | Kruskal-Wallis test<br>followed by Dunn's<br>multiple comparison test |
| *Otof*$^{-/-}$ + DualAAV2/6-TS<br>vs.<br>*Otof*$^{-/-}$ + DualAAV2/6-Hyb | ns | > 0.999999 | Kruskal-Wallis test<br>followed by Dunn's<br>multiple comparison test |
| *Otof*$^{-/-}$ + DualAAV2/6-TS<br>vs.<br>*Otof*$^{-/-}$ - AAV<br>injected ear | ns | > 0.999999 | Kruskal-Wallis test<br>followed by Dunn's<br>multiple comparison test |
| *Otof*$^{-/-}$ + DualAAV2/6-TS<br>vs.<br>*Otof*$^{-/-}$ - AAV<br>non-injected ear | ns | > 0.999999 | Kruskal-Wallis test<br>followed by Dunn's<br>multiple comparison test |
| *Otof*$^{-/-}$ + DualAAV2/6-Hyb<br>vs.<br>*Otof*$^{-/-}$ - AAV<br>injected ear | ns | 0.32 | Kruskal-Wallis test<br>followed by Dunn's<br>multiple comparison test |
| *Otof*$^{-/-}$ + DualAAV2/6-Hyb<br>vs.<br>*Otof*$^{-/-}$ - AAV<br>non-injected ear | ns | > 0.999999 | Kruskal-Wallis test<br>followed by Dunn's<br>multiple comparison test |
| *Otof*$^{-/-}$ - AAV<br>injected ear<br>vs.<br>*Otof*$^{-/-}$ - AAV<br>non-injected ear | ns | > 0.999999 | Kruskal-Wallis test<br>followed by Dunn's<br>multiple comparison test |

**Figure 2.9A.**

| Compared group | Statistical significance | *P*-value | Statistical test |
|---|---|---|---|
| WT + AAV2/6.eGFP | ns | > 0.999999 | Kruskal-Wallis test |

| | | | |
|---|---|---|---|
| vs.<br>WT + DualAAV2/6-TS | | | followed by Dunn's<br>multiple comparison test |
| WT + AAV2/6.eGFP<br>vs.<br>WT + AAV2/Anc80.eGFP | ns | > 0.999999 | Kruskal-Wallis test<br>followed by Dunn's<br>multiple comparison test |
| WT + AAV2/6.eGFP<br>vs.<br>Otof $^{-/-}$ + DualAAV2/6-TS | *** | 0.00002 | Kruskal-Wallis test<br>followed by Dunn's<br>multiple comparison test |
| WT + AAV2/6.eGFP<br>vs.<br>Otof $^{-/-}$ + DualAAV2/6-Hyb | *** | 0.0001 | Kruskal-Wallis test<br>followed by Dunn's<br>multiple comparison test |
| WT + AAV2/6.eGFP<br>vs.<br>Otof $^{-/-}$ + DualAAV2/Anc80-<br>TS | ** | 0.009 | Kruskal-Wallis test<br>followed by Dunn's<br>multiple comparison test |
| Otof $^{-/-}$ + DualAAV2/6-TS<br>vs.<br>Otof $^{-/-}$ + DualAAV2/6-Hyb | ns | > 0.999999 | Kruskal-Wallis test<br>followed by Dunn's<br>multiple comparison test |
| Otof $^{-/-}$ + DualAAV2/6-TS<br>vs.<br>Otof $^{-/-}$ + DualAAV2/Anc80-<br>TS | ns | > 0.999999 | Kruskal-Wallis test<br>followed by Dunn's<br>multiple comparison test |
| Otof $^{-/-}$ + DualAAV2/6-Hyb<br>vs.<br>Otof $^{-/-}$ + DualAAV2/Anc80-<br>TS | ns | > 0.999999 | Kruskal-Wallis test<br>followed by Dunn's<br>multiple comparison test |

## Chapter 2.4

**Figure 2.12**

| Compared group | Statistical<br>significance | $P$-value | Statistical test |
|---|---|---|---|
| WT P4<br>vs.<br>Otof $^{-/-}$ P4 | ns | > 0.999999 | Kruskal-Wallis test<br>followed by Dunn's multiple<br>comparison test |
| WT P4<br>vs.<br>WT P6 | ns | > 0.999999 | Kruskal-Wallis test<br>followed by Dunn's multiple<br>comparison test |
| Otof $^{-/-}$ P4<br>vs.<br>Otof $^{-/-}$ P6 | ns | > 0.999999 | Kruskal-Wallis test<br>followed by Dunn's multiple<br>comparison test |
| WT P6<br>vs. | * | 0.02 | Kruskal-Wallis test |

| | | | |
|---|---|---|---|
| *Otof* <sup>-/-</sup> P6 | | | followed by Dunn's multiple comparison test |
| WT P6 vs. WT P8 | * | 0.03 | Kruskal-Wallis test followed by Dunn's multiple comparison test |
| *Otof* <sup>-/-</sup> P6 vs. *Otof* <sup>-/-</sup> P8 | ns | > 0.999999 | Kruskal-Wallis test followed by Dunn's multiple comparison test |
| WT P8 vs. *Otof* <sup>-/-</sup> P8 | *** | < 0.0001 | Kruskal-Wallis test followed by Dunn's multiple comparison test |
| WT P8 vs. WT P10 | ns | > 0.999999 | Kruskal-Wallis test followed by Dunn's multiple comparison test |
| *Otof* <sup>-/-</sup> P8 vs. *Otof* <sup>-/-</sup> P10 | ** | 0.004 | Kruskal-Wallis test followed by Dunn's multiple comparison test |
| WT P10 vs. *Otof* <sup>-/-</sup> P10 | ns | 0.72 | Kruskal-Wallis test followed by Dunn's multiple comparison test |
| WT P10 vs. WT P12 | ** | 0.006 | Kruskal-Wallis test followed by Dunn's multiple comparison test |
| *Otof* <sup>-/-</sup> P10 vs. *Otof* <sup>-/-</sup> P12 | *** | 0.0009 | Kruskal-Wallis test followed by Dunn's multiple comparison test |
| WT P12 vs. *Otof* <sup>-/-</sup> P12 | ns | > 0.999999 | Kruskal-Wallis test followed by Dunn's multiple comparison test |
| WT P12 vs. WT P14 | ns | > 0.999999 | Kruskal-Wallis test followed by Dunn's multiple comparison test |
| *Otof* <sup>-/-</sup> P12 vs. *Otof* <sup>-/-</sup> P14 | ** | 0.007 | Kruskal-Wallis test followed by Dunn's multiple comparison test |
| WT B6 P14 vs. *Otof* <sup>-/-</sup> B6 P14 | ns | > 0.999999 | Kruskal-Wallis test followed by Dunn's multiple comparison test |

# List of abbreviations

| | |
|---|---|
| AAV | Adeno-associated virus |
| ABR | Auditory brainstem response |
| AK | Recombinogenic region from the F1 phage sequence |
| AMPA | α-amino-3-hydroxy-5-methyl-4-isoxazolepropionic acid receptor |
| AP | Recombinogenic region from the alkaline phosphate gene |
| AP-2 | Clathrin-adaptor-protein complex 2 |
| AZ | Active zone |
| CaMKIIδ | $Ca^{2+}$/calmodulin-dependent serine/threonine kinase II delta |
| CDS | Coding sequence |
| dsDNA | Double-stranded DNA |
| Dual-AAV-Hyb | Dual-AAV hybrid strategy |
| Dual-AAV-OV | Dual-AAV overlap strategy |
| Dual-AAV-TS | Dual-AAV trans-splicing strategy |
| CIE | Clathrin-independent endocytosis |
| CME | Clathrin mediated endocytosis |
| CN | Cranial nerve |
| CtBP2 | Transcriptional repressor carboxy-terminal binding protein 2 |
| DFNB9 | Autosomal recessive non-syndromic deafness 9 (*OTOF*-related deafness) |
| DPOAE | Distortion-product otoacoustic emission |
| E | Embryonic day |
| HC | Hair cell |
| Hyb | Hybrid |
| IHC | Inner hair cell |
| ITR | Inverted terminal repeat |
| MyoVI | Myosin VI |
| MyoVII | Myosin VII |

## List of abbreviations

| | |
|---|---|
| NS | Normal size |
| OHC | Outer hair cell |
| OTOF | Gene coding for otoferlin |
| Otof | Otoferlin |
| $Otof^{-/-}$ | Otoferlin knock-out mutant mouse model |
| $Otof^{I515T/I515T}$ | p.Ile515Thr otoferlint knock-in mutant mouse model |
| $Otof^{Pga/Pga}$ | *Pachanga* otoferlin mutant mouse model (p.Asp1767Gly) |
| OV | Overlap |
| OZ | Oversize/overload |
| P | Postnatal day |
| P2A | Self-cleaving P2A peptide |
| PBS | Phosphate buffered saline |
| [PI(4,5)P$_2$] | Phosphatidylinositol 4,5-bisphosphate |
| PolyA | Polyadenylation sequence |
| PSD | Post-synaptic density |
| Rab8b | Small GTPase Rab protein 8b |
| RRP | Readily releasable synaptic vesicle pool |
| RWM | Round window membrane |
| SA | Splice acceptor site |
| SD | Splice donor site |
| SGNs | Spiral ganglion neurons |
| Shank1a | SH3 and multiple ankyrin repeat domains protein 1 |
| SNARE | Soluble N-ethylmaleimide-sensitive factor attachment protein receptor complex protein |
| SPL | Sound pressure level |
| ssDNA | Single-stranded DNA |
| Syt | Synaptotagmin |
| TM | Transmembrane domain |
| TS | Trans-splicing |
| Vglut3 | Vesicular glutamate transporter 3 |
| WPRE | Woodchuck hepatitis virus post-transcriptional regulatory element |

WT          Wild-type mice

# Acknowledgements

## Acknowledgements

Last but not least, I deeply thank my family and friends for their support and encouragement throughout my Ph.D..

# Curriculum vitae

Date of birth: July 2nd, 1988

Place of birth: Sana'a, Yemen

## Education

---

05/2015-Present        **Sensory and Motor Neuroscience (Ph.D.)**, Göttingen
                       University of Göttingen

➢ Ph.D. thesis title: „Dual-AAV mediated transfer of full-length otoferlin cDNA into auditory inner hair cells and the effects of different mutations in the *OTOF* gene on the protein levels and cellular distribution of otoferlin in auditory inner hair cells "

➢ Supervisor:  Dr. Ellen Reisinger

10/2012-04/2015        **Developmental, Neural, Behavioral Biology (M.Sc.)**, Göttingen
                       University of Göttingen

➢ Major: Developmental Biology, Neurobiology, Immunology

➢ Master thesis title: „Ultrastructural otoferlin protein localization and gene delivery of full length otoferlin cDNA to inner hair cells "

➢ Supervisor:  Dr. Ellen Reisinger

10/2008-03/2012        **Molecular Medicine (B.Sc.)**, Göttingen
                       University of Göttingen

➢ Bachelor thesis title: „The impact of I515T missense mutation on otoferlin in inner hair cells at higher temperatures "

➢ Supervisor:  Dr. Ellen Reisinger

10/2007-07/2008        **Fachgebundene Hochschulreife**, Munich
                       Studienkollege at the Universities of the Federal State of Bavaria

➢ Major: M Course (for medical and biological university programs)

06/2006                **Secondary School Final Examination (Abitur)**, Sana'a, Yemen
                       Azal School

➢ Major: Science section

## Professional Experience

11/2014-03/2015      **Research Assistant**, University Medical Center Göttingen
➢      Inner Ear Lab, Department of Otolaryngology
➢      Employer: Dr. Ellen Reisinger

05-06/2013      **Research Assistant**, University Medical Center Göttingen
➢      Inner Ear Lab, Department of Otolaryngology
➢      Employer: Dr. Ellen Reisinger

05-12/2012      **Research Assistant**, University Medical Center Göttingen
➢      Inner Ear Lab, Department of Otolaryngology
➢      Employer: Dr. Ellen Reisinger

## Publications

**Al-Moyed H**, Cepeda AP, Jung S, Moser T, Kügler S, Reisinger E **(2019)**. A dual-AAV approach restores fast exocytosis and partially rescues auditory function in deaf otoferlin knock-out mice. *EMBO Mol Med*. 11(1): pii: e9396.

Strenzke N*, Chakrabarti R*, **Al-Moyed H***, Müller A, Hoch G, Pangrsic T, Yamanbaeva G, Lenz C, Pan KT, Auge E, Geiss-Friedlander R, Urlaub H, Brose N, Wichmann C**, Reisinger E** **(2016)**. Hair cell synaptic dysfunction, auditory fatigue and thermal sensitivity in otoferlin Ile515Thr mutants. *EMBO J*. 35(23): 2519-2535.

Jung S, Maritzen T, Wichmann C, Jing Z, Neef A, Revelo NH, **Al-Moyed H**, Meese S, Wojcik SM, Panou I, Bulut H, Schu P, Ficner R, Reisinger E, Rizzoli SO, Neef J, Strenzke N, Haucke V, Moser T **(2015)**. Disruption of adaptor protein 2μ (AP-2μ) in cochlear hair cells impairs vesicle reloading of synaptic release sites and hearing. *EMBO J*. 34(21): 2686-702.

Ambrus GG, **Al-Moyed H**, Chaieb L, Sarp L, Antal A, Paulus W **(2012)**. The fade-in- Short stimulation - Fade out approach to sham tDCS - Reliable at 1 mA for naive and experienced subjects, but not investigators. *Brain Stimul.* 5 (4): 499-504.